



THE UNIVERSITY OF QUEENSLAND
A U S T R A L I A

**Mars Entry Afterbody Radiative Heating: An Experimental Study of
Nonequilibrium CO₂ Expanding Flow**

Sangdi Gu

Bachelor of Engineering (Aerospace) Class I Honors

A thesis submitted for the degree of Doctor of Philosophy at

The University of Queensland in 2017

School of Mechanical and Mining Engineering

Abstract

This thesis presents an experimental study of high temperature CO₂ flows – focusing on CO₂ flows subjected to rapidly expanding conditions relevant to Mars entry and representative of the corner expansion around the shoulder, between the windward and leeward flows, on an entry capsule. This is an important but poorly understood aspect of spacecraft design. Past numerical research showed that, during Mars entry, the CO₂ 4.3 μm and 2.7 μm band radiation from the aforementioned expanding flow produce non-negligible contributions to the heating of the capsule afterbody. Consequently, this radiative heating should be considered in the sizing of the afterbody thermal protection systems (TPS). However, due to a lack of experimental research, the nonequilibrium characteristics of CO₂ expanding flows are not well understood. Therefore, to help with the design of future Mars entry vehicles, it is necessary to investigate such flows.

The X2 expansion tube was used to facilitate the current study. Three expansion tube test conditions with differing velocities – nominally 2.8 km/s, 3.4 km/s, and 4.0 km/s – were developed. Using a two-dimensional wedge model with a 54° convex corner along with the new conditions, flows with similarities to the expanding flow around the shoulder of an aeroshell at certain Mars entry conditions were created. Mid-wavelength infrared emission spectroscopy of the 4.3 μm and 2.7 μm bands were performed on the flow. The spectroscopic measurements were used to estimate the rotational and vibrational temperatures and the CO₂ number densities using a spectral fitting method. Supplementing the spectroscopic measurements, filtered images of the 4.3 μm and 2.7 μm bands were taken to provide a two-dimensional spatial map of the band radiance in the flow around the wedge. Estimates of the experimental inflow conditions were produced by solving for the intermediate test gas states using measurements of various properties of the operating condition. CO₂ spectroscopic measurements of the inflow along with measurements of the wedge model shock location and deduced post-shock conditions were also used to help characterize the test conditions. Using estimated inflow conditions, three-dimensional CFD simulations of the experiments were conducted using a two-temperature model. The computed results were compared to the available measurements to examine the appropriateness of the current numerical model at simulating the CO₂ flow.

Important qualitative results were obtained in this thesis in regards to the high temperature CO₂ expanding flow. The temperatures estimated in the wedge flow using both the 2.7 and 4.3 μm spectroscopic measurements were found to be the same. This provides some confidence to the validity of NEQAIR, using CDSD-4000, at predicting CO₂ radiation under gas-dynamic conditions which are more relevant to Mars entry. Using the estimated rotational and vibrational temperatures, the CO₂

thermal non-equilibrium in the expanding flow was shown to be small – less than 10%. As the experiments simulate the expanding flow around the shoulder of an entry vehicle, this result is consistent with previous state-specific numerical computations done for such flow. Using vibrational relaxation rates tuned for post-shock conditions, CFD simulations significantly over-estimated the thermal non-equilibrium in the expanding flow, indicating the CO₂ vibrational relaxation is faster in expanding conditions than in post-shock conditions. This result is consistent with past results for N₂ and CO, as well as CO₂ at lower temperatures.

The qualitative results seem to indicate that no complex thermal non-equilibrium effects occur in the expanding flow. This means that multi-temperature models, using appropriate thermochemical rates, along with the NEQAIR radiation code should be capable of accurately predicting the CO₂ radiation in the current experiment. However, this is not a general result as the experiments concern the flow around the shoulder of an entry vehicle. In fact, based on the current results as well as results from past studies of CO₂ expanding flows, it is speculated that complex non-equilibrium states form far downstream of the initial expansion rather than near the start of the expansion.

Lastly, some interesting anomalies were discovered from the analyses on characterizing the experimental test conditions. While no clear anomalies were observed in the 4.0 km/s experiments, the 2.8 and 3.4 km/s experiments did have obvious anomalies. For the 2.8 and 3.4 km/s conditions, the experimental freestream CO₂ number densities estimated from pitot pressure measurements were factors of 4 – 5 greater than that estimated from spectroscopic measurements. Additionally, for the 2.8 and 3.4 km/s conditions, the measured post-shock temperature of the wedge was found to be approximately 30 % lower than that computed using the available freestream estimates. The difficulty in characterizing similar CO₂ test conditions has been reported for other impulse facilities. This difficulty is believed to be due to the fact that generating test conditions in these impulse facilities involves nonequilibrium CO₂ expanding flow processes, which are poorly understood and which need to be studied in the first place.

Declaration by author

This thesis is composed of my original work, and contains no material previously published or written by another person except where due reference has been made in the text. I have clearly stated the contribution by others to jointly-authored works that I have included in my thesis.

I have clearly stated the contribution of others to my thesis as a whole, including statistical assistance, survey design, data analysis, significant technical procedures, professional editorial advice, financial support and any other original research work used or reported in my thesis. The content of my thesis is the result of work I have carried out since the commencement of my higher degree by research candidature and does not include a substantial part of work that has been submitted to qualify for the award of any other degree or diploma in any university or other tertiary institution. I have clearly stated which parts of my thesis, if any, have been submitted to qualify for another award.

I acknowledge that an electronic copy of my thesis must be lodged with the University Library and, subject to the policy and procedures of The University of Queensland, the thesis be made available for research and study in accordance with the Copyright Act 1968 unless a period of embargo has been approved by the Dean of the Graduate School.

I acknowledge that copyright of all material contained in my thesis resides with the copyright holder(s) of that material. Where appropriate I have obtained copyright permission from the copyright holder to reproduce material in this thesis and have sought permission from co-authors for any jointly authored works included in the thesis.

Publications during Candidature

Conference publications

Gu, S., Morgan, R. G., & McIntyre, T. J. (2017). Study of the Afterbody Radiation during Mars Entry in an Expansion Tube. In *55th AIAA Aerospace Sciences Meeting*. AIAA paper 2017-0212. Grapevine, Texas.

Morgan, R. G., Rees, B., Rutherford, J., Jefferey M. M., Sollart, M., Morris, N. A., Bassore, K., James, C. M., Wei, H., **Gu, S.**, Lewis, S. W., & Landsberg, W. (2015). Advanced Hypersonic Vehicle Component Testing using Pre-Heated Models and Infrared Scanning. In *7th Asia-Pacific International Symposium on Aerospace Technology (APISAT)*. Cairns, Australia.

Publications included in this thesis

No publications included.

Contributions by others to the thesis

No contributions by others.

Statement of parts of the thesis submitted to qualify for the award of another degree

None.

Research Involving Human or Animal Subjects

No animal or human participants were involved in this research.

Acknowledgements

I would like to thank my principal supervisor Professor Richard Morgan who gave me the opportunity to study here at The University of Queensland. He successfully obtained the grant to purchase the mid-infrared spectroscopy system, therefore, making the work done in this thesis possible. He also spent a lot of his time teaching me about how expansion tubes work when I first started as a PhD student. He also introduced me to everyone at the Centre for Hypersonics when I first arrived which allowed me to fit into the group quickly. Richard showed me a lot of faith and he gave me a lot of freedom to do my research. Knowing that he trusted me gave me confidence and this gets the best out of me. Lastly, he never forgot about my undergraduate thesis project – space elevators – which he reckons is a funny idea!

I would like to thank my associate supervisor Associate Professor Tim McIntyre as well. The weekly one-to-one meetings which he arranged were really helpful and I liked it a lot. His knowledge of spectroscopy was really valuable to me. He was also the first person to read this thesis; he read everything in detail and he gave me a lot of advice on improving the writing of the thesis.

Furthermore, I would like to thank my other associate supervisor Dr Aaron Brandis. He proposed the thesis topic. He also provided me the opportunity to visit NASA Ames for a month. He introduced me to a lot of his colleagues there and the numerous technical discussions we had gave me a lot of ideas on doing the research. Aaron also gave me numerous constructive feedback about my work which I am so grateful for.

I would also like to thank the X2 expansion tube operators – Ranjith, Rory and Tim - who operated for me when I was doing my experiments, as well as the senior students in the group – Umar, Steven, Chris, Han, David Gildfind and Troy – who helped me with my learning when I first arrived in the Centre for Hypersonics.

Lastly, I thank my parents and extended family.

Financial support

This research was supported by an Australian Government Research Training Program Scholarship.

Keywords

expansion tubes, mars, carbon dioxide, radiation, expanding flows, hypersonics, spectroscopy, aerothermodynamics

Australian and New Zealand Standard Research Classification

ANZSRC code: 020503 Non-linear Optics and Spectroscopy 30%,

ANZSRC code: 090107 Hypersonic Propulsion and Hypersonic Aerodynamics 50%

ANZSRC code: 091501 Computational Fluid Dynamics 20%

Field of Research (FoR) Classification

FoR code: 0901, Aerospace Engineering 100%

Contents

Abstract.....	I
Contents	VIII
List of Figures.....	XI
List of Tables	XIX
1 Introduction	1
1.1 Background	1
1.2 Research Motivations and Objectives	1
1.3 Thesis Outline	3
2 Literature Review	5
2.1 Simulation of Afterbody Radiation during Mars Entry	5
2.2 Carbon Dioxide Thermochemistry and Radiation	10
2.3 Experimental Studies of High Enthalpy Expanding Flows.....	16
2.4 Summary of Findings	20
3 Development of the Experimental Test Conditions.....	22
3.1 Introduction	22
3.2 Test Condition Requirements.....	23
3.3 Generating the Required Test Conditions in the X2 Expansion Tube	26
3.4 Characterization of the Experiment Freestream Conditions	27
3.4.1 Carbon Dioxide Freestream Excitation.....	28
3.4.2 PITOT Code.....	30
3.4.3 CFD.....	35
3.4.4 Shock Wave Comparison.....	40
3.5 Similarities of Experiments to Flight	44

3.6	Features of the Generated Freestream Conditions	49
3.6.1	Freestream Steady Flow Duration	49
3.6.2	Repeatability	53
3.6.3	Freestream Core Flow Size and Uniformity	55
3.7	Conclusion.....	58
4	Carbon Dioxide Radiation Measurements.....	59
4.1	Introduction	59
4.2	Emission Spectroscopy	59
4.2.1	System Description	59
4.2.2	Alignment	63
4.2.3	Calibration.....	65
4.2.4	Characteristics of CO ₂ spectroscopic measurements	70
4.2.5	Delay and duration of exposure	71
4.2.6	Shot-to-shot variation.....	72
4.3	Filtered Two-Dimensional Imaging	80
4.3.1	Methodology	80
4.3.2	Results.....	84
4.4	Conclusion.....	94
5	Temperatures and Carbon Dioxide Number Density Estimates.....	96
5.1	Introduction	96
5.2	Parametric Study of the Spectra	96
5.3	Nozzle Exit Freestream Results	107
5.4	Wedge Flowfield Results	114
5.5	Post Oblique Shock Results	128
5.6	Conclusion.....	137
6	Numerical Study and Comparison to Experimental Results	139
6.1	Introduction	139

6.2	Band Radiance Parametric Study	139
6.3	Numerical Simulation Methodology	143
6.4	Three-Dimensional Effects of the Test Model	147
6.5	Comparison between CFD and experiment	157
6.5.1	Shock Wave Location	157
6.5.2	Band Radiance	158
6.5.3	Temperatures and carbon dioxide number density	164
6.5.4	Thermal non-equilibrium	169
6.6	Influence of the Carbon Dioxide Dissociation Rate.....	172
6.7	Conclusion.....	180
7	Conclusions and Future Work	183
7.1	Summary of Work Done	183
7.2	Outcomes.....	184
7.3	Future Work	187
References	189	
A	Hypersonic Flow Background	205
A.1	Characteristics of High Enthalpy Flows.....	205
A.2	Transitions between Energy Levels	210
A.3	Numerical Modelling of Non-Equilibrium Flows.....	212
A.4	Impulse Facilities for Studying High Enthalpy Flows	214
B	Engineering Drawings of Cold Driver	218
C	IR Camera Dewar Modification Instructions	223
D	Eilmer3 Two-Temperature Model Configuration Script	228
D.1	Chemical Kinetics Model.....	228
D.2	Thermal Kinetics Model.....	229

List of Figures

Figure 2.1. The Viking aeroshell geometry and the location of the thermocouples [1].	7
Figure 2.2. Comparison of the CO ₂ total mass fraction contour from the Boltzmann and non-Boltzmann models [13].	9
Figure 2.3. The vibrational modes of carbon dioxide. Adapted from [25].	11
Figure 2.4. The peak infrared emission as a function of shock velocity. The dashed curve is the expected intensity with no chemical relaxation. [37]	13
Figure 2.5. Measured locations of the mid-infrared emission [55].	15
Figure 2.6. The unsteady expansion used to study high enthalpy expanding flows. [64]	17
Figure 2.7. Wedge model used by Igra [59] and Drewry [60].	18
Figure 2.8. Generation of expanding flow by Wilson [61] and Blom et al. [62].	18
Figure 3.1. X2 expansion tube with fixed volume driver. [83].	22
Figure 3.2. Two-dimensional test model geometry. Dimensions shown are in mm and degrees.	23
Figure 3.3. Various Mars entry trajectories. Adapted from [44].	24
Figure 3.4. CFD contour of vibrational-electronic temperature for the Stardust geometry at a time of t=46 s. The red arrows bound the region on the shock wave where the majority of the radiating expanding flow is created. [84].	24
Figure 3.5. The experimental freestream static pressure required for matching the total pressure behind the shock between experiment and flight. In addition, the MSL entry trajectory from Figure 3.3 is plotted.	25
Figure 3.6. Shock wave comparison between experimental measurements and CFD predictions [89].	28
Figure 3.7. Comparison of measured and predicted shock locations for reflected shock tube freestream conditions with different densities but the same enthalpy [53].	29
Figure 3.8. Estimate of the hold time of the secondary diaphragm rupturing process.	30
Figure 3.9. Flow diagram of the method utilized to estimate the test conditions using the PITOT code.	33
Figure 3.10. The CFD simulation domain. All blocks are divided in the x direction.	36
Figure 3.11. Measured and computed shock speeds at various locations along the acceleration tube. The vertical dashed line marks the end of the acceleration tube (nozzle inlet).	38
Figure 3.12. Comparison of acceleration tube wall pressure traces between experiment and CFD..	40
Figure 3.13. Shock wave comparison between experiment and simulation results.....	41

Figure 3.14. A region in the 2.8 km/s experimental condition with the same carbon dioxide number density and vibrational temperature as a region in the t=74.0s flight condition.....	46
Figure 3.15. A region in the 3.4 km/s experimental condition with the same carbon dioxide number density and vibrational temperature as a region in the t=69.3s flight condition.....	47
Figure 3.16. A region in the 4.0 km/s experimental condition with the same carbon dioxide number density and vibrational temperature as a region in the t=65.1s flight condition.....	48
Figure 3.17. The top, middle and bottom graph correspond to the pitot probe traces of the 2.8, 3.4 and 4.0 km/s condition from shot x2s2906, x2s2905 and x2s2904 respectively. High frequency noise has been removed using moving average.....	50
Figure 3.18. Details of the infrared sensor experiments, showing the (a) optical setup and (b) sensor measurement locations in mm (measurement direction is into the page).	51
Figure 3.19. Infrared sensor traces at various points in the flow around the test model at different freestream conditions. The dotted vertical black lines on each graph mark the region of steady flow.	52
Figure 3.20. Nozzle exit showing the boundary layer, expansion fan and core flow.	55
Figure 3.21. Conehead pitot probe measurements at the nozzle exit. The top, middle and bottom graph correspond to the 2.8, 3.4 and 4.0 km/s condition respectively. The error bar of each point is based on the noise of the experimental data.	57
Figure 4.1. Mid-infrared spectroscopy system setup.	60
Figure 4.2. Czerny-Turner spectrometer. Adapted from [115]....	61
Figure 4.3. General layout of the mid-wavelength infrared detector. [117]	62
Figure 4.4. External InSb quantum efficiency curve for the IRC806 camera. [118].....	63
Figure 4.5. Locations of emission spectroscopy measurements.	63
Figure 4.6. Wedge model with the alignment plate attached to both edges.	64
Figure 4.7. Diffraction grating showing the relationship of the higher order signals. [119].....	65
Figure 4.8. Higher order lines in nm for calibrating the 2.7 μm band measurement. Grating is centred at 2900 nm.....	66
Figure 4.9. Higher order lines in nm for calibrating the 4.3 μm band measurement. Grating is centred at 4700 nm.....	66
Figure 4.10. Spectral axis calibration using the higher order krypton lines for the measurements centred at 4700 nm, left, and 2900 nm, right.	66
Figure 4.11. LandCal R1500T blackbody source with the nitrogen purge tube.....	67
Figure 4.12. Setup for performing absolute radiance calibration.	67
Figure 4.13. Calibration function of the 2.7 μm band for an exposure time of 80 μs	69
Figure 4.14. Calibration function of the 4.3 μm band for an exposure time of 50 μs	69

Figure 4.15. Example of a horizontal emission spectroscopy measurement above the test model of the 2.7 μm band from the current work.....	70
Figure 4.16. Example of a horizontal emission spectroscopy measurement above the test model of the 4.3 μm band from the current work.....	70
Figure 4.17. Integration time of the infrared camera along with the pitot pressure traces and the infrared sensor traces. The figures on the left corresponds to the nozzle exit freestream experiment. The figures on the right corresponds to the expansion fan experiment.....	72
Figure 4.18. Absolute band radiance measured from emission spectroscopy for the 2.8 km/s condition at the different locations above the test model.....	73
Figure 4.19. Absolute band radiance measured from emission spectroscopy for the 3.4 km/s condition at the different locations above the test model.....	74
Figure 4.20. Absolute band radiance measured from emission spectroscopy for the 4.0 km/s condition at the different locations above the test model.....	75
Figure 4.21. Infrared sensor traces of the upper and lower bound emission spectroscopy measurements for the 2.8 km/s condition. Solid line corresponds to upper bound measurements. Dashed line corresponds to lower bound measurements.....	77
Figure 4.22. Infrared sensor traces of the upper and lower bound emission spectroscopy measurements for the 3.4 km/s condition. Solid line corresponds to upper bound measurements. Dashed line corresponds to lower bound measurements.....	77
Figure 4.23. Infrared sensor traces of the upper and lower bound emission spectroscopy measurements for the 4.0 km/s condition. Solid line corresponds to upper bound measurements. Dashed line corresponds to lower bound measurements.....	78
Figure 4.24. Setup of the filtered two-dimensional imaging experiment.....	81
Figure 4.25. Efficiency curves of optical elements compared with the CO ₂ 2.7 μm (left) and 4.3 μm (right) emission bands.....	81
Figure 4.26. Exposure time of the infrared camera for the 4.3 μm band filtered imaging experiments along with the pitot pressure traces and the infrared sensor traces.....	83
Figure 4.27. Comparison of the 4.3 μm band radiance. Solid lines are from emission spectroscopy. Dashed lines are from filtered images. The top, middle and bottom rows corresponds to the 2.8, 3.4 and 4.0 km/s conditions respectively. The left, middle and right columns corresponds to the 3.25, 5.75 and 8.25 mm measurements above the test model respectively.....	85
Figure 4.28. Comparison of the 2.7 μm band radiance. Solid lines are from emission spectroscopy. Dashed lines are from filtered images. The top, middle and bottom rows corresponds to the 2.8, 3.4 and 4.0 km/s conditions respectively. The left, middle and right columns corresponds to the 3.25, 5.75 and 8.25 mm measurements above the test model respectively.....	86

Figure 4.29. 4.3 μm band radiance of the flowfield around the wedge for the 2.8 km/s condition	88
Figure 4.30. 2.7 μm band radiance of the flowfield around the wedge for the 2.8 km/s condition	88
Figure 4.31. 4.3 μm band radiance of the flowfield around the wedge for the 3.4 km/s condition	89
Figure 4.32. 2.7 μm band radiance of the flowfield around the wedge for the 3.4 km/s condition	89
Figure 4.33. 4.3 μm band radiance of the flowfield around the wedge for the 4.0 km/s condition	90
Figure 4.34. 2.7 μm band radiance of the flowfield around the wedge for the 4.0 km/s condition	90
Figure 4.35. Extracted shock wave locations from the filtered images compared to the extracted shock wave locations from the high-speed videos.	91
Figure 4.36. 2.8 km/s condition. The upper bound and lower bounds are the left and right figures respectively.	92
Figure 4.37. 3.4 km/s condition. The upper bound and lower bounds are the left and right figures respectively.	92
Figure 4.38. 4.0 km/s condition. The upper bound and lower bounds are the left and right figures respectively.	93
Figure 4.39. Calculated band radiance ratio at different temperatures and carbon dioxide number densities (cm^{-3}), for a pathlength of 125 mm.	94
Figure 5.1. The effect of changing the vibrational temperature on the 4.3 μm spectral radiance curve. CO ₂ number density is kept constant at $1 \times 10^{16} \text{ cm}^{-3}$. Absolute spectral radiance curves are plotted on the left column. Normalized spectral radiance curves are plotted on the right column.	98
Figure 5.2. The effect of changing the rotational temperature on the 4.3 μm spectral radiance curve. Carbon dioxide number density is kept constant at $1 \times 10^{16} \text{ cm}^{-3}$. Absolute spectral radiance curves are plotted on the graphs on the left column. Normalized spectral radiance curves are plotted on the graphs on the right column.	99
Figure 5.3. The effect of changing the carbon dioxide number density (cm^{-3}) on the 4.3 μm spectral radiance curve. Absolute spectral radiance curves are plotted on the graphs on the left column. Normalized spectral radiance curves are plotted on the graphs on the right column.	100
Figure 5.4. The significance of self-absorption at various temperatures and carbon dioxide number densities. The 4.3 μm spectral radiance curves are scaled with the carbon dioxide number density of $1 \times 10^{16} \text{ cm}^{-3}$.	101
Figure 5.5. The effect of carbon monoxide number density (cm^{-3}) on the 4.3 μm spectral radiance curve. Carbon dioxide number density is kept constant at $1 \times 10^{16} \text{ cm}^{-3}$. Absolute spectral radiance curves are plotted on the graphs on the left column. Normalized spectral radiance curves are plotted on the graphs on the right column.	102
Figure 5.6. The effect of changing the vibrational temperature on the 2.7 μm spectral radiance curve. Carbon dioxide number density is kept constant at $1 \times 10^{16} \text{ cm}^{-3}$. Absolute spectral radiance curves	

are plotted on the graphs on the left column. Normalized spectral radiance curves are plotted on the graphs on the right column.	103
Figure 5.7. The effect of changing the rotational temperature on the 2.7 μm spectral radiance curve. Carbon dioxide number density is kept constant at $1 \times 10^{16} \text{ cm}^{-3}$. Absolute spectral radiance curves are plotted on the graphs on the left column. Normalized spectral radiance curves are plotted on the graphs on the right column.	104
Figure 5.8. The effect of changing the carbon dioxide number density (cm^{-3}) on the 2.7 μm spectral radiance curve. Absolute spectral radiance curves are plotted on the graphs on the left column. Normalized spectral radiance curves are plotted on the graphs on the right column.	105
Figure 5.9. The effect of carbon monoxide number density (cm^{-3}) on the absolute 2.7 μm spectral radiance curve. Carbon dioxide number density is kept constant at $1 \times 10^{16} \text{ cm}^{-3}$	106
Figure 5.10. The significance of self-absorption at various temperatures and carbon dioxide number densities. The spectral radiance curves are scaled with the carbon dioxide number density of $1 \times 10^{16} \text{ cm}^{-3}$	107
Figure 5.11. Spectral fitting showing the best least squares fit against the measured spectrum from the freestream (nozzle exit) of the 2.8 km/s condition.....	109
Figure 5.12. Spectral fitting showing the best least squares fit against the measured spectrum from the freestream (nozzle exit) of the 3.4 km/s condition.....	109
Figure 5.13. Spectral fitting showing the best least squares fit against the measured spectrum from the freestream (nozzle exit) of the 4.0 km/s condition.....	110
Figure 5.14. Examples of fitted spectrums. The bottom right graph shows an example of a fitted 2.7 μm band, while the others show fitted 4.3 μm bands.	115
Figure 5.15. The estimated temperatures and carbon dioxide number densities for the 2.8 km/s condition. The top row corresponds to the upper bound measurements and the bottom row corresponds to the lower bound measurements.	116
Figure 5.16. The estimated temperatures and carbon dioxide number densities for the 3.4 km/s condition. The top row corresponds to the upper bound measurements and the bottom row corresponds to the lower bound measurements.	116
Figure 5.17. The estimated temperatures and carbon dioxide number densities for the 4.0 km/s condition. The top row corresponds to the upper bound measurements and the bottom row corresponds to the lower bound measurements.	117
Figure 5.18. The measurements at 3.25 mm, 5.75 mm and 8.25 mm above the test model correspond to the top, middle and bottom row of plots respectively.....	119
Figure 5.19. Calculated ratio of upstream to downstream temperature, left, and CO_2 number density, right, for the Prandtl-Meyer expansion fan assuming calorically perfect gas.	121

Figure 5.20. The ratio of the vibrational temperature to the rotational temperature for the 2.8 km/s condition	122
Figure 5.21. The ratio of the vibrational temperature to the rotational temperature for the 3.4 km/s condition	123
Figure 5.22. The ratio of the vibrational temperature to the rotational temperature for the 4.0 km/s condition	123
Figure 5.23. Comparison of the rotational temperature, vibrational temperature and carbon dioxide number density derived from the 4.3 μm and 2.7 μm band for the 2.8 km/s condition. Plots on the top, middle and bottom rows correspond to measurements made at 3.25 mm, 5.75 mm and 8.25 mm above the test model respectively.	125
Figure 5.24. Comparison of the rotational temperature, vibrational temperature and carbon dioxide number density derived from the 4.3 μm and 2.7 μm band for the 3.4 km/s condition. Plots on the top, middle and bottom rows correspond to measurements made at 3.25 mm, 5.75 mm and 8.25 mm above the test model respectively.	126
Figure 5.25. Comparison of the rotational temperature, vibrational temperature and carbon dioxide number density derived from the 4.3 μm and 2.7 μm band for the 4.0 km/s condition. Plots on the top, middle and bottom rows correspond to measurements made at 3.25 mm, 5.75 mm and 8.25 mm above the test model respectively.	127
Figure 5.26. Flow around the wedge for the 2.8 km/s (a), 3.4 km/s (b) and 4.0 km/s (c) condition.	129
Figure 5.27. Estimated post-shock temperatures for nominal shock velocities of 3.1 and 3.75 km/s [44].....	131
Figure 5.28. Comparison of the computed shock wave location to the measured shock wave location.	136
Figure 6.1. Influence of the carbon dioxide number density (cm^{-3}) to the band radiance with no carbon monoxide. Each curve is normalized to the band radiance value at a carbon dioxide number density of $1.0 \times 10^{15} \text{ cm}^{-3}$	140
Figure 6.2. Influence of carbon monoxide number density (cm^{-3}) to the band radiance with carbon dioxide number density constant at $1.0 \times 10^{16} \text{ cm}^{-3}$. Each curve is normalized to the band radiance with zero carbon monoxide.....	140
Figure 6.3. Influence of thermal equilibrium temperature on band radiance at different CO ₂ number densities (cm^{-3}). Each curve is normalized to the band radiance value at 1000 K.	141
Figure 6.4. Influence of Tr - Tv non-equilibrium on band radiance at a constant CO ₂ number density of $1.0 \times 10^{16} \text{ cm}^{-3}$. The left column shows the influence of changing the Tr while Tv is constant. The right column shows the influence of changing the Tv while Tr is constant.	142

Figure 6.5. Dimensions of the three-dimensional simulation domain for simulating the flowfield around the wedge model. Also shown is the block topology.	145
Figure 6.6. Boundary conditions used for the simulation of the flowfield around the wedge. Also shown is the block topology.	146
Figure 6.7. Edge effects of the two-dimensional wedge model.....	147
Figure 6.8. A slice in each of the X-Z, X-Y and Y-Z plane showing the temperature contour.....	147
Figure 6.9. A slice in the X-Z plane at 5.75 mm above the top surface of the wedge model showing the temperature contour. Flow direction is from bottom to top.....	148
Figure 6.10. A slice in the Y-Z plane at 10 mm behind the convex corner showing the temperature contour.	148
Figure 6.11. Locations of the lines of sight across the test model extracted to study the variation of the flow properties along the width of the test model. Flow direction is from bottom to top.	149
Figure 6.12. Normalized carbon dioxide number density and temperature across lines of sight. Top, middle and bottom rows correspond to the 2.8, 3.4 and 4.0 km/s conditions.....	150
Figure 6.13. Carbon dioxide number density and temperature across lines of sight. Top, middle and bottom rows correspond to the 2.8, 3.4 and 4.0 km/s conditions.	151
Figure 6.14. Comparison of the band radiance calculated from two-dimensional and three-dimensional simulations. The left, middle and right figures correspond to the 2.8, 3.4 and 4.0 km/s conditions respectively. The two-dimensional radiation calculation assumes a path length of 100 mm.	154
Figure 6.15. Filtered images of the radiating flow beyond the edge of the wedge model; flow direction is from right to left. Vertical slices are extracted at various locations in the images and plotted in the graphs in the right column. The top, middle and bottom rows correspond to the 2.8, 3.4 and 4.0 km/s conditions respectively.....	156
Figure 6.16. Comparison of the measured shock wave locations to the simulated shock wave locations.	157
Figure 6.17. Scaling the CFD curve to match the experimentally measured curve at ‘point 1’ and ‘point 2’.....	159
Figure 6.18. Scaling factors for point 1 and 2 and for the 2.7 and 4.3 μm band. The top and bottom rows correspond to comparisons made with the PITOT code and spectroscopic measurement estimated inflow conditions respectively. The left, middle and right columns correspond to the measurements at 3.25, 5.75 and 8.25 mm above the test model.....	160
Figure 6.19. Comparison of post-shock band radiance between experiment and CFD using various chemical kinetics model [44]. The model ‘BC’ is the same model used in the current work.	161
Figure 6.20. The scaling factors behind normal shock waves derived by Cruden et al. [44].....	162

Figure 6.21. Comparison of the rotational temperature, vibrational temperature and CO ₂ number density between experiment and CFD for the 2.8 km/s condition. The top, middle and bottom row correspond to the 3.25, 5.75 and 8.25 mm measurement above the test model.	165
Figure 6.22. Comparison of the rotational temperature, vibrational temperature and CO ₂ number density between experiment and CFD for the 3.4 km/s condition. The top, middle and bottom row correspond to the 3.25, 5.75 and 8.25 mm measurement above the test model.	166
Figure 6.23. Comparison of the rotational temperature, vibrational temperature and CO ₂ number density between experiment and CFD for the 4.0 km/s condition. The top, middle and bottom row correspond to the 3.25, 5.75 and 8.25 mm measurement above the test model.	167
Figure 6.24. Comparison of the ratio between the vibrational temperature and rotational temperature from experiment and CFD. The top, middle and bottom row correspond to the 2.8, 3.4 and 4.0 km/s condition respectively. The left, middle and right column correspond to the 3.25, 5.75 and 8.25 mm measurement above the test model respectively.	170
Figure 6.25. The two-dimensional simulation domain of the wedge model along with the boundary conditions and the block topology. The figure on the right shows the zoomed in view of the simulation domain around the leading edge.	173
Figure 6.26. The two-dimensional simulation mesh.....	173
Figure 6.27. Comparison of the 2.7 and 4.3 μm band radiance from simulations using different CO ₂ dissociation rates. The left, middle and right columns correspond to the 2.8, 3.4 and 4.0 km/s conditions respectively.....	175
Figure 6.28. Comparison of the temperatures and CO ₂ number density from simulations using different CO ₂ dissociation rates. The top, middle and bottom rows correspond to the 2.8, 3.4 and 4.0 km/s conditions respectively.....	176
Figure 6.29. Locations of the extracted top and bottom streamlines data in Figure 6.30.....	179
Figure 6.30. Simulated CO ₂ mole fraction along the top and bottom streamline for different CO ₂ dissociation rates. The vertical black lines on each curve represents the approximate location of the expansion fan head.....	180

List of Tables

Table 2.1. MSL best-estimated-trajectory points freestream conditions. [12]	8
Table 2.2. Chemical reactions in low and medium velocity pure carbon dioxide freestreams.	14
Table 2.3. List of experiments performed for the study of high enthalpy expanding flow; sorted chronologically.	19
Table 3.1. The driver conditions and fill pressures required to generate the necessary experimental test conditions.	27
Table 3.2. Shock processed test gas states in the shock tube from thermochemical equilibrium analysis.....	32
Table 3.3. Test gas properties calculated by PITOT in the acceleration tube (nozzle inlet) after unsteady expansion.	34
Table 3.4. Equilibrium and calorically perfect gas freestream estimates (nozzle exit) from PITOT.34	
Table 3.5. Nozzle exit properties during the steady test time from CFD. The flathead pitot pressure is taken at a radial distance of 18 mm from the centerline. The conical pitot pressure is the average pressure measured across a 144 mm diameter. PG means perfect gas and EQ means thermochemical equilibrium.....	37
Table 3.6. Operating condition properties at the acceleration tube exit/nozzle inlet from CFD.	37
Table 3.7. Survey of low and medium velocity carbon dioxide conditions in expansion tubes.....	42
Table 3.8. The best estimate of the freestream (nozzle exit) conditions. The uncertainties were estimated from the variation and uncertainties of the measured properties of each operating condition.	
.....	43
Table 3.9. Summary of the corresponding MSL BET freestream condition for each experimental freestream condition.....	45
Table 3.10. Summary of steady duration times in μ s. Time is given relative to shock arrival.....	53
Table 3.11. Summary of the consistency of the measured operating condition properties. The presented uncertainty corresponds to the scatter of the measurements.	53
Table 3.12. Measured operating condition properties and estimated freestream properties for pitot survey shots.....	54
Table 4.1. Optical properties used for the emission spectroscopy work.	60
Table 4.2. The delay and duration of the exposure for the emission spectroscopy measurements. Delay is measured relative to shock arrival at the test model.	71

Table 4.3. Shock speeds and pressure measurements of the emission spectroscopy measurements at 3.25 mm above the test model for the 2.8 km/s condition. * = lower bound of radiation. † = upper bound of radiation.....	73
Table 4.4. Shock speeds and pressure measurements of the emission spectroscopy measurements at 5.75 mm above the test model for the 2.8 km/s condition. * = lower bound of radiation. † = upper bound of radiation.....	73
Table 4.5. Shock speeds and pressure measurements of the emission spectroscopy measurements at 8.25 mm above the test model for the 2.8 km/s condition. * = lower bound of radiation. † = upper bound of radiation.....	74
Table 4.6. Shock speeds and pressure measurements of the emission spectroscopy measurements at 3.25 mm above the test model for the 3.4 km/s condition. * = lower bound of radiation. † = upper bound of radiation.....	74
Table 4.7. Shock speeds and pressure measurements of the emission spectroscopy measurements at 5.75 mm above the test model for the 3.4 km/s condition. * = lower bound of radiation. † = upper bound of radiation.....	75
Table 4.8. Shock speeds and pressure measurements of the emission spectroscopy measurements at 8.25 mm above the test model for the 3.4 km/s condition. * = lower bound of radiation. † = upper bound of radiation.....	75
Table 4.9. Shock speeds and pressure measurements of the emission spectroscopy measurements at 3.25 mm above the test model for the 4.0 km/s condition. * = lower bound of radiation. † = upper bound of radiation.....	76
Table 4.10. Shock speeds and pressure measurements of the emission spectroscopy measurements at 5.75 mm above the test model for the 4.0 km/s condition. * = lower bound of radiation. † = upper bound of radiation.....	76
Table 4.11. Shock speeds and pressure measurements of the emission spectroscopy measurements at 8.25 mm above the test model for the 4.0 km/s condition. * = lower bound of radiation. † = upper bound of radiation.....	76
Table 4.12. Shock speed and pressure measurements for the experiments of freestream radiation measurement, for the 2.8 km/s condition.....	79
Table 4.13. Shock speed and pressure measurements for the experiments of freestream radiation measurement, for the 3.4 km/s condition.....	79
Table 4.14. Shock speed and pressure measurements for the experiments of freestream radiation measurement, for the 4.0 km/s condition.....	79
Table 4.15. Optical properties used for the filtered two-dimensional imaging work.....	81

Table 4.16. The moment and length of the exposure for the filtered imaging measurements. Delay is measured relative to shock arrival at the test model.....	84
Table 5.1. Range of parameters investigated for the parametric study.....	97
Table 5.2. Comparison of the estimated temperatures and number densities from the spectroscopic measurement and the best estimate of the temperatures and number densities from the PITOT code for the 2.8 km/s condition at the nozzle exit.....	109
Table 5.3. Comparison of the estimated temperatures and number densities from the spectroscopic measurement and the best estimate of the temperatures and number densities from the PITOT code for the 3.4 km/s condition at the nozzle exit.....	110
Table 5.4. Comparison of the estimated temperatures and number densities from the spectroscopic measurement and the best estimate of the temperatures and number densities from the PITOT code for the 4.0 km/s condition at the nozzle exit.....	110
Table 5.5. Measured ratio of upstream to downstream temperature and CO ₂ number density for the expansion fan, at 3.25 mm above the model.....	119
Table 5.6. Estimated freestream properties from both the PITOT code and spectroscopic measurements.....	130
Table 5.7. The measured post-shock temperature compared with the calculated frozen and equilibrium limits from two different freestream estimates.	131
Table 5.8. Mole fraction of helium required to match the frozen post-shock temperature to the measured post-shock temperature for the 2.8 and 3.4 km/s conditions.....	133
Table 5.9. The measured post-shock carbon dioxide number density compared with the calculated frozen and equilibrium limits from two different freestream estimates.	134
Table 5.10. Freestream condition tuned to match the post-shock frozen CO ₂ number density to the measured CO ₂ number density for the 2.8 and 3.4 km/s conditions.....	135
Table 5.11. Freestream conditions used to study the influence of having helium in the freestream.	136
Table 6.1. The kinetics model proposed by Cruden et al [44] for use with the modified Arrhenius equation.....	143
Table 6.2. Estimated freestream properties from both the PITOT code and radiation measurements used for the CFD simulation of the experiments.	145
Table 6.3. Comparison of the spectra fitting estimated temperatures and number densities, to the CFD centreline and average temperatures and number densities, for each line of sight.....	153
Table 6.4. Freestream properties used for the CFD simulation for the carbon dioxide dissociation rate study in this section.....	174

Table 6.5. The CO₂ mole fraction at the peak of the temperature curves in Figure 6.28. Also presented is the inflow and equilibrium post-shock CO₂ mole fractions.....177

1 Introduction

1.1 Background

During atmospheric entry, entry vehicles will encounter large heat transfers. To support the design of future atmospheric entry vehicles, it is important to investigate the aeroheating environment which the vehicle will encounter. The heat transfer to the entry vehicle is in the form of convection and radiation. This thesis specifically concerns the problem of radiative heating on the afterbody of vehicles during Mars entry, arising from expanding flows.

Protection of the entry vehicle afterbody is important for surviving atmospheric entry and preventing damage to the vital instruments which are normally contained in the rear of the entry vehicle. In the past, the effect of radiative heating on the afterbody of a Mars entry vehicle has been largely neglected [1]. Afterbody thermal protections were designed by considering only the convective heating [2]. However, in certain regions of the Mars entry trajectory, the radiative heat load is believed to be at least as large, if not larger, than the convective heat load on the vehicle afterbody [3] [4] [5] [6] [7]. The entry vehicle afterbody typically encompasses approximately 2/3 of the total exposed surface area, meaning that the afterbody thermal protection system (TPS) may make significant contributions to the total mass. Also, any extra TPS required on the afterbody will shift the centre of gravity of the vehicle towards the rear and adversely affecting stability. Hence, it is necessary to consider the radiative component of heat flux when designing the afterbody TPS for Mars entry [8].

1.2 Research Motivations and Objectives

Details of the thermochemical non-equilibrium and radiation processes in expanding flows encountered during Mars entry is not well understood and, therefore, it is unclear how well these processes are simulated using the current numerical models. An overview of the general thermochemical non-equilibrium and radiation processes involved in hypersonic flows is presented in appendix A.1 and A.2. Correct predictions of the radiative emission of a gas mixture requires accurate predictions of the species number densities and the excitation temperatures. Due to the thermochemical non-equilibrium encountered during Mars entry, calculating accurate number densities and excitation temperatures requires accurate thermochemical kinetics models. The Mars atmosphere mainly consists of CO₂. The non-equilibrium thermochemistry of CO₂ in expanding flow

has never been experimentally investigated in detail, though a significant amount of work has been done for the non-equilibrium thermochemistry in CO₂ shock layers. Hence, the current non-equilibrium thermochemical models - multi-temperature models - are designed and tuned for flow behind shock waves (an overview of multi-temperature models is presented in appendix A.3). Applying these models on expanding flows may produce inaccurate results. Furthermore, in addition to requiring the correct species number densities and the excitation temperatures, correct predictions of the radiative emission of a gas mixture also requires accurate radiation models. The validity of the current CO₂ radiation models has not been examined for nonequilibrium expanding flow conditions. Accordingly, to better define the afterbody radiative heating during Mars entry, there are significant needs to experimentally investigate the thermochemical non-equilibrium and radiation processes in CO₂ expanding flows.

Therefore, the objective of this thesis is to study the thermochemical nonequilibrium and radiation of CO₂ flows in the laboratory and examine the appropriateness of the current thermochemical and radiation models in describing the flows; the focus is on the CO₂ flow under expanding conditions relevant to Mars entry in particular. To achieve the objective, the specific goals of this thesis are to:

1. Design and characterize new conditions for an expansion tube facility (a synopsis of expansion tube facilities is presented in appendix A.4), which adequately replicate the Mars entry conditions where carbon dioxide radiation is important.
2. Assemble a mid-infrared spectroscopy system suitable for use with expansion tube experiments. In addition, a corresponding methodology for absolute radiance calibration of the mid-infrared spectroscopy measurements needs to be developed.
3. With the mid-infrared spectroscopy system, collect data to examine the various characteristics of the carbon dioxide radiating flow generated around the appropriate test model in the expansion tube experiments.
4. Perform numerical simulations of the experiments to assess the accuracy of the current thermochemical and radiation models by comparing to the data from experimental measurements.

1.3 Thesis Outline

The contents of the dissertation is structured as follows:

Chapter 2. A literature investigation is conducted to look at the work done relevant to the thermochemistry of carbon dioxide and the high enthalpy expanding flows. Simulations done to estimate the afterbody radiation during Mars entry are examined. Experiments conducted to study the non-equilibrium thermochemistry of carbon dioxide are discussed. A detailed list of previous experiments performed on high enthalpy expanding flows is presented.

Chapter 3. Three new X2 expansion tube conditions were developed to study the carbon dioxide radiation during Mars entry using a wedge model with a convex corner. Various characteristics of the new conditions were assessed by taking measurements of the operating condition properties, namely the shock speeds, wall pressures and pitot pressures. Work was done to try to accurately estimate the freestream properties for these new conditions. Similarities between the experimental conditions and actual Mars entry conditions were determined.

Chapter 4. The emission spectroscopy system used in the experiments is described along with the calibration procedure. The spectroscopy system was used to take measurements of the expansion tube freestream as well as horizontal measurements above the wedge model. Additionally, a filtered imaging system is described along with the calibration procedure. The filtered imaging system was used to take two-dimensional images of the flowfield around the test model. The spectroscopic measurements and filtered two-dimensional images are presented and assessed.

Chapter 5. Rotational and vibrational temperatures as well as the carbon dioxide number densities are derived from the emission spectroscopy measurements. The deduced temperatures and number densities from the radiation measurements of the freestreams are used to further characterize the inflow conditions. The derived temperatures and carbon dioxide number densities from the horizontal measurements above the test model are used for detailed investigation of the features of the high temperature CO₂ flowfield around the test model. Furthermore, the estimated post-shock temperatures and CO₂ number densities from the measurements above the test model are used to assess the accuracy of the estimated inflow conditions.

Chapter 6. The carbon dioxide radiation during Mars entry is assessed numerically in this section. A sensitivity study was carried out for carbon dioxide radiation to determine the importance of the various properties for intensity of the emission. Numerically computed radiation, temperatures and carbon dioxide number densities were compared to those derived from the experimental measurements in order to assess how well the current numerical models predict the carbon dioxide

radiating flow. The influence of the carbon dioxide dissociation rate on the flowfield emission, temperatures and carbon dioxide number densities are examined. Furthermore, the influence of having helium in the freestream is assessed to examine the possibility that the experiment freestream contained helium.

Chapter 7. The important findings from the dissertation is summarized here along with the conclusion. In addition, possible future works are recommended.

2 Literature Review

2.1 Simulation of Afterbody Radiation during Mars Entry

Experimental studies of radiating carbon dioxide expanding flows have not been found in past literature. However, work has been done numerically in simulating the afterbody radiation during Mars entry. From literature survey, the first known study of the effects of afterbody radiation during Mars entry was Gromov and Surzhikoy in 2002 [3]. They conducted viscous, finite rate chemistry, one temperature, axisymmetric simulations of the Mars Sample Return Orbiter (MSRO) aeroshell at four different trajectory points with velocities ranging from 5.7km/s to 3.5km/s. Their results showed that the afterbody radiative heat flux is of a comparable value to the afterbody convective heat flux for the entire range of velocity conditions simulated. They also showed that the peak radiative heat flux on the afterbody occurs at a later time than the peak afterbody convective heat flux during Mars entry. In their study, from the freestream conditions investigated, the highest afterbody radiative heat flux corresponded to the trajectory point with a velocity of 4.0km/s, while the highest convective heat flux calculated was at 5.2km/s. This is an interesting result because, in the forebody, the peak radiative heat flux generally occurs at a higher velocity than the convective heat flux. That is why, in the past, radiation was thought to be important only at high velocity conditions. However, it is now known that radiation can also be important at lower velocities.

In 2008, Rouzaud et al. [4] performed an independent numerical study of the heat transfer encountered by the MSRO during Mars entry. Using their own code, PHARAON, a 2-D axisymmetric, viscous simulation of the MSRO was conducted at the 5223 m/s velocity point on its trajectory, using the one-temperature model. Their results support the findings of Gromov and Surzhikov [3] showing that radiative heating is greater than convective heating at most locations on the afterbody. A consequence of this is that the afterbody radiative heat transfer cannot be neglected when sizing the afterbody heatshield for Mars entry.

Lino da Silva and Beck [5] were the first to perform afterbody radiative heat transfer calculations for a conventional blunt body entry vehicle, which does not have the step structure as seen on the MSRO afterbody. In 2011, they performed axisymmetric, two-temperature, finite rate chemistry simulations of two EXOMARS configurations; a small and a large configuration. They performed the simulations at six different trajectory points for the small configuration and five different trajectory points for the large configuration, with velocities ranging from 4.0km/s to 2.3km/s. For the large configuration, the

highest calculated radiative heat flux occurred at 2.8km/s. For the small configuration, the highest calculated radiative heat flux was at 3.0km/s. The results of Lino da Silva and Beck also showed that the afterbody radiation during Mars entry is produced by carbon dioxide molecules emitting in the mid infrared region. This explains why the afterbody radiation increases with decreasing velocity, coming to a peak at around 3km/s, since the decreasing velocity causes an increase in the amount of carbon dioxide molecules. Future Mars missions are proposed to use aerocapture trajectories and will involve low speed entry of very large vehicles [9] [10]. This may result in a trajectory in which the entry vehicle will spend more time at the velocity regime where incomplete CO₂ dissociation occurs. This further increases the importance of the carbon dioxide infrared radiation on the backshell heating of Mars entry vehicles [11]. Consequently, such an observation would mean that the heat shield sizing of future Mars entry aeroshells will need to account for significant carbon dioxide radiation.

In 2012, Fujita et al. [6] performed a three dimensional numerical study of a conceptual aeroshell at several points along a Mars aerocapture trajectory with a velocity ranging from 4.2km/s to 6km/s. The study was conducted using a two-temperature model for the thermochemistry while the SPRADIAN2 analysis package was used for the radiation calculations. The results of this study were consistent with that from the previous axisymmetric studies. Additionally, Fujita et al. showed that the afterbody radiation is produced purely by carbon dioxide emission in the 2.7 μm and 4.3 μm wavelength bands. According to Fujita et al. [6], a significant amount of backshell heating on a Martian aerocapture entry vehicle is caused by radiation from CO₂ ro-vibrational transitions. Fujita et al. produced three-dimensional computational fluid dynamics (CFD) simulations of a small Martian aerocapture spacecraft at five different flight conditions, corresponding to five different instances during the Martian entry. The different flight conditions had velocities ranging from 4.2 km/s to 5.9 km/s. Their CFD simulations were created using the two-temperature model to model the thermochemistry while using the Landau-Teller relaxation model to determine the vibrational relaxation. The chemical model had 11 species of gas along with a set of 22 reactions. It should be noted that no ionization was incorporated into the chemical model as the amount of ionization at those flight conditions is negligible. Their results showed that, under these conditions and at certain locations on the aftbody, the radiative heat transfer is comparable to the convective heat transfer. This is because the recombination during the expansion can create a significant density of vibrationally excited CO₂ and excited CO₂, as mentioned before, is shown to be able to produce significant radiation in the mid-infrared region under such entry conditions.

To further confirm the importance of the afterbody radiation during Mars entry, in 2013, Potter et al. [1] numerically investigated the hypothesis that the discrepancy between the thermocouple-derived heating on the afterbody of the Viking aeroshell and the respective CFD results is caused by the mid-

infrared carbon dioxide radiation. The Viking aeroshell contained two thermocouples on the afterbody, as shown on Figure 2.1. These thermocouples measure the total surface heating. Using a one-temperature model, they investigated one particular trajectory point with a velocity of 3.7km/s at 11700.5s after the start of the deorbit burn. Both the preflight and postflight convective heating predictions were lower than the flight thermocouple measurements. Hence, it was hypothesized that the discrepancy is caused by neglecting the radiative heating. At the aluminium surface thermocouple location, a good match in total heating is obtained after accounting for the radiative heating which is 65% of the total heating supporting the hypothesis. At the fiberglass surface thermocouple location, however, CFD significantly over estimates the total heating after accounting for the radiative heating. Potter et al. believes this shows the current inability to accurately calculate the afterbody aeroheating in general. They suggest significant effort should be made to improve our current ability of predicting the afterbody radiative and convective heating.

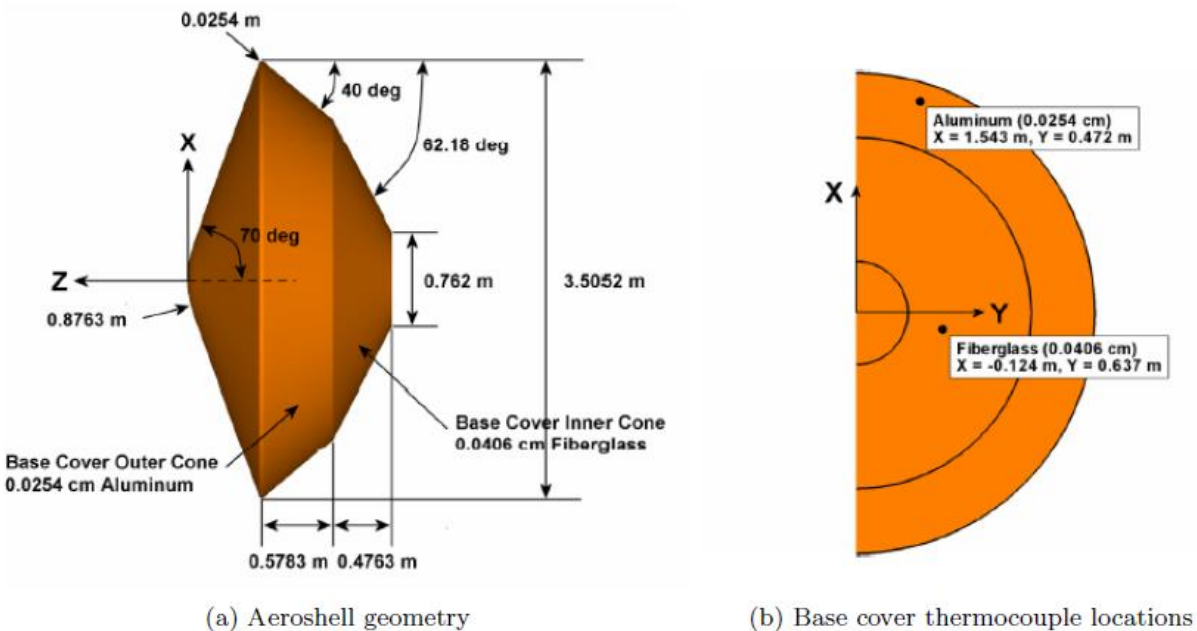


Figure 2.1. The Viking aeroshell geometry and the location of the thermocouples [1].

Recent numerical work on simulating the afterbody radiation during Mars entry was done by Brandis et al. in 2015 using the two-temperature model. The convective and radiative heat flux was calculated for the Phoenix and Mars Science Laboratory (MSL) aeroshell at various trajectory points. The results, consistent with previous studies, showed that the afterbody radiative heating is at least of a comparable value to the convective heating, if not dominant. Hence, although the afterbody radiative heating is small compared to the heating on the forebody, it is still significant compared to what the afterbody TPS is designed for. Additionally, they also conducted a code-to-code comparison of NASA's LAURA/HARA and DPLR/NEQAIR codes for calculating the afterbody radiation during Mars entry. Excellent agreement is observed at all locations on the aeroshell when calculation was

carried out using the full angular integration method. They also showed that the tangent slab method cannot be used to calculate the afterbody radiation because it significantly overestimates the radiation. Hence, the full angular integration method must be used for estimating the afterbody radiation during Mars entry.

Table 2.1. MSL best-estimated-trajectory points freestream conditions. [12]

	t , s	H , km	V_∞ , km/s	p_∞ , erg/cm ³	ρ_∞ , g/cm ³	T_∞ , K
1	45.1	59.3	5.866	4.29	0.265×10^{-7}	85.7
2	49.1	54.1	5.851	10.8	0.457×10^{-7}	127
3	55.5	46.0	5.793	32.9	0.120×10^{-6}	145
4	61.5	38.8	5.66	80.1	0.270×10^{-6}	157
5	65.1	34.7	5.515	131	0.431×10^{-6}	161
6	69.3	30.2	5.258	222	0.696×10^{-6}	168.5
7	74.0	25.8	4.862	366	1.140×10^{-6}	169.8
8	75.1	24.8	4.745	407	1.250×10^{-6}	172.1
9	80.5	20.8	4.144	629	1.860×10^{-6}	178.9
10	84.7	18.6	3.633	804	2.330×10^{-6}	182.7
11	90.5	16.3	3.023	1020	2.870×10^{-6}	188.1
12	97.6	14.5	2.426	1220	3.360×10^{-6}	192.2

Another recent numerical study was done by Surzhikov [7] in 2016 using an advanced multi-temperature model involving multiple vibrational temperatures. The study consisted of the full flowfield simulation of the MSL aeroshell at numerous points, shown on Table 2.1, on its estimated entry trajectory. The trajectory point estimates used by Surzhikov are known as the best-estimated-trajectory (BET) and it was first reported by Edquist et al. [12] for use in their numerical study. The study by Edquist et al. contains only the heat flux solutions for the forebody while Surzhikov provides the heat flux solutions for the afterbody as well. Surzhikov's results showed that the radiative heat flux at any point on the afterbody is either of a comparable value to or significantly greater than the corresponding convective heat flux for all the trajectory points studied. In fact, the result showed that the overall difference between the radiative and convective heating increases with decreasing velocity. This results from the convective heating decreasing with decrease in velocity while the radiative heating does not change. Apart from the first trajectory point, the absolute value of the afterbody radiative heating at any location remains roughly the same throughout the entry trajectory. A peak in radiative heating does occur at trajectory points 7 and 8 but this is marginal. The afterbody radiative heating at the first trajectory point is an order of magnitude less than the rest and this is most likely due to the very low density. Also, this study reinforced previous findings as it showed that the radiative heating on the afterbody is caused by the 2.7 μm and 4.3 μm emission bands of carbon dioxide molecules.

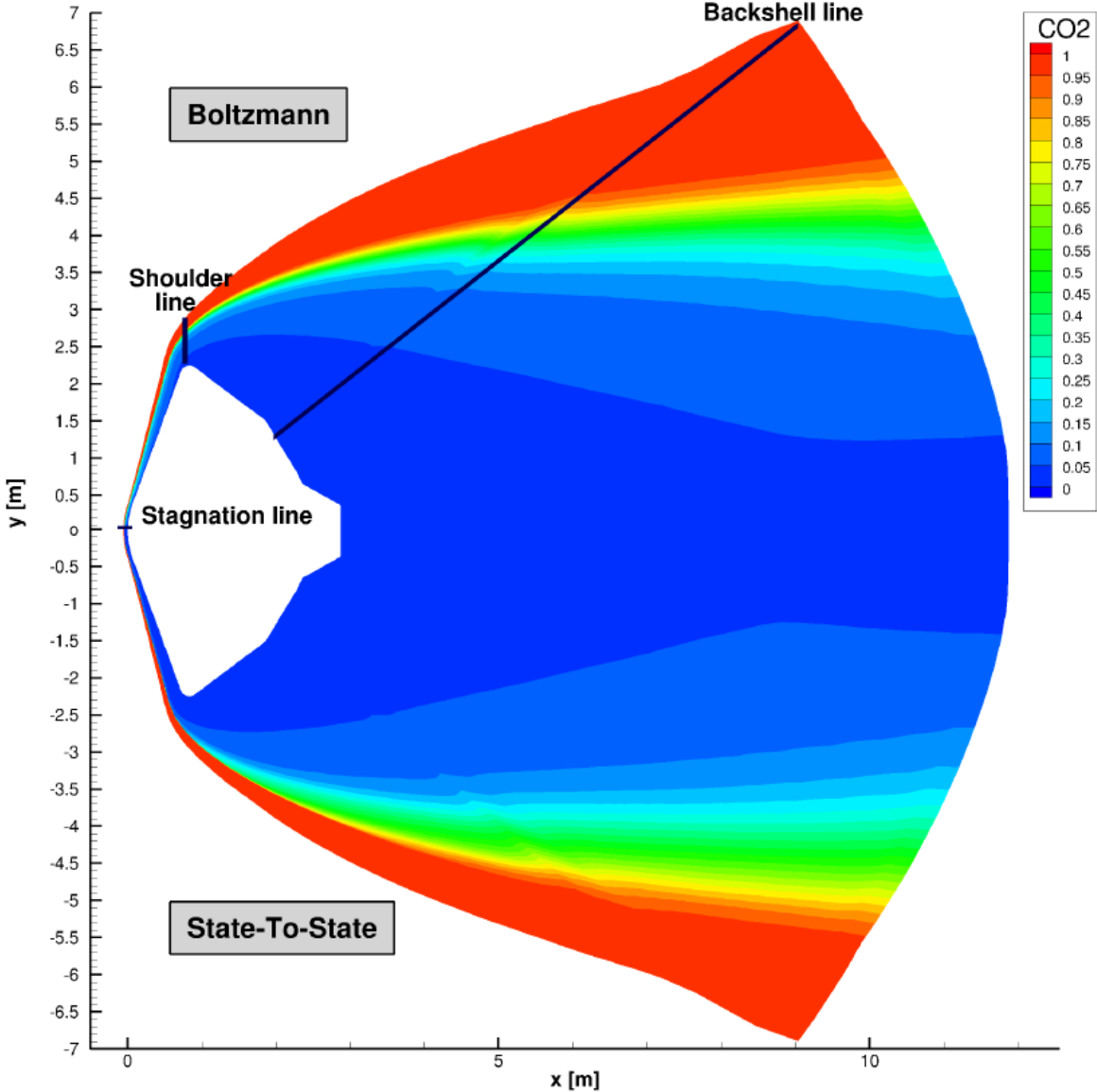


Figure 2.2. Comparison of the CO₂ total mass fraction contour from the Boltzmann and non-Boltzmann models [13].

The most recent work was done by Sahai et al. [14] [13] using reduced order non-Boltzmann models (an overview of non-Boltzmann models is presented in appendix A.3). In their more recent work in 2017 in reference [13], Sahai et al. used their reduced order non-Boltzmann thermochemical model to perform an axisymmetric simulation of the Mars Science Laboratory. This result is compared with the result from using the conventional one-temperature model. The translational temperature and total CO₂ mass fraction, Figure 2.2, compared well between the two simulation results at all locations in the flowfield. Furthermore, the CO₂ vibrational population distribution calculated from both simulations match along the stagnation line and the shoulder line on Figure 2.2. However, the vibrational population distribution along the backshell line on Figure 2.2 does not match between the two simulations. A non-Boltzmann distribution in the vibrational population is seen along the backshell line. In this region, significant over-population of the upper vibrational states was predicted

by the non-Boltzmann model, which could not be captured by the Boltzmann model. The over-population of the upper states may be caused by the state-resolved CO₂ recombination process [15] [16] [17]. In summary, the result of Sahai et al. indicates that the shock layer and expanding flow around the shoulder can be modelled by Boltzmann thermochemical models but the flow in and around the wake cannot.

2.2 Carbon Dioxide Thermochemistry and Radiation

The afterbody radiation during Mars entry is produced primarily by carbon dioxide molecules. High importance is given to the accurate prediction of the vibrational relaxation and chemical dissociation of carbon dioxide because it is required in order to accurately determine the radiative heating on the body surface. The carbon dioxide molecule has three vibrational modes, as shown on Figure 2.3. The radiation is in the mid-infrared region of the spectrum and is produced by ro-vibrational transitions of the carbon dioxide molecules. In particular, the radiation is produced by the 2.7 μm and 4.3 μm bands of carbon dioxide. The ro-vibrational transition causing the 4.3 μm band is produced by single quantum transitions in the ν_3 asymmetric stretching mode with the rotational energy level either remaining the same or changing by a single quantum level [18] [19]. These transitions are called fundamental transitions and produce the strongest radiation emissions [20]. The probability of multiquantum vibrational transitions in a single vibrational mode, known as overtones, are lower and, thus, have lower emission levels compared to those of fundamental transitions [21]. The 2.7 μm band corresponds to the simultaneous transitions in the ν_1 and ν_3 vibrational modes and the ν_2 and ν_3 vibrational modes [22]. This is called a combination band. Specifically, the 2.7 μm band emission corresponds to the de-excitations $\Delta\nu_1 = \Delta\nu_3 = 1$, where ν_1 and ν_3 both decrease by 1 quanta, and $\frac{\Delta\nu_2}{2} = \Delta\nu_3 = 1$, where ν_2 decreases by 2 quanta and ν_3 decreases by 1 quanta [23]. Like with the overtones bands, combination bands are weaker than the fundamental bands [24]. Carbon dioxide also has an emission band at 15 μm which is caused by fundamental transitions in the bending mode, ν_2 . However, the 15 μm band is not considered important in the context of the radiative heat transfer during Mars entry because it is negligibly weak [8]. Lastly, the symmetric stretch mode, ν_1 , is IR inactive because the vibrational motion of the symmetric bond does not cause a change in dipole moment. Therefore, transitions in this mode do not produce infrared radiation, except in combination with some other event (such as scattering).

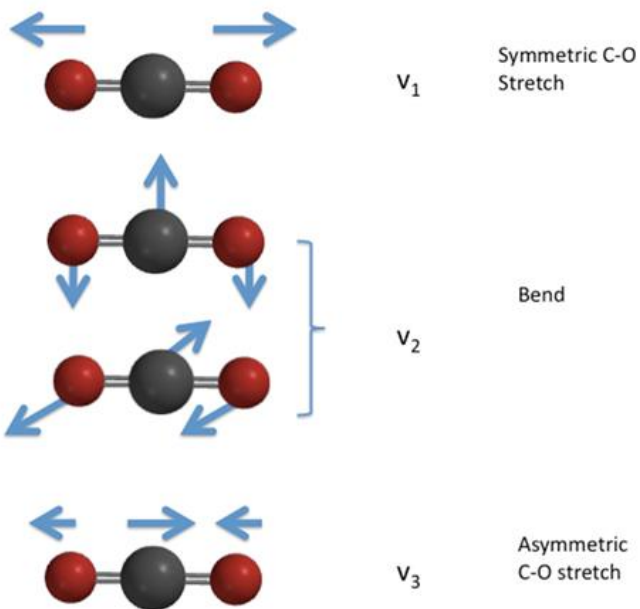


Figure 2.3. The vibrational modes of carbon dioxide. Adapted from [25].

The non-equilibrium thermochemistry of carbon dioxide has been of interest since the 1950s. Of particular interest is the carbon dioxide vibrational relaxation rate and the carbon dioxide dissociation rate. Numerous experiments have been conducted to investigate the carbon dioxide dissociation rate assuming the Arrhenius relationship. Burmeister and Roth [26], Ebrahim and Sandeman [27] and Saxena et al. [28] provide good summaries of the previous experiments done on investigating the carbon dioxide dissociation rates as well as the results of their own experiments. These previous experiments were all conducted in either reflected shock tubes or non-reflected shock tubes (a synopsis of both facilities is presented in appendix A.4). Therefore, the results are relevant in the context of post-shock non-equilibrium. Numerous methods have been used to experimentally measure the carbon dioxide dissociation rate. Optical techniques used include IR emission/absorption, UV absorption of the carbon dioxide, laser schlieren and oxygen atomic resonance absorption spectroscopy [28]. Most experiments were conducted with varying amounts of inert gases, including N₂, Ar and Kr, used to dilute the carbon dioxide gas in the experiments. Diluents are used to obtain post-shock temperatures which do not get lowered significantly by the chemical reactions [27]. However, some experiments have also been done with pure carbon dioxide [27]. The carbon dioxide dissociation rate constant derived from all these experiments, fitting to the Arrhenius equation, can vary by almost an order of magnitude at certain temperatures. A significant portion of this discrepancy is recently discovered to be caused by the derived carbon dioxide rate constant having a dependence on pressure [28]. Saxena et al. [28] performed experiments and showed that, at a constant temperature, the carbon dioxide dissociation rate constant varies by about 50% over 9,000 – 80,000 Pa. The Arrhenius relationship assumes the rate constant to be dependent only on

temperature. Therefore the Arrhenius equation derived for the carbon dioxide dissociation reaction will vary depending on the post-shock pressure in which the experiment was performed. Furthermore, the carbon dioxide recombination rate has been experimentally measured by various researchers as well [29] [30] [31]. The rates were measured behind a shock wave propagating through a carbon monoxide (CO) – nitrous oxide (N_2O) mixture. The variation seen between the recombination rates measured from different studies is similar to that seen for the dissociation rate [31]. Additionally, the carbon dioxide recombination rates derived from measured dissociation rates matched the measured recombination rates within the variations [31]. However, the carbon dioxide recombination rate has never been measured in the context of expanding flow.

Like with the carbon dioxide dissociation rate, numerous experiments have been conducted to investigate the carbon dioxide vibrational relaxation. Previous experiments done to investigate the carbon dioxide vibrational relaxation include that by Griffith et al. [32], Greenspan & Blackman [33], Johannesen et al. [34], Zienkiewicz & Johannesen [35], Simpson et al. [36] and Camac [37]. Conflicting results were observed in these independent studies. Griffith et al. and Greenspan & Blackman studied the vibrational relaxation of carbon dioxide in a non-reflected shock tube using an interferometer and they claimed that each of the vibrational modes of carbon dioxide relax at different rates. This claim is not consistent with theoretical predictions [38]. Johannesen et al. and Zienkiewicz & Johannesen studied the vibrational relaxation of carbon dioxide in a non-reflected shock tube using an interferometer and they also believed that the different vibrational modes of carbon dioxide relax at different rates. In addition, Johannesen et al. and Zienkiewicz & Johannesen claimed that the relaxation time, τ_v , in the Landau-Teller theory depends on the degree of non-equilibrium as well as the translational temperature and pressure. Nevertheless, Zienkiewicz & Johannesen mentioned that although they claim that τ_v depends on more than just temperature and pressure, it is only important for the purposes of a detailed understanding of the vibrational relaxation phenomena; assuming τ_v to be dependent on only the temperature and pressure is sufficient for practical calculations. Simpson et al. [36] used the Mach-Zehnder interferometry technique to measure the variation of density behind the shock in a shock tube. Comparison of the density measurements with theoretical calculations using excitation of different vibrational modes of carbon dioxide showed that the measured density variation had the best match with the theoretical calculation corresponding to excitation of all vibrational modes. Furthermore, Simpson et al. showed that the relaxation time, τ_v , is a function of temperature and pressure alone. Camac [37] used an electron beam technique to measure the density behind the shock in a shock tube. Additionally, an InSb sensor was used to measure the infrared emission from the asymmetric stretching mode behind the shock. Camac investigated a velocity range of around 1.5 - 6.5km/s with initial fill pressures ranging from 0.015 to 0.12 torr. Results of the infrared sensor measurement, which gives a direct measurement of the vibrational energy of the gas,

showed that the maximum intensity occurs at around 3 - 4km/s, as shown on Figure 2.4. The decrease in vibrational energy is caused by the decrease in radiating species due to dissociation, which occurs at about 3km/s as is also shown on Figure 2.4. This is the first published work showing that the carbon dioxide radiation decreases with increase in freestream velocity when beyond a certain velocity. Further findings from the experimental results of Camac [37] include the observation that the chemical excitation is about two orders of magnitude slower than the vibrational excitation. Camac's analysis also showed that, for velocities around 3.5km/s and lower, all four vibrational modes of carbon dioxide relax together behind the shock and are in equilibrium with the rotational modes. The equilibration of the vibrational modes of carbon dioxide behind the shock is an important result and it supports results of Simpson et al. [36]. Indeed the modern day belief is that all the carbon dioxide vibrational modes relax at the same rate [28]. Furthermore, like Simpson et al., Camac claimed that the relaxation time, τ_v , in the Landau-Teller equation is a function of only temperature and pressure.

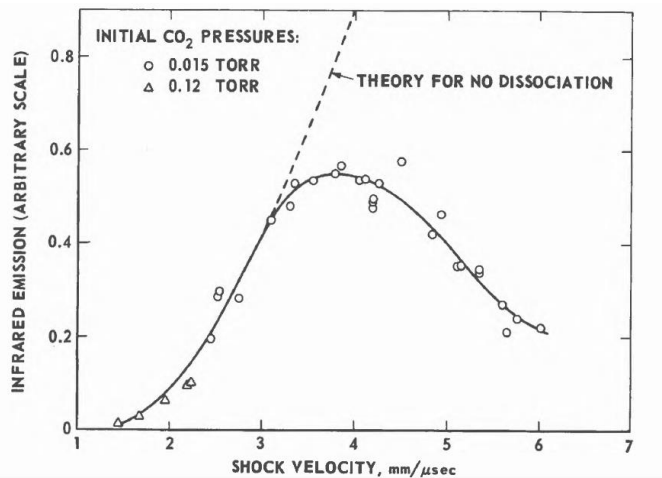


Figure 2.4. The peak infrared emission as a function of shock velocity. The dashed curve is the expected intensity with no chemical relaxation. [37]

Additionally, non-Boltzmann distribution in the vibrational population in carbon dioxide has been observed experimentally. Oehlschlaeger et al. [39] and Saxena et al. [28] have experimentally observed the incubation region immediately behind the shock front. The incubation region occurs behind the shock front and prior to the onset of steady dissociation. The incubation region occurs due to the finite rate relaxation of the vibrational modes. Dissociation cannot proceed unless the vibrational levels near the dissociation threshold are populated and a steady dissociation rate does not occur until the vibrational population is at a steady-state. Due to the high bond energy of CO₂, 125.7 Kcal/mol, a considerably greater time is required for the population of the highest vibrational energy levels compared to the population of the low-lying energy levels, thus resulting in an incubation period. Furthermore, population inversion in the vibrational population of carbon dioxide can be created in expanding flows. This is experimentally demonstrated when a heated mixture of CO₂-N₂-

He or CO₂-N₂-H₂O is expanded through a supersonic nozzle [40] [41] [42] [43]. Mixing the CO₂ with N₂ and H₂O or He is critical for producing the population inversion. The population inversion in the vibrational mode of the CO₂ molecule is created in this way for using it as the laser gain medium in gasdynamic lasers.

Recent work on investigating the carbon dioxide thermochemistry and radiation in a non-reflected shock tube has been done by Cruden et al. [44]. They performed a series of experiments studying the radiation behind a normal shock generated in their non-reflected shock tube with shock velocities ranging from 3km/s to 7.5km/s. They discovered that the infrared radiation is greatest at 3-4 km/s with a freestream pressure of one torr. This is consistent with the result by Camac [37]. For conditions with velocity below 5 km/s, the chemistry behind shock waves in pure carbon dioxide involves only the three reactions show in Table 2.2. This is because the temperatures involved behind the shock are low enough so that the presence of atomic carbon and ionic species is negligible [44]. Another result presented by Cruden et al. is that the numerically calculated band radiance behind shock waves travelling in pure carbon dioxide can be reconciled with the corresponding experimental measurements by applying a scaling factor. They found that by scaling the numerical radiance from Cruden's kinetic model near the end of the trace to match the experimental radiance, the entire band radiance trace matches. However, this scaling factor is different for different velocity conditions and different wavelength bands. Thus, the entirety of the discrepancy cannot be explained by a single scaling. Consequently, further investigation is required in order to understand the reason for the discrepancies.

Table 2.2. Chemical reactions in low and medium velocity pure carbon dioxide freestreams.

Name	Equation
Carbon dioxide dissociation	CO ₂ + M → CO + O + M
Oxygen dissociation	O ₂ + M → O + O + M
Oxygen exchange	CO ₂ + O → CO + O ₂

A plasma torch investigation of the radiation from high temperature carbon dioxide gas has been conducted by Depraz et al. [45]. They took radiation measurements of an atmospheric pressure carbon dioxide plasma with temperatures ranging from 1000 K-5000 K. Emission spectroscopy of the carbon dioxide 2.7 μm and 4.3 μm bands was made and a comparison was carried out with predictions made using the CDSD-4000 CO₂ spectroscopic database [46]. Good agreement was observed for both the radiating bands. Further validation of CDSD-4000 under equilibrium conditions was shown by Lemal et al. [47]. Using the experimental measurements of Depraz et al. as well as other experimental measurements of CO₂ radiation under thermochemical equilibrium conditions, Palmer and Cruden

[48] validated the implementation of the CDSD-4000 database in the NEQAIR radiation code [49] for simulating CO₂ radiation. Thus, the NEQAIR code is believed to be accurate at describing CO₂ radiation at equilibrium conditions.

Very little experimental work relating to non-equilibrium CO₂ expanding flows can be found in past literature. A study of low temperature, T=600 – 1400 K, CO₂ expansion through a nozzle showed that the vibrational de-excitation in the expansion is 1.1 ± 0.4 times faster than the vibrational excitation behind shock waves [50]. Another notable work on CO₂ expanding flows would be that of Maclean and Holden [51]. They believed that the CO₂ freestream generated in their reflected shock tube was frozen at a complex non-equilibrium thermochemical state due to the expansion in the nozzle. This belief arose from the fact that the shock standoff they measured in their experiment did not match the shock standoff calculated in the CFD of their experiment. The shock standoff in their experiment is significantly larger than the calculated value. This is believed to be due to the complex vibrational relaxation of CO₂ because the discrepancy in shock standoff was not seen when air is used as the test gas. Later works by Maclean and Holden [52] [53] provides further experimental evidence supporting this belief. This topic is investigated in detail in sections 3.4.1 and 3.4.4. The results of Maclean and Holden motivated Doraiswamy et al. [54] to use a non-Boltzmann model to describe the CO₂ expanding flow through a nozzle. They attempted to capture the non-Boltzmann effects believed to be present in the nozzle expansion in the reflected shock tube. The numerical model developed is a reduced order state specific model. For an unspecified reason, the result of the nozzle CFD done using the state specific model only showed minor nonequilibrium effects. In fact, the same nozzle simulation conducted using the two temperature model showed more nonequilibrium at the nozzle exit than that of the state specific model.

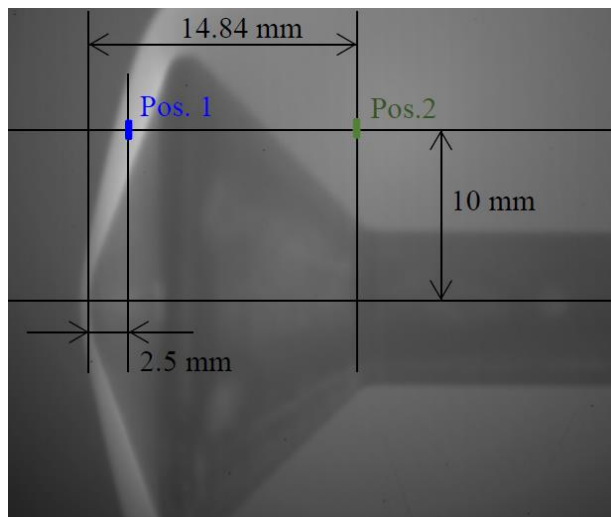


Figure 2.5. Measured locations of the mid-infrared emission [55].

At the time of writing, Takayanagi et al. [55] is conducting independent carbon dioxide radiation experiments relevant to Mars entry in an expansion tube. In their study, Takayanagi et al. used a scaled aeroshell model. They tested two freestream conditions. Condition 1 has an estimated freestream velocity of 8.4 km/s and temperature of 2880 K. Condition 2 has an estimated freestream velocity of 5.9 km/s and temperature of 2330 K. Similar to the work concerned in this thesis, the optical method Takayanagi et al. used in their study is emission spectroscopy. Mid-infrared emission spectroscopy measurements were taken at the two positions shown on Figure 2.5 to study the carbon dioxide radiation in both the forebody and afterbody. It is understood that further work and analysis of the carbon dioxide radiation will be published in the future.

2.3 Experimental Studies of High Enthalpy Expanding Flows

Although only few experimental studies of high enthalpy CO₂ expanding flows could be found in literature, numerous studies involving other species have been found. A significant amount of research was done on non-equilibrium expanding flow during the 1960s and 70s. A summary of the past studies of high enthalpy expanding flows is presented in Table 2.3. All experiments in Table 2.3 were conducted in impulse facilities with the exception of the works of Bender et al. [56] and Park [57] [58] which were conducted in an electric-arc plasma wind tunnel. The high enthalpy expanding flows were created either by the rupture of a diaphragm, resulting in a non-steady expansion as shown on Figure 2.6, or through a nozzle, resulting in a steady expansion. The exception are the studies conducted by Igra [59] and Drewry [60] from the Institute of Aerospace Studies in the University of Toronto. In these studies the expanding flow was generated using a wedge test model with a convex corner, shown on Figure 2.7, aligned such that a shockless flow is created on the expansion surface. The expanding flow generated around the convex corner is referred to as a Prandtl-Meyer expansion. Another form of the Prandtl-Meyer expansion fan was generated by Wilson [61] and Blom et al. [62] by producing a symmetrical expansion using two convex corner wedges, as shown on Figure 2.8.

In the previous expanding flow studies, the research interest includes studying the recombination of oxygen, nitrogen and argon as well as the vibrational behavior of carbon monoxide, nitrogen and oxygen. To study these nonequilibrium processes, the generated expanding flow was diagnosed using numerous methods.

Various interferometry techniques have been used to diagnose the flow. Mach-Zehnder and microwave interferometry were used to study the chemical processes while holographic interferometry was used to study the vibrational process. Static pressure measurements also give information about the thermochemical kinetics of the expanding flow. Nagamatsu et al. [63] used

static pressure measurements along the axis of the nozzle to determine the region in the nozzle where the flow is considered in thermochemical equilibrium and where the flow is considered frozen. The spectrum line reversal (SLR) and infrared band reversal techniques are commonly used to provide estimates of the vibrational temperature. The SLR and infrared band reversal are both emission-absorption techniques where relative emission and absorption of a certain line or band is measured simultaneously. The simultaneous measurements of emission and absorption allows for an analysis to estimate the vibrational temperature, assuming a Boltzmann distribution in the vibrational energy levels. The purely absorption technique, which monitors the population density of a particular vibrational state, can also be used to deduce the vibrational temperature by assuming a Boltzmann distribution. Likewise, the infrared emission measurement of the CO fundamental band can also be used to deduce the vibrational temperature, given the assumption of a Boltzmann distribution of the vibrational levels.

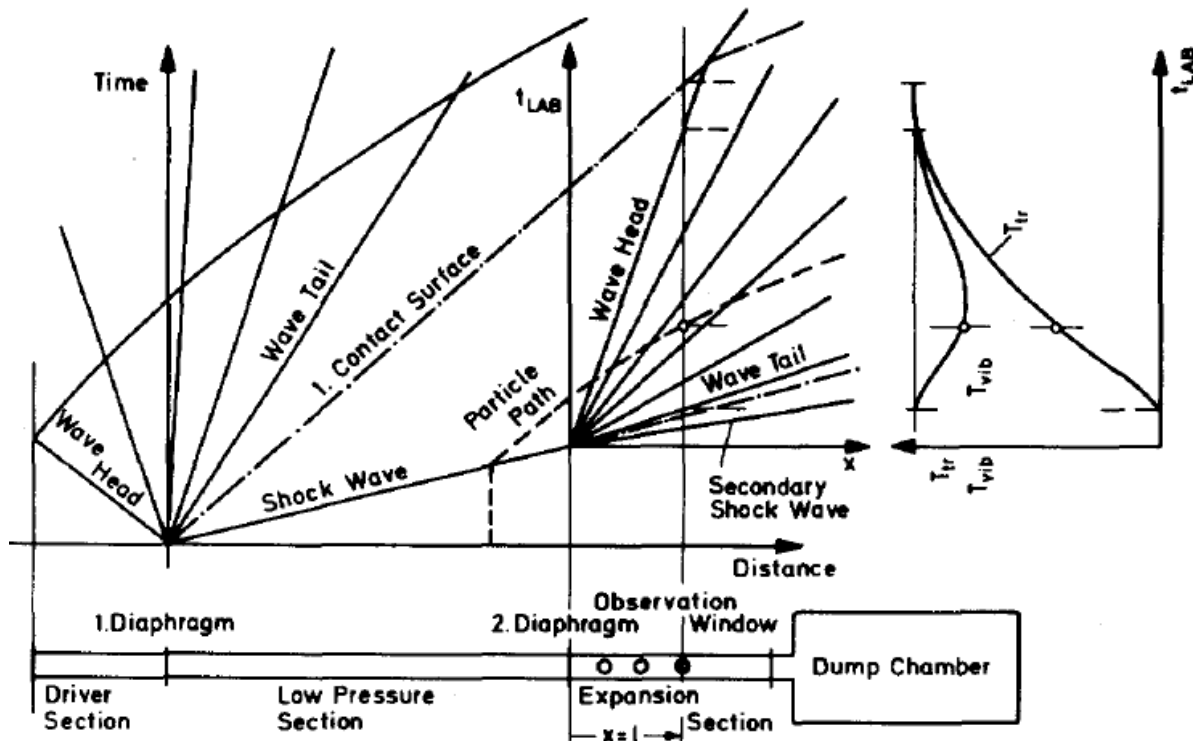


Figure 2.6. The unsteady expansion used to study high enthalpy expanding flows. [64]

Spectrally resolved infrared measurements conducted by Bender et al. [56] allow for the vibrational population distribution to be estimated to investigate the validity of the Boltzmann assumption. Bender et al. determined the vibrational population distribution of carbon monoxide in an expanding flow by measuring the infrared emission spectra. The expanding flow was created in a three-dimensional nozzle using argon, which passed through an electric discharge in an arc jet, injected with carbon monoxide. The result indicated that the vibrational population deviates from the Boltzmann distribution during the expansion for the studied case of carbon monoxide. Sharma et al.

[65] in 1993 focused on measuring the vibrational state populations in nitrogen molecules under expanding flow. Sharma et al. used Raman scattering to measure the vibrational populations in the ground vibrational state and the first seven excited vibrational states of nitrogen in an expanding flow. The expanding flow was created using a two-dimensional nozzle in a reflected shock tube. The results showed that the vibrational states measured are populated in a Boltzmann distribution. Lastly, it is important to mention that Sharma et al. [65] [66] stated that previous studies of diatomic species N₂ and CO indicated the vibrational relaxation time in expanding flows can be up to two orders of magnitude faster than the relaxation time behind shock waves. These past results for N₂ and CO are consistent with the past result for CO₂ at lower temperatures [50], as mentioned in the previous section.

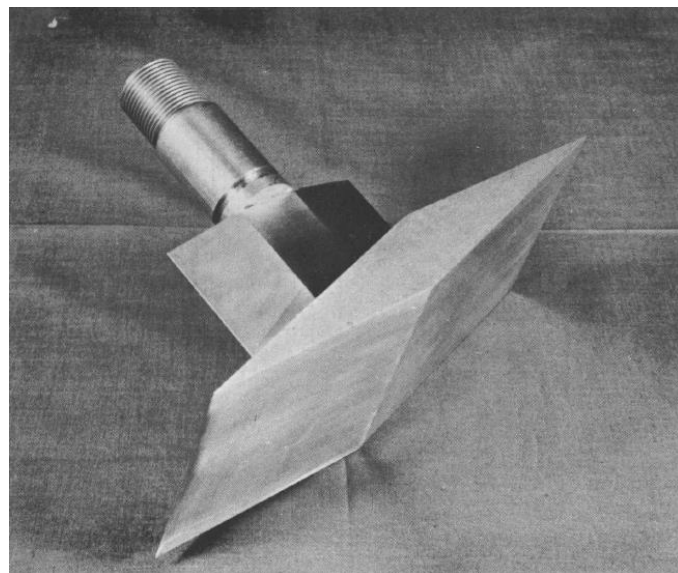


Figure 2.7. Wedge model used by Igra [59] and Drewry [60].

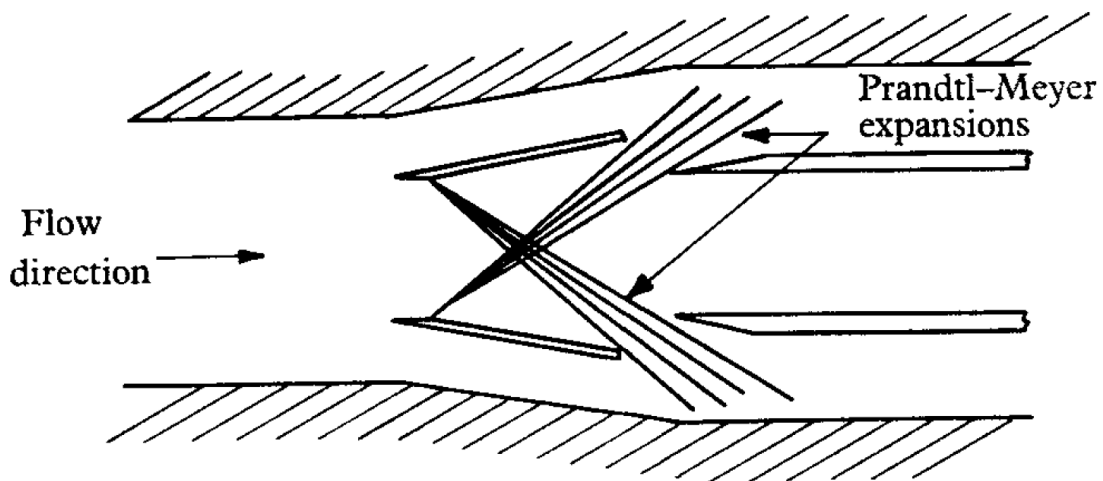


Figure 2.8. Generation of expanding flow by Wilson [61] and Blom et al. [62].

Table 2.3. List of experiments performed for the study of high enthalpy expanding flow; sorted chronologically.

Investigators	Year	Expansion Type	Measuring Technique	Research Interest
Nagamatsu et al. [63] [67]	1961 & 1965	Nozzle Expansion	Static Pressure measurement at nozzle axis	Thermochemistry of air and nitrogen
Wilson [61]	1962	Prandtl-Meyer Expansion	Mach-Zehnder interferometry, UV absorption	Recombination of O ₂
Hurle et al. [68]	1964	Nozzle Expansion	Spectrum line reversal	Vibrational behaviour of N ₂
Holbeche et al. [69] [70]	1964	Unsteady Expansion	Spectrum line reversal	Vibrational behaviour of O ₂ , N ₂ and CO
Drewry [60]	1967	Prandtl-Meyer expansion	Mach-Zehnder interferometry	Recombination of O ₂
Hall et al. [71]	1967	Nozzle Expansion	Spectrum line reversal	Vibrational behaviour of N ₂ and CO
Russo [72]	1967	Nozzle Expansion	Infrared band reversal	Vibrational behaviour of CO
Park [57]	1968	Nozzle Expansion	Visible emission spectroscopy	Ionic recombination of N
Rich [73]	1968	Nozzle Expansion	Infrared band reversal	Vibrational behaviour of N ₂ and CO
Blom and Pratt [62]	1969	Prandtl-Meyer expansion	Infrared band Reversal	Vibrational behaviour of CO
Igra and Glass [59]	1970	Prandtl-Meyer expansion	Mach-Zehnder interferometry	Ionic recombination of Ar
Dunn et al. [74]	1970	Nozzle Expansion	Microwave interferometry, Langmuir probes for electron temperature and density nozzle axis, visible radiation emission	Dissociative recombination of nitrogen
McLaren and Appleton [75]	1970	Unsteady Expansion	Infrared band emission	Vibrational behaviour of CO
Von Rosenberg et al. [76]	1971	Nozzle Expansion	Infrared band emission	Vibrational behaviour of CO
Just et al. [64]	1971	Unsteady Expansion	Infrared band reversal	Vibrational behaviour of CO
Cleaver et al. [77]	1973	Unsteady Expansion	Absorption measurements at 2283 A	Vibrational behaviour of O ₂

Park [58]	1973	Nozzle Expansion	Visible to near-infrared emission spectroscopy	Electron and electronic temperatures in a nitrogen-hydrogen mixture
Sebacher et al. [78]	1974	Nozzle Expansion	Electron beam technique to determine vibrational temperature	Vibrational behaviour of N ₂ and air
Nasser et al. [79]	1977	Unsteady Expansion	Infrared band reversal	Vibrational relaxation of CO
Beck et al. [80]	1978	Unsteady Expansion	Absorption at 493 nm and wall pressure measurements	Recombination of I ₂
Bender et al. [56]	1978	Nozzle expansion	Infrared emission spectroscopy	Vibrational behaviour of CO
Sharma et al. [65] [66]	1993	Nozzle expansion	Spontaneous Raman scattering, holographic interferometry and static pressure measurement along nozzle axis	Vibrational behaviour of N ₂

2.4 Summary of Findings

Apart from the work in progress of Takayanagi et al. [55], no experimental work has been done on specifically studying the afterbody radiative heating during Mars entry. However, work relevant to the study of afterbody radiative heating during Mars entry does exist. This includes numerical simulations of aeroheating to Mars entry vehicles, experiments studying the non-equilibrium thermochemistry of carbon dioxide flows in post-shock conditions and experiments studying high enthalpy expanding flows involving species other than CO₂.

Numerous simulations of Mars entry vehicles at velocities below 6 km/s showed that the afterbody radiative heating is comparable to the convective heating. The radiative heating is produced by carbon dioxide molecules emitting mid-infrared radiation. In particular, the radiation is from the 2.7 μm and 4.3 μm bands of carbon dioxide. The non-equilibrium thermochemistry of carbon dioxide has been studied extensively in the past at post-shock conditions. One of the particular interests was whether the separate CO₂ vibrational modes have separate relaxation rates. The current belief is that the CO₂ vibrational modes maintain equilibrium with each other and, thus, have the same relaxation rate. Also, the Landau-Teller equation was shown to model the CO₂ vibrational relaxation well as the vibrational relaxation time, τ_v , was shown to be a function of the translation temperature and pressure only. Additionally, numerous independent research studies on measuring the CO₂ vibrational relaxation time, τ_v , showed consistent results. However, many independent studies measuring the CO₂ dissociation rates showed results which differ by up to an order of magnitude. It is unclear how these CO₂ thermochemical characteristics will differ under expanding flow conditions because not enough

study on the thermochemical kinetics have been done under expanding flow conditions. Nevertheless, high enthalpy expanding flows involving species other than carbon dioxide have been studied extensively in the past. The expanding flows have been studied in nozzles, around convex corners and under unsteady expansions. An important result from the past studies is that vibrational relaxation is consistently seen to be faster under expanding flow conditions compared to post-shock conditions. Also, experiments have shown that it is possible to have over-population of the high lying energy states during expansion. Nevertheless, non-Boltzmann distributions do not always occur during expansion as some experiments show that the population of the energy states maintain a Boltzmann distribution.

3 Development of the Experimental Test Conditions

3.1 Introduction

Fundamental to the investigation of afterbody radiation during Mars entry is performing ground-based measurements to obtain high quality experimental data. This requires generating the expanding flow around the afterbody of Mars entry aeroshells in a ground test facility. While the Centre for Hypersonics at the University of Queensland has both a reflected shock tube and an expansion tube (a synopsis of both facilities is presented in appendix A.4), the latter is selected as the preferred facility to perform the experiments. This is because, as stated by Maclean and Holden [51] and Hollis et al. [81], the reflected shock tube is not suitable because the carbon dioxide conditions generated by the facility is believed to freeze at a complex non-equilibrium thermochemical state. This would result in a test condition with significant thermal excitation and a distorted chemical composition [82]. This is not desirable as the ideal experimental test condition should have minimal chemical dissociation and minimal thermal excitation. Furthermore, accurately characterizing these carbon dioxide test conditions in reflected shock tubes would be a challenge [54]. These problems of reflected shock tubes are less pronounced in expansion tubes. Therefore, an expansion tube is used to generate the CO₂ test conditions in this thesis. The layout and dimensions of the facility is shown in Figure 3.1.

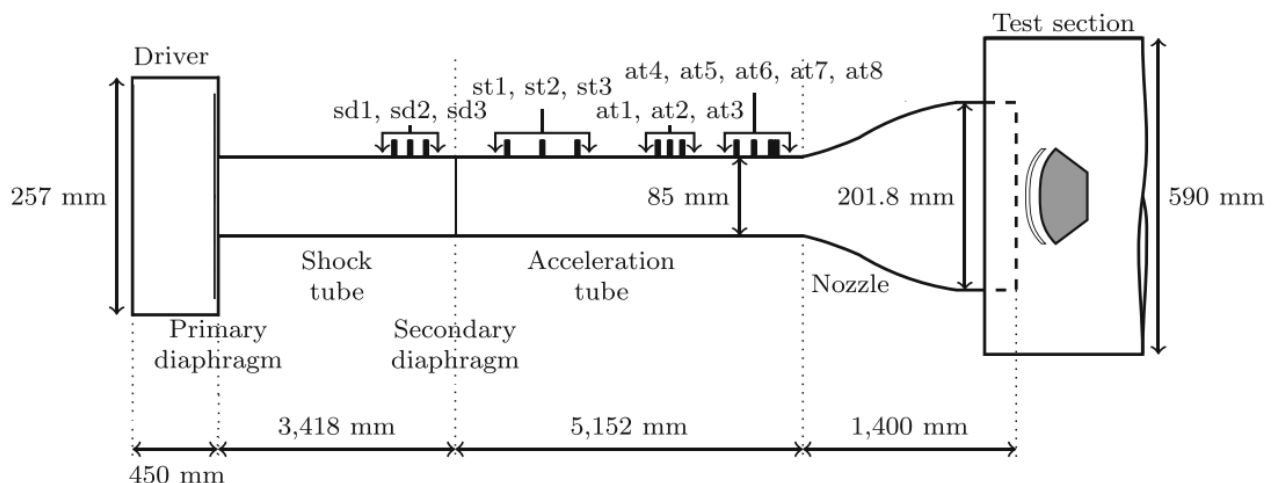


Figure 3.1. X2 expansion tube with fixed volume driver. [83]

In this chapter, three different velocity conditions, nominally at 2.8 km/s, 3.4 km/s and 4.0 km/s, with sufficient test time and core flow size are developed in the expansion tube to study the CO₂ expanding flow using a wedge model with a convex corner. Based on the literature review in chapter 2, these conditions are chosen because the afterbody radiation is important over this velocity range. Although the atmosphere of Mars consists of CO₂ and small amounts of N₂ and Ar, pure carbon dioxide is used as the test gas since the afterbody radiation of interest is produced entirely by carbon dioxide molecules. An in-depth analysis is conducted to produce a good estimate of the freestream condition generated in the expansion tube for each of the three conditions. Using the estimated experimental inflow conditions, CFD simulations were done to investigate the similarities between the expanding flow created around the test model and the expanding flow around a Mars entry capsule.

3.2 Test Condition Requirements

It is necessary to generate a flowfield around the test model that has similarities to the flowfield around a flight vehicle at the velocity conditions where carbon dioxide radiation is important. The test model for the study, shown in Figure 3.2, is a two dimensional oblique shock expansion wedge model with a width of 100 mm; the expanding flow is generated around the convex corner. Using the oblique shock expansion model, similarity to flight can be achieved by matching the total pressure behind the shock wave, in addition to matching the total specific enthalpy. Matching the total pressure behind the shock involves matching the total pressure behind the oblique shock of the test model in the experiment to the total pressure behind the shock of the entry body at the respective flight conditions. This gives the similarity between a flight condition and an experimental test condition.

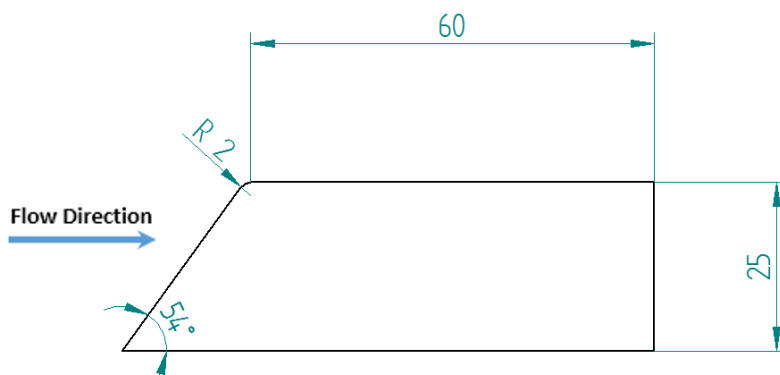


Figure 3.2. Two-dimensional test model geometry. Dimensions shown are in mm and degrees.

Cruden et al. [44] highlighted that the strongest carbon dioxide radiation behind a normal shock in low pressure carbon dioxide occurred at around 3-4 km/s and the radiation intensity decreases as velocity increases up to 6 km/s. Thus, it is of interest to study this velocity region in this thesis. A

plot of freestream density at room temperature versus flight velocity is shown on Figure 3.3 for flight trajectories of different Mars entry vehicles. As the MSL is the most recent Mars entry trajectory, the MSL trajectory is used to develop similar freestream conditions in the X2 expansion tube for the study concerned in this thesis. Three points on the MSL trajectory are chosen having freestream velocities of 2.8 km/s, 3.4 km/s and 4.0 km/s. The chemical contributions to the total enthalpy is negligible for the conditions concerned in this work. Therefore, matching the total enthalpy simply involves matching the freestream velocity between experiment and flight. Like with Cruden et al. [44], for the purposes of studying the carbon dioxide radiation, pure carbon dioxide is used as the test gas.

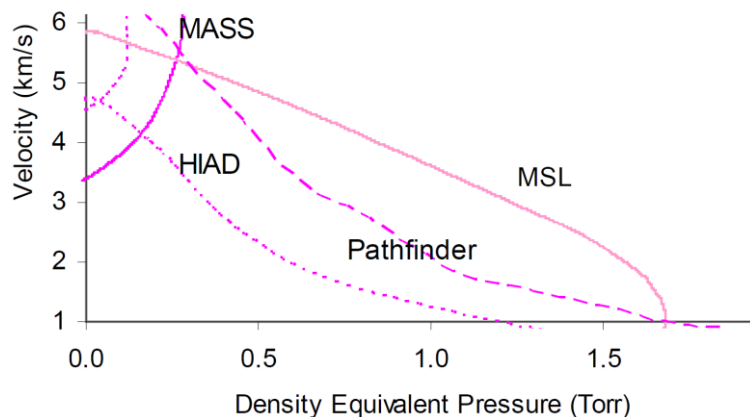


Figure 3.3. Various Mars entry trajectories. Adapted from [44].

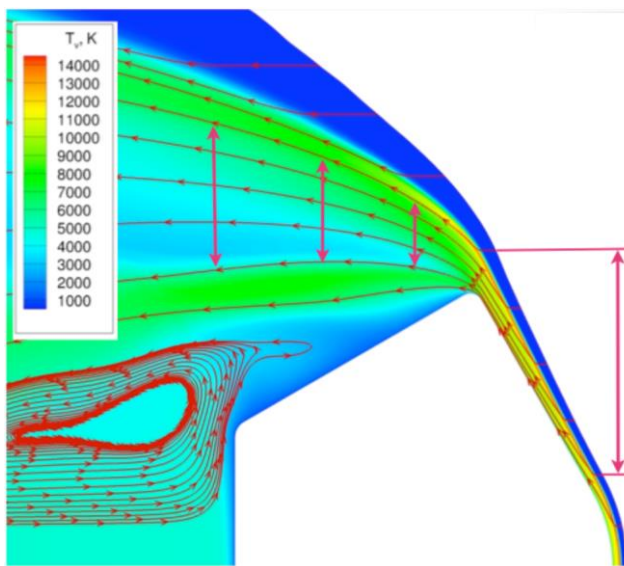


Figure 3.4. CFD contour of vibrational-electronic temperature for the Stardust geometry at a time of $t=46$ s. The red arrows bound the region on the shock wave where the majority of the radiating expanding flow is created. [84]

Matching the total pressure behind the shock between flight and experiment is less simple. The total enthalpy of the flow remain constant across a shock wave because the shock does not add any heat,

nor does it do any work. However, as the flow across a shock is not isentropic, the total pressure of the flow decreases across a shock. The total pressure loss increases with increase in shock angle and Mach number. Since the shock of the flight vehicle is detached, the total pressure behind the shock of each streamline will be different due to the curvature of the shock. Additionally, the angle at which each streamline enters the shock depends on the angle of attack. Thus, the total pressure of each streamline behind the shock depends on where the streamline encounters the shock wave as well as the angle of attack of the flight vehicle, in addition to the other conventional flow parameters such as freestream velocity and pressure. However, for an axisymmetric, zero angle of attack case, the majority of the radiative expanding flow forms along streamlines originating from the oblique shock region of the shock wave. This is shown on Figure 3.4 in the case of Earth re-entry. During the MSL Mars entry at velocities around 2.8 km/s to 4.0 km/s, the angle of this shock wave is approximately 80° to the freestream at zero angle of attack. Therefore, a shock angle of 80° in flight is used for the purposes of performing the total pressure scaling behind the shock in this work.

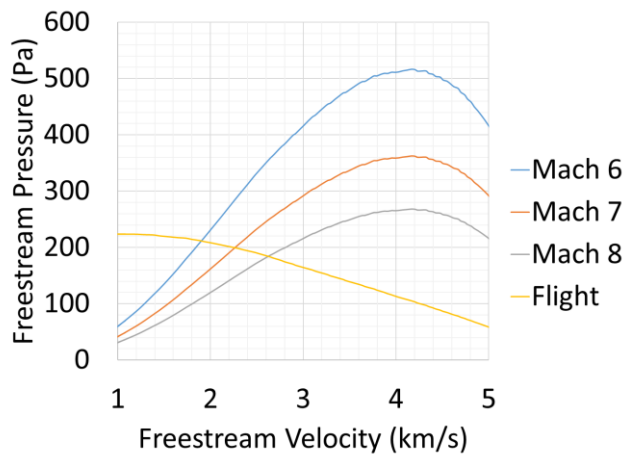


Figure 3.5. The experimental freestream static pressure required for matching the total pressure behind the shock between experiment and flight. In addition, the MSL entry trajectory from Figure 3.3 is plotted.

Figure 3.5 presents the freestream pressure required to be generated in the expansion tube for similarity with the MSL trajectory. The analysis was done using perfect gas equations for the shock wave and isentropic compression calculations. The result is a function of the experiment freestream Mach number which, according to the PITOT code [85], can be between Mach 6 to Mach 8 for the 2.8 to 4.0 km/s carbon dioxide conditions generated in X2. Furthermore, the PITOT code predicts a freestream temperature of roughly 1200-1400 K for these carbon dioxide freestream conditions. Therefore, a heat capacity ratio of 1.195, corresponding to that of carbon dioxide at 1300 K, is assumed in this analysis for the experiment freestream. Using these Mach numbers and heat capacity ratio, the corresponding shock angle over the 54 degree turn angle of the test model would be about 70 degrees and this is used in the analysis.

3.3 Generating the Required Test Conditions in the X2 Expansion Tube

From the analysis in the previous section, the three desired test conditions require velocities of 2.8 km/s, 3.4 km/s and 4.0 km/s with freestream static pressures of around 200 to 400 Pa. These test conditions are unique for the X2 expansion tube as they have much lower pressures and lower enthalpies than existing conditions. The current free piston driver conditions used in the X2 expansion tube are used to generate high enthalpy conditions. Hence, in order to generate the desired conditions, a new driver was designed and built. The subsequent shock tube and acceleration tube fill pressures required to generate the desired test conditions needed to be determined for the new driver. In addition to generating the desired freestream properties, an important consideration made when designing the expansion tube conditions was minimizing the noise in the test flow. Expansion tube conditions are well known to have a significant amount of noise. This is believed to be due to acoustic disturbances transferred from the expanded driver gas [86]. All frequency components of the acoustic disturbance in the test gas are focused into a narrow frequency bandwidth during the unsteady expansion causing significant noise during the test time. The noise in the test flow can be reduced by reducing the transmission of acoustic disturbances from the expanded driver gas to the test gas prior to the expansion of the test gas. This can be done by designing the conditions such that the speed of sound in the shock processed test gas is at least 1.25 times larger than the speed of sound in the expanded driver gas [87]. Meeting this requirement permits the contact surface to act like an acoustic buffer which attenuates the transmission of acoustic disturbances from the expanded driver gas to the test gas.

The preliminary design of the experimental flow condition was conducted using the PITOT code [85] with equilibrium chemistry. The aim was to determine the required shock tube and acceleration tube fill pressures, as well as the required driver rupture pressure and speed of sound, to generate the required test conditions while also trying to meet the acoustic buffer requirement. Table 3.1 shows the required driver conditions and fill conditions determined from analysis using the PITOT code. A pure helium driver gas at room temperature was found to be suitable for generating the 3.4 km/s and 4.0 km/s conditions, while a mixture of helium and argon at room temperature was used as the driver gas to generate the 2.8 km/s. Hence, a free piston was not necessary to compress the driver gas for the purpose of heating. Consequently, these conditions were generated by simply breaking a diaphragm at the end of the chamber containing the pressurized driver gas. This driver will be referred to as the ‘cold driver’. Engineering drawings of the cold driver are shown in appendix B. For this cold driver, the corresponding rupture pressure required was 2 MPa for generating the desired

conditions. Aluminum 5005 H34 with a thickness of 0.6mm was selected as the primary diaphragm to obtain this rupture pressure.

An important design consideration of the cold driver is its length. It is not necessary to use the entire driver tube. For the purposes of conserving helium gas, the length of the driver tube simply needs to be long enough to delay the arrival of the reflected unsteady expansion waves from the primary diaphragm at the nozzle exit. This is required to prevent premature termination of steady test time. One-dimensional CFD simulations of the X2 expansion tube were conducted using the L1d3 code [88] to investigate the wave processes. This resulted in a conservative driver length of 0.45 m being selected.

To execute a shot, the fixed volume of the driver is first evacuated and then filled with the driver gas until the primary diaphragm ruptures. For the 2.8 km/s condition, the 10% argon is filled first and then the helium is filled until rupture. For this condition, it is important fill the helium slowly to ensure adequate mixing with argon. Failure to do so results in an unusable condition with no steady flow.

Table 3.1. The driver conditions and fill pressures required to generate the necessary experimental test conditions.

Condition	Driver Gas Composition	Rupture Pressure (MPa)	Driver Gas Temperature (K)	Driver Gas Speed of Sound (m/s)	Shock Tube Fill Pressure (Pa)	Acceleration Tube Fill Pressure (Pa)
2.8 km/s	90 % Helium 10% Argon	2	293	740	600	40
3.4 km/s	100 % Helium	2	293	972	600	30
4.0 km/s	100 % Helium	2	293	972	600	10

3.4 Characterization of the Experiment Freestream Conditions

For accurate interpretation of experimental results, it is critically important to determine the state of the test flow exiting the nozzle for each experimental condition. The freestream velocity, pressure, temperature and thermochemical state of the test flow exiting the nozzle all need to be determined. These properties of the freestream cannot be easily measured directly. The properties of the expansion tube condition which are measured are the primary shock speed, secondary shock speed, acceleration tube wall pressure, freestream conehead pressure and freestream pitot pressure. The conehead

pressure is measured using 15° half angle conical probes. These measurements along with various numerical modelling methods are used to provide an estimate of the freestream for the three new expansion tube conditions.

3.4.1 Carbon Dioxide Freestream Excitation

Before presenting the analysis done to estimate the freestream conditions in this work, it is necessary to review the phenomenon of the thermochemical freezing of carbon dioxide freestreams generated in impulse facilities. Reviews of previous work [51] [53] [52] have shown that similar freestream test conditions as the ones concerned in this work, generated in other impulse facilities, are believed to suffer from freezing at an excited non-equilibrium thermochemical state. This phenomenon was first discovered by Maclean and Holden [51] for their experiment where a frozen flow was believed to be created in their LENS reflected shock tube for a 5 MJ/kg total enthalpy condition with pure carbon dioxide as the test gas. Maclean and Holden showed that the shock standoff on the test model measured in the experiment was significantly greater than what they predicted in their CFD. This is shown on Figure 3.6 (a) where the CFD result (blue contour) is overlaid on top of the experimental measurement. They believe this mismatch was caused by the carbon dioxide freestream being frozen at a non-equilibrium state because excess energy frozen in the thermal and chemical modes in the freestream increases shock standoff. Research was conducted at simulating the non-equilibrium condition at the nozzle exit of the reflected shock tube using advanced thermochemical models [54]. However, the numerical work failed to reproduce the non-equilibrium condition required to generate the correct shock stand-off. In fact, the numerical simulation showed that equilibrium was expected at the nozzle exit. This phenomenon of thermochemical excitation of carbon dioxide in the freestream is yet to be reproduced numerically. This is claimed to be due to the current lack of a detailed thermochemical model for carbon dioxide expanding flow. Nevertheless, it is also necessary to mention that no detailed experimental study has been done to confirm that there is excess thermochemical excitation in CO_2 freestreams generated by reflected shock tubes.

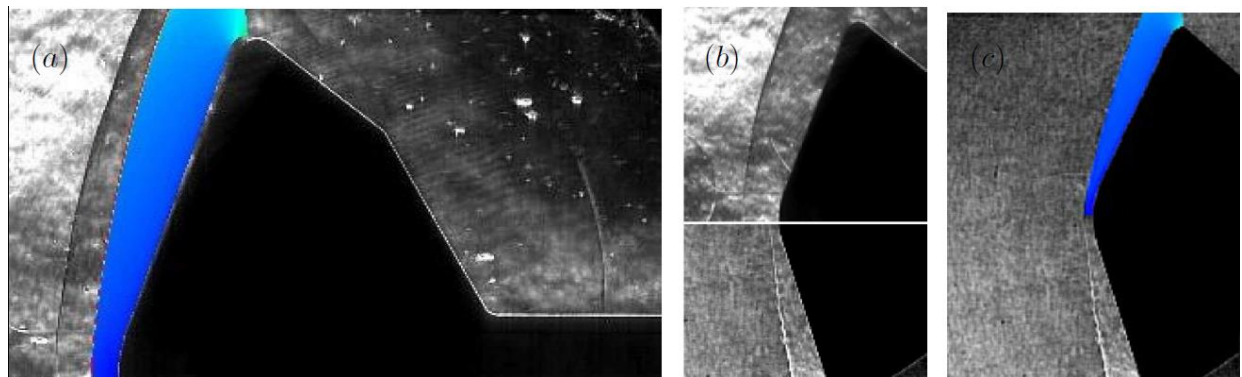


Figure 3.6. Shock wave comparison between experimental measurements and CFD predictions [89].

Following on from the experimental work of Maclean and Holden [51], Holden et al. [52] performed equivalent experiments in the LENS expansion tube with matched freestream total enthalpy and using the same test model. The shock standoff measured in the expansion tube was significantly smaller than that measured in the reflected shock tube. This is shown in Figure 3.6 (b). The expansion tube shock standoff also showed excellent agreement with CFD, shown in Figure 3.6 (c). Since it is known that expansion tubes generate freestream conditions with less thermochemical excitation when compared to reflected shock tubes, the result supports the belief that thermochemical freezing is the cause of the mismatch in shock standoff in Maclean and Holden's [51] measurements. More recent work by Maclean et al. [53] provides additional evidence supporting this belief. From their result shown in Figure 3.7, the mismatch in shock standoff distance, S/S_{CFD} , in their reflected shock tube experiments increases with decrease in freestream density, while keeping the freestream enthalpy constant at 5 MJ/kg. Thermochemical non-equilibrium is known to increase with decrease in density. Therefore, this result indicates that their shock wave mismatch is related to thermochemical non-equilibrium processes occurring in their reflected shock tube nozzle. Nevertheless, it may be incorrect to believe that carbon dioxide freestreams generated in any expansion tube will be at thermochemical equilibrium. For example, Hollis and Prabhu [90] showed that the 8.5 MJ/kg carbon dioxide freestream generated in the HYPULSE expansion tube is possibly also frozen at an excited thermochemical state.

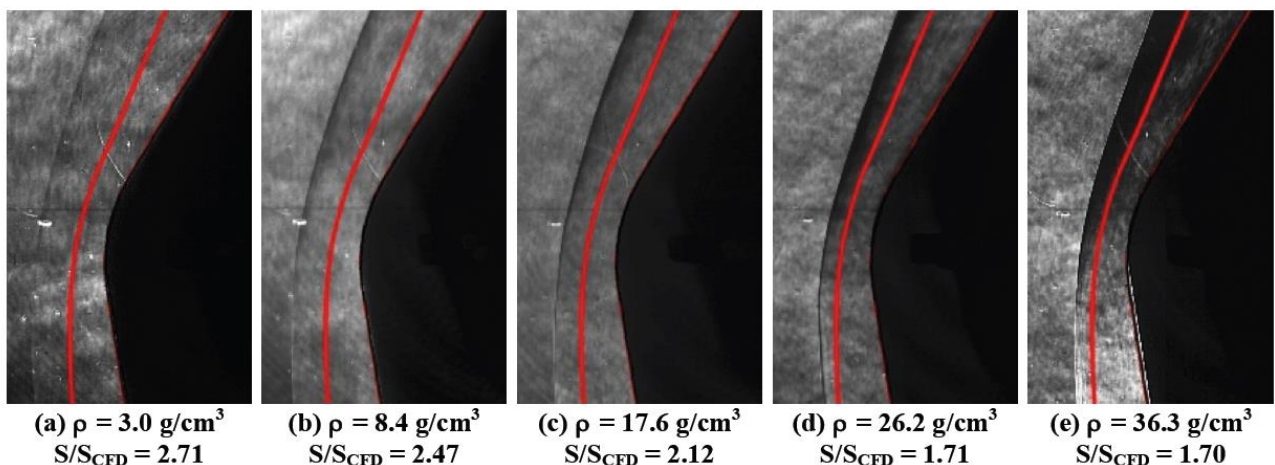


Figure 3.7. Comparison of measured and predicted shock locations for reflected shock tube freestream conditions with different densities but the same enthalpy [53].

The degree of thermochemical excitation in the freestream is believed to be dependent on the flow density and the time for expansion involved in generating the freestream [53] [90] [91]. The severity of the freezing increases with decreasing density. In addition, the degree of the freezing is most severe when the flow is generated in a reflected shock tube as the flow is expanded in a very short duration of time. However, it is possible to obtain equilibrium freestream conditions in reflected shock tubes

if the freestream density is relatively high, in the order of 10^{-2} kg/m³ [90] [91]. Likewise, very low density equilibrium conditions can be produced in very long expansion tubes such as the LENS XX facility due to the long time for expansion involved for the test gas. The freestream conditions concerned in the current work have very low density and the length of the X2 expansion tube is much shorter than the length of LENS XX. Hence, work was conducted to investigate the possibility of freestream excitation in the conditions generated for this thesis. This work is presented in section 3.4.4 as well as section 5.3.

3.4.2 PITOT Code

The PITOT code [85] is a tool which is used to produce an estimate of the expansion tube test conditions and it is similar to the *CHEETah* code [92] used to characterize the LENS XX expansion tube conditions. The PITOT code is a zero dimensional code which solves for the flow properties of the driver, test and accelerator gas at different states during the process of producing the hypervelocity test flow in the expansion tube. The PITOT code simulates the expansion tube processes by using isentropic expansion and compressible flow relations at the equilibrium and perfect gas limits. Since the PITOT code is a state to state code, it determines the final property of the test gas at the nozzle exit by calculating for each state of the test gas as it evolves from its initial fill state. Using the measured primary shock speed, secondary shock speed, acceleration tube wall pressure, freestream conehead pressure and freestream pitot pressure, the PITOT code will provide an estimate of the freestream properties.

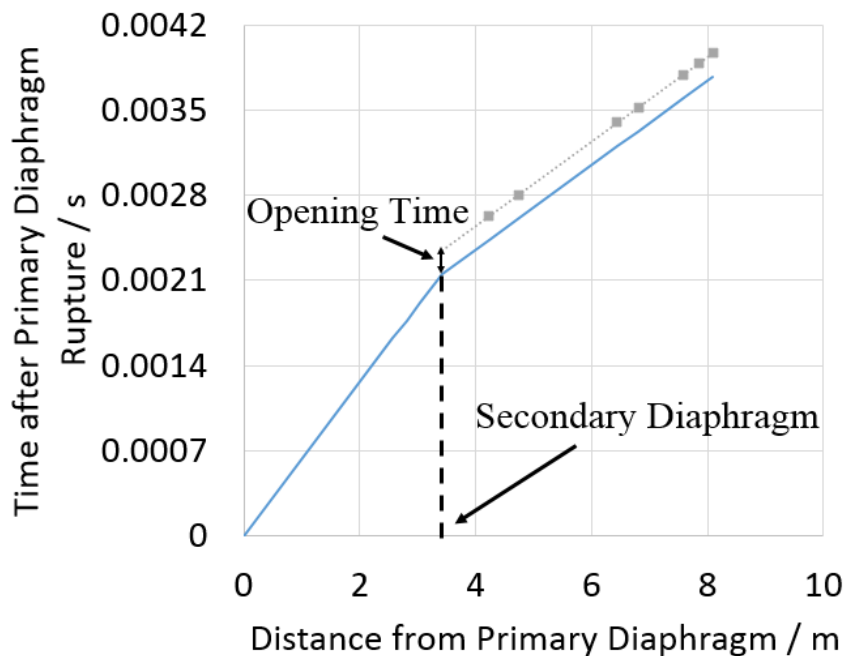


Figure 3.8. Estimate of the hold time of the secondary diaphragm rupturing process.

To estimate the freestream test condition, the PITOT code first estimates the properties of the shock processed test gas using the measured primary shock velocity. Since we are able to measure the velocity of the primary shock, the pressure and temperature of the test gas in the shock tube is regarded as being equal to that behind the shock. This is always calculated using thermochemical equilibrium analysis due to the high pressures and low velocities involved. Determining the velocity of the shock processed test gas in the shock tube is less trivial. As the shock tube properties in these cold driver conditions are relatively low density, the Mirels' effect [93] is important. The Mirels' effect describes the mass entrainment of the core flow by the boundary layer, which occurs behind shock waves propagating in tubes. In the current work, the Mirels' effect acts to increase the velocity of the test gas to that of the shock wave in the asymptotic limit.

Additionally, it was discovered that a fully reflected shock forms at the primary diaphragm. As discussed by Bakos and Morgan [94], even extremely thin secondary diaphragms have a significant opening time resulting in the creation of a reflected shock, the strength of which depends on the opening time of the diaphragm. This opening time was determined by observing the temporal displacement of the path of the shock wave. This is shown as an x-t diagram on Figure 3.8. The blue line represents the path of the shock wave assuming the diaphragm opens instantaneously. The gray points represent the measured arrival times of the shock wave at various locations. The secondary diaphragm used for all the conditions in this work is a sheet of 12 μm thick aluminum foil. Analysis of multiple runs showed that the diaphragm opening time of the 2.8 km/s condition was about 200 μs while the opening time of the 3.4 km/s and 4.0 km/s condition was about 150 μs . These opening times would create a fully reflected shock. Thus, the test gas state after being processed by the fully reflected shock needs to be calculated. This is done by solving for the stagnated post shock condition in the lab reference frame. The calculation of the test gas state after the reflected shock is done assuming thermochemical equilibrium; this is a widely used assumption in reflected shock tubes [95]. The stagnated condition is fundamentally dependent on the measured primary shock velocity and shock tube fill pressure. This stagnated state is the final state of the test gas in the shock tube, before its expansion into the acceleration tube. Hence, it is used as the input for the unsteady expansion into the acceleration tube.

Along with the measured wall pressure and shock wave velocity in the acceleration tube, the test gas state at the inlet of the acceleration tube is used to predict the test gas properties at the nozzle inlet. Assuming an unsteady isentropic expansion to a known pressure, the flow properties of the unsteadily expanded test gas in the acceleration tube can be calculated. In the PITOT code, the isentropic expansion to a certain pressure is controlled by an expansion factor. CFD simulations, discussed further in the next section, revealed that, for the conditions in the current work, the acceleration tube

wall pressure is approximately equal to the core flow static pressure. Hence, the expansion factor in the PITOT code is tuned such that the test gas pressure in the acceleration tube, as predicted by the isentropic expansion, matches with the measured wall pressure. Since the isentropic expansion is expanded to the measured wall pressure, the resulting estimate of the test gas velocity and temperature in the acceleration tube is, consequently, believed to be a good estimate of the true value. However, the accuracy of this estimate is highly dependent on the validity of the isentropic assumption for the unsteady expansion. Given that the velocity of the test gas in the acceleration tube is limited by the measured velocity of the shock wave and the theoretical velocity behind the shock wave, a check can be made with regards to the physical validity of the estimated test gas velocity.

Table 3.2. Shock processed test gas states in the shock tube from thermochemical equilibrium analysis.

Condition	Measured Shock Velocity ($\frac{m}{s}$)	State	P (Pa)	T (K)	V ($\frac{m}{s}$)	M	$\rho (\frac{kg}{m^3})$
2.8 km/s - x2s2906	1590 ± 10	s2	24400	1380	1580	2.88	0.0936
		s2r	299000	2360	0	0	0.654
3.4 km/s - x2s2905	1940 ± 10	s2	36400	1800	1930	3.09	0.106
		s2r	490000	2750	0	0	0.863
4.0 km/s - x2s2904	1985 ± 10	s2	38500	1860	1980	3.13	0.108
		s2r	526000	2810	0	0	0.899

The estimated conditions in the acceleration tube are then used as the input for a steady isentropic expansion which simulates the nozzle expansion process. In the PITOT code, the isentropic expansion is performed using a variable area ratio. This area ratio is tuned such that the estimated nozzle exit condition matches the radially averaged conehead pressure measured during the test time in the core flow. A unique solution exists for the area ratio to obtain a match with the averaged conical pitot probe measurements. The results of the isentropic expansion calculation through the nozzle are then used to estimate the freestream state of the test gas. Since the PITOT code estimate of the freestream condition is based on tuning to the measured conical pitot pressure, a comparison with the measured flathead pitot pressure will give an independent check of the accuracy of the estimated freestream condition. This is an independent check because different conical probe pressures can be obtained at the same pitot pressure, and vice versa. The conditions in the current work yielded excellent agreement, within 10%, between the flathead pitot probe measurement and the calculated pitot pressure using the estimated freestream conditions. Hence, it is believed that this PITOT code method provides a good estimate of the test condition properties. A summary of the method employed to estimate the test conditions using the PITOT code is provided in Figure 3.9.

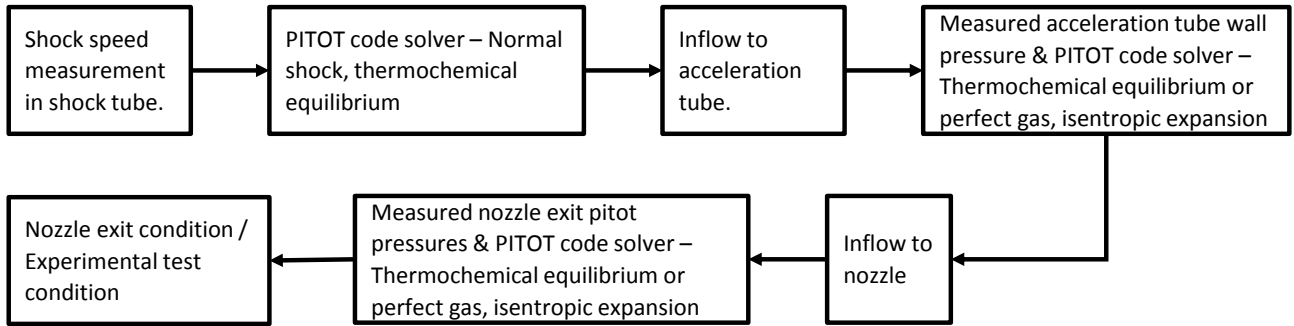


Figure 3.9. Flow diagram of the method utilized to estimate the test conditions using the PITOT code.

The particular pitot survey shots x2s2906 (2.8 km/s), x2s2905 (3.4 km/s) and x2s2904 (4.0 km/s) are used for the subsequent analyses in characterizing the freestreams. The estimated test gas condition in the shock tube for these particular shots are presented in Table 3.2. State ‘s2’ refers to the test gas state after being shock processed by the primary shock. State ‘s2r’ refers to the test gas state after being shock processed by the reflected shock. The estimated test gas condition, after the unsteady expansion, in the acceleration tube is presented in Table 3.3. Finally, the nozzle exit conditions for these shots are presented in Table 3.4. The measured shock speeds presented were calculated from the time of flight between two pressure transducers. The shock speeds in the shock tube were calculated from the pressure transducers SD2 and SD3, which are located near the end of the shock tube, while the shock speeds in the acceleration tube were calculated from AT4 and AT6, which are located near the end of the acceleration tube, as shown in Figure 3.1. The uncertainties associated with the measured shock speeds presented in Table 3.2 and Table 3.3 include errors from distance uncertainties associated with the location and size of each sensor, uncertainty of when (time) the shock arrives at the sensors and the sampling rate error of the data acquisition system. The uncertainties associated with the measured pitot pressures presented in Table 3.4 are based on the noise of the experimental data. More information on the uncertainties of shock speed and pressure measurements in the X2 expansion tube can be found in reference [83].

The measured primary shock speeds of 1580, 1930, and 1985 m/s for the 2.8, 3.4 and 4.0 km/s conditions are used to calculate the shock processed test gas conditions in the shock tube shown in Table 3.2. The isentropic unsteady expansion of the shock processed test gas into the acceleration tube is tuned to expand to the measured wall pressures of approximately 2500, 2600 and 960 Pa for the 2.8, 3.4 and 4.0 km/s conditions respectively to estimate the test gas properties in the acceleration tube shown on Table 3.3. The isentropic steady expansion of the test gas through the nozzle is tuned, through the nozzle area ratio, to expand to the measured conehead pitot pressures of approximately 1350, 1510 and 840 Pa for the 2.8, 3.4 and 4.0 km/s conditions respectively to estimate the test gas properties at the nozzle exit shown on Table 3.4. These conehead pitot pressures used for the tuned solution represents the average pressure measured across a 144 mm diameter at the nozzle exit.

Table 3.3. Test gas properties calculated by PITOT in the acceleration tube (nozzle inlet) after unsteady expansion.

Condition	Measured Shock Velocity ($\frac{m}{s}$)	Analysis	P (Pa)	T (K)	v ($\frac{m}{s}$)	M	$\rho (\frac{kg}{m^3})$
2.8 km/s - x2s2906	2880 ± 20	Perfect Gas	2510	1450	2710	4.8	0.0089
		Equilibrium	2510	1360	2660	4.8	0.0096
3.4 km/s - x2s2905	3570 ± 20	Perfect Gas	2620	1660	3300	5.3	0.0076
		Equilibrium	2620	1800	3310	5.3	0.0077
4.0 km/s - x2s2904	4060 ± 30	Perfect Gas	958	1530	3940	6.6	0.0030
		Equilibrium	956	1670	3950	6.5	0.0030

Table 3.4. Equilibrium and calorically perfect gas freestream estimates (nozzle exit) from PITOT.

Condition	Measured Flathead Pressure (kPa)	Analysis	P _{PITOT} (kPa)	P (Pa)	T (K)	V ($\frac{m}{s}$)	M	CO ₂ Mole Fraction
2.8 km/s	13.2 ± 2.9	Perfect Gas	12.1	355	1190	2870	5.7	0.92
		Equilibrium	12.7	323	1010	2800	5.9	1.00
3.4 km/s	14.5 ± 1.4	Perfect Gas	14.6	360	1370	3480	6.2	0.76
		Equilibrium	14.5	341	1400	3490	6.3	1.00
4.0 km/s	9.2 ± 0.9	Perfect Gas	8.9	150	1280	4070	7.5	0.73
		Equilibrium	9.1	139	1300	4090	7.6	1.00

The freestream estimates were calculated with both the frozen and equilibrium limits using the PITOT code. The frozen estimate of the freestream was calculated based on freezing the thermochemical state of the test gas at the stagnated state in the shock tube by assuming a calorically perfect gas for the expansions. The equilibrium limit was calculated based on equilibrium calculations of each state of the test gas as it travels through the expansion tube. The starting point for both the equilibrium and perfect gas calculations is the condition behind the reflected shock in the shock tube, s2r, on Table 3.2. The result on Table 3.4 shows that while the freestream solution is tuned to match the measured conical pitot pressure, the estimated pitot pressure matched well with the measured pitot pressure (measured at a radial offset of 18 mm from the nozzle centreline) for both the equilibrium and perfect gas calculations. Furthermore, the frozen and equilibrium bounds of the tuned solutions are not significantly large for the estimated macroscopic flow properties of pressure, temperature, velocity and the Mach. The bounds for the 3.4 km/s and 4.0 km/s conditions are particularly small, while the 2.8 km/s condition showed a slightly larger bound. It can be inferred from the results that any

thermochemical non-equilibrium involved would not have had too great of an effect on the macroscopic flow properties when using PITOT to estimate the freestream condition. This is a positive result as, consequently, it allows the thermochemical state of the freestream to be estimated separately from the macroscopic state. As shown on Table 3.4, a large bound exists for the vibrational and chemical state of the freestream. As mentioned in section 3.4.1, it is unclear if these conditions will be in thermochemical equilibrium at the nozzle exit. Therefore, work is carried out in section 3.4.4 to determine the thermochemical state of the freestreams, which is important for the correct interpretation of experimental results [96].

3.4.3 CFD

To supplement the inflow predictions made using the PITOT code method, further work is done to help characterize the freestream by performing transient two-dimensional axisymmetric CFD simulations of the expansion tube after the rupture of the secondary diaphragm. The simulation is done using the Eilmer3 code [97], which is the in-house CFD code and it is a finite-volume Navier-Stokes flow solver for structured grids. The expansion tube simulation domain is shown in Figure 3.10. The stagnated test gas condition in the shock tube, shown in Table 3.2, is used as the constant inflow for the CFD simulation. The initial fill condition in the simulation domain is air at 40, 30 and 10 Pa for the 2.8, 3.4 and 4.0 km/s condition respectively. The simulation includes viscosity and turbulence. The simulation is conducted using both perfect gas and thermochemical equilibrium for the carbon dioxide test gas to obtain a bound for the possible solution. Thermochemical equilibrium is also used for the air which is initially filled in the domain. The turbulence model used is the Baldwin-Lomax model. The simulation was conducted with a CFL number of 0.3. Boundary layer clustering is done but no clustering is done in the axial direction. In the acceleration tube and nozzle, there are 81 elements in the radial direction and 8813 elements in the axial direction. In the acceleration tube, the axial grid spacing is 1 mm and the radial maximum and minimum grid spacing is 0.9 mm and 0.15 mm respectively. In the nozzle, the axial grid spacing is 0.4 mm. At the nozzle exit, the radial maximum and minimum grid spacing is 2.1 mm and 0.37 mm respectively. The flow in the shock tube is not simulated as it is believed to be well defined from the thermochemical equilibrium PITOT code estimates [98]. This is because the viscous influences in the shock tube are considered negligible due to the high pressure. Viscous effects are important only starting from the acceleration tube where pressures are lower. Therefore only flow beyond the shock tube is simulated. The same pitot survey shots in section 3.4.2, x2s2906 (2.8 km/s), x2s2905 (3.4 km/s) and x2s2904 (4.0 km/s), are analyzed.

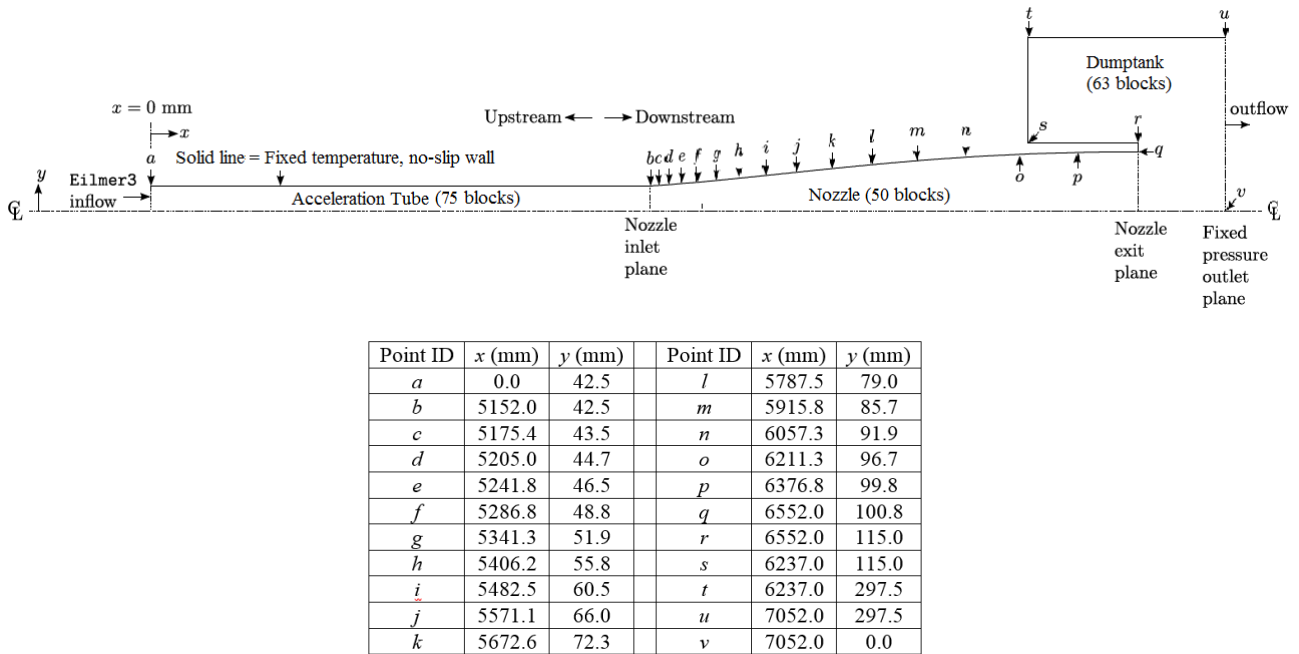


Figure 3.10. The CFD simulation domain. All blocks are divided in the x direction.

The computed test gas properties at the nozzle exit are shown in Table 3.5. These properties are extracted at the tube centreline. It is interesting to examine the differences in flow properties between the thermochemical equilibrium solution and the perfect gas solution. The freestream pressure does not change much between the equilibrium and perfect gas solutions. However, the freestream temperature differs significantly. The perfect gas solution computes a temperature that is significantly lower than that from the equilibrium calculations. This is because the perfect gas calculation does not account for the energy transfer from the thermal and chemical modes which would occur during the thermochemical equilibrium expansion. Thus, in the perfect gas solution, the thermal and chemical modes are frozen, and excess energy is not transferred to the translational mode. This is a well understood result in the context of expanding flows. Another observation from Table 3.5 is that the freestream velocity differs significantly between the perfect gas and equilibrium solutions. The result shows that assuming perfect gas produces a lower velocity compared to that assuming thermochemical equilibrium. This is consistent with the findings of Meyers et al. [91] who showed that thermochemical freezing in expanding flows decreases the flow velocity. Furthermore, thermochemical freezing in the expanding flow is seen to increase pitot pressure at the nozzle exit by around 20 – 40 % for the current conditions. As the nozzle exit static pressures are similar between the frozen and equilibrium cases, this increase in pitot pressure seems to be due to the increase in Mach number with freezing, which itself is due to the decrease in temperature with freezing.

Table 3.5. Nozzle exit properties during the steady test time from CFD. The flathead pitot pressure is taken at a radial distance of 18 mm from the centerline. The conical pitot pressure is the average pressure measured across a 144 mm diameter. PG means perfect gas and EQ means thermochemical equilibrium.

Condition	Measured		Analysis	Conical / Pitot Pressure (kPa)	P (Pa)	T (K)	v ($\frac{m}{s}$)	M	CO_2 Mole Fraction
	Conehead / Flathead	Pressure (kPa)							
2.8 km/s	1.4 ± 0.3 /	PG		1.3 / 12.8	304	623	2390	6.2	0.92
	13.2 ± 2.9	EQ		1.2 / 10.9	309	1150	2760	5.5	1.00
3.4 km/s	1.5 ± 0.2 /	PG		1.7 / 18.4	355	625	2820	6.9	0.76
	14.5 ± 1.4	EQ		1.5 / 14.3	383	1600	3350	5.7	1.00
4.0 km/s	0.8 ± 0.1 /	PG		0.7 / 8.4	90.0	450	3240	9.3	0.73
	9.2 ± 0.9	EQ		0.5 / 5.5	97.4	1410	3890	7.0	1.00

Table 3.6. Operating condition properties at the acceleration tube exit/nozzle inlet from CFD.

Condition	Measured Shock Speed ($\frac{m}{s}$)	Measured Wall Pressure (kPa)	Analysis	Shock Speed ($\frac{m}{s}$)	Wall Pressure (kPa)
2.8 km/s - x2s2906	2880 ± 20	2.5 ± 0.3	Perfect Gas	2270	2.2
			Equilibrium	2440	2.6
3.4 km/s - x2s2905	3570 ± 20	2.6 ± 0.3	Perfect Gas	2650	2.2
			Equilibrium	2970	2.6
4.0 km/s - x2s2904	4060 ± 30	1.0 ± 0.1	Perfect Gas	2980	0.95
			Equilibrium	3370	1.24

To assess the validity of the CFD solutions it is necessary to compare the measured operating condition properties, namely the nozzle exit pitot pressure, secondary shock speed and wall pressure in the acceleration tube, to the equilibrium and perfect gas bounds of the computed values. From Table 3.5 and Table 3.6, the perfect gas and equilibrium bounds of the computed pitot pressure and acceleration tube wall pressure roughly contains the measured values. However, as shown in Table 3.6, the computed perfect gas and equilibrium bounds of the shock speeds do not contain the measured values. The shock speeds from both CFD and experiments were calculated from the time of flight between the location of AT4 and AT6 shown in Figure 3.1. The computed shock speeds differ from the measured values by at least 15 - 25 %. This is not expected as the Eilmer3 CFD code has been shown to produce solutions that have a good match, better than 3%, with the measured secondary

shock speeds [99] [100] [101] [102] [103]. Additionally, the more surprising aspect is that the CFD under-estimates the shock speed. The same simulations performed in one-dimension using the L1d code also showed this observation. The substantial under-prediction of the shock speeds by CFD is a surprising result, as CFD is well known to over-estimate the shock speeds.

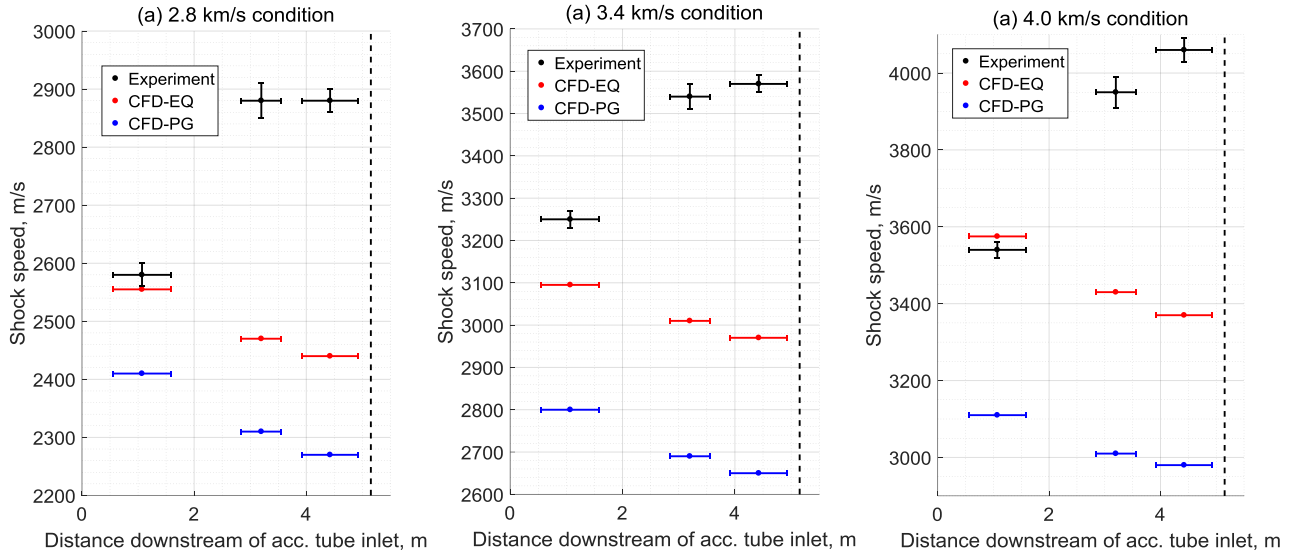


Figure 3.11. Measured and computed shock speeds at various locations along the acceleration tube.
The vertical dashed line marks the end of the acceleration tube (nozzle inlet).

The measured shock speeds at other locations along the acceleration tube were compared to the two-dimensional axisymmetric CFD computations as well, and the results are presented in Figure 3.11. The vertical error bars represent the uncertainties of the shock speed measurements, while the horizontal error bars show the region between two points (locations of pressure transducers) used to calculate the shock speeds from time of flight. The results show that, in general, CFD over-estimates the shock speeds at all locations along the tube. The exception is the 4.0 km/s condition where the equilibrium CFD marginally over-predicts the shock speed near the acceleration tube inlet. The best agreement between the CFD prediction and measurement is observed near the inlet of the acceleration tube. Interestingly, the CFD shock speed decreases along the tube while the experimental shock speed increases along the tube, resulting in the large disagreement in shock speed near the end of the acceleration tube. The decrease in shock speed along the tube, shown in the CFD, is caused by viscosity. The cause of the increase in shock speed along the tube, shown in the experiments, is unclear. For the 2.8 km/s and 3.4 km/s condition, the experimental shock speed increases up to a certain point, while for the 4.0 km/s condition, the experimental shock speed seems to increase through the entire length of the tube. For all conditions, the experimental results show no shock speed attenuation. These behaviours have been confirmed through numerous repeated runs. The

acceleration behaviour of the experimental shock waves could be related to the complex influences of the secondary diaphragm rupture (not simulated in CFD) [104].

The cause of the general under-estimate of shock speed by the CFD in the current work is unknown. The inlet condition for the simulation is the fully reflected shock condition in Table 3.2 calculated based on the shock tube fill pressure and measured primary shock speed. This fully reflected shock inlet condition results in the upper bound of the secondary shock speed. Consequently, the acceleration tube inlet condition required to generate the correct shock speed in the simulation would not be physically consistent with the shock tube fill pressure and measured primary shock speed. Therefore the incorrect simulated shock speed is likely not due to an incorrect inlet condition. The shock speed discrepancy might be due to reasons relating to simulating relatively low enthalpy and low pressure carbon dioxide conditions in the expansion tube. The previous CFD simulations of the expansion tube are for higher enthalpy conditions where the secondary shock speed range from 5 – 10 km/s, or high pressure conditions where the freestream pitot pressure is greater than 1 MPa. Hence, the results in this work indicate that further investigations are required in order to better model low enthalpy and low pressure carbon dioxide test conditions in the expansion tube using CFD.

Interestingly, good agreement of the acceleration tube wall pressure traces were found between experiment and CFD, even though the shock speeds in the acceleration tube differed significantly between experiment and CFD. The acceleration tube wall pressure traces are presented in Figure 3.12 for pressure transducers AT4 and AT6, which are located near the end of the tube. The results show that the equilibrium CFD computes the acceleration tube wall pressure traces particularly well for the 2.8 km/s and 3.4 km/s conditions, while the perfect gas and equilibrium CFD simulations bound the experimental traces for the 4.0 km/s condition. Note that, as various upstream processes are not simulated due to the constant inlet condition, CFD does not predict the correct termination of test flow, as shown in Figure 3.12.

Due to the significant discrepancy in the shock speed, the freestream (nozzle exit) properties estimated by CFD are concluded as unreliable. The freestream estimate made by PITOT is believed to be the better representation of the actual freestream because it is tuned to match the measured operation condition properties. Therefore, subsequent interpretations of experimental results were carried out using the PITOT code estimates.

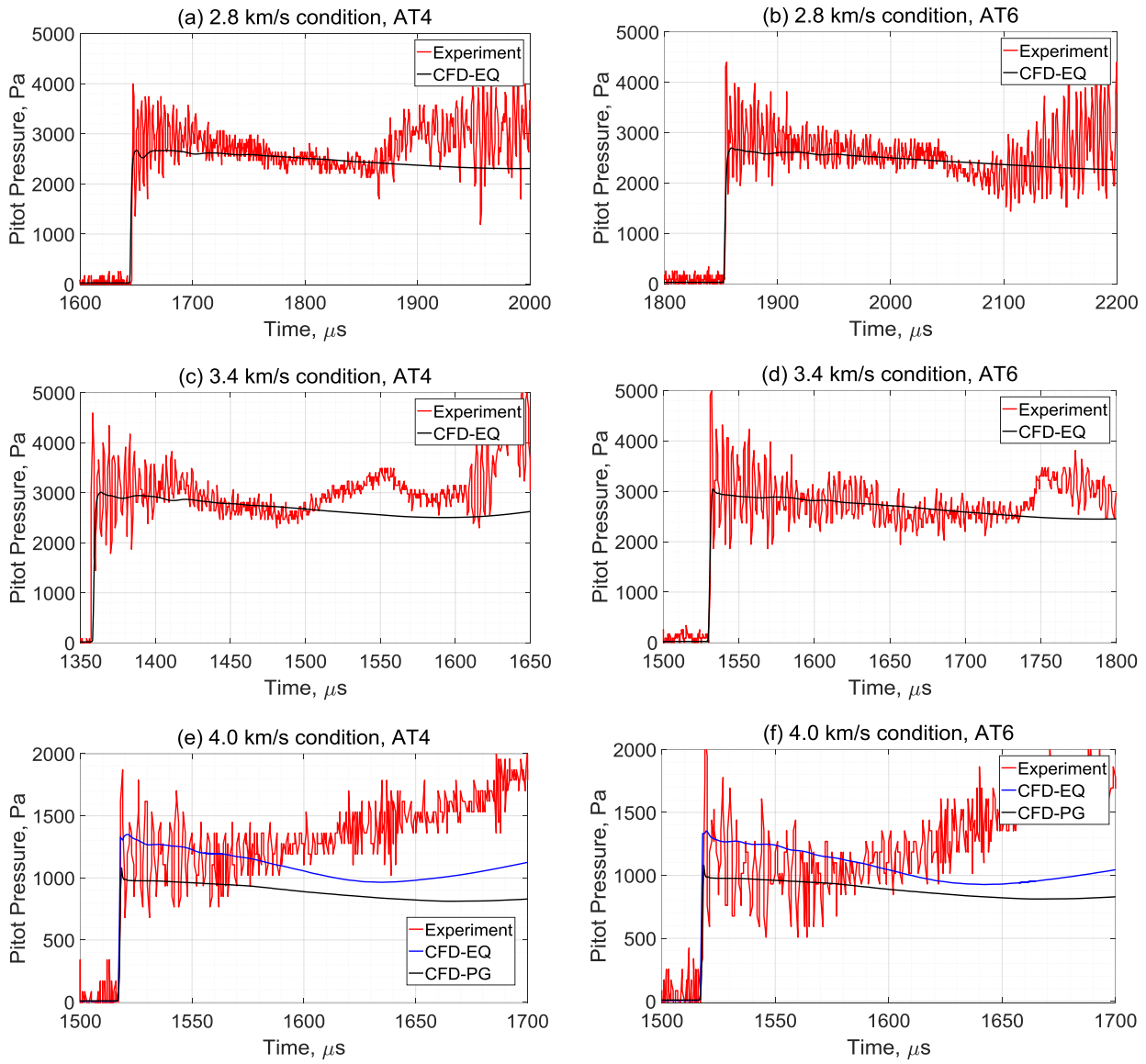


Figure 3.12. Comparison of acceleration tube wall pressure traces between experiment and CFD.

3.4.4 Shock Wave Comparison

As mentioned in section 3.4.1, it is not clear if the carbon dioxide freestream in this project is at thermochemical equilibrium or frozen at an excited state. To investigate the thermochemical state of the freestream in the current work, a shock wave comparison is conducted for the estimated freestream conditions in the present work. Maclean and Holden [51] believe that a comparison of the measured shock wave of the test model against the computed shock wave of the test model using CFD with estimated equilibrium inflow properties is believed to be a good indicator of whether or not there is freezing of the vibrational and chemical energy modes in the freestream. This is because having excess energy stored in the thermochemical modes increases the shock standoff. Although CFD has been shown in the previous section to be incapable of describing transient CO₂ flow in an expansion tube, CFD simulations using the two-temperature model has been shown to be capable of

predicting the steady state CO₂ shock wave location closely for similar inflow conditions [52] [89] [53] [105]. Therefore, a mismatch in shock wave location would likely be due to an incorrectly defined inflow condition rather than errors relating to the numerical modelling of the shock layer.

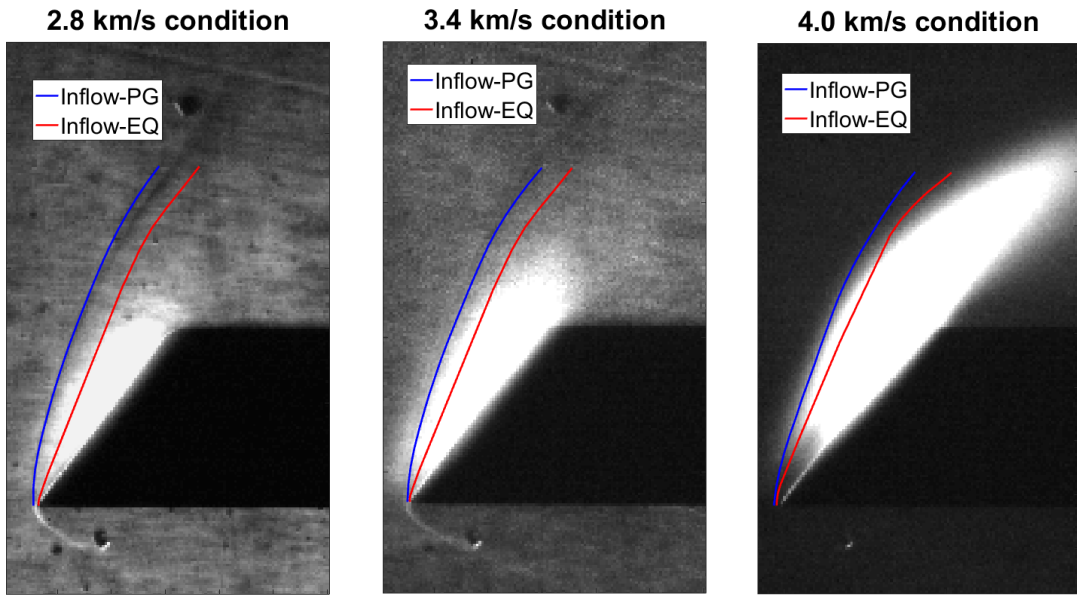


Figure 3.13. Shock wave comparison between experiment and simulation results.

For this study, the freestream estimates from the PITOT code in Table 3.4 are used because the CFD results presented in the previous section are shown to be incorrect due to the inconsistency with experimental shock speed measurements. The CFD of the flow over the wedge was conducted using the Eilmer3 code [97] in a two-dimensional domain. A detailed description of the two-dimensional wedge simulation domain is presented in section 6.6. A two-temperature simulation was carried out using the finite rate chemistry model presented by Cruden et al. [44] for low enthalpy carbon dioxide mixtures. The Landau-Teller model [106] is used to model the V-T exchange using the vibrational relaxation times, τ_v , provided by Park et al. [107]. This thermochemical model is discussed in further detail in section 6.3. Experimental measurements of the shock wave location are done by taking high-speed schlieren videos for the 2.8 and 3.4 km/s condition. For the 4.0 km/s condition, the shock wave location is measured using high-speed videos of the flow luminosity as it is sufficiently strong to allow the visualization of the location of the shock wave. In the high speed videos, images are taken every 8 μs and the exposure time for each image is 4 μs . The measured location of the shock wave remains approximately constant during the steady test time which is discussed further in section 3.6.1.

In Figure 3.13, numerically estimated shock waves using both the equilibrium and perfect gas estimates of the freestream conditions, shown in Table 3.4, are compared to the measured shock wave location during the test time. The measured shock wave is clearly further away from the test model than that calculated using the equilibrium inflow condition. This discrepancy is likely too large to be

attributed to the numerical modelling of the wedge flowfield. On the other hand, Figure 3.13 shows that the frozen freestream estimate gives a good match for the shock wave. The frozen inflow gives such a good match with the measured shock waves that the blue line entirely covers the measured shock waves in the schlieren images. Consequently, the result may indicate that the freestream in the experiment is frozen at an excited thermochemical state.

Table 3.7. Survey of low and medium velocity carbon dioxide conditions in expansion tubes.

Facility	Expansion length (m)	v ($\frac{m}{s}$)	Expansion time (ms)	ρ ($\frac{kg}{m^3}$)	Shock wave match	References
University of Illinois HET	3.96	3050	1.3	0.0144	Yes	[90] [108]
CUBRC LENS XX Condition 1	33.9	3880	8.7	0.0018	Yes	[101]
CUBRC LENS XX Condition 2		4780	7.1	0.0008	Yes	[101]
GASL HYPULSE	14.1	4770	3.0	0.0058	No	[90] [109] [110]
X2 – 2.8 km/s		2800	2.3	0.0017	No	Present work
X2 – 3.4 km/s	6.53	3490	1.9	0.0013	No	Present work
X2 – 4.0 km/s		4090	1.6	0.0006	No	Present work

It is interesting to compare the result of the shock wave comparison for the conditions in the current work with results for similar carbon dioxide conditions generated in other expansion tubes around the world. The comparison is presented in Table 3.7. The expansion length is defined as the distance from the secondary diaphragm to the test section. The density value is the estimated density of the flow at the test section. The expansion time value is approximated by dividing the expansion length by the estimated freestream velocity. This comparison is carried out to assess if the result of the shock wave comparison in the current work is consistent with the results from previous works for the belief that the shock wave mismatch is due to thermochemical excitation in the freestream.

The HET condition was used by Sharma et al. [111] [108] to study the shock standoff and surface heat transfer of various diameter sphere models and a scaled MSL model at various angles of attack. Sharma et al. showed an excellent agreement for the shock wave comparison between the experimental and numerical results calculated assuming an equilibrium inflow. Hence, it is believed

that the freestream condition is in equilibrium. So even though the HET is shorter than X2, the condition generated is in equilibrium, probably because the density involved in their work is an order of magnitude higher than that concerned in the current work. This higher density in the HET condition could make it less susceptible to freezing. The conditions generated in LENS XX by Maclean et al. [53] were used to study the surface heat transfer, surface pressure and shock standoff on a 7-in diameter spherical capsule model. Excellent agreement of the shock wave location was seen in the numerical to experimental comparison using an equilibrium inflow. Hence, the freestream condition was also believed to be equilibrated. The LENS XX generates an equilibrium freestream at a similar density as that concerned in this work. This could be because the LENS XX is much longer than X2. This results in a longer expansion time which promotes thermochemical equilibration. The condition generated in HYPULSE by Hollis and Perkins [109] was used to study the surface heat transfer on a 70° sphere cone Mars entry aeroshell model. Schlieren images were taken during the experiments. Using the schlieren images, Hollis and Prabhu [90] compared the measured shock wave location to that calculated numerically using an equilibrium inflow. A poor agreement was observed, with the measured shock standoff distance being twice as large as that calculated numerically. This likely shows that the freestream condition had excess thermochemical energy. The HYPULSE is not significantly longer than X2 and the HYPULSE condition does not have a significantly higher density than the X2 conditions in the current work.

Table 3.8. The best estimate of the freestream (nozzle exit) conditions. The uncertainties were estimated from the variation and uncertainties of the measured properties of each operating condition.

Condition	P (Pa)	T (K)	Tv (K)	V ($\frac{m}{s}$)	M	Mole Fraction CO ₂ / CO / O ₂ / O	CO ₂ Number Density (cm ⁻³)
2.8 km/s	355 ± 70	1190 ± 90	2350 ± 80	2870 ± 140	5.7 ± 0.3	(0.92 ± 0.02) / 0.054 / 0.0267 / 0.0	(2.0 ± 0.4) x 10 ¹⁶
3.4 km/s	360 ± 40	1370 ± 90	2750 ± 80	3480 ± 140	6.2 ± 0.3	(0.76 ± 0.04) / 0.158 / 0.076 / 0.006	(1.4 ± 0.2) x 10 ¹⁶
4.0 km/s	150 ± 30	1280 ± 100	2810 ± 80	4070 ± 150	7.5 ± 0.4	(0.73 ± 0.04) / 0.18 / 0.083 / 0.007	(6.2 ± 1.3) x 10 ¹⁵

In the context of investigating the shock wave mismatch due to the possible thermochemical excitation in the inflow, the results of the shock wave comparison in the current work seems to be consistent with the results from previous works. As discussed by Maclean and Holden, using the expansion tube does help to prevent freezing in the freestream [51], however, it does not guarantee an equilibrium freestream. It could still depend on the length of the expansion tube as well as the density of the flow.

As the perfect gas estimated inflows provide the best match to shock wave location, these estimates will be considered the best estimates of the freestream flow properties produced using the PITOT code. These perfect gas estimated inflow conditions are summarized in Table 3.8 along with the estimated uncertainties. The PITOT code was used to generate these uncertainties, which represent the bounds of the estimated test conditions, based on the possible variation of the shock speed and pressure measurements when considering the shot-to-shot variations and uncertainties of the measurements [83]. The result showed that static pressure (and density) was the most sensitive and uncertain freestream parameter with variations of around 10 – 20 % in all cases. On the other hand, velocity was shown to be the least sensitive parameter with variations of less than 5 % in all cases.

As mentioned in section 3.4.1, no detailed study has been done to confirm that the discrepancy in the shock standoff is indeed due to excess thermochemical excitation in the freestream. It is also possible that the mismatch in the location of the shock wave is caused by incorrect estimates of the other flow properties. This is because the mismatch of the shock wave location between the measurement and that calculated from the equilibrium inflow is not as significant as the mismatch encountered by Maclean and Holden [51] shown in Figure 3.6. Hence, there is still uncertainty in regards to the actual condition of the experimental inflows. Therefore, further characterization of the inflow conditions are presented in sections 5.3 and 5.5 with the aid of spectroscopic measurements.

3.5 Similarities of Experiments to Flight

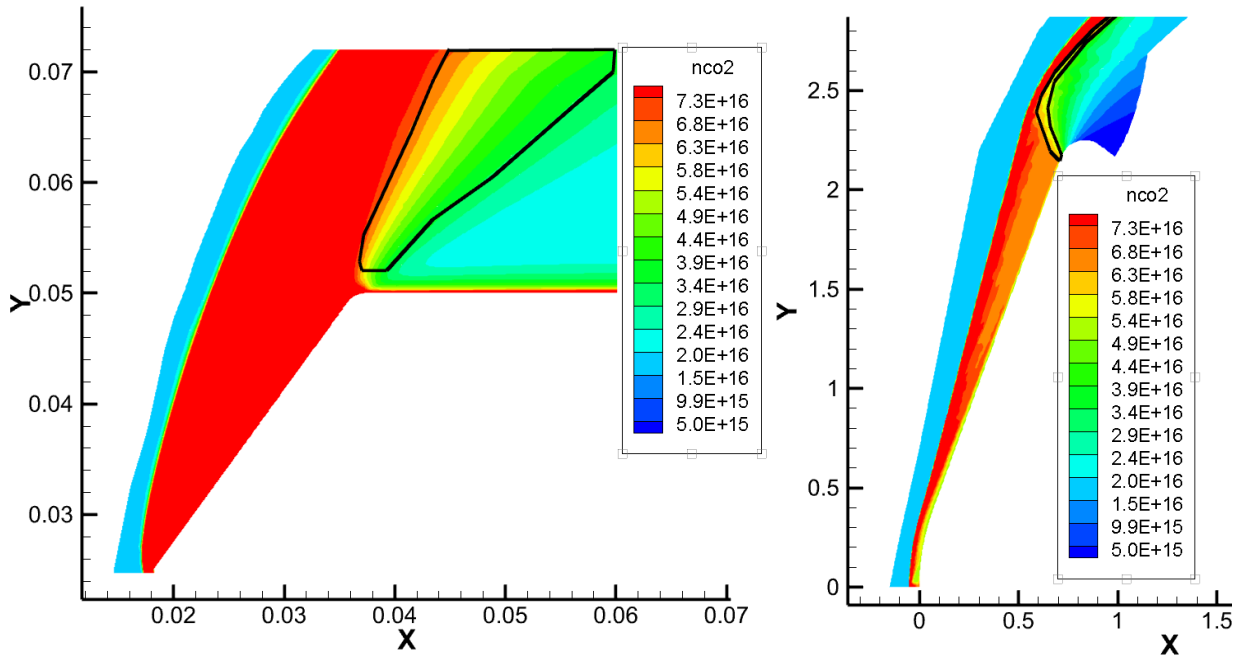
To show that the conditions of our experimental measurements have similarities to flight, it is important to map regions in the flowfield in the experiment to regions in the flowfield around an entry vehicle in flight. This is done by identifying regions in the flowfield around an entry vehicle that have the same carbon dioxide number density and temperature as that in equivalent locations in the experimental flowfield. The carbon dioxide number density and temperature are chosen as the properties to be mapped because the mid-infrared radiation that is being investigated is most dependent upon these two properties. Asymmetric CFD simulations of the Mars Science Laboratory (MSL) using the two-temperature model, described in detail in section 6.3, were conducted using various freestream conditions corresponding to the MSL best-estimated trajectory (BET) [12]. Pure carbon dioxide was used as the flight freestream chemical composition for consistency with the experimental condition. This produces an approximation of the flight vehicle flowfield. Two-dimensional simulations of the wedge model using the estimated expansion tube freestream conditions in Table 3.8 were computed with the same two-temperature model. This produces an approximation of the experimental flowfield. It is then possible to determine at which trajectory

points the experimental conditions are most relevant to, as well as which region of the afterbody flowfield the experiment simulates.

Table 3.9. Summary of the corresponding MSL BET freestream condition for each experimental freestream condition.

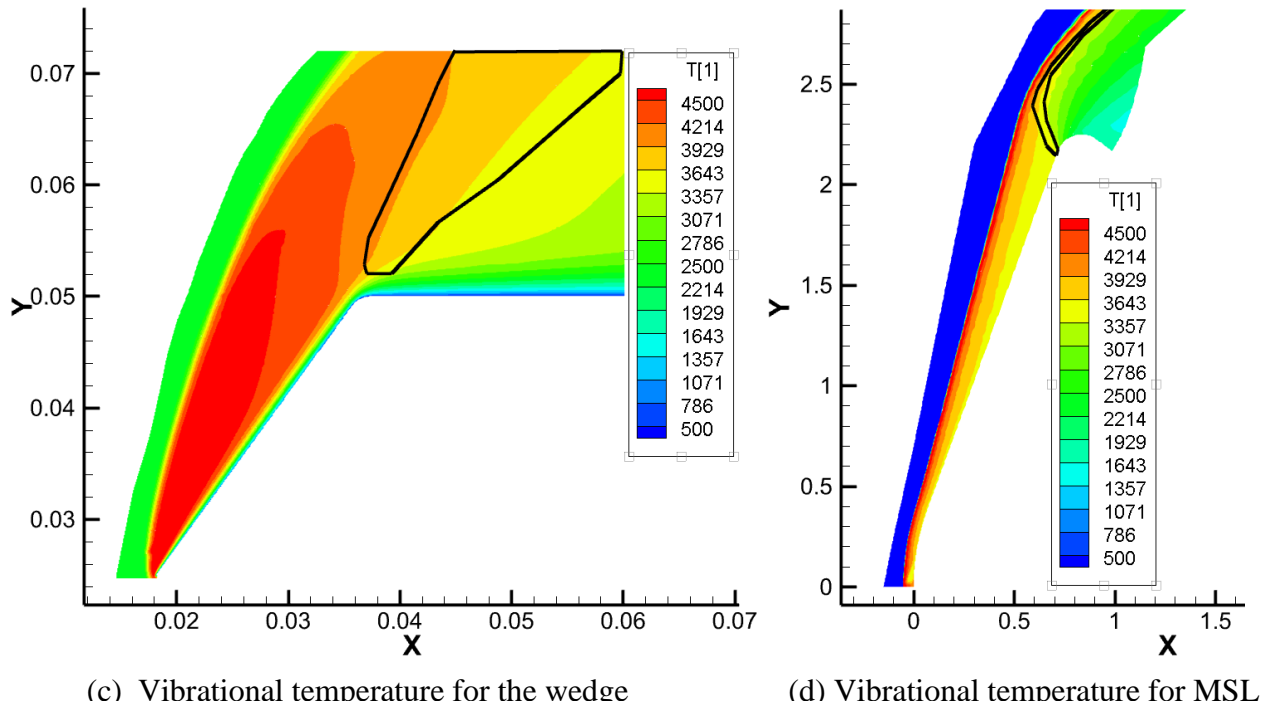
Experimental Freestream Condition	Flight Freestream Condition				Flowfield Similarity Region Properties	
	Time (s)	P_{static} (Pa)	T (K)	$V (\frac{m}{s})$	T_v (K)	CO_2 number density (cm^{-3})
Nominal Velocity						
2.8 km/s	74.0	36.6	170	4860	3600 - 3900	$3.9 \times 10^{16} - 6.3 \times 10^{16}$
3.4 km/s	69.3	22.2	169	5260	3200 - 3500	$1.0 \times 10^{16} - 1.3 \times 10^{16}$
4.0 km/s	65.1	13.1	161	5520	3400 - 3900	$4.7 \times 10^{15} - 6.4 \times 10^{16}$

As shown in Figure 3.14 to Figure 3.16, it is possible to identify a point on the MSL flight trajectory where the vibrational temperature and carbon dioxide number density in a region of the flowfield is approximately the same as that in a region of the experimental flowfield. The black line encloses the similarity regions and the results are summarized in Table 3.9. Figure 3.14 to Figure 3.16 show that the expanding flow generated in the experiment is simulating the temperature and CO_2 number density in the expanding flow around the shoulder of the Mars entry vehicle, which contributes to the total afterbody radiative heating. As shown in Table 3.9, the 2.8, 3.4 and 4.0 km/s test conditions in the current work approximately simulate the 74.0 s, 69.3 s and 65.1 s points on the MSL best estimate trajectory respectively. Surzhikov [7] showed, through numerical simulations, that the CO_2 afterbody radiative heating is comparable in magnitude to the corresponding afterbody convective heating on the MSL entry capsule at these flight trajectory points. Consequently, the afterbody radiation is important at these flight conditions justifying the choice of experimental conditions in this work. It is important to note that the region of similarity shown in this section is considered weak similarity as the process which produce the state of similarity is not matched exactly with flight.



(a) CO₂ number density for the wedge

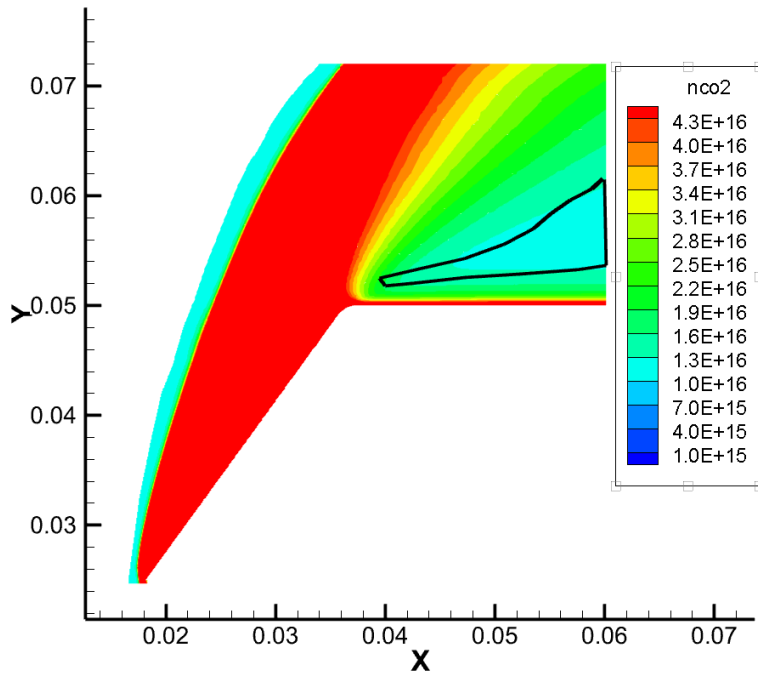
(b) CO₂ number density for MSL



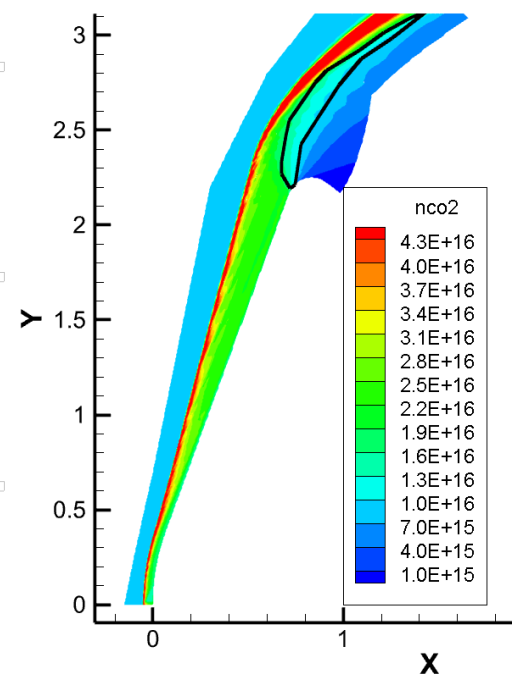
(c) Vibrational temperature for the wedge

(d) Vibrational temperature for MSL

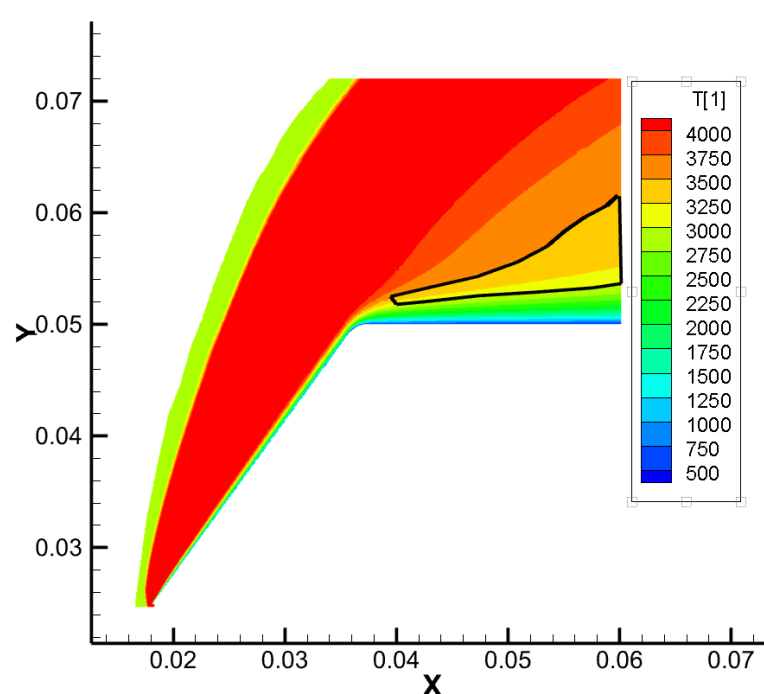
Figure 3.14. A region in the 2.8 km/s experimental condition with the same carbon dioxide number density and vibrational temperature as a region in the t=74.0s flight condition.



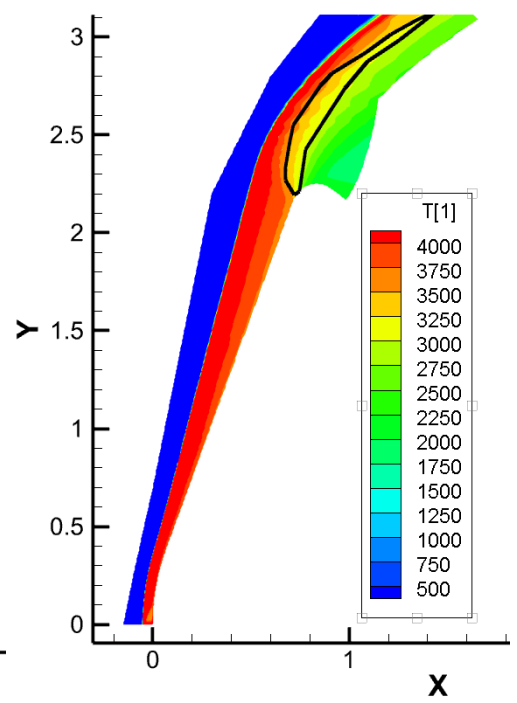
(a) CO₂ number density for the wedge



(b) CO₂ number density for MSL

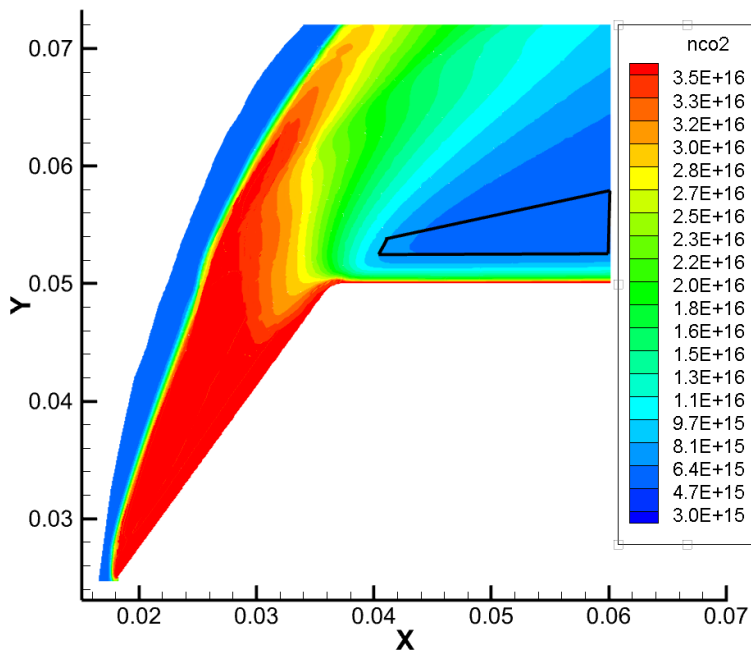


(c) Vibrational temperature for the wedge

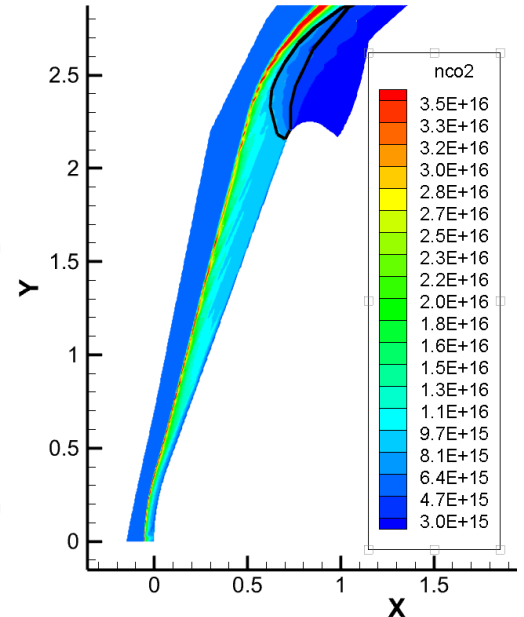


(d) Vibrational temperature for MSL

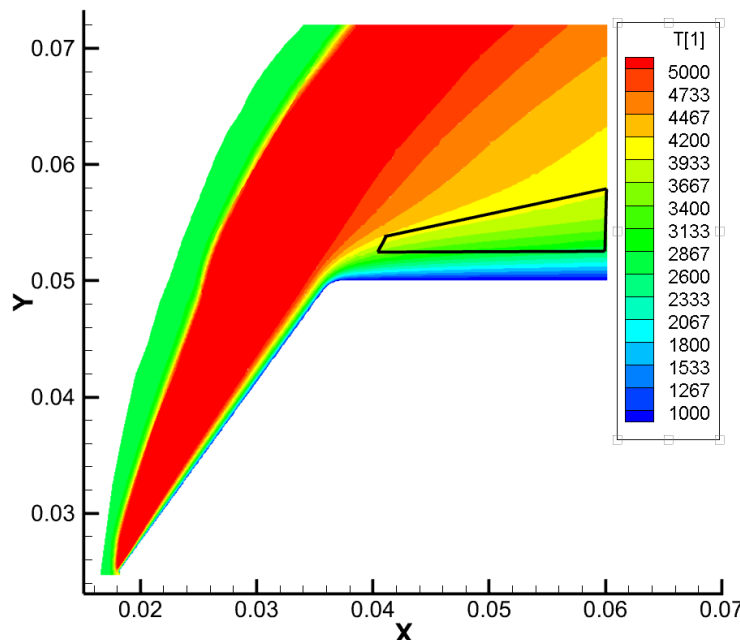
Figure 3.15. A region in the 3.4 km/s experimental condition with the same carbon dioxide number density and vibrational temperature as a region in the t=69.3s flight condition.



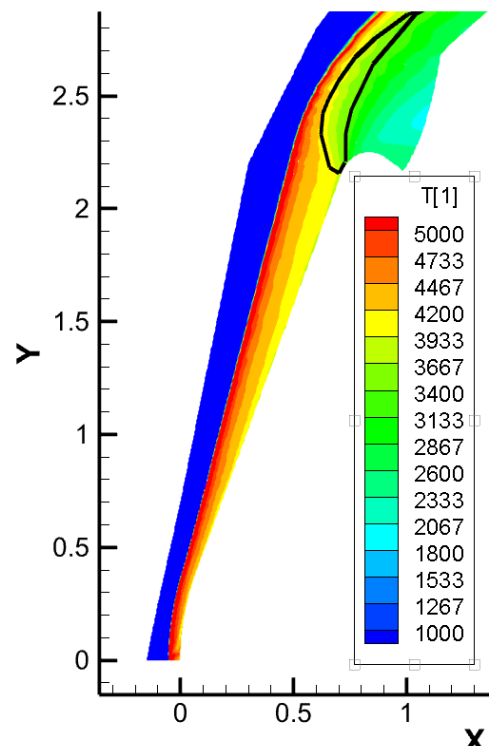
(a) CO₂ number density for the wedge



(b) CO₂ number density for MSL



(c) Vibrational temperature for the wedge



(d) Vibrational temperature for MSL

Figure 3.16. A region in the 4.0 km/s experimental condition with the same carbon dioxide number density and vibrational temperature as a region in the t=65.1s flight condition.

3.6 Features of the Generated Freestream Conditions

To assess the quality of the three new expansion tube conditions, it is necessary to evaluate the steady flow duration, shot-to-shot consistency and the size and uniformity of the core flow. The steady flow duration and core flow size and uniformity of the freestream can be assessed by taking pitot probe measurements at the nozzle exit. The shot-to-shot consistency of the conditions are assessed by observing the variation in the measured shock speeds, acceleration tube wall pressures and nozzle exit pitot pressures from multiple shots.

3.6.1 Freestream Steady Flow Duration

For the expansion tube conditions to be useable, there must be a duration of steadiness in the freestreams. This then allows for a period of steady flowfield to be generated around the test model. Generating a period of steadiness in the flowfield around the test model is essential for performing emission spectroscopy which will be used to diagnose the flowfield. Measuring the pitot pressure at the nozzle exit allows the steady duration to be identified. Figure 3.17 shows that the steady flow durations of all three conditions is more than 100 μs . The pitot traces show that the 2.8 km/s condition has the longest test time of 170 μs while the 3.4 km/s condition has the shortest test time of 105 μs . A pattern which can be observed is that the time taken for the steady flow to arrive, relative to the shock arrival, increases with decreasing velocity. This is consistent with intuition because the accelerator gas and the nozzle startup would take longer to complete at lower velocities. The most important feature which can be seen in Figure 3.17 is that the unsteadiness feature during the steady duration occurs at low frequencies. The period of the unsteadiness is in the order of tens of microseconds. The consequence of this is that, when taking radiation images, longer exposure times should be used in order to average out the unsteadiness. If the exposure time is too short, the unsteadiness may influence the result of the radiation measurement.

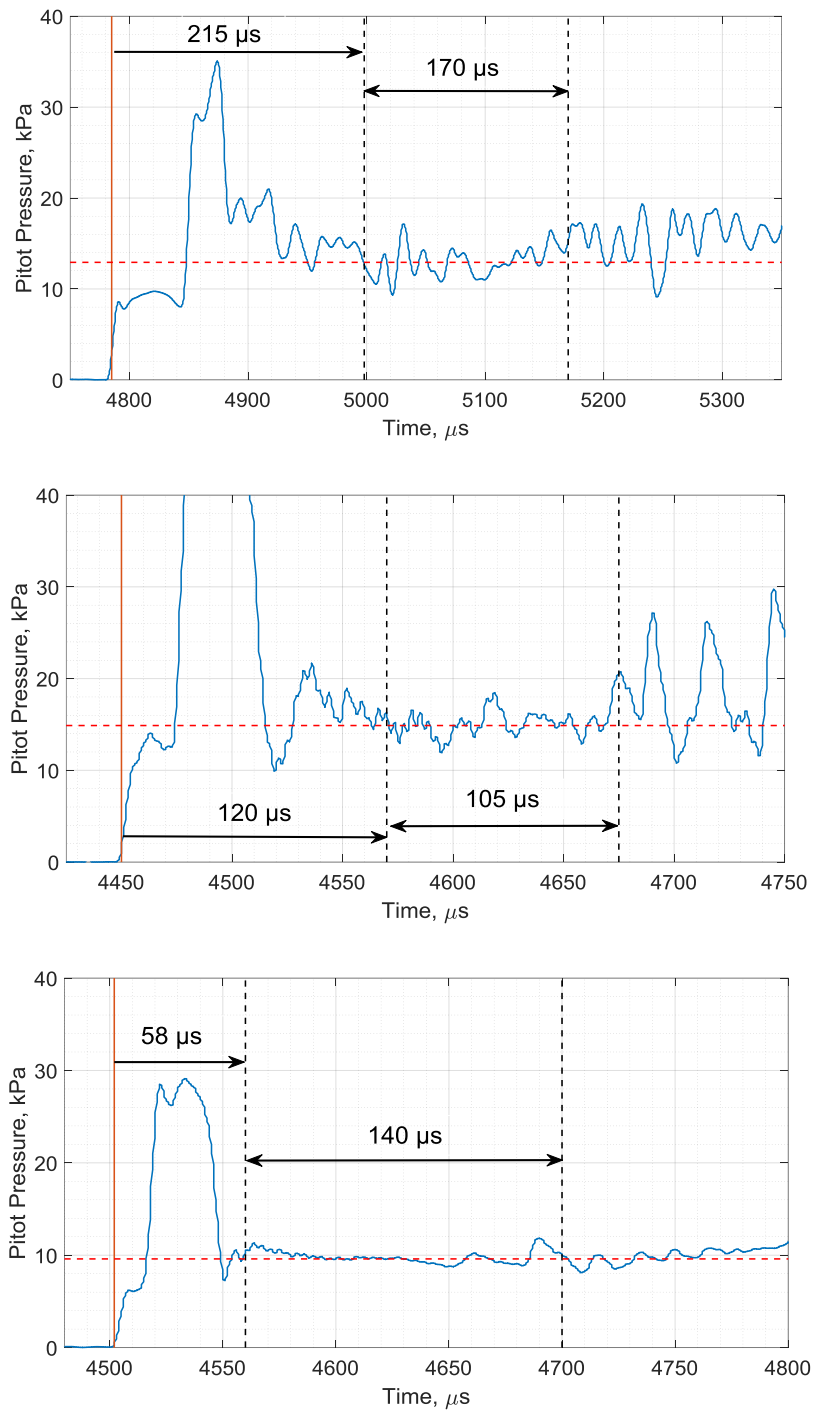


Figure 3.17. The top, middle and bottom graph correspond to the pitot probe traces of the 2.8, 3.4 and 4.0 km/s condition from shot x2s2906, x2s2905 and x2s2904 respectively. High frequency noise has been removed using moving average.

It is important to note that the actual steady test time available for imaging is the steady duration of the flowfield, generated by the expansion tube freestream, around the test model. This duration will be different from the steady duration of the freestream as determined by the pitot probes. The steady duration of the test model flowfield will always be less than the steady duration of the freestream due to the time needed for the flowfield to reach steady state. The duration of the steady flowfield of the

test model is determined from time resolved radiation measurements using an infrared sensor as shown in Figure 3.18. Determining the precise start and finish time of this steady duration is important. The emission spectroscopy acquires only a single frame, hence, it is very important to expose the spectroscopy system at the correct moment in time. An infrared sensor was used to measure the radiation emission at various locations in the flowfield generated around the test model. The sensor used for the continuous point measurement is the Mullard ORP 13. The detector is an intrinsic InSb photoconductive detector and it is sensitive to radiation with wavelength between $1 \mu\text{m}$ and $5 \mu\text{m}$. Figure 3.18 (b) shows the measured locations in the flowfield which are marked by the red points. The sensor is positioned to take focused measurements along lines of sight parallel to the width of the test model as shown in Figure 3.18 (a). The region captured is a rectangle of size of $5.0 \text{ mm} \times 1.8 \text{ mm}$ in the flowfield. The measurement locations were selected to lie along two streamlines as shown in Figure 3.18 (b). On each streamline, a measurement was taken in the shock layer, the expansion fan center and the expansion fan back.

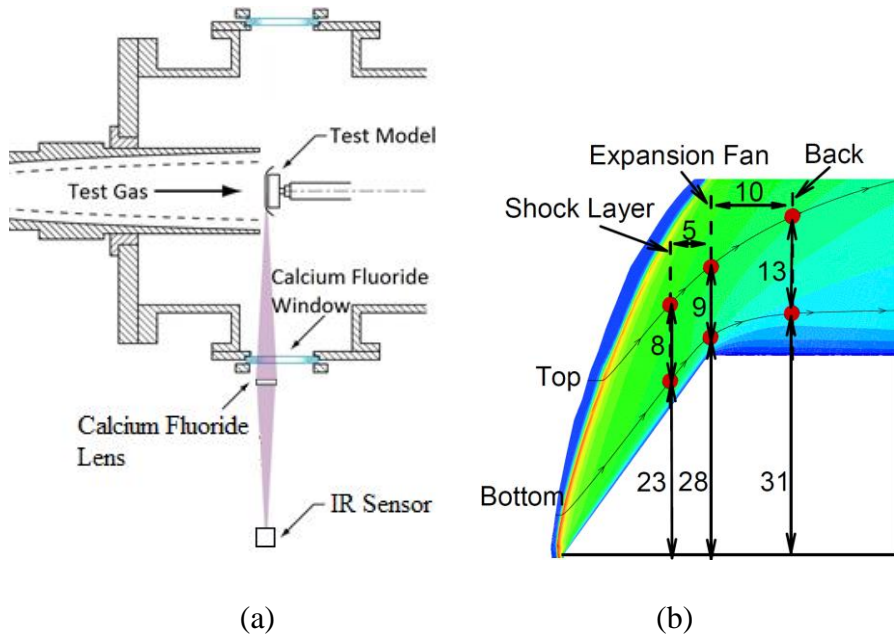


Figure 3.18. Details of the infrared sensor experiments, showing the (a) optical setup and (b) sensor measurement locations in mm (measurement direction is into the page).

The traces at all the measured points for all the conditions are shown in Figure 3.19. The sensor measurements cannot be accurately calibrated to obtain absolute spectral radiance, therefore the results are presented using the raw data in volts. From these traces, it is possible to determine the duration of time in which the flowfield remains steady. This duration, for all the measured locations in the flowfield, is summarized in Table 3.10. Consistent with the pitot pressure traces, the result shows that the 2.8 km/s condition has the longest steady duration of $118 \mu\text{s}$, whereas the 3.4 km/s has the shortest steady duration of $53 \mu\text{s}$. For all conditions, the measured steady duration of the flowfield

is greater than 50 μ s and this is sufficient to obtain emission spectroscopy data with good signal to noise ratio. The window of steady test time found from the radiation traces lies within the window of steady test time found from the pitot traces as expected. In Table 3.10, comparison of when the steady duration begins shows that the start of the test time in the flowfield occurs about 10-50 μ s after the start of the test time of the freestream. This shows that the steady flowfield around the model takes a finite time to develop. The information in Table 3.10 is used to select the moment of exposure and the exposure time when performing the radiation measurements in chapter 4.

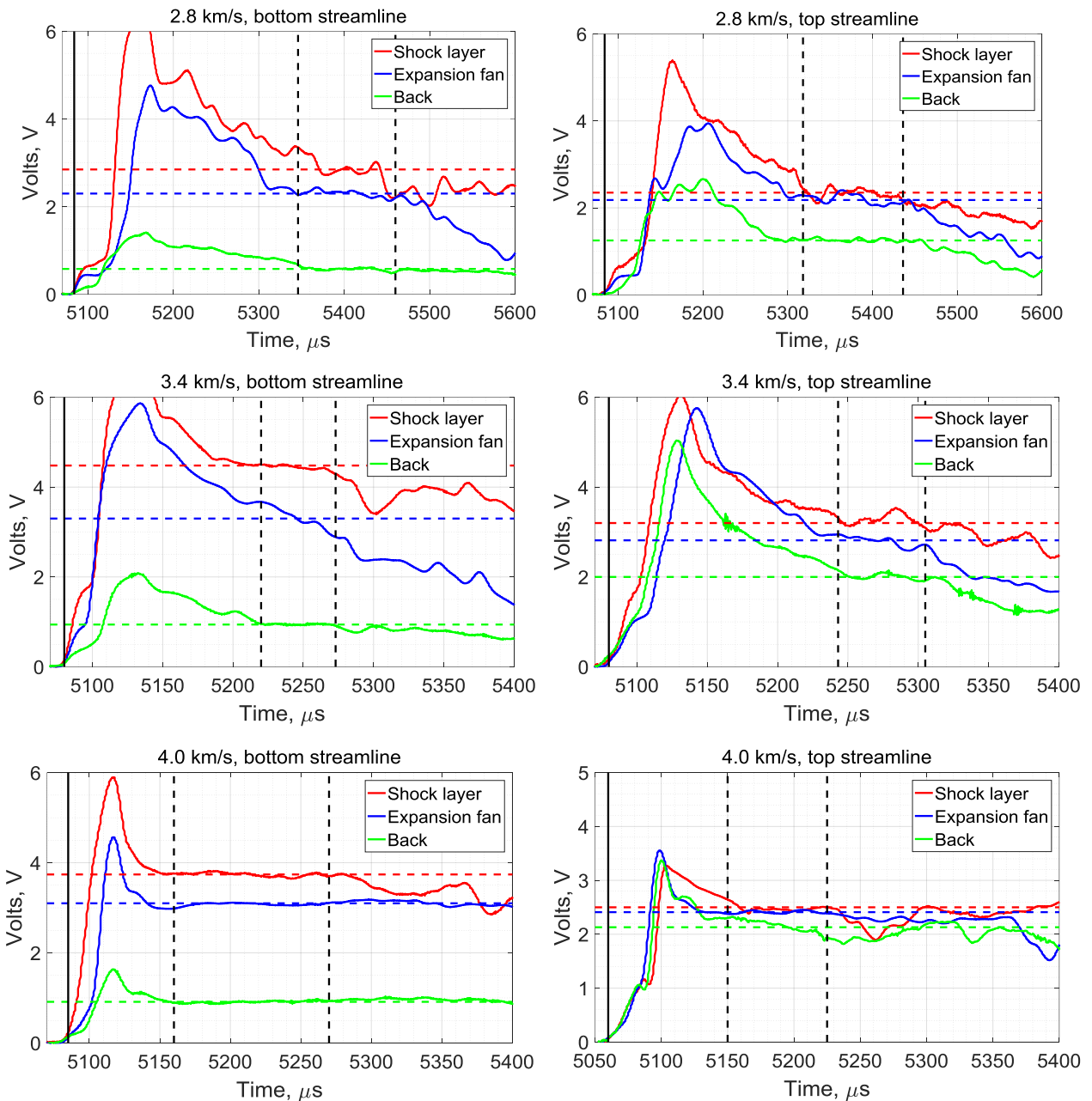


Figure 3.19. Infrared sensor traces at various points in the flow around the test model at different freestream conditions. The dotted vertical black lines on each graph mark the region of steady flow.

Table 3.10. Summary of steady duration times in μ s. Time is given relative to shock arrival.

Condition	Freestream (Pitot probe)			Streamline	Flowfield (Infrared sensor)		
	Start	Finish	Duration		Start	Finish	Duration
2.8 km/s	215	385	170	Bottom	262	376	114
				Top	238	356	118
3.4 km/s	120	225	105	Bottom	140	193	53
				Top	163	224	61
4.0 km/s	58	198	140	Bottom	75	185	110
				Top	90	165	75

3.6.2 Repeatability

Using the cold driver, due to the spontaneous nature of the rupture of the primary diaphragm when the nominal rupture pressure is reached, it is important to investigate the repeatability of the expansion tube conditions. To do this, the measured operating condition properties – primary and secondary shock speed, acceleration tube wall pressure and nozzle exit conehead and pitot pressure – from numerous shots for each condition are assessed. The result is summarized in Table 3.11 showing the average and the bounds of the measured values which cover the uncertainty of each individual measurement. The shock speed measurements and acceleration tube wall pressure measurements summarized on Table 3.11 correspond to the average from around 50 shots for each condition. The pitot probes measurements correspond to the average from about 25 shots for each condition. The pitot pressures, both conehead and flathead, are taken at the same consistent location, which is at approximately 40 mm in the radial direction from the centreline of the nozzle. From Table 3.11, the measured data for various operating condition properties showed reasonable repeatability for all three test conditions.

Table 3.11. Summary of the consistency of the measured operating condition properties. The presented uncertainty corresponds to the scatter of the measurements.

	2.8 km/s	3.4 km/s	4.0 km/s
Primary Shock Velocity / m/s	1630 ± 60		1990 ± 70
Secondary Shock Velocity / m/s	2850 ± 130	3610 ± 90	3950 ± 130
Acceleration Tube Wall Pressure / kPa	2.3 ± 0.3	2.6 ± 0.3	1.2 ± 0.2
Nozzle Exit Conehead Pressure / kPa	1.3 ± 0.2	2.1 ± 0.5	1.2 ± 0.2
Nozzle Exit Pitot Pressure / kPa	10.8 ± 1.6	17.3 ± 1.5	14.0 ± 1.0

The repeatability of the condition can be judged based on the shot-to-shot variation in shock speed. Since the 3.4 km/s and 4.0 km/s condition both use the same driver and the same shock tube fill pressure, the primary shock velocity is fundamentally the same. Reasonable repeatability is seen for the primary and secondary shock velocity for all conditions. The percentage variations of 3 – 4% in the primary shock speed and 2 – 4 % in secondary shock speed is commonly seen in the other conditions generated in the X2 expansion tube. The result is summarized in Table 3.11 which shows the average shock speed and the corresponding range. Likewise, with the shock speed measurements, the acceleration tube wall pressure measurements can also be used to observe the repeatability of the expansion tube conditions. Consistent with the shock speed analysis, the acceleration tube wall pressure measurements shows reasonable consistency for the test conditions as well. The variation of the acceleration tube wall pressure is less than 15 %. Furthermore, the pitot probe pressure measurements at the nozzle exit is also used to assess the consistency of the conditions. The pitot pressure is a more sensitive variable than both the shock speed and wall pressure. Despite this, reasonable consistency is still observed for the measurements where the percentage variation is less than about 20 %. Overall, the repeatability of the measured operation condition properties for the conditions in this work are similar to that seen for X2 expansion tube conditions driven using the free piston driver. This is the case even though the driver used in this work causes operation to be less controllable compared to the free piston driver.

Table 3.12. Measured operating condition properties and estimated freestream properties for pitot survey shots.

Condition	2.8 km/s			3.4 km/s			4.0 km/s		
Shot Number	2896	2897	2906	2887	2890	2905	2886	2892	2904
Primary Shock Speed (m/s)	1580	1650	1580	1930	1940	1940	2050	1990	1980
Secondary Shock Speed (m/s)	2930	2950	2880	3570	3520	3570	3900	3960	4010
Acc. Tube Wall Pressure (kPa)	2.20	2.40	2.50	2.53	2.70	2.60	1.05	1.26	0.96
Conical Pitot Pressure (kPa)	1.20	1.30	1.35	1.41	1.58	1.51	0.85	1.02	0.84
Freestream P_{static} (Pa)	310	330	355	347	391	360	161	197	150
Freestream T (K)	1170	1260	1190	1370	1380	1370	1280	1320	1280
Freestream V (m/s)	2920	2970	2870	3480	3430	3480	4030	3910	4070

To further study the repeatability of the conditions, freestream estimates were calculated and compared for multiple pitot survey shots using the PITOT code method discussed in section 3.4.2 with perfect gas isentropic expansions. The measured operating condition properties for each of the pitot survey shots are shown in Table 3.12 along with the corresponding estimated freestream conditions calculated from these measurements. From the results, the inflow parameter with the

greatest variation is the freestream static pressure. This variation is particularly large for the 4.0 km/s condition where the maximum and minimum pressure is seen to differ by 31 %. The variation is smaller for the 2.8 km/s and 3.4 km/s condition - 14 % and 13 % respectively. The relatively large variations in inflow pressure, particularly for the 4.0 km/s condition, is likely because the conditions have very low absolute pressures. On the other hand, the temperature and velocity differ by no more than 10 %. However, velocity is the most sensitive freestream parameter to the flowfield radiation. Therefore, from Table 3.12, the inflow velocity variation of 201 m/s and 169 m/s seen in the 2.8 and 4.0 km/s condition respectively can still cause noticeable changes to the flowfield radiation emission around the wedge. Further study of the shot-to-shot variation is presented in section 4.2.6.

3.6.3 Freestream Core Flow Size and Uniformity

The flow exiting the nozzle has a central component and a boundary layer as shown in Figure 3.20. Additionally, an expansion fan is generated at the nozzle exit. The core flow is defined as the region undisturbed by the boundary layer and the expansion fan. Hence, in the expansion tube, the size of the freestream is never equal to the nozzle exit diameter. The size of the core flow must be large enough such that the boundary layer and the expansion fan does not interact with the flowfield generated around the test model. The wedge model has a width of 100 mm and a height of 25 mm. The highest measurement above the test model is at 8.25 mm above the test model. Therefore, as an absolute minimum the core flow, assuming to be circular, needs to have a diameter of 106 mm in order to cover the test model entirely, as well as the flowfield up to 8.75 mm above the test model where the emission spectroscopy measurement are taken. It is, however, preferred to have some margin available. Furthermore, in addition to having a large enough core flow size, it is desirable that the flow properties remain constant radially within the core flow.

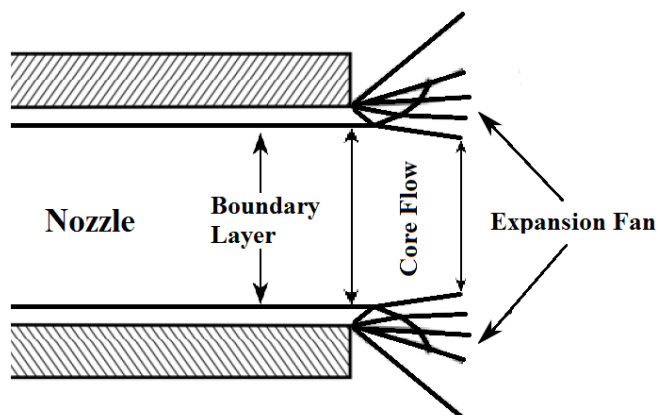


Figure 3.20. Nozzle exit showing the boundary layer, expansion fan and core flow.

To assess the size and uniformity of the core flow at the nozzle exit, pitot probe measurements are taken radially along a 144 mm distance at the nozzle exit plane. Nine pitot probes are used and all pitot probes are equally spaced 18 mm from each other with the middle pitot centered with the centerline of the nozzle. The results are shown in Figure 3.21. Firstly, it can be seen that, for all conditions, the core flow diameter is greater than 144 mm as the boundary layer is not captured by any of the sensors in the pitot rake. This is considered a large core flow compared to other X2 expansion tube conditions. This core flow size is more than enough to accommodate the 100 mm wide test model. However, the measurements show significant changes in the flow properties at different radial locations in the core flow. This non-uniformity of the core flow is particularly severe for the 3.4 and 4.0 km/s condition where the minimum and maximum measured pitot pressure differ by around 100%. The shape of the non-uniformity is similar between the 3.4 and 4.0 km/s condition where the pitot pressure is lowest in the center and increases away from the center. On the other hand, the opposite is seen in the 2.8 km/s condition where the pitot pressure is greatest near the center and decreases away from the center. It is unclear in what way the freestream non-uniformity would influence the flowfield around the test model. Nevertheless, to account for this non-uniformity, the tuned freestream estimate using the PITOT code is done using the average pitot pressure measured at various radial locations in the core flow. Tuning the freestream condition to pitot pressure measurements made at a single location may result in a freestream that is misleading of the actual freestream. This is particularly the case if the measurement is taken at the center or edge of the core flow. That is why the PITOT code estimated freestream properties in section 3.4.2 and 3.6.2 were tuned to the average conehead pressure measurement resulting in an estimate that is a better representation of the entire core flow.

The cause of the non-uniformity of the core flow is unknown. The non-uniformity may be caused by the expansion through the contoured nozzle. The contoured nozzle was not designed for the conditions in the current work and contoured nozzles are particularly susceptible to produce non-uniformities when operated off-design [112]. The reason for the core flow non-uniformity could also be caused by non-uniformity in the nozzle inflow. Chue et al. [113] showed that the nozzle inflow in expansion tubes can be non-uniform which, consequently, would cause a non-uniform nozzle exit condition. The results of the CFD simulations discussed in section 3.4.3 were also examined to study the core flow size and uniformity. Due to the inability of the simulation to compute the correct shock speed, however, the results are believed to be unreliable. The simulations, predicting core flow non-uniformities of less than 15%, were unable to simulate the measured pitot pressure profile and degree of non-uniformity shown in Figure 3.21.

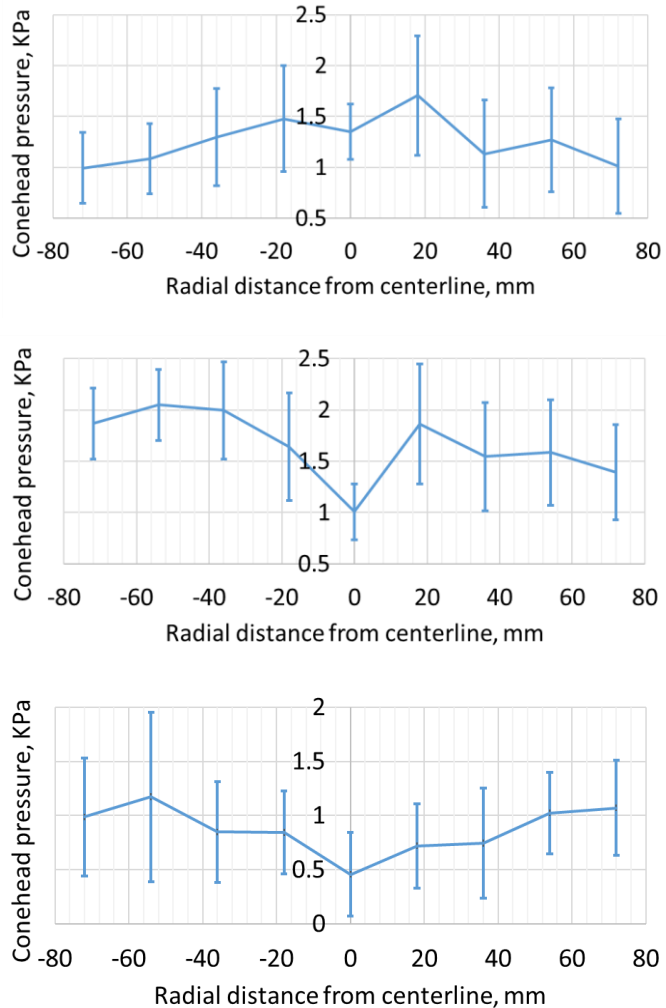


Figure 3.21. Conehead pitot probe measurements at the nozzle exit. The top, middle and bottom graph correspond to the 2.8, 3.4 and 4.0 km/s condition respectively. The error bar of each point is based on the noise of the experimental data.

Another property to investigate is the location of the expansion fan head which originates at the nozzle exit wall corner. The location of the expansion fan head is of concern because it may significantly decrease the core flow size in the axial direction as shown on Figure 3.20. It is particularly important to locate the expansion fan head in the current experiment because measurement of the flow around the wedge is taken as far as 50 mm beyond the nozzle exit. The expansion fan can also extend into the flowfield around the test model causing erroneous results. Therefore, it should be checked that the expansion fan head does not come near the test model. This can be checked from CFD simulations. However, as mentioned before, the CFD simulation results of the expansion tube freestream conditions are believed to be inaccurate because the shock speeds were simulated incorrectly. Nevertheless, the CFD simulations results at the nozzle exit, discussed in section 3.4.3, were still used to give a rough approximate of the location of the expansion fan head. The radial component of the flow velocity was used to estimate the location of the expansion fan head. The results, from both

thermochemical equilibrium and perfect gas calculations, show that the expansion fan head does not come within 20 mm of the test model even as far as 80 mm downstream of the nozzle exit.

3.7 Conclusion

Three low velocity, low pressure expansion tube conditions have been developed for the purposes of creating carbon dioxide radiation conditions relevant to Mars entry in the X2 expansion tube. This included the design of a new fixed volume driver, for the expansion tube. The test time and core flow size of these new conditions have been assessed. The conditions were seen to produce a steady flowfield around the two-dimensional wedge model lasting at least 50 μ s. The core flow at the nozzle exit was measured to be more than 144 mm in diameter which is more than enough to accommodate the 100 mm wide two-dimensional wedge model. Work was also done to estimate the experimental freestream properties created by the expansion tube. The PITOT code and CFD using the Eilmer3 code were used to provide the freestream estimates. However, the estimate from CFD is deemed unreliable due to the inability of the simulation to compute shock speeds close to the measured shock speeds. The estimate from the PITOT code is regarded as the more accurate estimate of the freestream properties as it incorporates the measured operating condition properties to produce the estimate. Furthermore, the possibility of excess thermochemical excitation in the generated freestream is examined. This is done by comparing the experimentally measured shock wave of the test model to CFD simulated shock waves using both equilibrium and perfect gas freestream estimates computed using the PITOT code. The results showed that the perfect gas estimate produced a better match of shock wave location. This may indicate that the test condition has excess thermochemical excitation. Further work to investigate the degree of freestream thermochemical excitation is presented in section 5.3. In addition, using the PITOT code estimated inflow conditions, CFD simulations showed that the expanding flow generated in the three expansion tube experiments simulate the expanding flow around the shoulder of the MSL entry vehicle at three different trajectory points.

4 Carbon Dioxide Radiation Measurements

4.1 Introduction

Using the expansion tube conditions discussed in the previous chapter, along with the wedge test model, high temperature CO₂ flows are created around the test model. These flows around the test model are investigated by taking radiation measurements. Radiation measurements of both the 2.7 μm band and 4.3 μm band of carbon dioxide, which are the two strongest emission bands of carbon dioxide [44] are discussed in this chapter. The radiation data is taken using the method of emission spectroscopy and filtered imaging. Emission spectroscopy measurements provides spectrally resolved radiation measurements in one spatial dimension, while the filtered images measures the band radiance in two spatial dimensions.

To perform emission spectroscopy of the CO₂ bands, a new mid-infrared spectroscopy system had to be assembled. A description of the newly assembled spectroscopy system, along with the calibration method used to obtain the absolute spectral radiance, is presented in section 4.2. To supplement the emission spectroscopy data, filtered images are taken for both the 2.7 μm and 4.3 μm band. The images are calibrated to obtain the absolute band radiance.

Multiple experiments were performed at the same nominal condition to examine the influence of shot-to-shot variations. The radiation measurements are used to assess the qualitative characteristics of CO₂ radiation. Also, the calibrated emission spectroscopy data are particularly useful for deducing the temperatures and CO₂ number densities for detailed analyses of the high temperature CO₂ flows.

4.2 Emission Spectroscopy

4.2.1 System Description

A new spectroscopy system capable of performing mid-wavelength infrared spectroscopy on impulse facilities is assembled during the study. The layout of this new spectroscopy system is shown in Figure 4.1. The layout is analogous to the UV spectroscopy system used previously by Jacobs [114]

in X2 non-reflected shock tube experiments. The spectrograph model and infrared camera model is identical to that used by Cruden et al. [44] at NASA Ames for their shock tube measurements. The spectroscopy system contains three main components; the focusing optics, the spectrometer and the detector/camera.

Table 4.1. Optical properties used for the emission spectroscopy work.

Imaged spatial length	42.7 mm
Magnification	0.24
Depth of field	100 mm
Circle of confusion	17 pixels
Focusing optics f-number	10
Entrance slit width	100 μ m

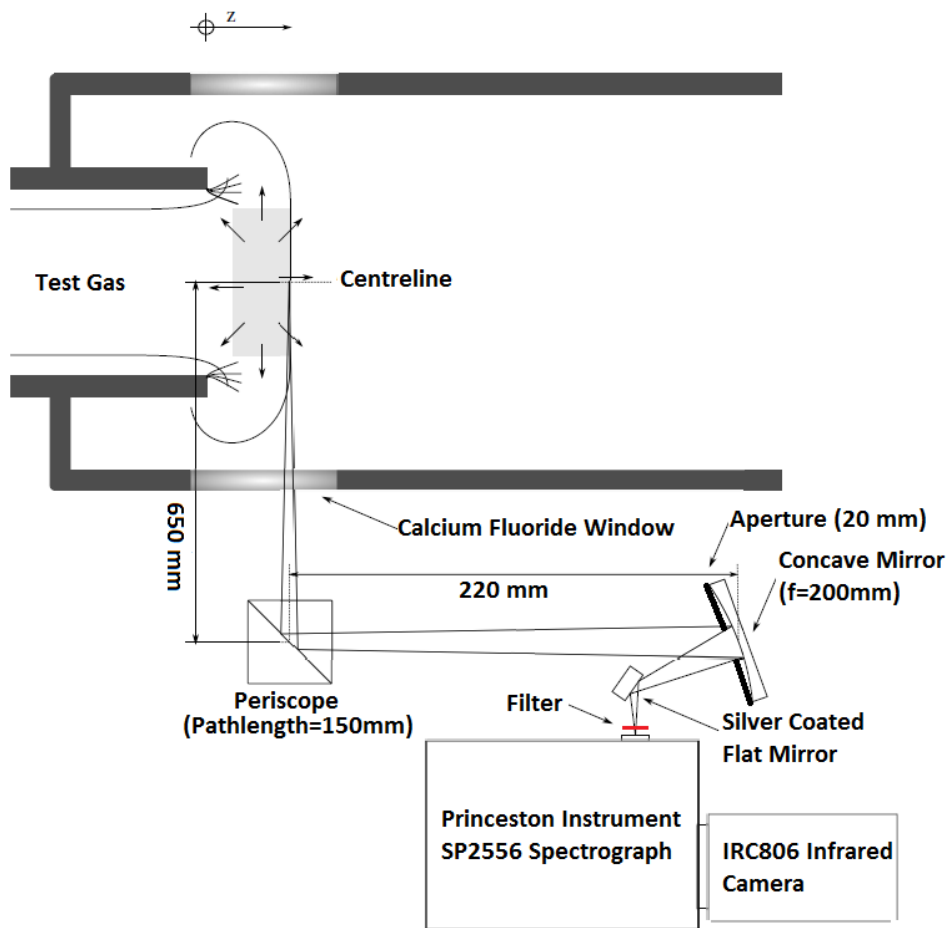


Figure 4.1. Mid-infrared spectroscopy system setup.

To take spectroscopic measurements, the radiation of interest must be focused onto the entrance slit of the spectrometer and this is achieved through the focusing optics. Details of the properties of the focusing optics used in the emission spectroscopy experiments performed in this thesis is shown in

Table 4.1. The focusing optics is setup to provide the desired magnification so that the desired spatial range of around 43 mm is imaged which captures the shock front and the expanded flow region, as well as the expansion fan. A 20 mm diameter aperture is placed on the concave mirror; the aperture is large enough to allow adequate signal intensity but small enough to have the required depth of field for the acceptable circle of confusion. For a depth of field of 100 mm (width of the test model), the circle of confusion is 17 pixels, which corresponds to only 3% of the total amount of pixels in the spatial dimension (512 pixels) and corresponds to an equivalent imaged spatial distance of 1.3 mm. It is also important to note that the turning angle of the focusing mirror is made as small as possible to minimize the comatic aberration of the optical system.

Part of the signal attenuation is caused by windows and mirrors in the focusing optics system. Thus, appropriate selection of the mirror coating and window material is necessary. The front surface of all the mirrors inside the focusing optics and spectrometer is coated with silver for good reflectivity in the mid infrared spectrum. Calcium fluoride, which has a transmission of greater than 95% through a 5mm thickness in the mid-infrared region, is selected as the window material. It is desirable to only observe the first order spectra. Therefore, to prevent higher order effects in the emission spectroscopy images, appropriate filters are incorporated in the focusing optics too. When doing emission spectroscopy of the $4.3 \mu\text{m}$ band, a longpass filter is used to filter out all radiation with wavelength below $3.7 \mu\text{m}$ (Gengenbach Instruments – ILP3700). When doing emission spectroscopy of the $2.7 \mu\text{m}$ band, a wide bandpass filter is used to remove all signal with wavelength below $2.25 \mu\text{m}$ (Gengenbach Instruments – IWBP 2250 – 3810).

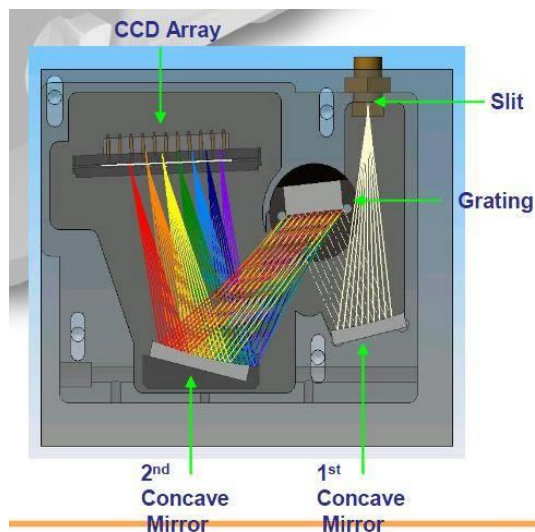


Figure 4.2. Czerny-Turner spectrometer. Adapted from [115].

The spectrometer used is the Princeton Instrument Acton SP2556. It is a Czerny-Turner spectrometer configured for imaging. The layout of the spectroscopy is shown in Figure 4.2. The SP2556 spectrometer has an f-number of 6.5, thus, the f-number of the focusing optics is selected to be bigger

than this in order to prevent overfill of the optical components inside the spectrometer. The grating used is a 17.5g/mm reflective grating blazed at 4.2 μm . Selection of the grating line density requires consideration of the dispersion, camera array width and the bandwidth of wavelength which needs to be viewed simultaneously. The bandwidths of the 2.7 and 4.3 μm CO₂ bands are large, thus a coarse 17.5g/mm grating was selected in order to allow the entire bandwidth to be imaged. The resulting bandwidth is approximately 1400 nm. The grating blaze is selected at 4.2 μm for the best reflectivity of the CO₂ 4.3 μm band. The grating is coated in gold while the mirrors in the spectrometer are coated in silver. Also, it is necessary to minimize the absorption of the image signal by ambient carbon dioxide and water vapour. Hence, the optical path in the spectrometer is purged with dry nitrogen during the acquisition of a spectral image. The spectrograph is purged at 20L/min for 45 minutes prior to the experiment as recommended by the manufacturer [116].

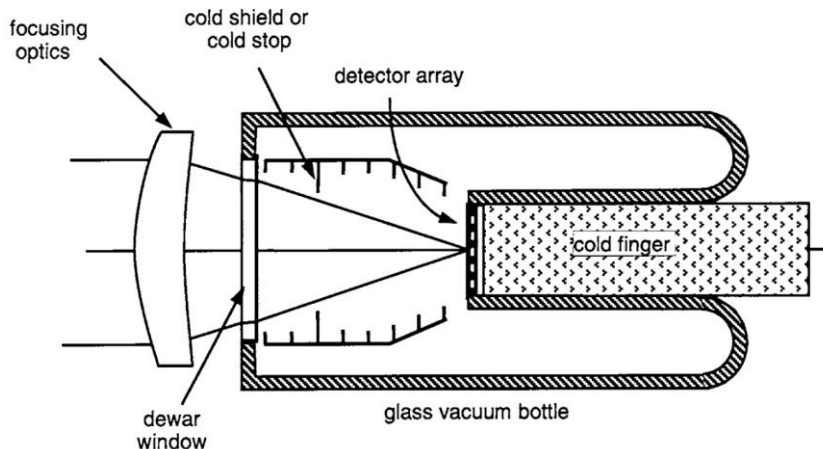


Figure 4.3. General layout of the mid-wavelength infrared detector. [117]

The mid-wavelength infrared camera used in the spectroscopy system is the IRC806HS by IRCameras. The 640 x 512 focal plane array (FPA) of the IRC806HS has a pixel pitch of 20 μm and it is made from indium antimonide (InSb). The FPA dimension is 12.8 mm x 10.24 mm. The 12.8 mm dimension is used as the wavelength axis while the 10.24 mm dimension is used as the spatial axis for the emission spectroscopy experiments. The FPA is housed inside a dewar which is cooled by liquid nitrogen to 77 K while in operation. This arrangement is shown in Figure 4.3. Modifications to the dimensions of the dewar had to be made such that the signal from the spectrometer is incident on the FPA when the camera is attached to the spectrometer. Details of the modification can be found in appendix C. The FPA collects photons and generates electrons. The amount of electrons generated by the detector is directly proportional to the number of photons received. The amount of electrons generated is then correlated into counts as the output value by the camera for the measurement. The counts varies linearly with the imaged radiance and exposure time. This linearity has been verified by Cruden et al. [44] as well as independently in the current study. Additionally, in Figure 4.3, the

dewar enclosure contains a window; and behind the window contains a cold shield. The cold shield allows the passing of radiation from the imaged scene but help prevent the passing of other radiation. Furthermore, the camera has a very large sensitivity range. This is illustrated by the camera's quantum efficiency curve in Figure 4.4. This is why a filter is incorporated into the focusing optics in order to filter out the higher orders of the lower wavelength radiation. Otherwise, the camera will detect higher order radiation.

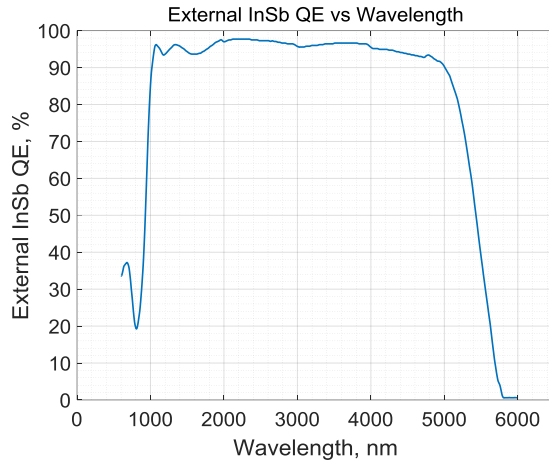


Figure 4.4. External InSb quantum efficiency curve for the IRC806 camera. [118]

4.2.2 Alignment

When doing the emission spectroscopy experiments, the first step involves aligning the test model to the correct location relative to the expansion tube. The centre of the test model, widthwise, is aligned with the center of the expansion tube. The leading edge of the wedge model is aligned with the exit plane of the nozzle. Heightwise, the centre of the wedge model is offset to 5 mm below the centreline of the nozzle. Once the test model is aligned, the spectroscopy system is aligned with the test model.

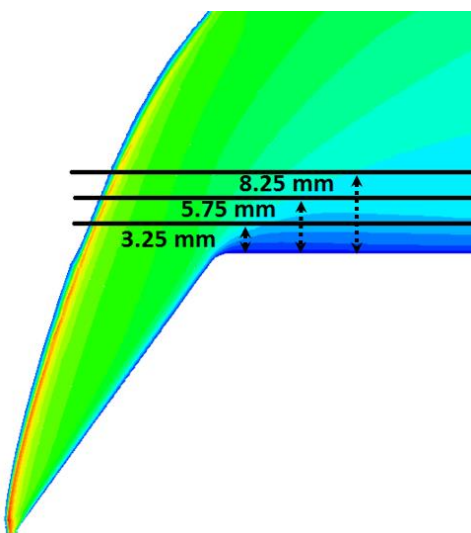


Figure 4.5. Locations of emission spectroscopy measurements.

The emission spectroscopy system is used to take horizontal measurements at three different height above the test model, 2.50 mm apart, as indicated by the horizontal black lines in Figure 4.5. The measurement covers the entire region from the shock wave to the back of the test model, through the expansion fan. Aligning the spectroscopy system requires the following:

- Align the spectroscopy system such that the measurements are horizontal and the lines of sight measured are parallel to the width of the two-dimensional model.
- Adjust the focusing optics to obtain correct magnification of the image.
- The location of the image in the spatial dimension must be set at the correct location.
- The spectroscopy system must be focused with the centreline of the model/expansion tube.

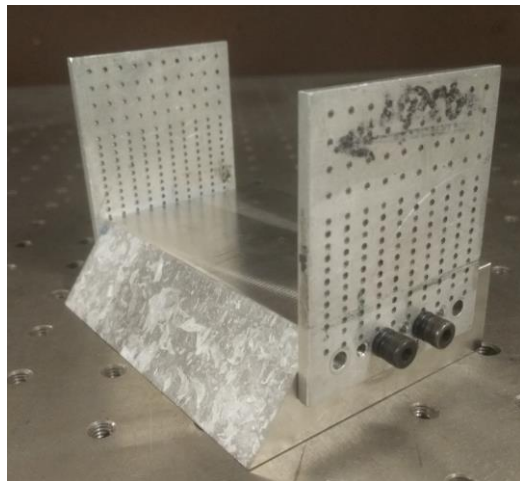


Figure 4.6. Wedge model with the alignment plate attached to both edges.

To align the spectroscopy system, the optical components are placed approximately at the correct location. Then, 3 mm thick vertical alignment plates with 1.5 mm diameter holes are installed on both edges of the test model, as shown in Figure 4.6. A laser pointer is set up by passing the laser through corresponding holes through both alignment plates at a relevant height above the test model. This sets the laser up at the correct location to create a visual line of sight that is parallel with the width direction of the test model. This laser path is used to align the spectroscopy system such that the line of sight measured is parallel to the width of the model. To check that the system takes horizontal measurements, a row of holes of the alignment plates at the relevant height above the test model is backlit to confirm that the system is aligned with the row of holes. To focus the spectroscopy system, a backlit knife edge is setup at the centreline of the expansion tube. The location of the spectrometer is adjusted such that a sharp image of the knife edge is obtained. The focus and alignment procedure of the spectroscopy system is iterative; the procedures are repeated until the system takes horizontal images of approximately the desired magnification and is focused with the centreline of the expansion

tube while the lines of sight are aligned with the width of the model. The same setup is used to take measurements at all three heights above the test model by adjusting the height of the optics table on which the spectroscopy system rests. In addition to taking spectroscopic measurements of the flow around the wedge, spectroscopic measurements are also taken of the expansion tube freestream to help characterize the inflow condition. The same setup of the spectroscopy system is used for the freestream measurements. This is done by removing the test model and adjusting the optics table such that the spectroscopy system looks through the centreline of the expansion tube.

4.2.3 Calibration

The mid-infrared spectroscopic measurements in the current work are calibrated in a similar way to that of Cruden [11]. As discussed by Cruden, absolute radiation measurements require calibration in the three dimensions; spectral dimension (x axis), spatial dimension (y axis) and radiance magnitude dimension (z axis).

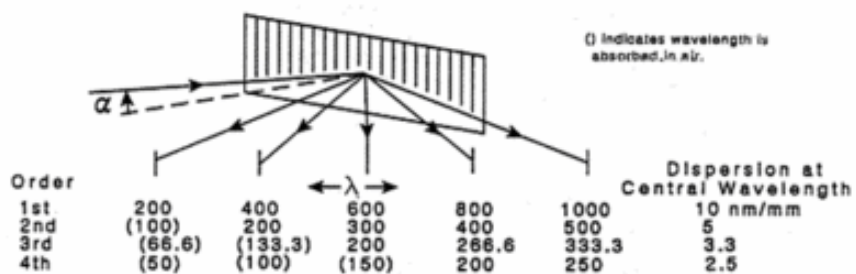


Figure 4.7. Diffraction grating showing the relationship of the higher order signals. [119]

The spectral calibration of such a spectroscopy system is generally done using atomic line sources. However, line sources are unavailable in the mid-infrared. So, instead, the higher order signals from mercury or krypton lamps are used. The diffraction grating in the spectrometer produces higher order signals on top of first order signals with the relationship as shown on Figure 4.7. The calibration in this work is done using the Krypton 6031 pencil lamp. Radiation measurement of the lamp is taken by placing the lamp at the spectrometer entrance slit. The higher order Krypton lines used to calibrate the $4.3\text{ }\mu\text{m}$ and $2.7\text{ }\mu\text{m}$ band measurements are shown in Figure 4.8 and Figure 4.9 respectively. Using some of the identified higher order lines, the spectral axis is calibrated by finding the linear best fit equation as shown in Figure 4.10. The normal of residuals are 3.69 and 1.83 for the 4700 nm and 2900 nm centred measurements respectively, which indicates a very good linear fit. The wavelength dispersion is determined to be about 2.25 nm/pixel for both the 4700 nm and 2900 nm centred measurements. This corresponds to a bandwidth of approximately 1440 nm for the current system.

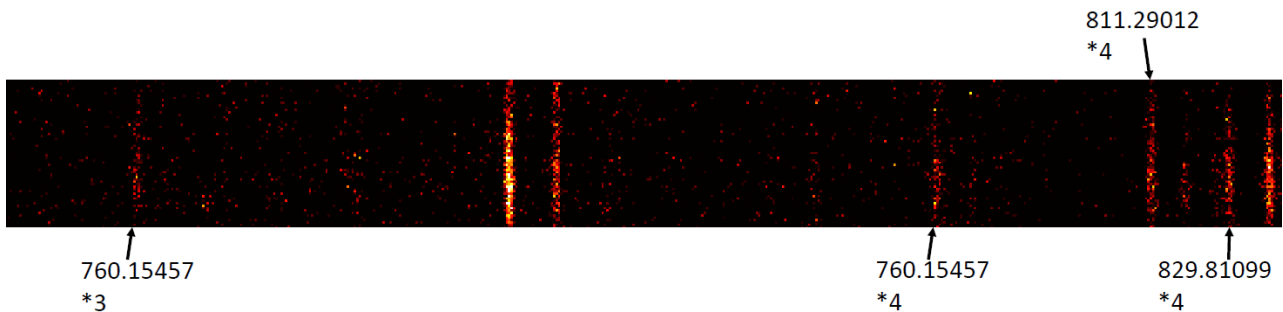


Figure 4.8. Higher order lines in nm for calibrating the $2.7\text{ }\mu\text{m}$ band measurement. Grating is centred at 2900 nm .

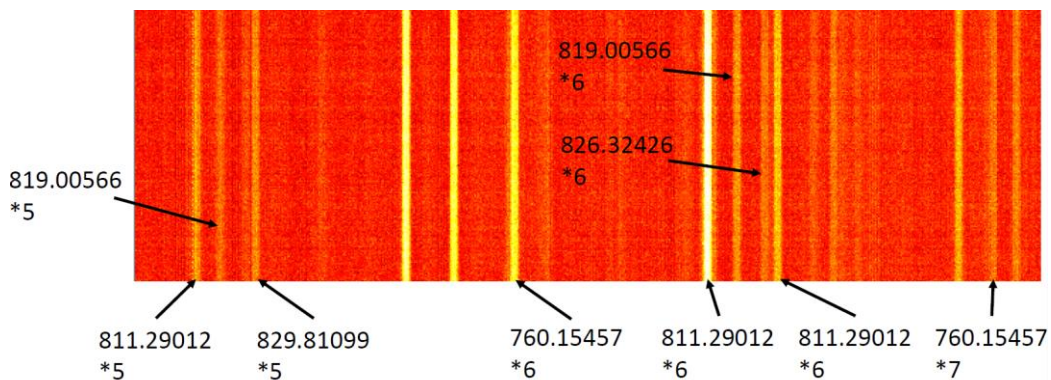


Figure 4.9. Higher order lines in nm for calibrating the $4.3\text{ }\mu\text{m}$ band measurement. Grating is centred at 4700 nm .

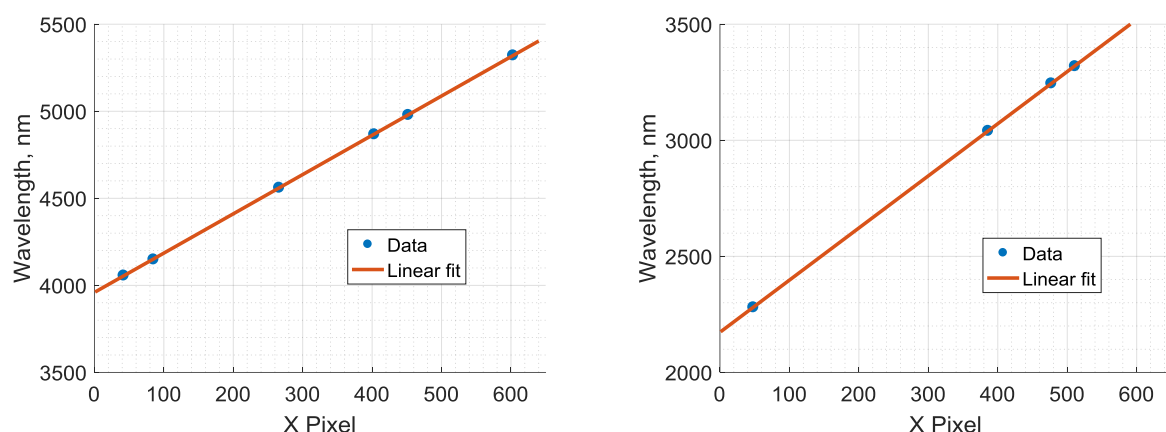


Figure 4.10. Spectral axis calibration using the higher order krypton lines for the measurements centred at 4700 nm , left, and 2900 nm , right.

To calibrate the spatial dimension, the vertical alignment plates attached on the edges of the two-dimensional wedge model was used to provide the spatial calibration. A light source was placed behind the alignment plates to provide the illumination of the alignment holes and, subsequently, radiation measurements of the illuminated holes were taken. As the spacing between the holes are known, the spatial axis can be calibrated. For the magnification used in the current experiments, the

spatial dispersion is approximately 0.0833 mm/pixel which corresponds to a spatial range of 42.7 mm.

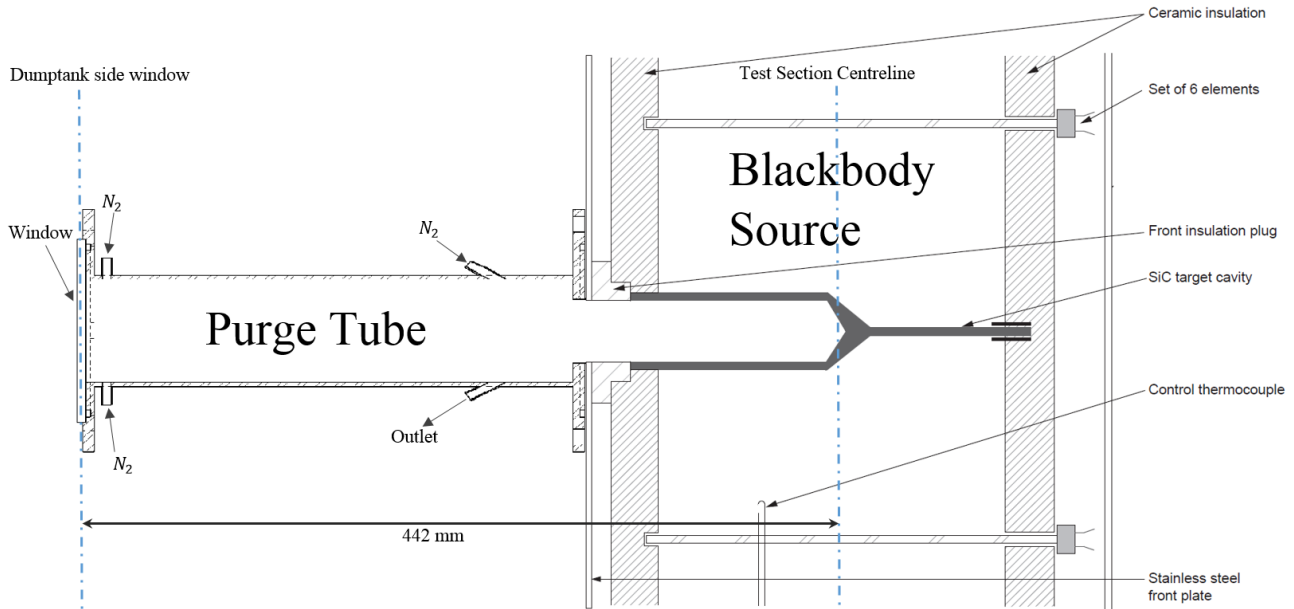


Figure 4.11. LandCal R1500T blackbody source with the nitrogen purge tube.

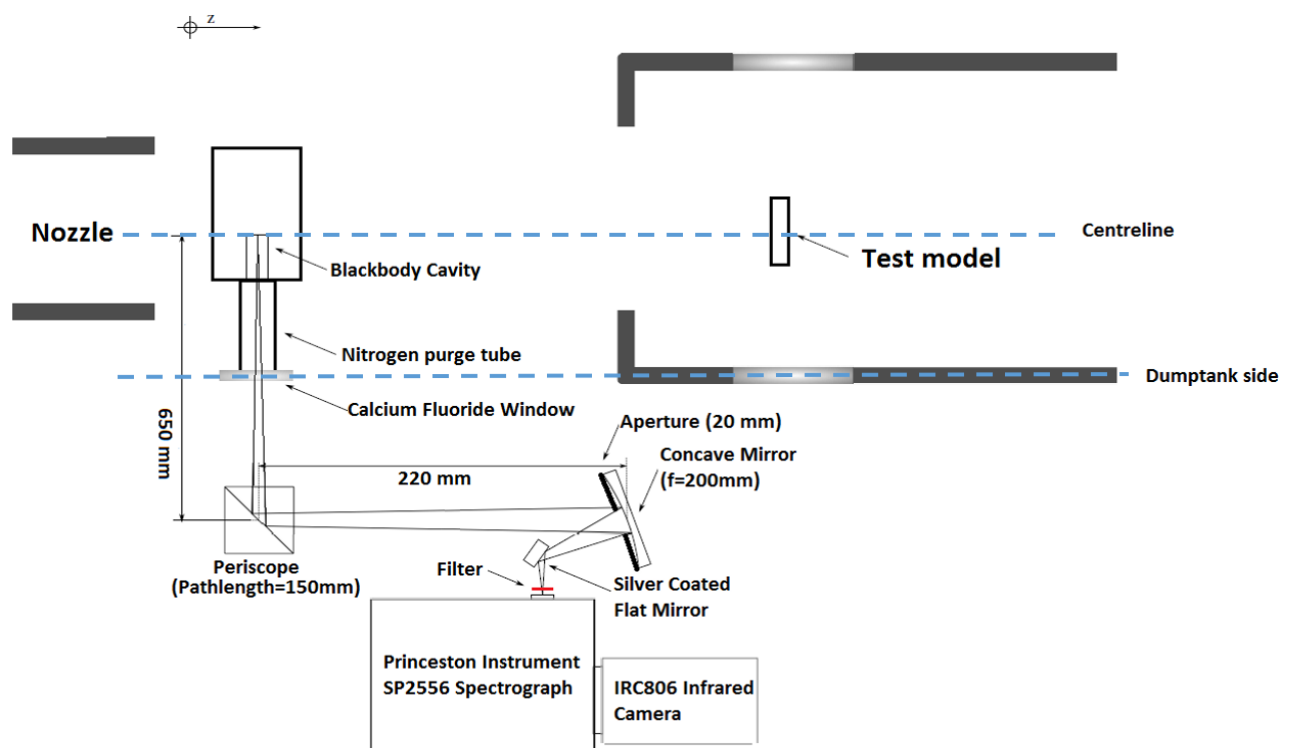


Figure 4.12. Setup for performing absolute radiance calibration.

It is necessary to determine the absolute spectral radiance of the measured results. However, infrared cameras produce readings in counts. Hence, calibration is required to find the ratio of radiance observed to counts generated in order to convert the reading in counts to radiance. Calibration of the absolute radiation in units of radiance was achieved using a known source of radiation to determine

the radiance - count relationship of the spectroscopy system for every pixel of the image. In particular, calibration of the mid-wavelength infrared spectroscopy system requires a blackbody cavity source. Such a calibration source produces blackbody radiation at a certain temperature. Given the temperature, the theoretical radiance of the blackbody calibration source is an easy value to obtain. Here, the calibration is performed using the LandCal R1500T blackbody cavity shown on Figure 4.11. It is a blackbody radiance source, with an emissivity of 0.99, and it is uniform over a 1 inch diameter [11]. As discussed by Eichmann [120], using a radiance source for calibration of the spectroscopy system allows the entire spectroscopy system, including the focusing optics, to be calibrated. Therefore, without altering any aspect of the experimental setup of the optics, the conical end of the blackbody cavity is placed where the test model would be. This is shown on Figure 4.12. This allows the back surface of the cavity to be in focus and this is important because it is only on this surface that uniformity of radiation is guaranteed.

The development of the radiance calibration methodology also requires consideration of the absorption of the image signal in the atmosphere. A tube is attached to the front plate of the blackbody cavity, as shown on Figure 4.11. Both the volume of the tube and the volume inside the cavity is purged with nitrogen during calibration. The purpose of this is to make sure the absorption path length remains the same during both experiment and calibration. The volume inside the cavity in particular must be purged because the carbon dioxide molecules inside the cavity will get heated up to higher temperatures resulting in different absorption properties to room temperature carbon dioxide. Hence, error in calibration will occur if the cavity is not purged even if the total unpurged path length remains the same between experiment and calibration. During experiments, the distance between the model and the dumptank window is under vacuum, hence the image signal will not be absorbed in this region. Consequently, the same must be maintained during the calibration. So, as the back end of the blackbody cavity is at the dumptank centreline, analogously, the front end of the tube (with the window) is at the same location as the window of the dumptank, as shown on Figure 4.12. Thus, purging this entire section simulates the vacuum path length between the model and the dumptank window during the experiment.

When performing the calibration, the blackbody source is heated up to $1773K \pm 10K$ while nitrogen is purged in the purge tube. Given the uncertainty of the temperature of the calibration source, the uncertainty of the calibrated radiance measurement is around $\pm 2.0\%$ and $\pm 2.5\%$ for the $4.3 \mu m$ and $2.7 \mu m$ band respectively. Images of the calibration source, as well as the dark frames, are taken at different locations along the spatial axis. This allows calibration along the entire spatial dimension. The images of the calibration source at the different spatial locations after taking away the dark frames are pieced together to form a single calibration image. This final calibration image is then related to

the known radiance value of the calibration source. This obtains the final calibration function. The calibration function is then used to directly obtain the absolute radiance of the experimental measurements.

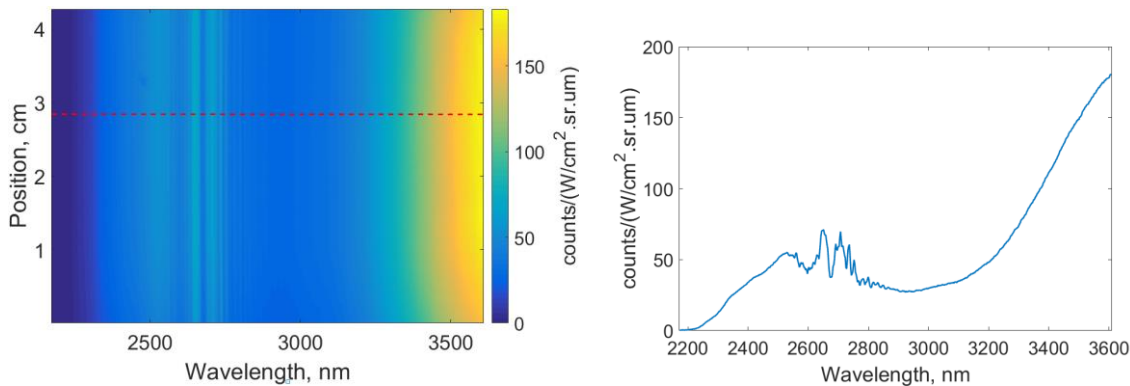


Figure 4.13. Calibration function of the $2.7 \mu\text{m}$ band for an exposure time of $80 \mu\text{s}$.

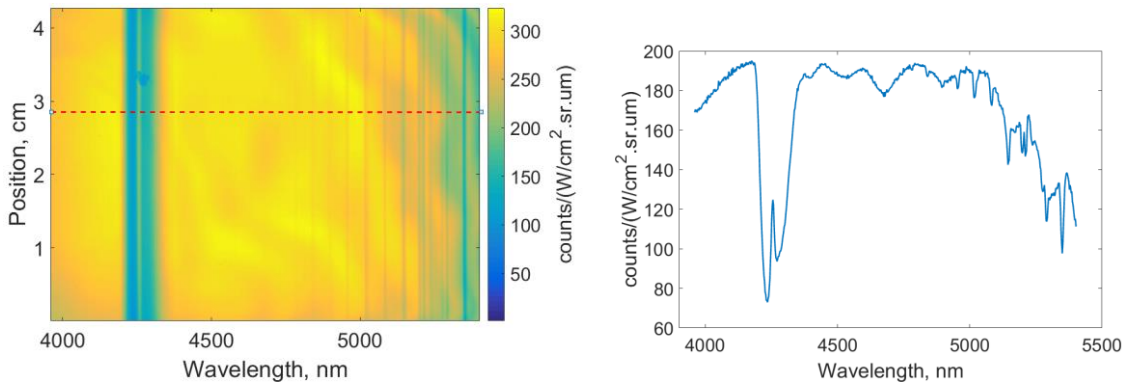


Figure 4.14. Calibration function of the $4.3 \mu\text{m}$ band for an exposure time of $50 \mu\text{s}$

Examples of the final calibration functions for the $2.7 \mu\text{m}$ and $4.3 \mu\text{m}$ band measurements are shown on Figure 4.13 and Figure 4.14 respectively. Various absorption features, particularly the well-known CO₂ $4.3 \mu\text{m}$ absorption band, can be observed in the calibration function of the $4.3 \mu\text{m}$ band. These absorption features arise from the unpurged length of the optical path which is approximately 815 mm between the dump tank window and the spectrometer entrance slit. The absorption features in the current work is believed to have minimal influences on the accuracy of the calibration as long as the unpurged pathlength remains the same between experiment and calibration [55] [121]. Therefore, the use of the purge tube on the blackbody furnace during calibration is critical. For a given wavelength, the calibration function along the column does have some observable random variations as well. This is due to each pixel in the FPA having slightly different sensitivities. Therefore, an individual calibration function is determined for every pixel in the image. Another observation from Figure 4.13 and Figure 4.14 is that the spectroscopy system is significantly less efficient for taking $2.7 \mu\text{m}$ band measurements compared to the $4.3 \mu\text{m}$ band measurements. This is due to the spectrometer grating being blazed at $4.2 \mu\text{m}$.

4.2.4 Characteristics of CO₂ spectroscopic measurements

Examples of the final calibrated emission spectroscopy measurements above the wedge model are shown in Figure 4.15 and Figure 4.16. The features of the CO₂ spectra obtained in the current work is consistent with that obtained by Cruden et al. [44] and Takayanagi et al. [55] who used very similar spectroscopy systems to take measurements in their impulse facilities. The 2.7 μm band measurements have significantly more noise compared to the 4.3 μm band measurements. This is because, in addition to the fact that the spectroscopy system is less efficient at measuring radiation at around 2.7 μm, the CO₂ 2.7 μm band emission is weaker than the CO₂ 4.3 μm band emission. For both the 2.7 μm and 4.3 μm band measurements, the numerous lines of CO₂ radiation are not resolved. This is expected as the large spectral bandwidth of 1440 nm, required to capture the entire CO₂ band, has a dispersion of 2.25 nm/pixel, which would never resolve the fine features of CO₂ emission. For the current work, the inability to resolve the lines of CO₂ in the spectroscopy measurements is not an issue.

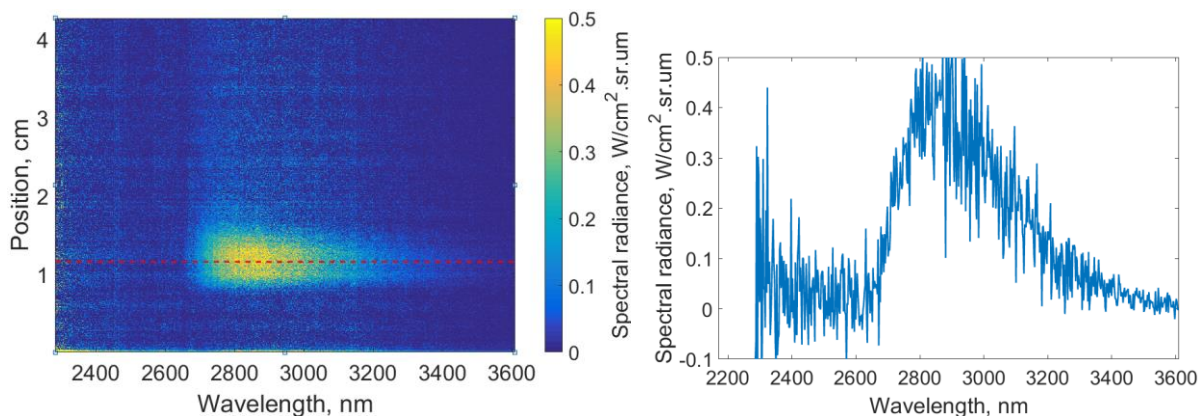


Figure 4.15. Example of a horizontal emission spectroscopy measurement above the test model of the 2.7 μm band from the current work.

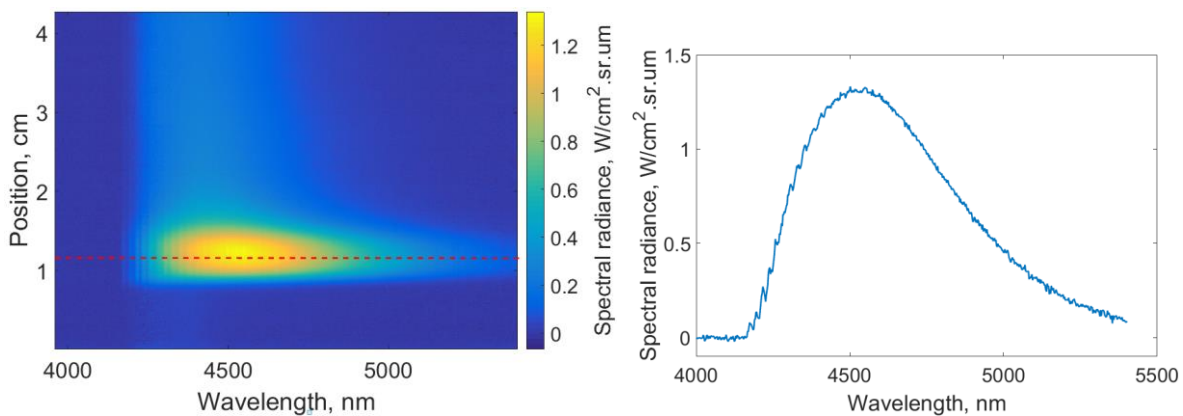


Figure 4.16. Example of a horizontal emission spectroscopy measurement above the test model of the 4.3 μm band from the current work.

4.2.5 Delay and duration of exposure

In this study, the emission spectroscopy is conducted for both the nozzle exit flow, and the flow through the oblique shock and Prandtl-Meyer expansion fan of the test model. The emission spectroscopy measurements are taken at a selected moment during the test time. Using the steady test times determined in section 3.6.1, the delay and duration of exposure used for the emission spectroscopy measurement in this work is shown in Table 4.2. Also during each test, an infrared sensor is used to obtain a continuous measurement of the radiating flow throughout the duration of the experiment. The temporally resolved infrared measurements have been described in section 3.6.1. Having a continuous radiation measurement is necessary to ensure that the spectral image is acquired during the steady test flow. In the freestream experiments, the sensor measures the freestream radiation at the nozzle exit. In the expansion fan experiment, the sensor measures the radiation at a point 5 mm vertically above the convex corner. In addition to that, three pitot probes (two flathead and one conehead) are placed about 20 mm below the wedge (approximately 40 mm radially from the nozzle centreline) to obtain continuous pitot pressure measurements from the freestream. Examples of these traces are shown on Figure 4.17 for the different conditions and different experiments. The integration time of the infrared camera is shown to be made during the steady test time of the flow for all cases.

Table 4.2. The delay and duration of the exposure for the emission spectroscopy measurements. Delay is measured relative to shock arrival at the test model.

Experiment	Condition	Delay / μs	Exposure time / μs
Freestream	2.8 km/s	200	176
	3.4 km/s	130	72
	4.0 km/s	60	104
Expansion Fan	2.8 km/s	266	110
	3.4 km/s	152	50
	4.0 km/s	84	80

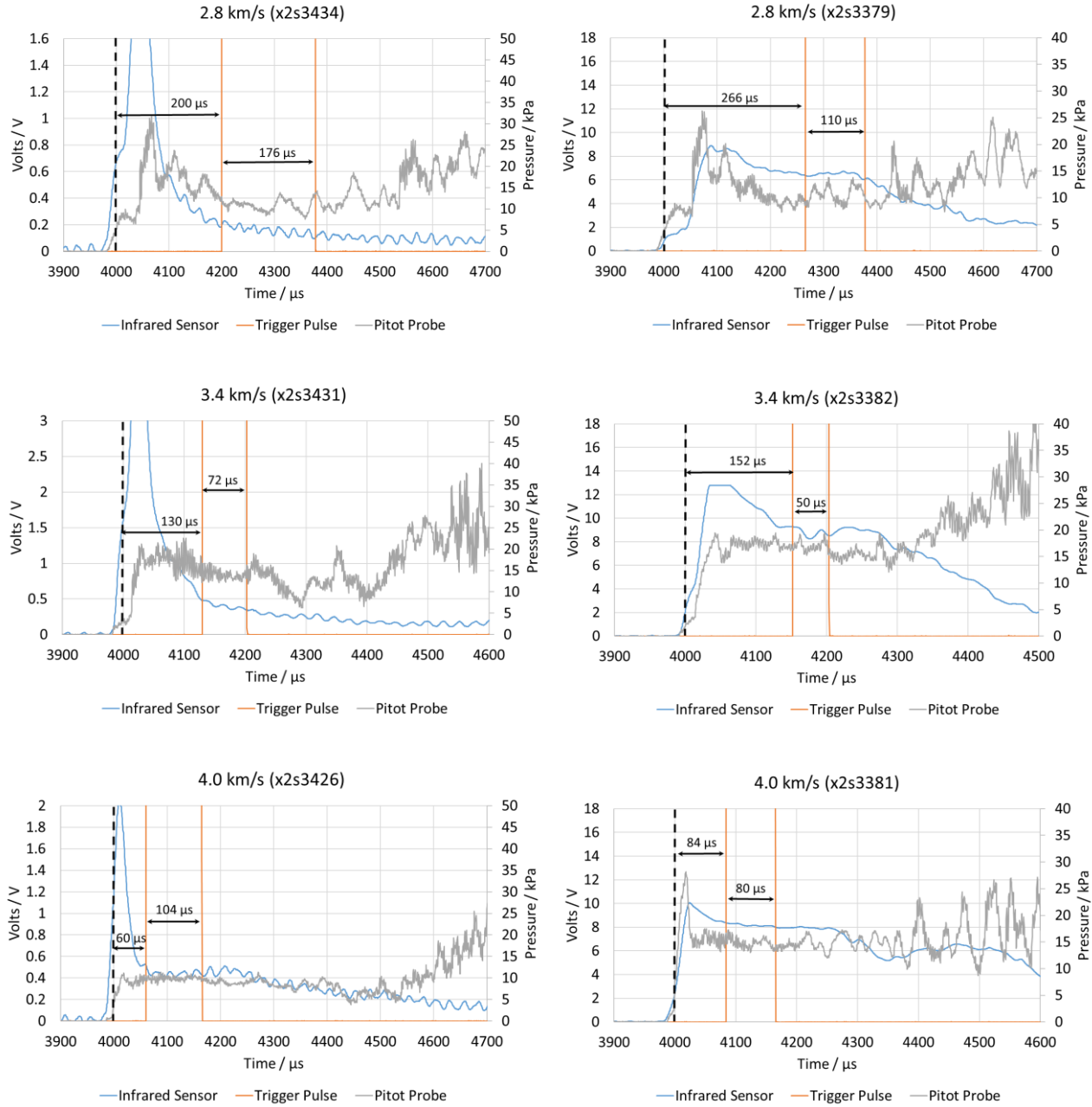


Figure 4.17. Integration time of the infrared camera along with the pitot pressure traces and the infrared sensor traces. The figures on the left corresponds to the nozzle exit freestream experiment. The figures on the right corresponds to the expansion fan experiment.

4.2.6 Shot-to-shot variation

As multiple experiments were performed at the same nominal condition, the emission spectroscopy measurements of the 4.3 μ m band for the flow around the wedge is used to examine the shot-to-shot variation. The measurements are taken at 3.25 mm, 5.75 mm and 8.25 mm above the test model, as shown on Figure 4.5. As discussed by Sheikh [122], examining the integrated band radiance is a good way to investigate the repeatability because it is highly sensitive to flow variations. The measured absolute band radiances are shown on Figure 4.18, Figure 4.19 and Figure 4.20 for the 2.8 km/s, 3.4

km/s and 4.0 km/s condition respectively. It can be seen that the shot-to-shot variation is significant for the 2.8 km/s and 3.4 km/s condition, while the shot-to-shot variation for the 4.0 km/s is less significant. Nevertheless, for all the conditions, the shot-to-shot variation observed is significantly greater than the uncertainty of the absolute radiance calibration, which is only $\pm 2\%$ for the $4.3 \mu\text{m}$ band. Furthermore, calibration of the experimental data with two different calibration functions obtained two weeks apart (the start and middle of the experimental campaign) showed differences of less than 5 % and, thus, are overshadowed by the shot-to-shot variations as well.

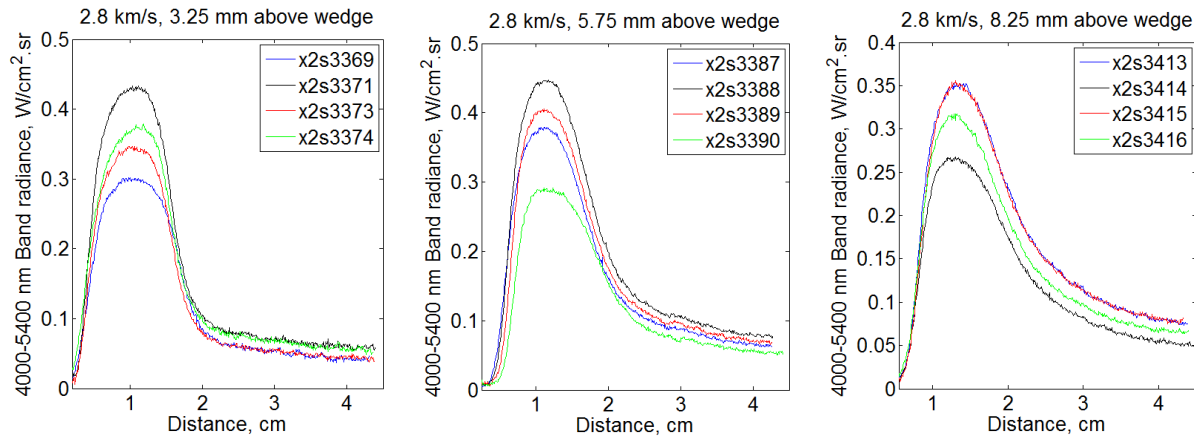


Figure 4.18. Absolute band radiance measured from emission spectroscopy for the 2.8 km/s condition at the different locations above the test model.

Table 4.3. Shock speeds and pressure measurements of the emission spectroscopy measurements at 3.25 mm above the test model for the 2.8 km/s condition. * = lower bound of radiation. † = upper bound of radiation.

Shot number	Primary shock speed (m/s)	Secondary shock speed (m/s)	Acc. tube pressure (kPa)	Pitot pressure (kPa)	Conehead pressure (kPa)
x2s3369*	1620 ± 20	2930 ± 40	2.5 ± 0.4	11.1 ± 2.8	1.4 ± 0.4
x2s3371†	1620 ± 30	2890 ± 30	2.6 ± 0.3	10.9 ± 3.0	1.3 ± 0.3
x2s3373	1580 ± 30	2770 ± 30	2.1 ± 0.3	10.0 ± 2.5	1.3 ± 0.2
x2s3374	1610 ± 20	2810 ± 30	2.4 ± 0.3	10.4 ± 3.1	1.3 ± 0.3

Table 4.4. Shock speeds and pressure measurements of the emission spectroscopy measurements at 5.75 mm above the test model for the 2.8 km/s condition. * = lower bound of radiation. † = upper bound of radiation.

Shot number	Primary shock speed (m/s)	Secondary shock speed (m/s)	Acc. tube pressure (kPa)	Pitot pressure (kPa)	Conehead pressure (kPa)
x2s3387	1660 ± 40	2880 ± 30	2.6 ± 0.4	12.4 ± 3.0	1.4 ± 0.3
x2s3388†	1560 ± 30	2720 ± 30	2.2 ± 0.3	11.6 ± 3.0	1.4 ± 0.3
x2s3389	1580 ± 30	2770 ± 30	2.0 ± 0.3	9.2 ± 2.6	1.1 ± 0.2
x2s3390*	1660 ± 20	2890 ± 30	2.3 ± 0.4	11.4 ± 2.8	1.5 ± 0.4

Table 4.5. Shock speeds and pressure measurements of the emission spectroscopy measurements at 8.25 mm above the test model for the 2.8 km/s condition. * = lower bound of radiation. † = upper bound of radiation.

Shot number	Primary shock speed (m/s)	Secondary shock speed (m/s)	Acc. tube pressure (kPa)	Pitot pressure (kPa)	Conehead pressure (kPa)
x2s3413†	1680 ± 20	2970 ± 30	2.6 ± 0.4	11.2 ± 2.8	1.4 ± 0.2
x2s3414*	1630 ± 20	2950 ± 30	2.5 ± 0.4	11.8 ± 3.0	1.6 ± 0.4
x2s3415†	1650 ± 20	2950 ± 30	2.1 ± 0.4	12.3 ± 3.2	1.4 ± 0.3
x2s3416	1600 ± 20	2820 ± 30	2.1 ± 0.3	10.4 ± 2.7	1.3 ± 0.3

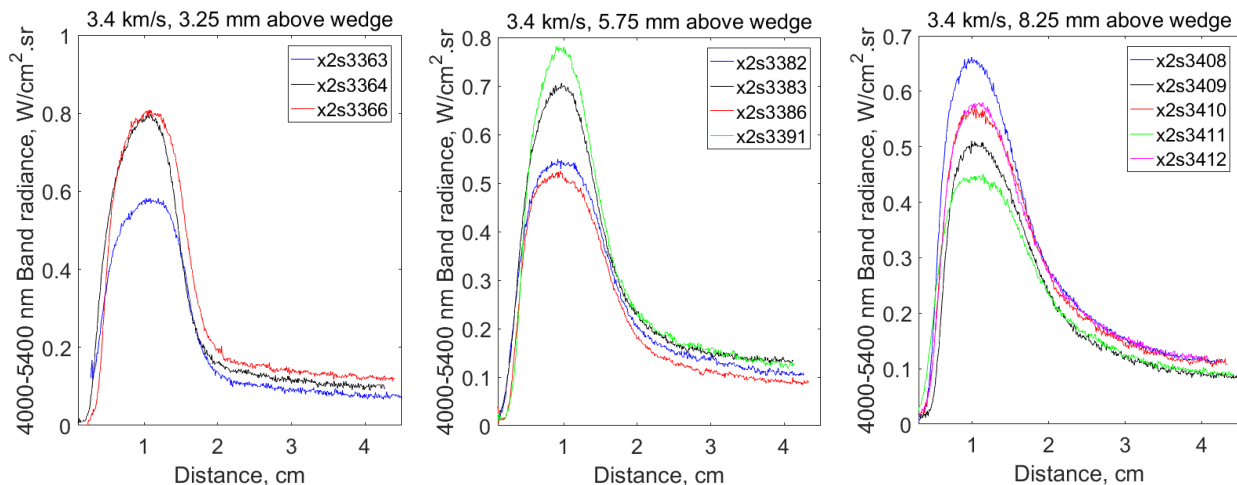


Figure 4.19. Absolute band radiance measured from emission spectroscopy for the 3.4 km/s condition at the different locations above the test model.

Table 4.6. Shock speeds and pressure measurements of the emission spectroscopy measurements at 3.25 mm above the test model for the 3.4 km/s condition. * = lower bound of radiation. † = upper bound of radiation.

Shot number	Primary shock speed (m/s)	Secondary shock speed (m/s)	Acc. tube pressure (kPa)	Pitot pressure (kPa)	Conehead pressure (kPa)
x2s3363*	2050 ± 30	3700 ± 40	2.8 ± 0.3	20.2 ± 2.3	2.4 ± 0.4
x2s3364	1960 ± 40	3580 ± 40	2.5 ± 0.4	16.4 ± 2.0	1.7 ± 0.2
x2s3366†	2010 ± 30	3600 ± 40	2.7 ± 0.3	17.0 ± 1.7	1.9 ± 0.2

Table 4.7. Shock speeds and pressure measurements of the emission spectroscopy measurements at 5.75 mm above the test model for the 3.4 km/s condition. * = lower bound of radiation. † = upper bound of radiation.

Shot number	Primary shock speed (m/s)	Secondary shock speed (m/s)	Acc. tube pressure (kPa)	Pitot pressure (kPa)	Conehead pressure (kPa)
x2s3382	2030 ± 30	3620 ± 40	2.5 ± 0.4	16.0 ± 1.6	1.7 ± 0.2
x2s3383	2020 ± 30	3600 ± 40	2.4 ± 0.4	18.8 ± 3.0	2.0 ± 0.3
x2s3386*	2000 ± 40	3630 ± 40	2.5 ± 0.2	17.7 ± 2.6	2.0 ± 0.3
x2s3391†	2030 ± 30	3620 ± 40	2.5 ± 0.3	15.8 ± 2.0	1.6 ± 0.2

Table 4.8. Shock speeds and pressure measurements of the emission spectroscopy measurements at 8.25 mm above the test model for the 3.4 km/s condition. * = lower bound of radiation. † = upper bound of radiation.

Shot number	Primary shock speed (m/s)	Secondary shock speed (m/s)	Acc. tube pressure (kPa)	Pitot pressure (kPa)	Conehead pressure (kPa)
x2s3408†	1980 ± 30	3620 ± 60	2.6 ± 0.3	18.2 ± 3.0	1.9 ± 0.2
x2s3409	2010 ± 30	3600 ± 40	2.5 ± 0.3	17.7 ± 2.8	2.1 ± 0.3
x2s3410	2020 ± 30	3600 ± 40	2.5 ± 0.3	16.1 ± 1.9	1.8 ± 0.2
x2s3411*	2020 ± 30	3600 ± 40	2.7 ± 0.3	18.6 ± 2.3	2.6 ± 0.4
x2s3412	1990 ± 30	3580 ± 40	2.5 ± 0.3	17.3 ± 2.3	1.7 ± 0.2

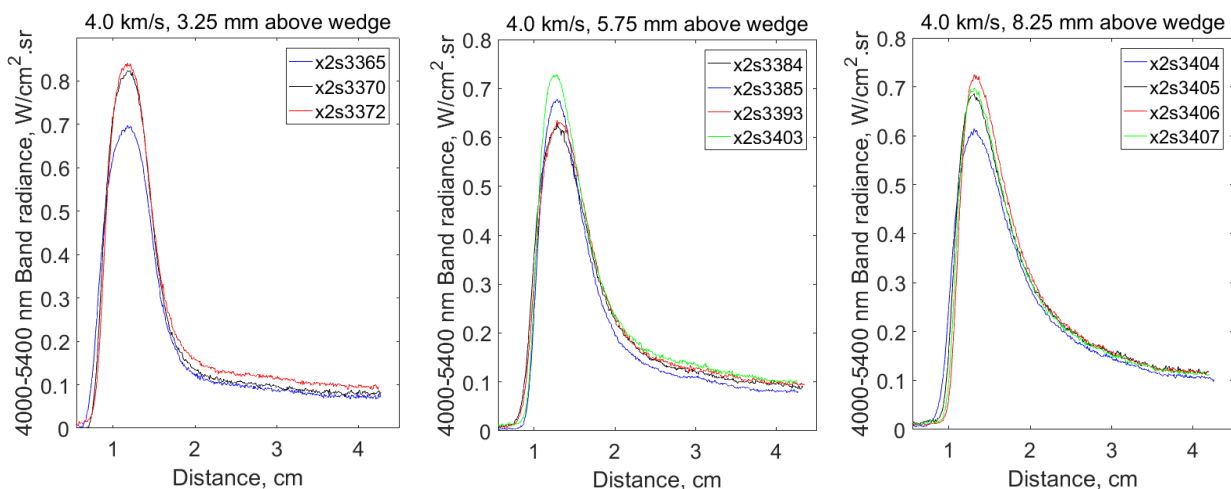


Figure 4.20. Absolute band radiance measured from emission spectroscopy for the 4.0 km/s condition at the different locations above the test model.

Table 4.9. Shock speeds and pressure measurements of the emission spectroscopy measurements at 3.25 mm above the test model for the 4.0 km/s condition. * = lower bound of radiation. † = upper bound of radiation.

Shot number	Primary shock speed (m/s)	Secondary shock speed (m/s)	Acc. tube pressure (kPa)	Pitot pressure (kPa)	Conehead pressure (kPa)
x2s3365*	1990 ± 30	3950 ± 40	1.1 ± 0.2	13.0 ± 1.3	1.0 ± 0.1
x2s3370	2000 ± 30	3910 ± 50	1.1 ± 0.1	14.2 ± 0.9	1.1 ± 0.1
x2s3372†	1990 ± 30	4050 ± 50	1.1 ± 0.1	14.6 ± 0.9	1.2 ± 0.1

Table 4.10. Shock speeds and pressure measurements of the emission spectroscopy measurements at 5.75 mm above the test model for the 4.0 km/s condition. * = lower bound of radiation. † = upper bound of radiation.

Shot number	Primary shock speed (m/s)	Secondary shock speed (m/s)	Acc. tube pressure (kPa)	Pitot pressure (kPa)	Conehead pressure (kPa)
x2s3384*	2020 ± 30	4040 ± 40	1.1 ± 0.1	14.7 ± 1.8	1.2 ± 0.2
x2s3385	2020 ± 40	4010 ± 50	1.1 ± 0.1	13.5 ± 0.7	1.1 ± 0.1
x2s3393	2020 ± 30	4090 ± 50	1.2 ± 0.2	13.4 ± 1.3	1.1 ± 0.1
x2s3403†	2000 ± 30	4040 ± 50	1.2 ± 0.1	13.7 ± 1.1	1.1 ± 0.1

Table 4.11. Shock speeds and pressure measurements of the emission spectroscopy measurements at 8.25 mm above the test model for the 4.0 km/s condition. * = lower bound of radiation. † = upper bound of radiation.

Shot number	Primary shock speed (m/s)	Secondary shock speed (m/s)	Acc. tube pressure (kPa)	Pitot pressure (kPa)	Conehead pressure (kPa)
x2s3404*	1980 ± 30	3910 ± 40	1.2 ± 0.1	15.2 ± 1.8	1.4 ± 0.2
x2s3405	2010 ± 30	3830 ± 50	1.3 ± 0.1	14.8 ± 1.3	1.3 ± 0.1
x2s3406†	1990 ± 30	3880 ± 30	1.1 ± 0.1	15.0 ± 2.0	1.4 ± 0.1
x2s3407	2010 ± 30	3880 ± 50	1.1 ± 0.1	14.7 ± 0.9	1.3 ± 0.1

The variation observed in the radiation measurement of the wedge flow is not reflected in the operating condition measurements - shock speed, wall pressure and pitot pressure. For the 3.25 mm measurements of the 2.8 km/s condition, no correlation can be seen between the repeatability of the various shock speed and pressure measurements in Table 4.3 (the uncertainties of the shock speed and pressure measurements have been described in section 3.4.2) and the radiation measurements in Figure 4.18. From the shock speed and pressure measurements in Table 4.3, the outlier seems to be

shot x2s3373. However, from the corresponding radiation measurements, shot x2s3373 lies within the upper and lower bounds of all the measurements. The upper and lower bounds of the radiation measurement are x2s3371 and x2s3369 respectively. Conversely, from the shock speed and pressure measurements, x2s3371 and x2s3369 seems to be very similar condition. The same are observed when accessing the other measurements for all three conditions; there is no correlation between the degree of consistency in the shock speed and pressure measurements and the degree of consistency in the radiation measurement.

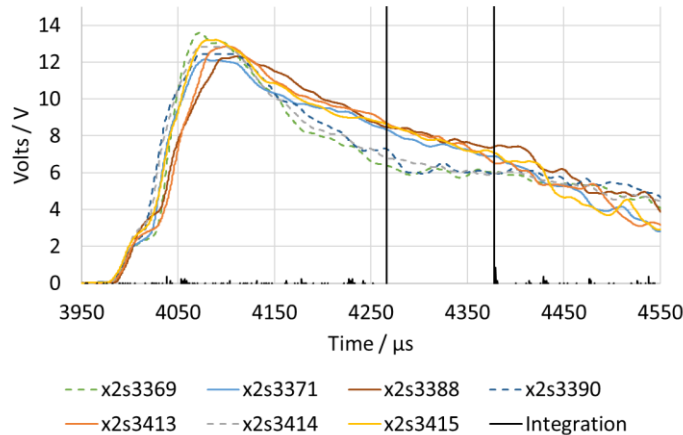


Figure 4.21. Infrared sensor traces of the upper and lower bound emission spectroscopy measurements for the 2.8 km/s condition. Solid line corresponds to upper bound measurements. Dashed line corresponds to lower bound measurements.

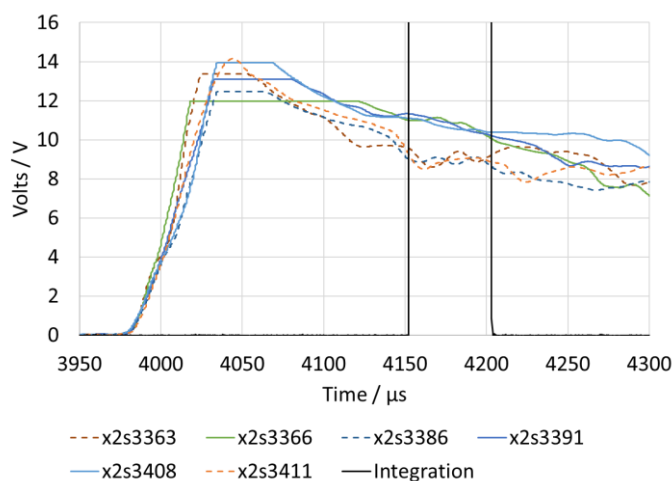


Figure 4.22. Infrared sensor traces of the upper and lower bound emission spectroscopy measurements for the 3.4 km/s condition. Solid line corresponds to upper bound measurements. Dashed line corresponds to lower bound measurements.

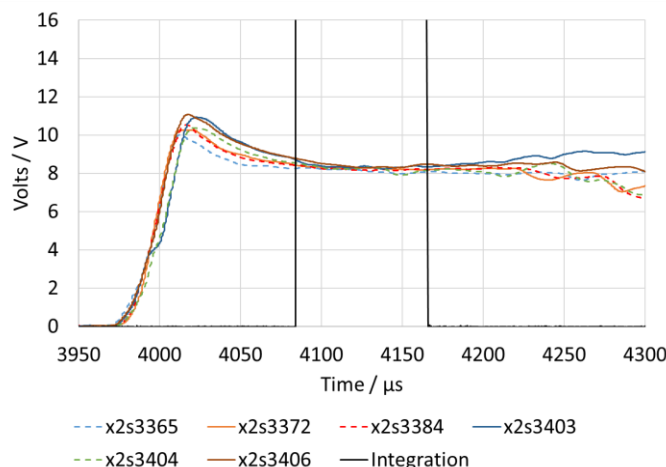


Figure 4.23. Infrared sensor traces of the upper and lower bound emission spectroscopy measurements for the 4.0 km/s condition. Solid line corresponds to upper bound measurements. Dashed line corresponds to lower bound measurements.

The cause of the large variation seen in the radiation measurements remains unclear. However, the shot-to-shot variation is not caused by issues relating to the delay and duration of the exposure time. The measured radiation from the emission spectroscopy varies because the actual radiation produced in the experiment during the test time truly does vary. This is proved by assessing the infrared sensor traces taken of the flowfield around the wedge model. The shot-to-shot discrepancies seen in the emission spectroscopy measurements are reflected consistently in the infrared sensor traces. The infrared sensor traces for the upper and lower bound emission spectroscopy measurements in Figure 4.18 - Figure 4.20 are shown in Figure 4.21 - Figure 4.23. The result shows that the variation seen in the emission spectroscopy measurement is not caused due to errors in the measurement. The result shows that the variation is observed because the radiation emission produced is actually different during the entire duration of the steady test time. For example, the measured band radiance of shots x2s3371 is much greater than that measured for shot x2s3369, as shown on Figure 4.18. This is consistent in the infrared sensor traces for these shots shown on Figure 4.21; the sensor reading shows that the x2s3371 shot has a greater reading than that of the x2s3369 shot in the entire period of the steady radiation. Hence, the variation is not an artifact of issues relating to the delay and duration of the exposure time. The same is seen when examining the other measurements for all three conditions. Furthermore, for the 4.0 km/s condition, the smaller variation seen in the emission spectroscopy measurements in Figure 4.20 is consistent with the smaller variation observed in the infrared sensor traces in Figure 4.23, when compared to that of the 2.8 and 3.4 km/s conditions.

The shot-to-shot variation of the freestream radiation measurements are also investigated. Emission spectroscopy measurements of the freestream radiation were taken for only the $4.3 \mu\text{m}$ band because the $2.7 \mu\text{m}$ band is too weak. The radiation measurements as well as the corresponding operating condition properties are presented in Table 4.12, Table 4.13 and Table 4.14 for the 2.8, 3.4 and 4.0

km/s conditions respectively. The uncertainties of the band radiance measurements presented in the tables correspond to the noise of the measurements, while the uncertainties of the shock speed and pressure measurements presented in the tables have been described in section 3.4.2. The band radiance values are averaged between 1.0 mm to 3.0 mm downstream of the nozzle exit. It seems that the shot-to-shot variation of the inflow radiation can vary by up to around 20 %, although the uncertainty of each measurement is also quite large due to the noise. All three conditions have similar degrees of variation for the inflow radiation measurements. The inflow measurements of the 2.8 and 3.4 km/s condition do not have larger variations than that of the 4.0 km/s condition, contrary to that seen in the measurements above the test model. This result is supported by the infrared sensor traces of the freestream. Therefore, along with the measurements of the expansion tube operating properties, the inflow radiation measurements do not seem to provide any correlations to the large shot-to-shot variation of the measurements above the test model for the 2.8 and 3.4 km/s conditions.

Table 4.12. Shock speed and pressure measurements for the experiments of freestream radiation measurement, for the 2.8 km/s condition.

Test	Primary shock speed (m/s)	Secondary shock speed (m/s)	Acc. tube pressure (kpa)	Pitot pressure (kpa)	Conical probe pressure (kpa)	Band Radiance (W/cm ² .sr)
x2s3432	1650 ± 20	2890 ± 40	2.3 ± 0.3	10.4 ± 2.9	1.3 ± 0.3	0.0044 ± 0.001
x2s3433	1620 ± 20	2880 ± 30	2.3 ± 0.3	10.4 ± 2.5	1.2 ± 0.2	0.0040 ± 0.001
x2s3434	1680 ± 20	2960 ± 30	2.4 ± 0.4	11.1 ± 2.6	1.3 ± 0.3	0.0037 ± 0.001

Table 4.13. Shock speed and pressure measurements for the experiments of freestream radiation measurement, for the 3.4 km/s condition.

Test	Primary shock speed (m/s)	Secondary shock speed (m/s)	Acc. tube pressure (kpa)	Pitot pressure (kpa)	Conical probe pressure (kpa)	Band Radiance (W/cm ² .sr)
x2s3429	2020 ± 30	3560 ± 40	2.7 ± 0.4	16.3 ± 1.7	2.3 ± 0.3	0.0073 ± 0.001
x2s3430	2020 ± 30	3640 ± 40	2.7 ± 0.4	16.4 ± 1.8	2.1 ± 0.2	0.0064 ± 0.001
x2s3431	2000 ± 30	3650 ± 40	2.4 ± 0.3	18.8 ± 2.2	2.6 ± 0.4	0.0062 ± 0.001

Table 4.14. Shock speed and pressure measurements for the experiments of freestream radiation measurement, for the 4.0 km/s condition.

Test	Primary shock speed (m/s)	Secondary shock speed (m/s)	Acc. tube pressure (kpa)	Pitot pressure (kpa)	Conical probe pressure (kpa)	Band Radiance (W/cm ² .sr)
x2s3426	2020 ± 30	3990 ± 50	1.1 ± 0.1	13.6 ± 0.9	1.0 ± 0.2	0.0087 ± 0.001
x2s3427	1980 ± 30	3980 ± 50	1.2 ± 0.1	14.2 ± 1.2	1.1 ± 0.1	0.0069 ± 0.001
x2s3428	2020 ± 30	3980 ± 50	1.2 ± 0.1	14.1 ± 1.3	1.1 ± 0.1	0.0083 ± 0.001

The possibility of the phenomenon of shock wave instability in the shock tube [123] [124] causing the shot-to-shot variation has been investigated as well. This possibility was concluded as unlikely because, firstly, empirical results for CO₂ showed that, for the shock tube conditions in the current work, the shock should be stable [123], and, secondly, any instability and distortion to the shock processed test gas in the shock tube should disappear by the time the test gas reaches the nozzle exit.

The results in this section may suggest that the flowfield radiation around the test model is very sensitive to small changes to the inflow for the 2.8 and 3.4 km/s condition in particular. Nevertheless, the rather large shot-to-shot variations can be overcome in the current study. The only issue with having a high shot-to-shot variation is that it would make comparing the measurements at different locations difficult for a given freestream condition. However, from Figure 4.21 - Figure 4.23, the traces of the lower bound measurements are seen to match very well with each other and the traces of the upper bound measurements are seen to match very well with each other. The consequence of this is that the comparison of the measurements made at different heights above the test model can be done by comparing lower bounds with lower bounds and upper bounds with upper bounds.

4.3 Filtered Two-Dimensional Imaging

Filtered two-dimensional imaging of the flowfield around the test model is performed to supplement the emission spectroscopy measurements. The emission spectroscopy measurements have only one spatial dimension. The filtered images do not have spectral resolution, but it does have two spatial dimensions. Therefore, the filtered two-dimensional images provide valuable information of the variation of the intensity of the 2.7 and 4.3 μm band at different locations in the flowfield.

4.3.1 Methodology

The arrangement of the filtered two-dimensional imaging experiment is shown on Figure 4.24. The filtered two-dimensional imaging is conducted for both the 2.7 μm and 4.3 μm bands. The imaging system involves using a filter in front of the infrared camera to allow transmission of only the 2.7 μm or 4.3 μm band. The filtered image for the 2.7 μm band is produced using a wide bandpass filter which filters out all signal with wavelength below 2.25 μm and above 3.81 μm. The filtered image for the 4.3 μm band is produced using a longpass filter to remove all signal with wavelength below 3.7 μm. The optical properties of the system are summarized in Table 4.15. The dimensions of the filtered image are approximately 74.1 x 59.3 mm, using an 80 mm focal length lens. An aperture of 5 mm is used and placed in front of the lens and, given a depth of field of 100 mm, the circle of confusion is 4.7 pixels. As is with the emission spectroscopy system, the filtered imaging system is

aligned using the alignment plate method discussed in section 4.2.2. Using this method, the images acquired are made to look along the width of the test model by making sure the camera can see through the alignment holes at both edges of the test model. The imaging system is focused by placing a sharp edge at the centerline of the test model and adjusting the lens such that a sharp image of the sharp edge is obtained.

Table 4.15. Optical properties used for the filtered two-dimensional imaging work.

Imaged spatial dimension	74.1 x 59.3 mm
Magnification	0.17
Depth of field	100 mm
Circle of confusion	4.7 pixels
Focusing optics f-number	16
Test model to lens length	545 mm
Lens to camera FPA length	94 mm

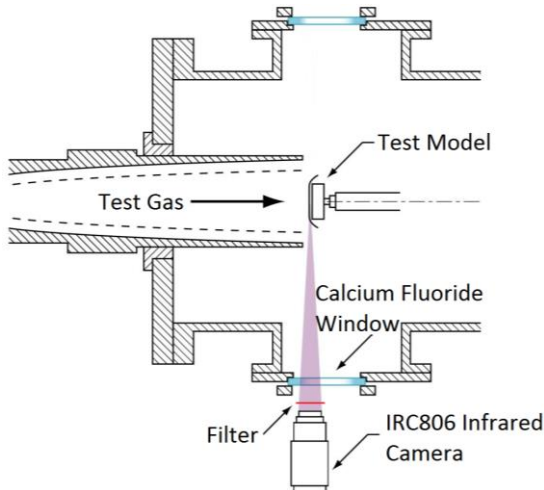


Figure 4.24. Setup of the filtered two-dimensional imaging experiment.

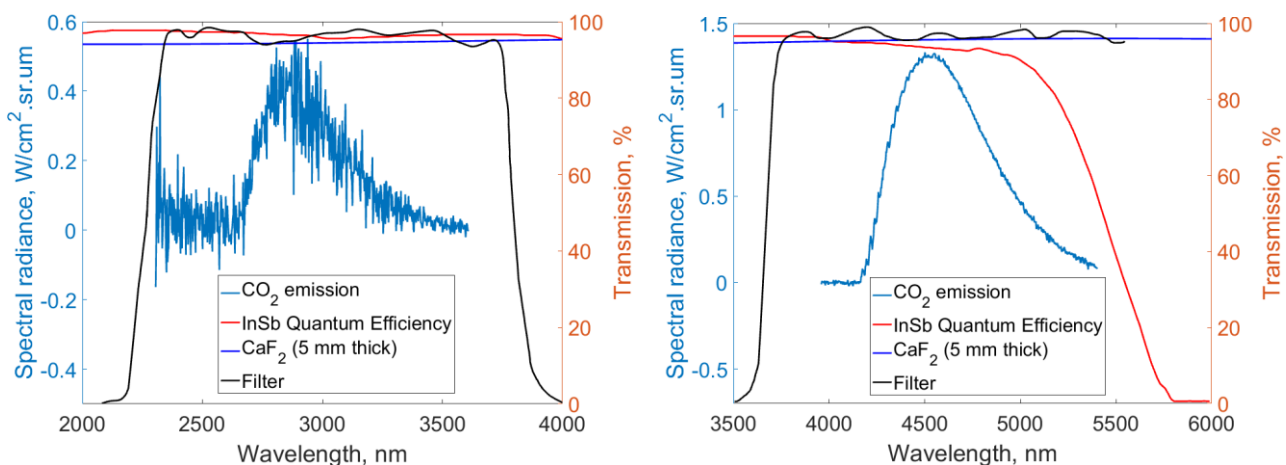


Figure 4.25. Efficiency curves of optical elements compared with the CO₂ 2.7 μm (left) and 4.3 μm (right) emission bands.

To calibrate for the absolute band radiance of the filtered images, images are taken of the same blackbody calibration source used to calibrate the emission spectroscopy system. The calibration source is positioned as shown in Figure 4.12 with the purge tube attached and purged with nitrogen gas, as for the calibration of the spectroscopic measurements. Multiple images are taken such that all pixels in the FPA are accounted for. For the 2.7 μm band measurements, the transmission of the calcium fluoride window and lens, filter and infrared camera quantum efficiency are all approximately constant across the spectral bandwidth of the CO₂ emission band as shown on Figure 4.25. Therefore, these optical elements are considered to be constant with wavelength. The calibration function for the 2.7 μm band, $f_{2.7 \mu\text{m}}$, which relates the counts generated to the band radiance observed, is given by

$$f_{2.7 \mu\text{m}} = \frac{C}{\int_{2260}^{3800} B(\lambda, T) * \varepsilon d\lambda} \quad 4.1$$

where C is the image of the calibration source in counts, B(λ, T) is the Planck equation for the blackbody spectral radiance, λ is the wavelength, T is the temperature and ε is the blackbody emissivity. The calibration function is obtained by dividing the image of the calibration source, C, by the blackbody band radiance of the calibration source (temperature of 1773 K and emissivity of 0.99) across the transmission bandwidth of the filter (2260 nm to 3800 nm). For the 4.3 μm band measurements, although transmission of the calcium fluoride window, calcium fluoride lens and filter remain approximately constant across the spectral bandwidth of the CO₂ emission band, the quantum efficiency does exhibit some wavelength dependences towards the end of the band. The calibration function for the 4.3 μm band, $f_{4.3 \mu\text{m}}$ is given by

$$f_{4.3 \mu\text{m}} = \frac{C}{\int_{3650}^{5750} B(\lambda, T) * \varepsilon * E(\lambda) d\lambda} * 0.9 \quad 4.2$$

To calibrate the 4.3 μm band measurement the blackbody spectral radiance of the calibration source is first multiplied by the external quantum efficiency of the InSb detector, E(λ). The resulting spectral radiance is integrated between the cut-on wavelength of the filter, 3650 nm, and the cut-off wavelength of the InSb quantum efficiency curve, 5750 nm, to obtain a band radiance value. The image of the calibration source is then divided by this band radiance value to obtain an initial relationship between the counts generated and radiance observed. The final calibration function is obtained by multiplying this image by a representative value for the FPA quantum efficiency for the 4.3 μm CO₂ emission band. This is selected as 0.9 because this is approximately the average quantum efficiency within the majority of the 4.3 μm CO₂ emission band. As the exposure time used in acquiring the calibration images is different to that used in the experiment, the calibration functions

are scaled linearly to the exposure time used in the experiment (the linearity with exposure time been checked). The $4.3\text{ }\mu\text{m}$ absorption band from ambient CO_2 does not influence the accuracy of the $4.3\text{ }\mu\text{m}$ band radiance calibration as its bandwidth is much narrower than the hot CO_2 emission band and it is at a lower wavelength. Also, the absorption band is weak - about 10 % for the 190 mm optical path length in atmosphere in the current arrangement. Calibration of the spatial dimensions on the images is performed, as for the emission spectroscopy measurements, by imaging backlit alignment plate holes as discussed in section 4.2.3.

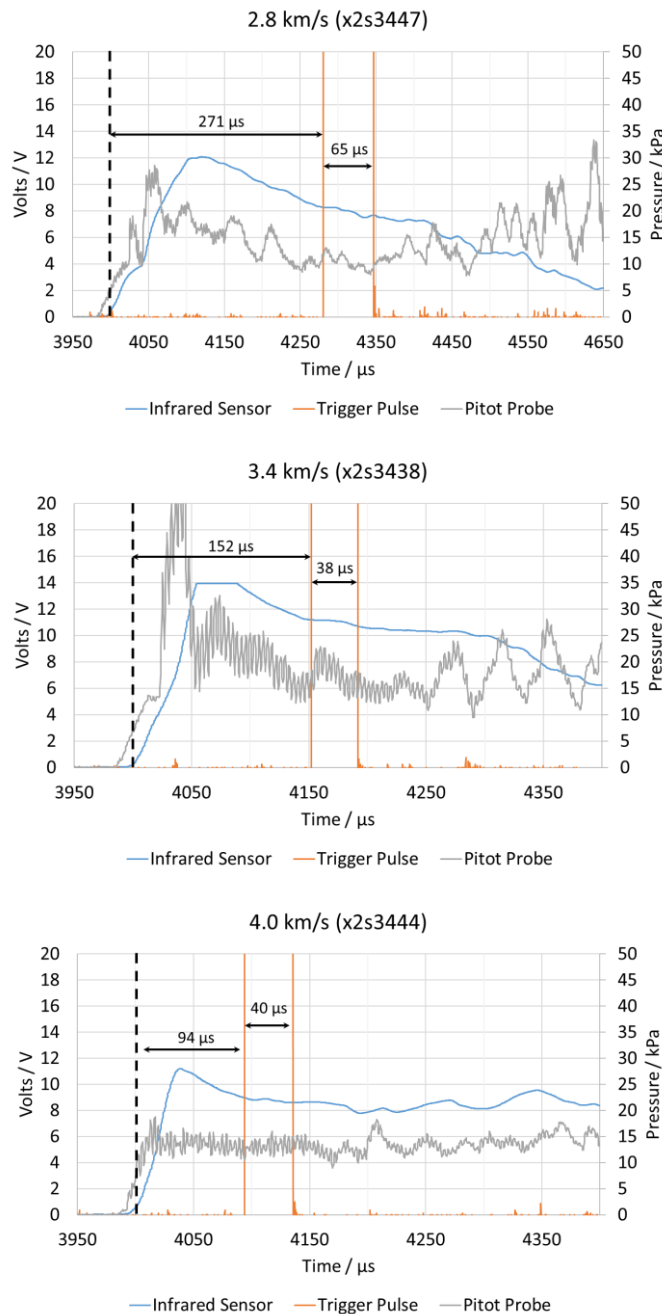


Figure 4.26. Exposure time of the infrared camera for the $4.3\text{ }\mu\text{m}$ band filtered imaging experiments along with the pitot pressure traces and the infrared sensor traces.

Identical to the emission spectroscopy experiments, an infrared sensor was used to obtain a continuous measurement of the radiating flow around the wedge and three pitot probes were placed below the wedge to obtain continuous pitot pressure measurements. The delays relative to the arrival of the shock wave at the test section and the exposure time used for the filtered images are summarized in Table 4.16. The exposure time used for the 2.7 μm band filtered imaging is the same as that used for the emission spectroscopy work of the wedge flow, presented in section 4.2.5. However, the exposure time for the imaging of the 4.3 μm band was shortened to avoid saturating the image. Examples of the exposure for the 4.3 μm band filtered images are shown on Figure 4.26; the exposure is made during the steady test time of the flow.

Table 4.16. The moment and length of the exposure for the filtered imaging measurements. Delay is measured relative to shock arrival at the test model.

Experiment	Condition	Delay / μs	Exposure time / μs
4.3 μm	2.8 km/s	271	65
	3.4 km/s	152	38
	4.0 km/s	94	40
2.7 μm	2.8 km/s	256	110
	3.4 km/s	152	50
	4.0 km/s	84	80

4.3.2 Results

It is first necessary to compare the absolute band radiance measured from the emission spectroscopy system and the absolute band radiance measured from the filtered two-dimensional imaging. This is done to assess the accuracy of the absolute radiation measurements. The absolute radiance measurement acquired from the emission spectroscopy and filtered images are independent of each other. The two measurements are obtained from two independent calibration methods. The band radiance obtained from the emission spectroscopy measurements are derived from spectrally resolved radiation measurements. On the other hand, the band radiance in the filtered images is measured as an integrated quantity. Hence good agreement between the two measurements would indicate good accuracy of the absolute radiation measurements from both techniques. From the filtered images, data at the spatial locations of the emission spectroscopy measurements in Figure 4.5 are extracted, which are horizontal measurements through the shock layer and expansion fan. Comparison between the two sources of measurements is made for both the 2.7 and 4.3 μm bands. The results are shown on Figure 4.27 and Figure 4.28.

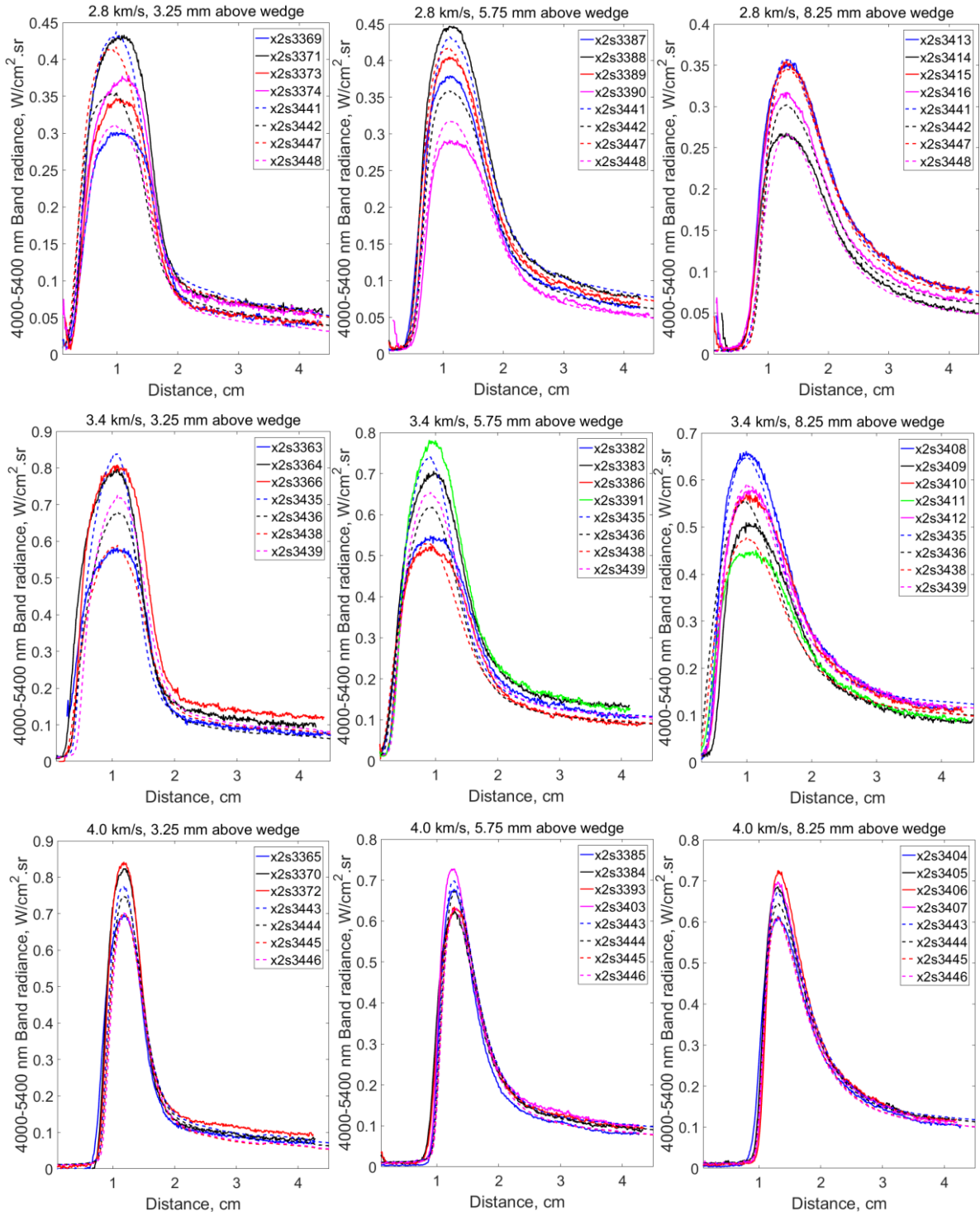


Figure 4.27. Comparison of the $4.3 \mu\text{m}$ band radiance. Solid lines are from emission spectroscopy. Dashed lines are from filtered images. The top, middle and bottom rows corresponds to the 2.8, 3.4 and 4.0 km/s conditions respectively. The left, middle and right columns corresponds to the 3.25, 5.75 and 8.25 mm measurements above the test model respectively.

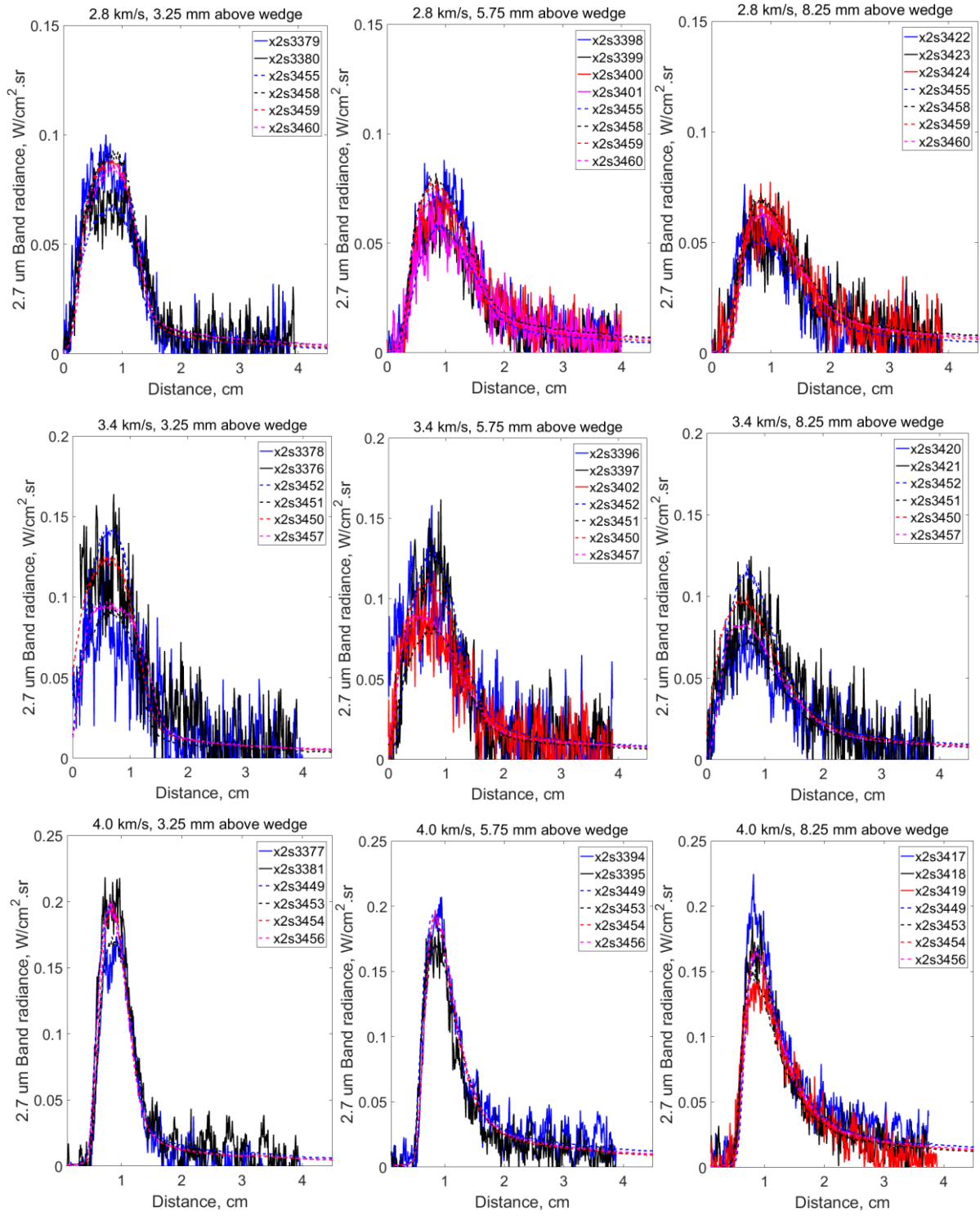


Figure 4.28. Comparison of the 2.7 μm band radiance. Solid lines are from emission spectroscopy. Dashed lines are from filtered images. The top, middle and bottom rows corresponds to the 2.8, 3.4 and 4.0 km/s conditions respectively. The left, middle and right columns corresponds to the 3.25, 5.75 and 8.25 mm measurements above the test model respectively.

The results show that the band radiance from the emission spectroscopy measurements and the band radiance from the filtered images match for all cases; the degrees of shot-to-shot variations observed from the two different types of measurement match as well. Since the spectral radiance of the 2.7 and 4.3 μm emission bands vary spectrally, the measurements from emission spectroscopy are generally considered more accurate. This is because these measurements are spectrally resolved and, thus, allows the absolute radiance calibration process to account for spectrally dependent factors. As the filtered images are not spectrally resolved, the system needs to be spectrally independent in order for the calibrated results to be accurate. Consequently, in the current work, the reason why the measurements from the filtered images and measurements from emission spectroscopy matched well is because the filtered imaging system used in this work does not have any component with significant spectral dependence, as mentioned previously in section 4.3.1. Furthermore, any minor errors from the calibration of the filtered images should be overshadowed by the shot-to-shot variations anyway.

The degree of shot-to-shot variation (up to 40 % for the 2.8 and 3.4 km/s conditions and up to 20 % for the 4.0 km/s condition) seen in the emission spectroscopy measurements and in the filtered images are the same. This shows further consistency between the two types of radiation measurements. Also, when comparing the degree of shot-to-shot variation between the 2.7 μm band measurement and 4.3 μm band measurement, similarly large shot-to-shot variations are seen from both bands. Like the 4.3 μm band measurements, the 2.7 μm band measurements have shot-to-shot variations that are significantly larger than the $\pm 2.5\%$ uncertainty of the measurements due to the calibration source temperature.

As the filtered images capture the radiation in the entire flowfield in two-dimensions, it allows us to look at the degree of variation in radiation measured between shots at different locations in the flowfield. The comparison also allows the variation of the location of the shock wave to be observed. The comparison is done by normalizing the filtered images with the filtered image of the measurement corresponding with the smallest radiation. For the 2.8 km/s condition, in Figure 4.29 and Figure 4.30, the 4.3 and 2.7 μm images are normalized with the image of shot x2s3448 and x2s3455 respectively. For the 3.4 km/s condition, in Figure 4.31 and Figure 4.32, the 4.3 and 2.7 μm images are normalized with the image of shot x2s3438 and x2s3451 respectively. For the 4.0 km/s condition, in Figure 4.33 and Figure 4.34, the 4.3 and 2.7 μm images are normalized with the image of shot x2s3446 and x2s3453 respectively. For the normalized figures, at a particular spatial location, a value of one represents an exact agreement with the lowest radiance shot, while a normalized value of less than one and greater than one means that the radiance is less than and greater than the radiance of the lowest radiance shot respectively.

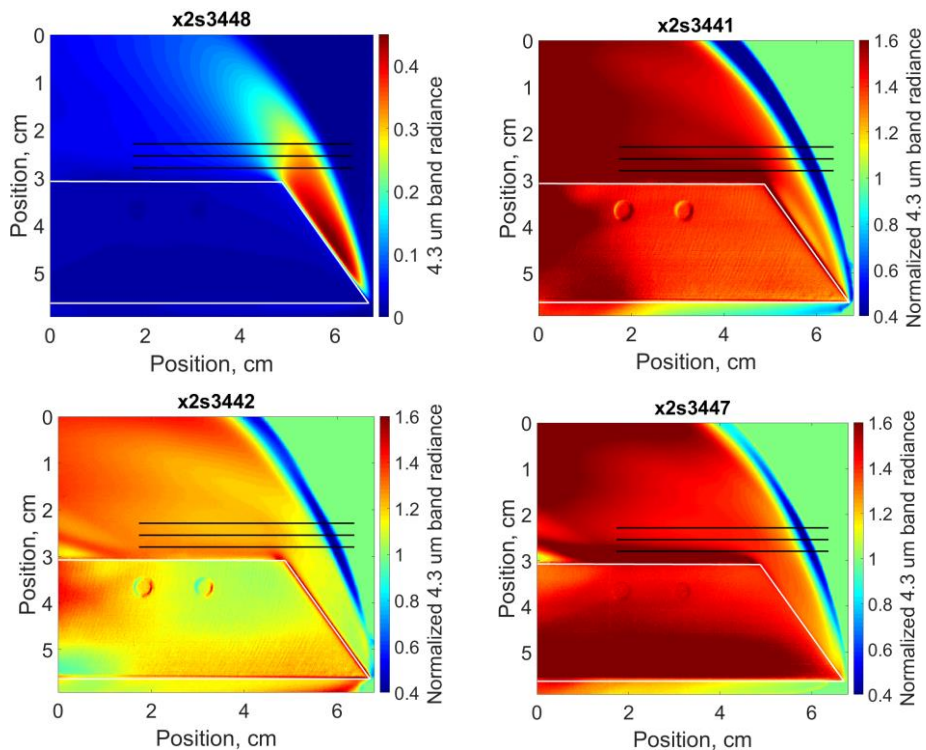


Figure 4.29. 4.3 μm band radiance of the flowfield around the wedge for the 2.8 km/s condition.

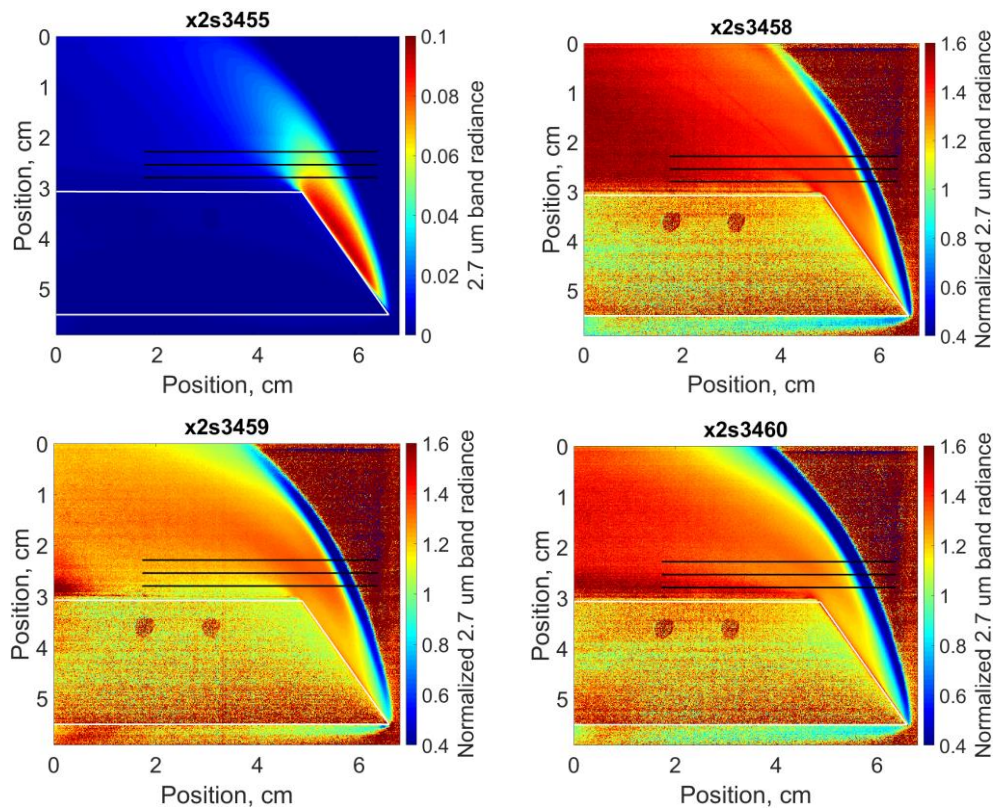


Figure 4.30. 2.7 μm band radiance of the flowfield around the wedge for the 2.8 km/s condition.

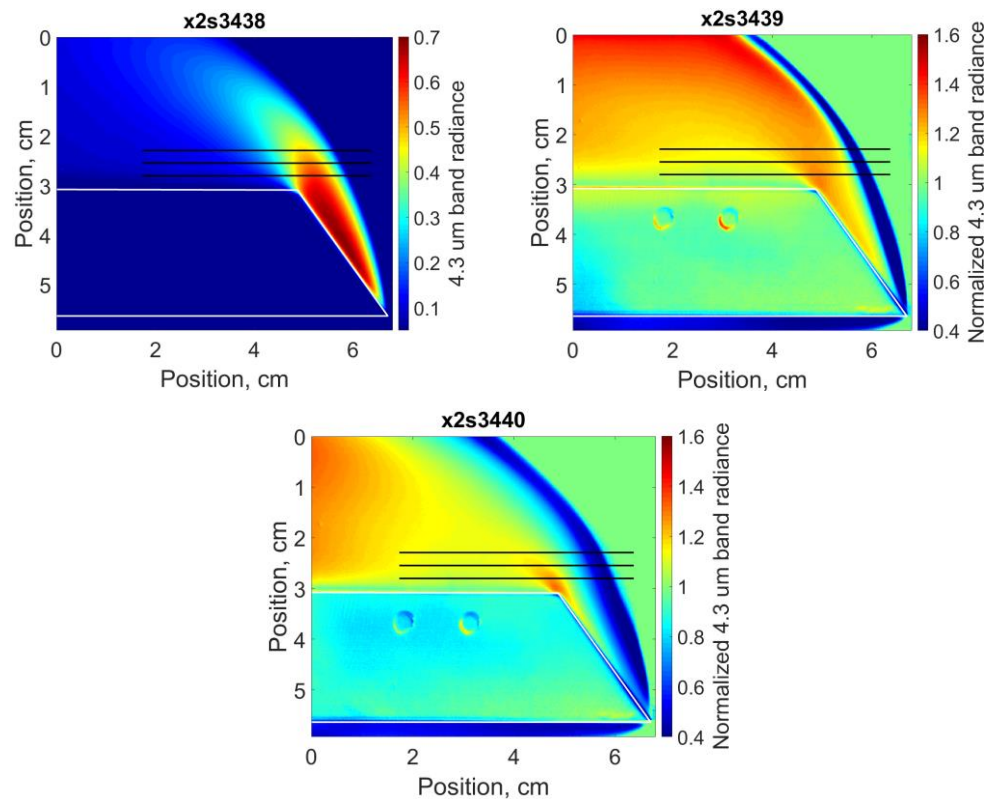


Figure 4.31. $4.3 \mu\text{m}$ band radiance of the flowfield around the wedge for the 3.4 km/s condition.

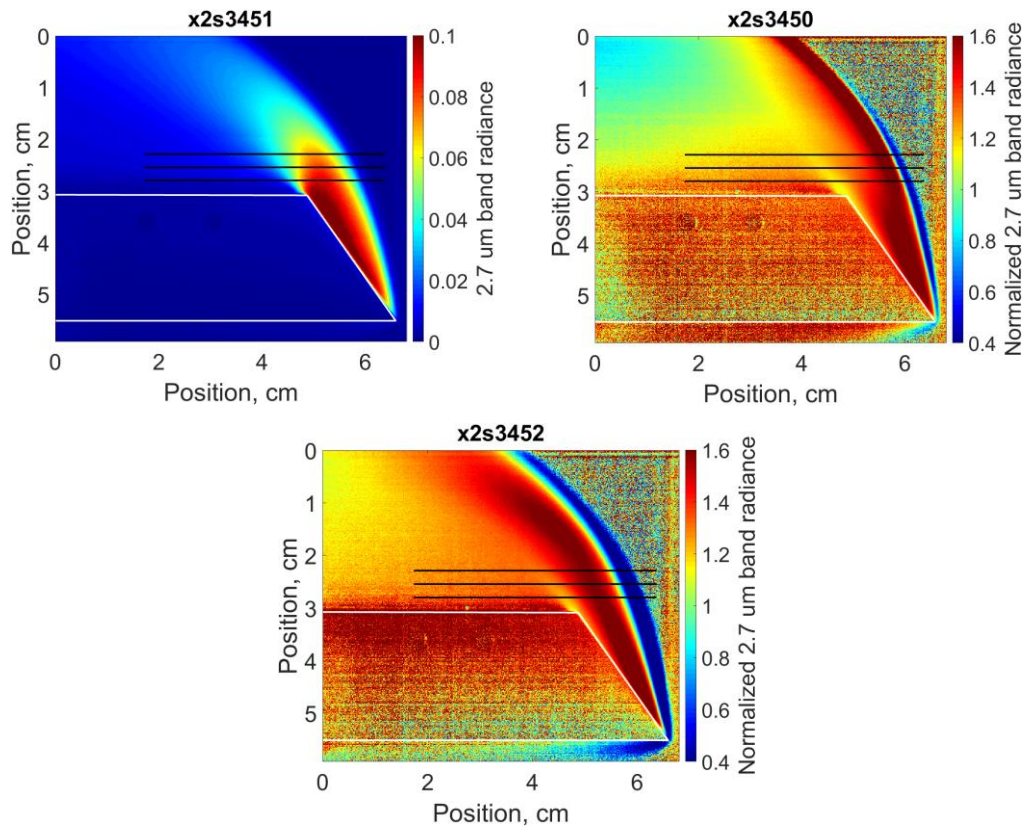


Figure 4.32. $2.7 \mu\text{m}$ band radiance of the flowfield around the wedge for the 3.4 km/s condition.

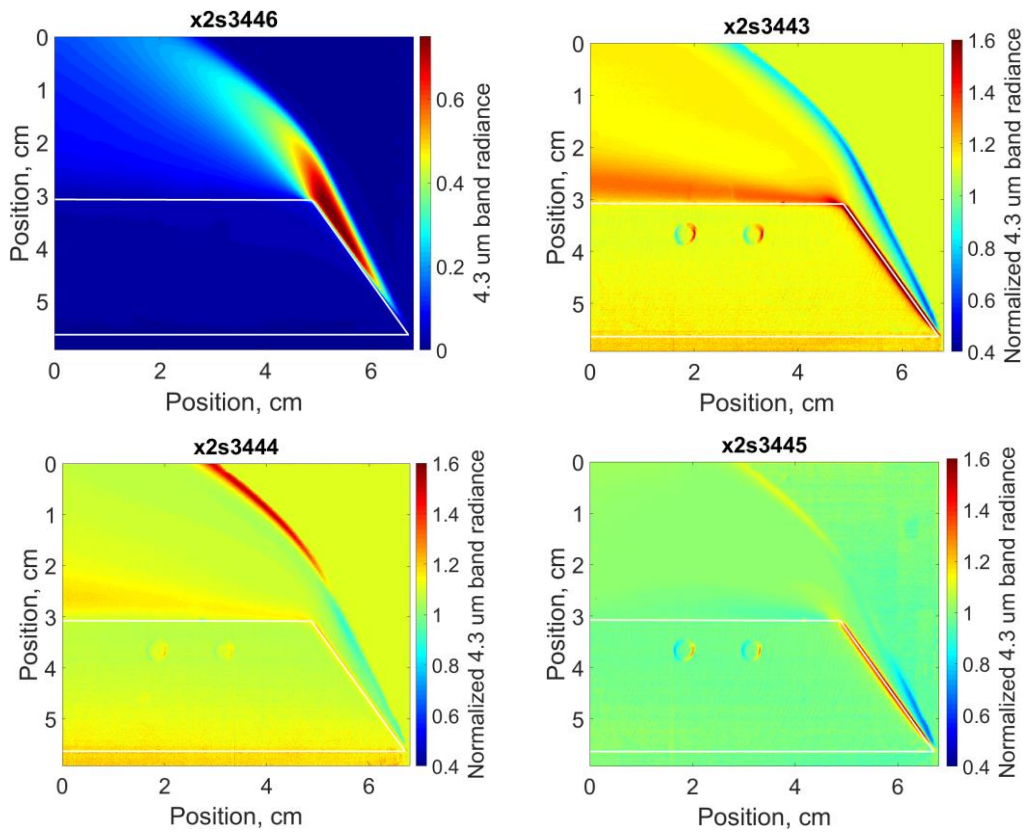


Figure 4.33. 4.3 μm band radiance of the flowfield around the wedge for the 4.0 km/s condition.

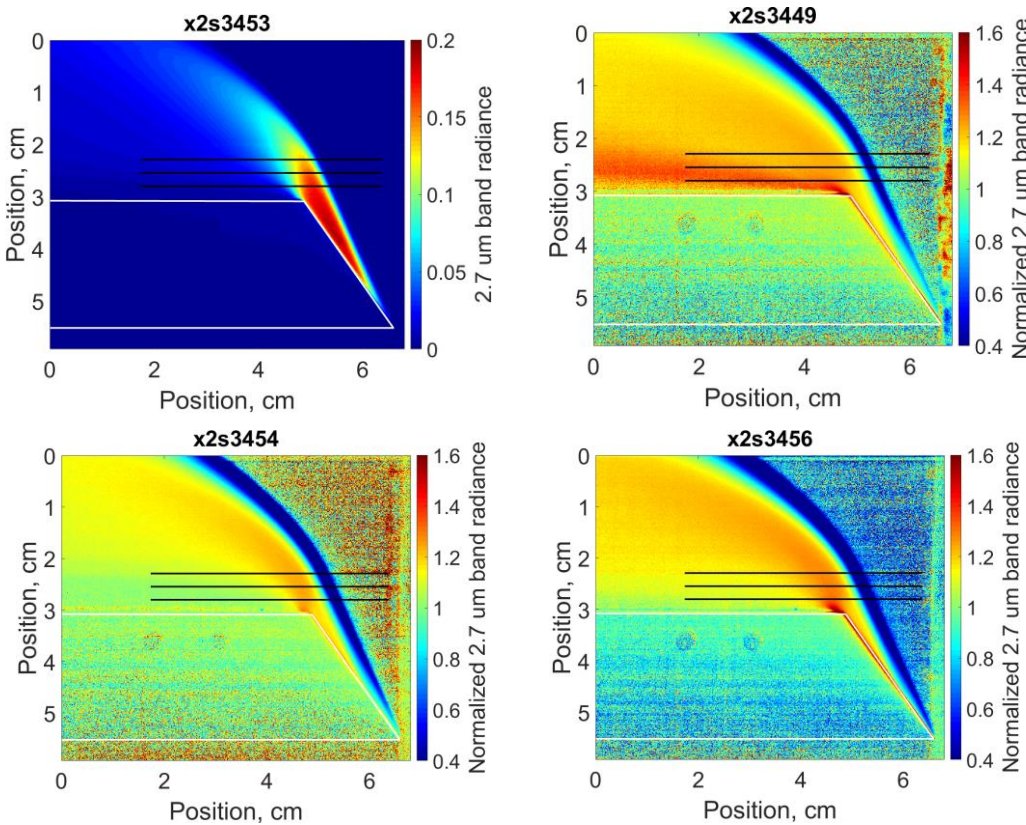


Figure 4.34. 2.7 μm band radiance of the flowfield around the wedge for the 4.0 km/s condition.

The results on Figure 4.29 to Figure 4.34 show the shot-to-shot variation in the flowfield radiation as well as the shot-to-shot variation in the shock wave location. Generally, for the same nominal freestream condition, it can be observed that the shot with the lowest radiation intensity has the largest shock standoff whereas the shot with the greatest radiation has the smallest shock standoff. This is true for both the 2.7 μm and 4.3 μm band. The degree of shot-to-shot variation seen in the radiation intensity is also reflected in the shot-to-shot variation of the shock wave location. As mentioned previously, the 2.8 and 3.4 km/s has large shot-to-shot variations whereas the 4.0 km/s condition has a much smaller shot-to-shot variation. Hence, in general, the 4.0 km/s condition has a smaller shot-to-shot variation of the shock wave location compared to the 2.8 and 3.4 km/s condition. Additionally, in general, the shot-to-shot percentage variation in radiation is seen to be larger in the post-shock region and smaller in the expanded flow region.

In Figure 4.35, shock wave locations are extracted from the 4.3 μm band filtered images and compared to the shock wave locations measured from the high-speed schlieren (density gradient) videos for the 2.8 and 3.4 km/s condition. For the 4.0 km/s condition, the shock wave locations extracted from the filtered images are compared to that measured from the luminosity (from the visible spectrum) in the high-speed video. The results show that, for all three conditions, the shock wave locations extracted from the 4.3 μm band filtered images are duly consistent with the shock wave locations measured from the high-speed videos which measured different properties.

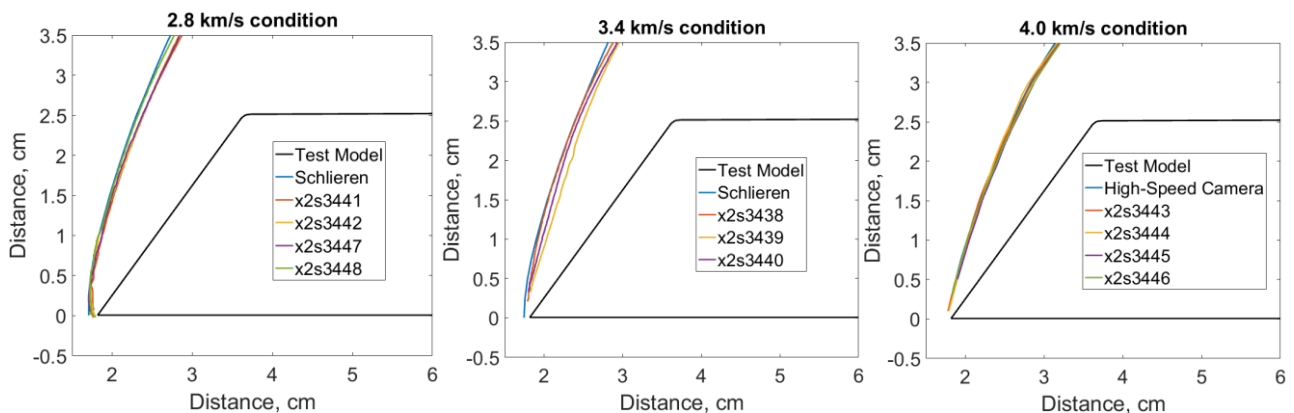


Figure 4.35. Extracted shock wave locations from the filtered images compared to the extracted shock wave locations from the high-speed videos.

Another useful analysis to conduct with the filtered images is to compare the ratio between the 4.3 μm and 2.7 μm band at different locations in the flowfield. The comparison is done by normalizing the 4.3 μm filtered images with the 2.7 μm filtered images. In this study, for each nominal freestream condition, the 4.3 μm band image with the smallest and largest shock standoff is divided by the 2.7 μm band image with the smallest and largest shock standoff respectively. The results are shown on Figure 4.36 to Figure 4.38.

An interesting result is observed for the 2.8 km/s condition, in Figure 4.36, where the onset of 2.7 μm band radiation is observed significantly later (further downstream) than the onset of the 4.3 μm band radiation. This is not observed in the 3.4 km/s and 4.0 km/s conditions. This might be caused by complex thermal non-equilibrium near the immediate vicinity of the shock front. In section 2.2, it was mentioned that non-Boltzmann population distributions of the vibrational energy levels in CO₂ can occur near the immediate vicinity of the shock front. This non-equilibrium region was experimentally found to be more pronounced in lower enthalpy conditions [39] [28], which may explain the why the feature in Figure 4.36 is not seen in the 3.4 and 4.0 km/s conditions. Also mentioned in section 2.2, the 4.3 μm band corresponds to the fundamental transitions of the v_3 asymmetric stretching vibrational mode [19], whereas the 2.7 μm band corresponds to the simultaneous transitions in the v_1 and v_3 and the v_2 and v_3 vibrational modes [22]. Thus, the cause of the observation seen in Figure 4.36 might also be related to the possible separate excitation of the different vibrational modes of the CO₂, in addition to the possible non-Boltzmann population distribution at the immediate vicinity of the shock front. However, the possibility of separate excitation of the different vibrational modes of CO₂ is less likely, as discussed in section 2.2.

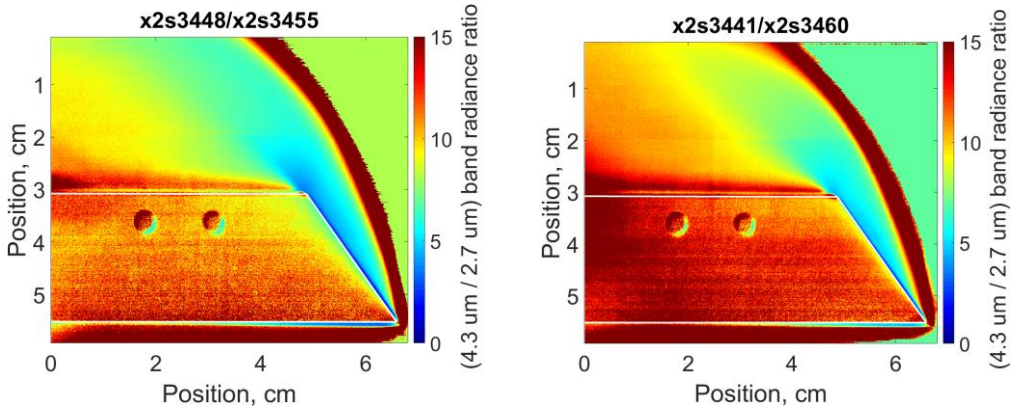


Figure 4.36. 2.8 km/s condition. The upper bound and lower bounds are the left and right figures respectively.

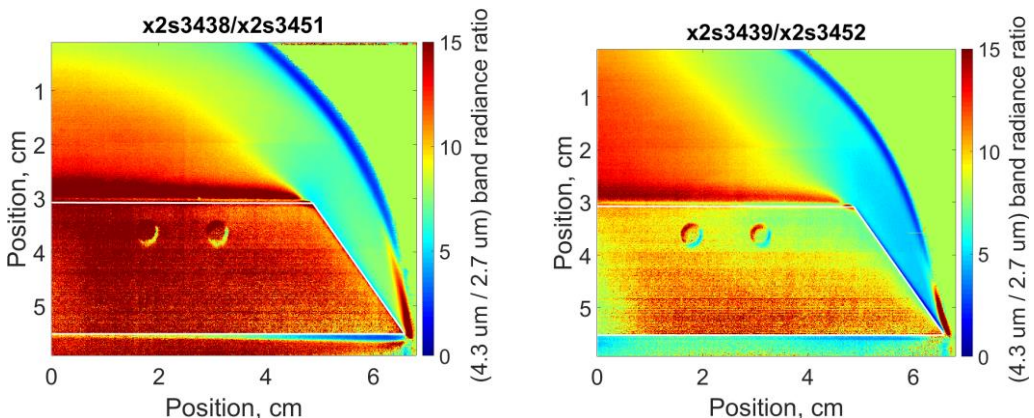


Figure 4.37. 3.4 km/s condition. The upper bound and lower bounds are the left and right figures respectively.

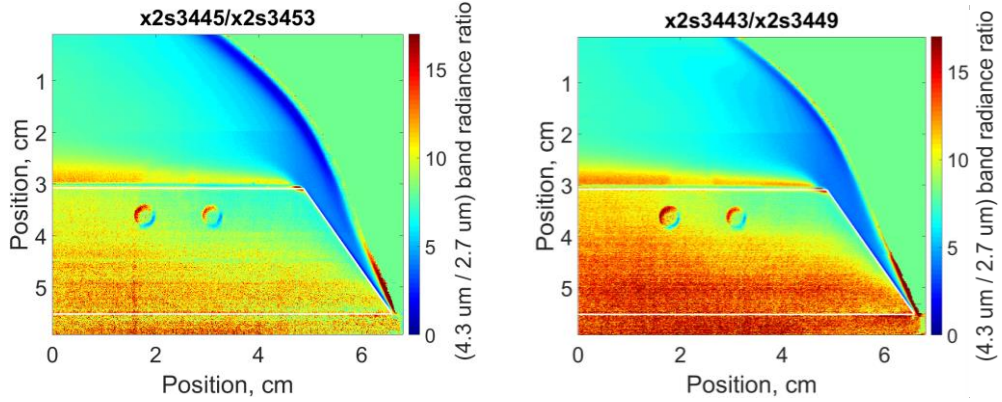


Figure 4.38. 4.0 km/s condition. The upper bound and lower bounds are the left and right figures respectively.

For the $4.3 \mu\text{m}$ to $2.7 \mu\text{m}$ band radiance ratio at different locations in the flowfield around the test model, the results show that it is dependent on temperature. The ratio increases with decrease in temperature. This trend is confirmed with NEQAIR [49] calculations, shown in Figure 4.39. In the shock layer, the $4.3 \mu\text{m}$ band is a factor of around 5 greater than the $2.7 \mu\text{m}$ band for the 2.8 and 3.4 km/s condition. For the 4.0 km/s condition, the $4.3 \mu\text{m}$ band is a factor of around 3 greater than the $2.7 \mu\text{m}$ band in the shock layer. Hence, the radiative heating from the $2.7 \mu\text{m}$ band is regarded as non-negligible for the forebody heating, compared to the total radiative heating. In the expanded flow region, the $4.3 \mu\text{m}$ band is about 10 times greater than the $2.7 \mu\text{m}$ band for the 2.8 km/s and 3.4 km/s condition. For the 4.0 km/s condition, the $4.3 \mu\text{m}$ band is a factor of around 6 greater than the $2.7 \mu\text{m}$ band in the expanded flow region. It is also important to mention that the ratio between the $4.3 \mu\text{m}$ and $2.7 \mu\text{m}$ band depends on the carbon dioxide number density in addition to temperature as shown in Figure 4.39. This is because the $4.3 \mu\text{m}$ band has more self-absorption than the $2.7 \mu\text{m}$ band. At any given temperature, the ratio of the $4.3 \mu\text{m}$ band radiance to the $2.7 \mu\text{m}$ band radiance increases with decrease in carbon dioxide number density and/or path length. Therefore, the intensity of the $2.7 \mu\text{m}$ band is comparable to the intensity of the $4.3 \mu\text{m}$ band under conditions of high temperature and high carbon dioxide number density and/or long path length. Under conditions of low temperature and low carbon dioxide number density and/or short path length, the $2.7 \mu\text{m}$ band may be considered negligible compared to the $4.3 \mu\text{m}$ band. Consequently, it may be established that, depending on the freestream velocity and the carbon dioxide number density and length of the radiating wake region, the $2.7 \mu\text{m}$ band may be considered negligible for the afterbody heating under some conditions.

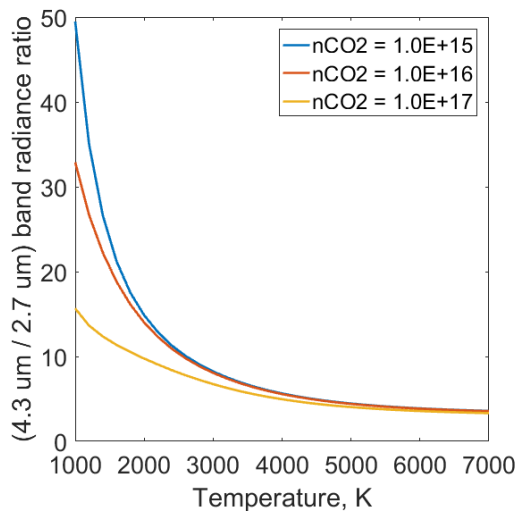


Figure 4.39. Calculated band radiance ratio at different temperatures and carbon dioxide number densities (cm^{-3}), for a pathlength of 125 mm.

4.4 Conclusion

Similar to that used by Cruden et al. [44], a new emission spectroscopy system capable of measuring mid-infrared radiation was assembled, along with a methodology to calibrate for the absolute spectral radiance. Horizontal spectroscopic measurements were taken above the test model, along lines of sight parallel to the width of the test model. Moderate shot-to-shot variations of the band radiance, up to 20 %, were observed for the 4.0 km/s condition. Larger shot-to-shot variations were observed in the measurements for the 2.8 and 3.4 km/s conditions, where the peak band radiation was seen to vary by up to 40 %. Such significant shot-to-shot variations in the 2.8 and 3.4 km/s conditions could not be correlated with the measured operating condition properties. Spectroscopic measurements of the freestream of each condition were also taken. The calibrated results were presented and compared between different shots. Similar to the measurements of the operating condition properties, all three conditions were seen to have similar degrees of variations in the inflow radiation measurements; the variation of the inflow measurements from the 2.8 and 3.4 km/s conditions were not seen to be larger than that from the 4.0 km/s condition. Therefore, it is unclear what is causing the larger shot-to-shot variation seen in the 2.8 and 3.4 km/s conditions. It could be that these conditions are more sensitive to the inflow than the 4.0 km/s condition. The spectroscopic data are particularly useful for estimating the rotational temperature, vibrational temperature and CO_2 number densities of the measurements, which are valuable for detailed investigations of the CO_2 flows. This is carried out in the next chapter.

To supplement the spectroscopic measurements, filtered two-dimensional images of the flowfield around the test model were taken for each condition. A description of the filtered imaging system and the calibration methodology was presented. To assess the accuracy of the radiation measurements,

the band radiance from the emission spectroscopy measurements is compared to the band radiance measured from the filtered images. A match between the measurements from the two independent techniques is observed. In addition, the degree of shot-to-shot variations seen in the emission spectroscopy measurements was confirmed by the filtered images. For all three conditions, the shock wave locations extracted from the filtered images matched well with the shock wave locations extracted from high-speed videos. The ratio of the $4.3\text{ }\mu\text{m}$ band intensity to the $2.7\text{ }\mu\text{m}$ band intensity was also studied using the filtered images. The result showed that the ratio decreases with increase in temperature. This means that the $2.7\text{ }\mu\text{m}$ band has a relatively higher contribution to the total radiative heating at higher temperatures. This trend is consistent with numerical calculations using the NEQAIR code. The result from the NEQAIR code also showed that the relative contribution of the $2.7\text{ }\mu\text{m}$ band increases with increase in carbon dioxide number density and/or radiating pathlength. Therefore, the influence of the $2.7\text{ }\mu\text{m}$ band to the total afterbody heating may be considered negligible under certain conditions.

5 Temperatures and Carbon Dioxide Number Density Estimates

5.1 Introduction

The emission spectroscopy measurements discussed in the previous chapter can be used to estimate the rotational temperature, vibrational temperature and CO₂ number density. This is done by using the NEQAIR v14.0 radiation code [49] to generate numerical spectral radiance curves which are fitted to the measured spectral radiance curves. In this chapter, the behaviour of the shape of the CO₂ emission band on the various input parameters are first investigated. Then, using the spectroscopic measurements of the expansion tube freestream discussed in the previous chapter, spectral fitting is done to deduce the inflow rotational temperature, vibrational temperature and CO₂ number density to help further characterize the experimental test conditions. Furthermore, using the horizontal spectroscopic measurements above the test model, the rotational temperature, vibrational temperature and CO₂ number density are determined at the measurement locations. The deduced temperatures and number densities are used to examine various characteristics of the high temperature carbon dioxide flowfield. Additionally, the estimated post-shock temperatures and number densities from the measurements above the test model are used to further characterize the inflow conditions. It should be noted that none of the extracted properties from spectral fitting are direct measurements as such, but are estimates obtained to be most consistent with the spectral data using the best knowledge of radiation processes as contained in NEQAIR and the associated modelling.

5.2 Parametric Study of the Spectra

Before any curve fitting is conducted, a study is carried out to look at how each input variable for the calculation of the spectral radiance in NEQAIR can influence the shape of the spectral radiance curve. The parameters which can influence the spectral radiance curve is the rotational temperature, vibrational temperature, carbon dioxide number density and carbon monoxide number density. The other parameters – translational temperature and electronic temperature – do not change the magnitude and shape of the spectral radiance curve, for both the 2.7 and 4.3 μm band.

The range of parameters conducted for the parametric study is shown in Table 5.1. The range of parameters is selected based on predictions of the CO₂ flow encountered in the current experiments. More specifically, based on the work in chapter 3, the temperature of the freestream should be between 1000 K to 2000 K and the carbon dioxide number density of the freestream should be between, approximately, $1 \times 10^{15} \text{ cm}^{-3}$ and $1 \times 10^{16} \text{ cm}^{-3}$. Based on the work in chapter 6, in the flow around the wedge, the temperature of the gas should be between 2000 K to 7000 K and the carbon dioxide number density should be between $1 \times 10^{16} \text{ cm}^{-3}$ and $1 \times 10^{17} \text{ cm}^{-3}$. The amount of CO relative to CO₂ should range from less than 30 % in the freestream to up to around 100 % in the flow around the wedge. In addition, the line of sight length used in the parametric study is a representative value for the actual line of sight length measured in the emission spectroscopy experiments and this is discussed further in section 6.4.

Table 5.1. Range of parameters investigated for the parametric study.

Temperature / K	CO ₂ number density / cm ⁻³	CO ₂ to CO number density ratio	Line of sight length
1000 - 7000	$1 \times 10^{15} - 1 \times 10^{17}$	1:0 – 1:1	125 mm

Figure 5.1 shows the numerical spectra for the 4.3 μm band. In the figure, the vibrational temperature is changed while the rotational temperature is kept constant. The left column shows the absolute spectra while the right column shows the normalized spectra (normalized at an arbitrary wavelength within the range of peaks for the corresponding temperature). From the figure, increasing the vibrational temperature decreases the magnitude of the peak. Increasing the vibrational temperature also increases the width of the band, by increasing the radiation emitted in the tail. Furthermore, in most cases, increasing the vibrational temperature shifts the peak of the spectrum towards the higher wavelength.

Similar to Figure 5.1, Figure 5.2 shows how the 4.3 μm band changes when the rotational temperature is changed while the vibrational temperature is kept constant. From the figure, increasing the rotational temperature always increases the magnitude of the peak of the band. At lower vibrational temperatures, increasing the rotational temperature shifts the peak of the band towards the higher wavelength and increases the width of the band by increasing the radiation emitted in the tail. However, at higher temperatures, changing the rotational temperature does not create a distinct shift to the spectral location of the peak of the band. In addition, at higher vibrational temperatures, changing the rotational temperature does not distinctly change the width of the band of the band. Nevertheless, at higher temperatures, changing the rotational temperature still causes distinct changes in the shape of the spectrum, which can be observed when examining the normalized spectrums.

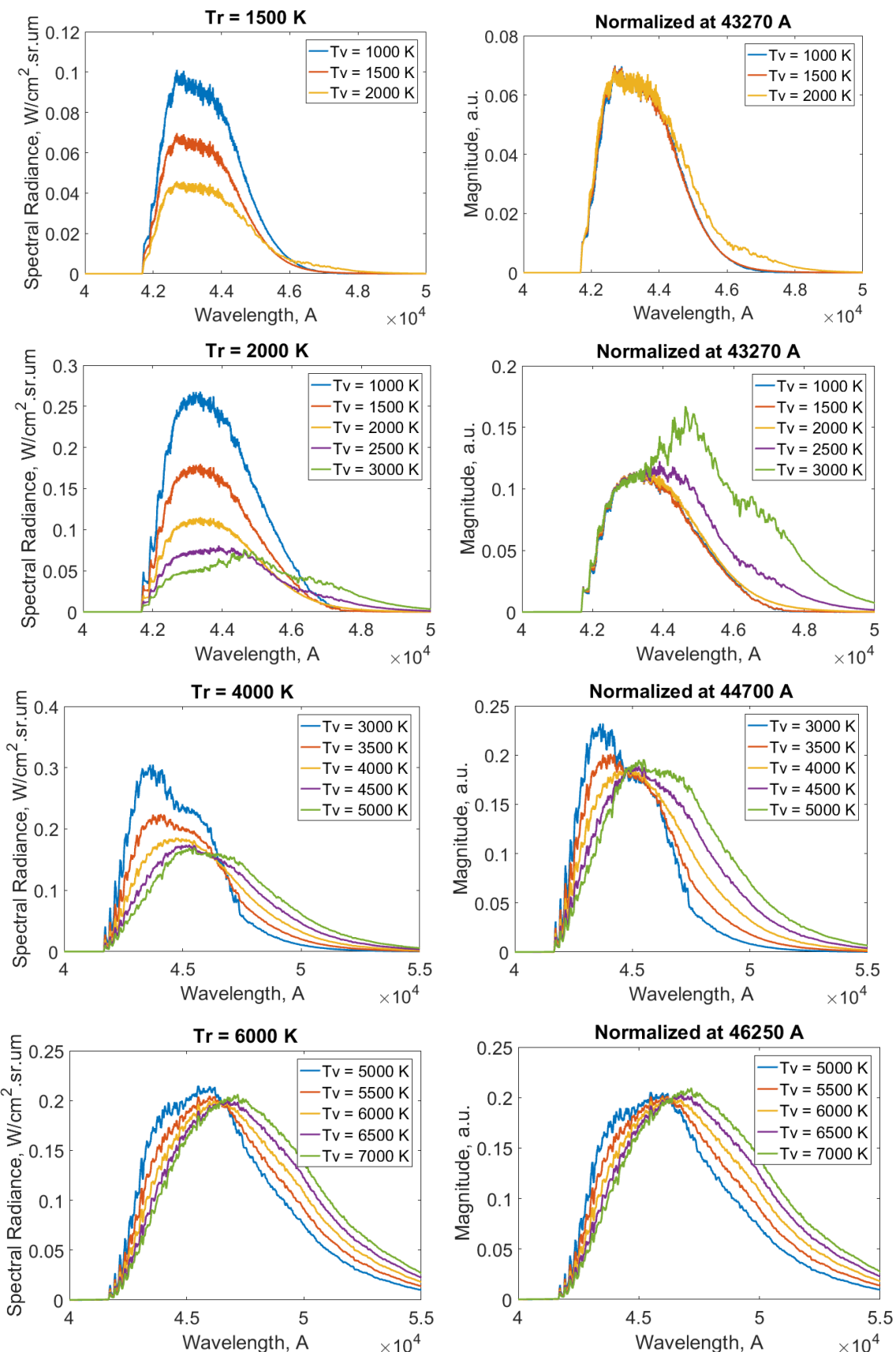


Figure 5.1. The effect of changing the vibrational temperature on the 4.3 μm spectral radiance curve. CO₂ number density is kept constant at $1 \times 10^{16} \text{ cm}^{-3}$. Absolute spectral radiance curves are plotted on the left column. Normalized spectral radiance curves are plotted on the right column.

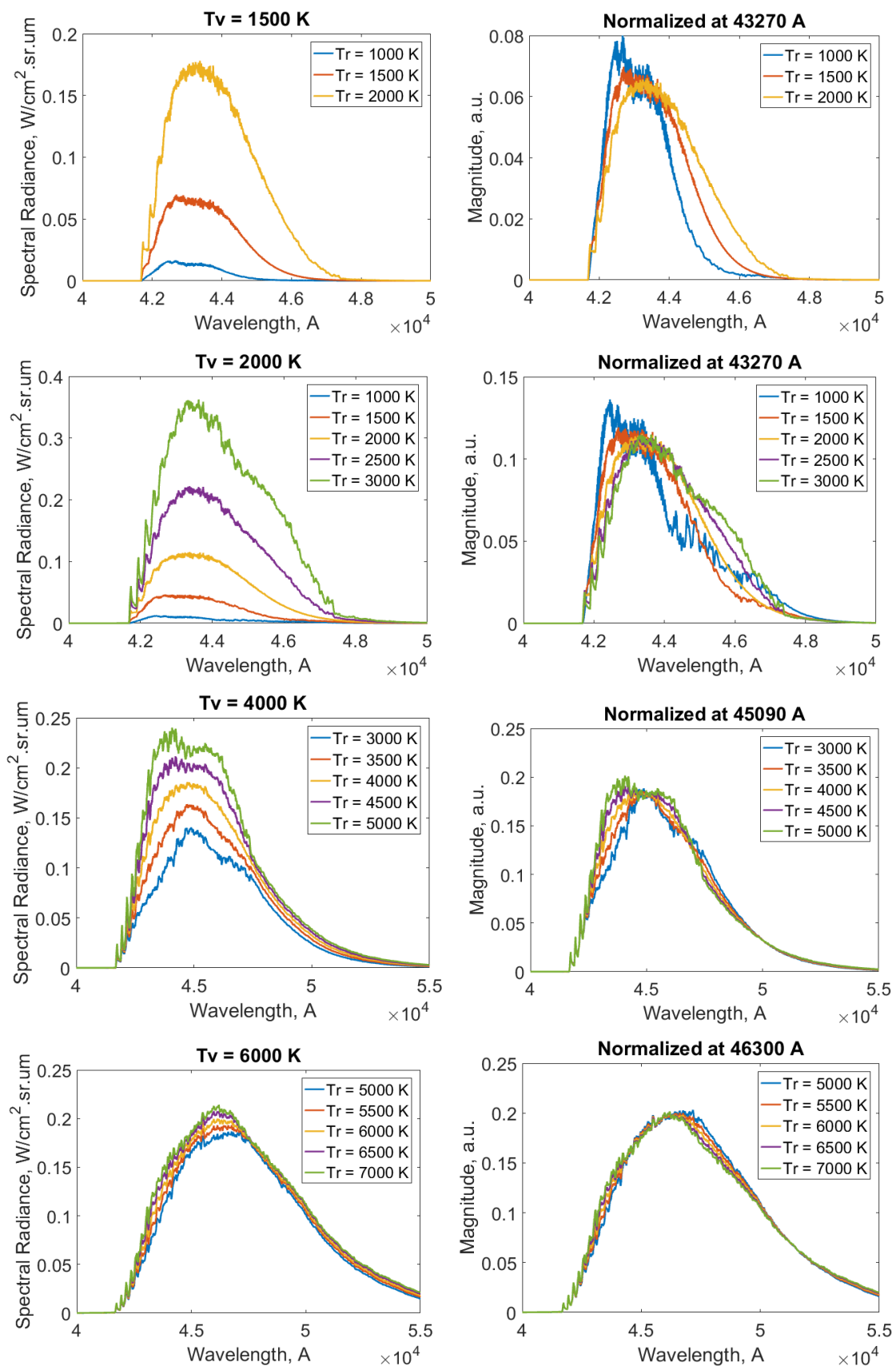


Figure 5.2. The effect of changing the rotational temperature on the 4.3 μm spectral radiance curve. Carbon dioxide number density is kept constant at $1 \times 10^{16} \text{ cm}^{-3}$. Absolute spectral radiance curves are plotted on the graphs on the left column. Normalized spectral radiance curves are plotted on the graphs on the right column.

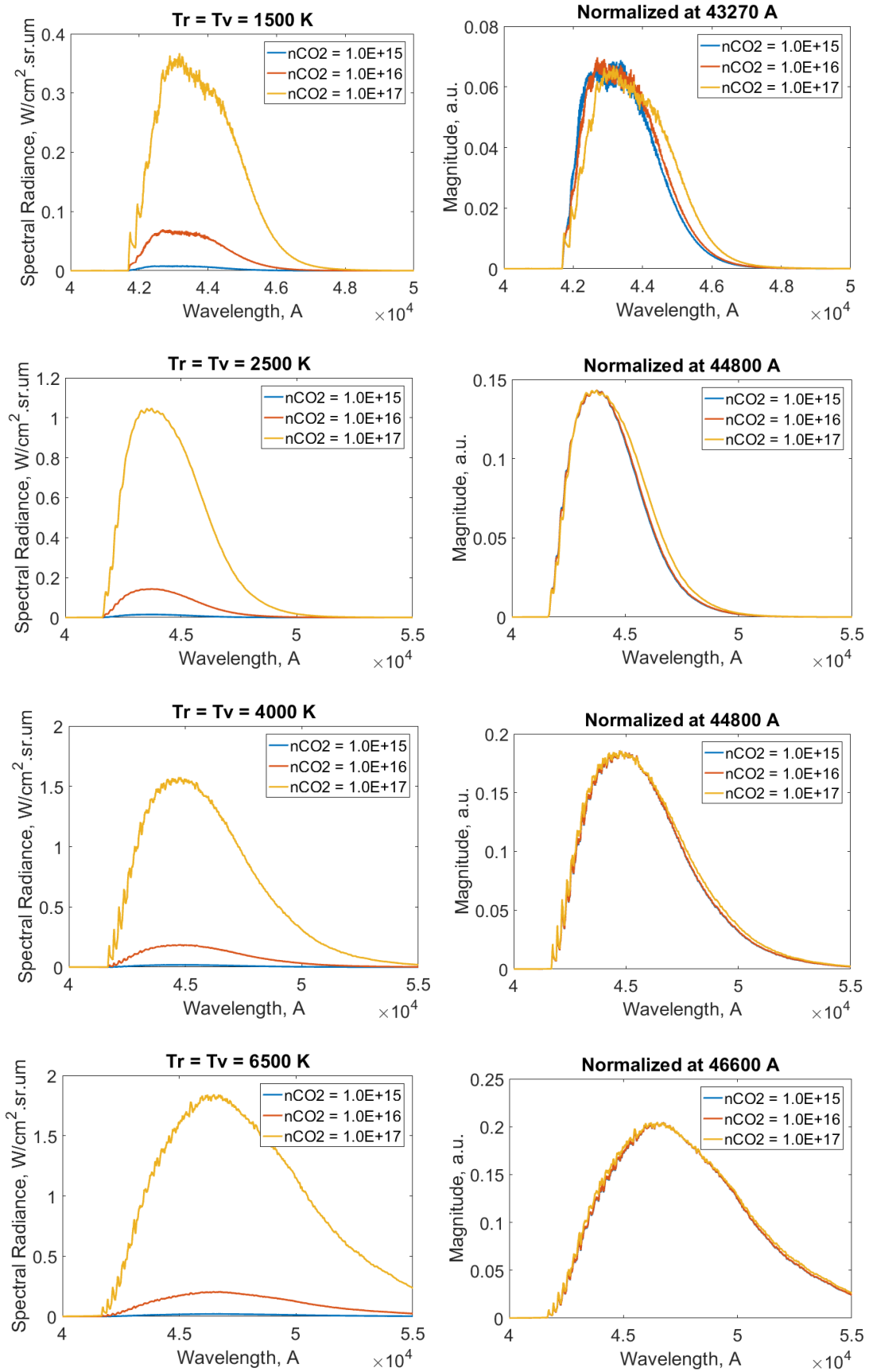


Figure 5.3. The effect of changing the carbon dioxide number density (cm^{-3}) on the $4.3 \mu\text{m}$ spectral radiance curve. Absolute spectral radiance curves are plotted on the graphs on the left column. Normalized spectral radiance curves are plotted on the graphs on the right column.

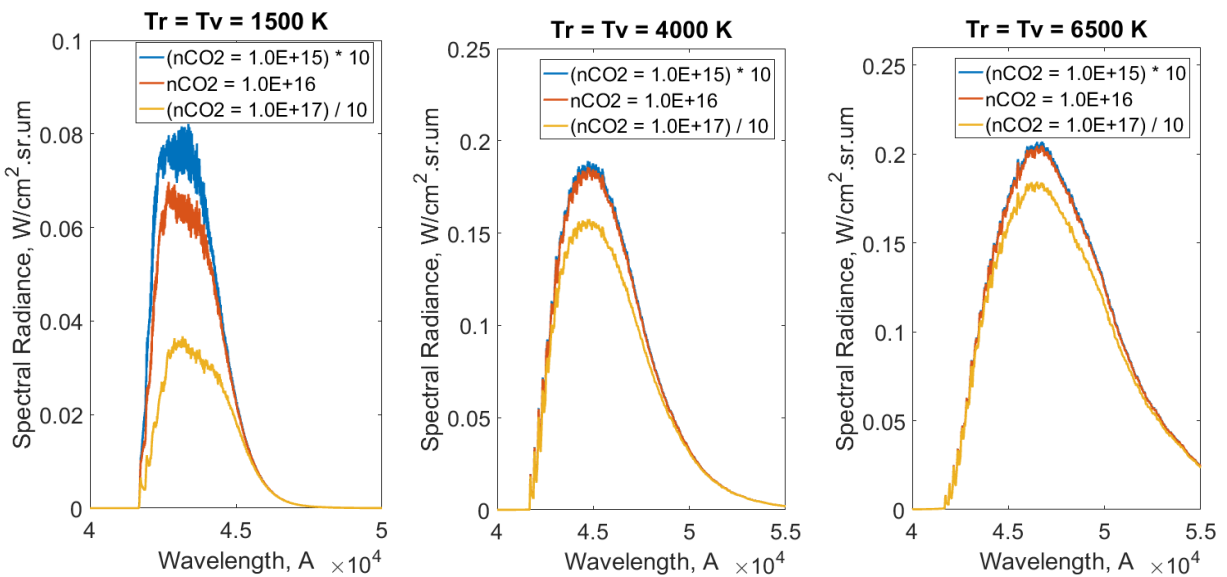


Figure 5.4. The significance of self-absorption at various temperatures and carbon dioxide number densities. The $4.3 \mu\text{m}$ spectral radiance curves are scaled with the carbon dioxide number density of $1 \times 10^{16} \text{ cm}^{-3}$.

Figure 5.3 shows how the $4.3 \mu\text{m}$ band changes when the CO_2 number density is changed while the temperatures remain constant. From the figure, the influence of the CO_2 number density is to scale the spectrum by a constant scaling factor. The exception to this is at conditions where the temperature is low, around 1500 K, and carbon dioxide number density is high, around $1 \times 10^{17} \text{ cm}^{-3}$. However, such a condition is not believed to exist in the current work. Consequently, the temperatures can be determined independently of the CO_2 number density by using scaled spectral radiance curves to perform the spectral fitting. However, from Figure 5.4 which shows the linear scaling of the $4.3 \mu\text{m}$ band by the CO_2 number density, the $4.3 \mu\text{m}$ spectra do not scale with CO_2 number density ratios in most cases. This means that the CO_2 number density in most cases cannot be estimated directly from linear scaling of the spectral curve. This is because, in most cases, self-absorption occurs. The results in Figure 5.4 indicate that the condition must be at higher temperatures, greater than 4000 K, and lower CO_2 number densities, less than $1 \times 10^{16} \text{ cm}^{-3}$, in order to be optically thin; such conditions should not be seen in the present work. Therefore, the $4.3 \mu\text{m}$ band is generally optically thick for the conditions concerned in this work.

As mentioned before, CO molecules can effectively influence the $4.3 \mu\text{m}$ band measurements. Figure 5.5 shows how the $4.3 \mu\text{m}$ band changes when the CO number density is changed, while the temperatures remain constant. From the figure, at lower temperatures around 1500 K, the CO number density has no influence on the $4.3 \mu\text{m}$ band. However, at higher temperatures, the influence of CO number density on the shape of the $4.3 \mu\text{m}$ band is to scale the spectrum by a constant scaling factor. Consequently, as both the CO_2 and CO cause the same effect on the shape of the spectral curve, there

is no unique solution for the number density of these two species when doing spectral fitting. Therefore, a ratio of CO₂ to CO needs to be assumed to estimate the CO₂ number density.

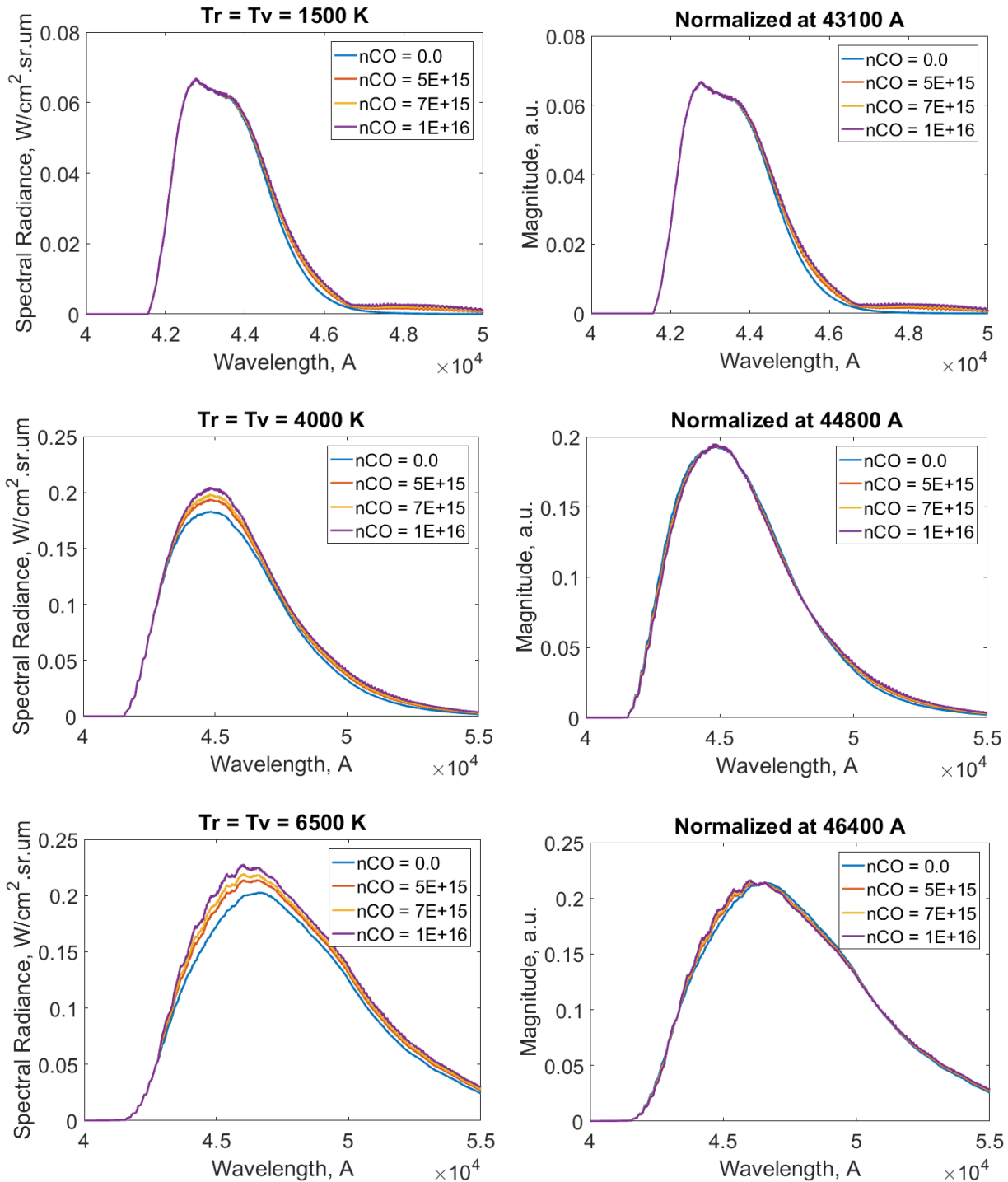


Figure 5.5. The effect of carbon monoxide number density (cm^{-3}) on the $4.3 \mu\text{m}$ spectral radiance curve. Carbon dioxide number density is kept constant at $1 \times 10^{16} \text{ cm}^{-3}$. Absolute spectral radiance curves are plotted on the graphs on the left column. Normalized spectral radiance curves are plotted on the graphs on the right column.

From the observations in Figure 5.1 to Figure 5.5, the methodology for performing the spectral fitting for the $4.3 \mu\text{m}$ band is to first estimate the rotational and vibration temperatures. The temperatures can be estimated independently of number density. The temperatures are estimated by finding the

best fit spectrum by comparing normalized spectra. Once the temperatures are estimated, spectral fitting using absolute spectra is conducted to estimate the CO₂ number densities. As there are no unique solutions for the number densities of CO₂ and CO, the CO₂ number densities are estimated with uncertainties determined from the bounds of the ratio of CO₂ number density to CO number density shown in Table 5.1.

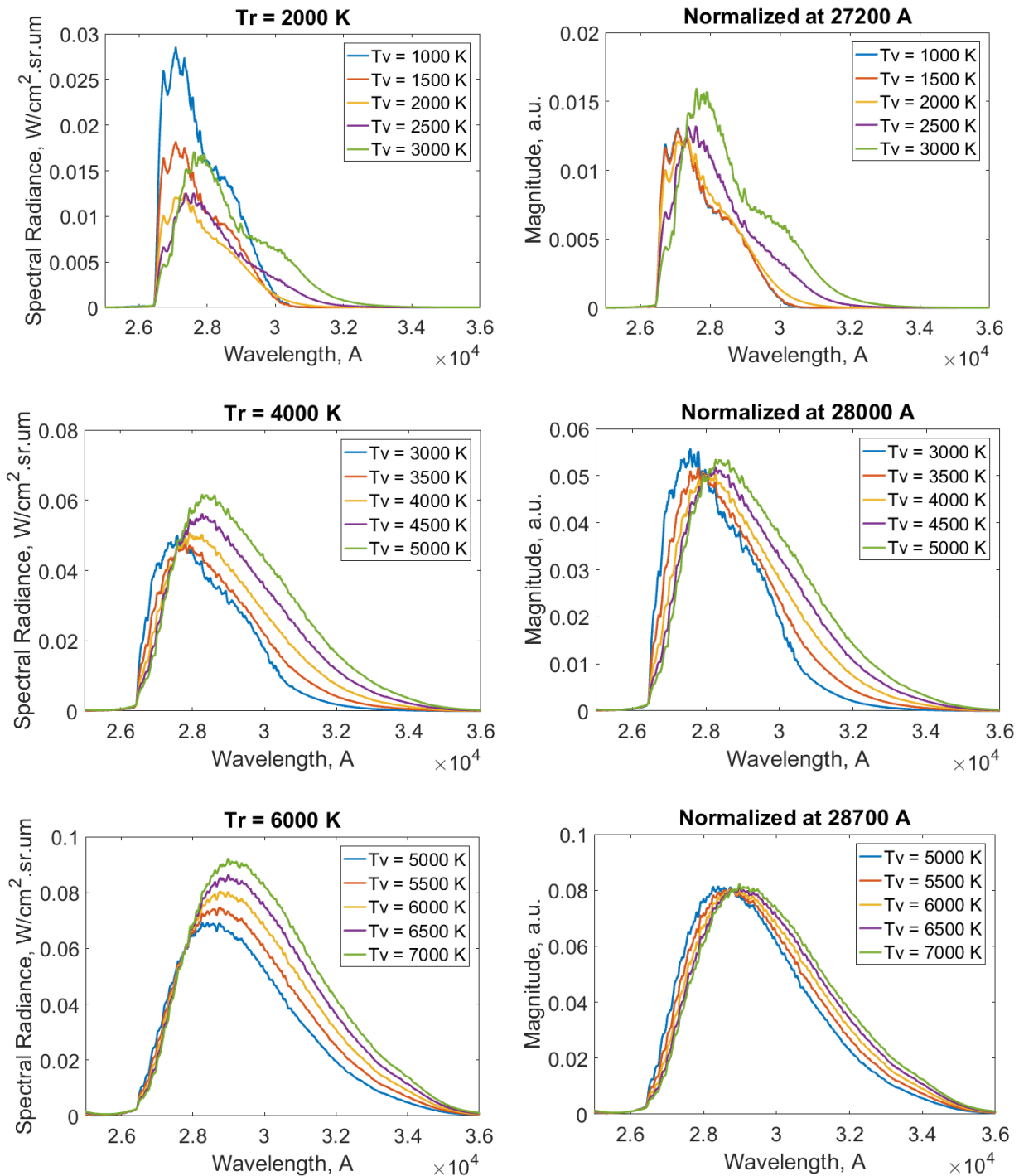


Figure 5.6. The effect of changing the vibrational temperature on the 2.7 μm spectral radiance curve. Carbon dioxide number density is kept constant at $1 \times 10^{16} \text{ cm}^{-3}$. Absolute spectral radiance curves are plotted on the graphs on the left column. Normalized spectral radiance curves are plotted on the graphs on the right column.

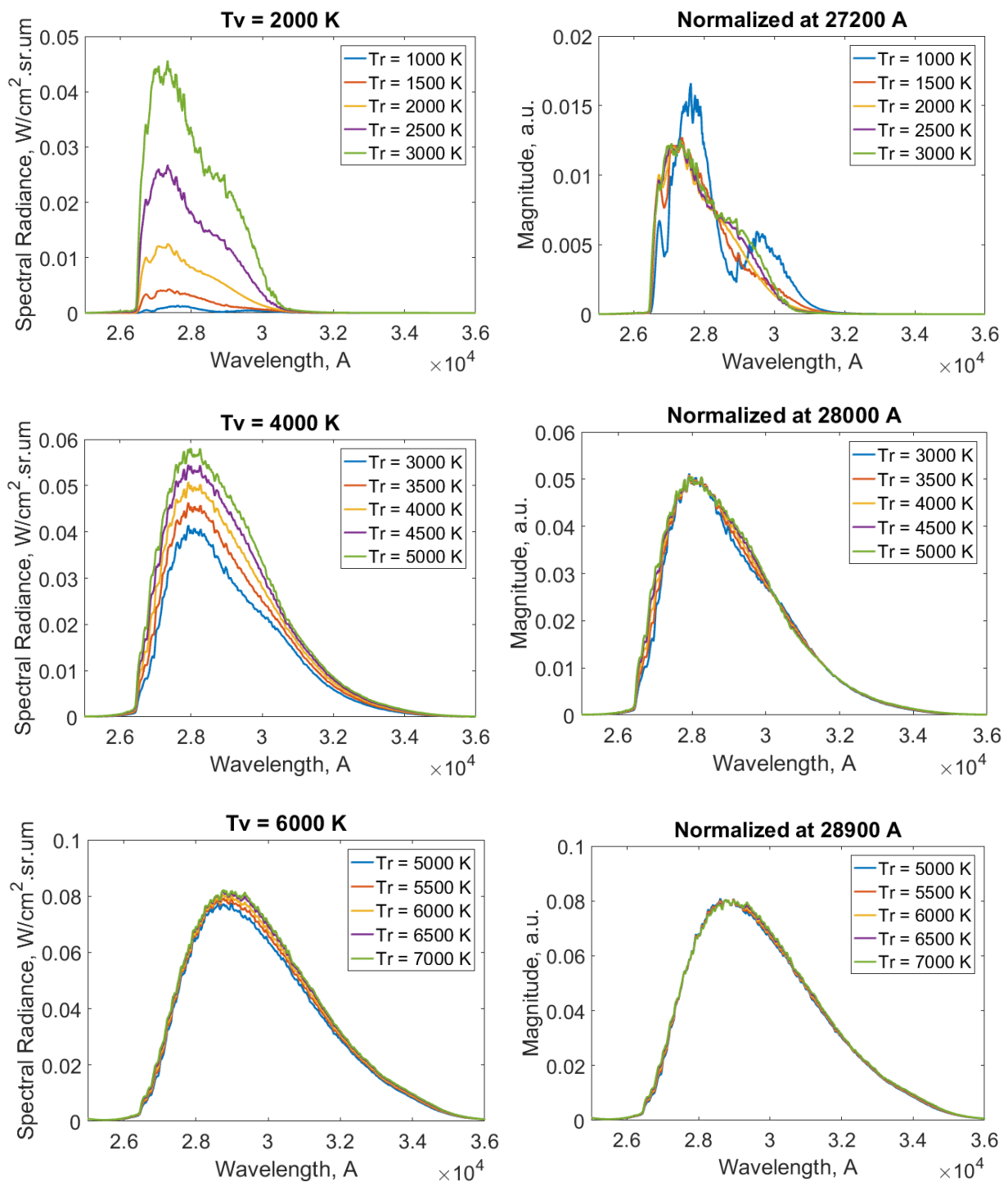


Figure 5.7. The effect of changing the rotational temperature on the $2.7 \mu\text{m}$ spectral radiance curve. Carbon dioxide number density is kept constant at $1 \times 10^{16} \text{ cm}^{-3}$. Absolute spectral radiance curves are plotted on the graphs on the left column. Normalized spectral radiance curves are plotted on the graphs on the right column.

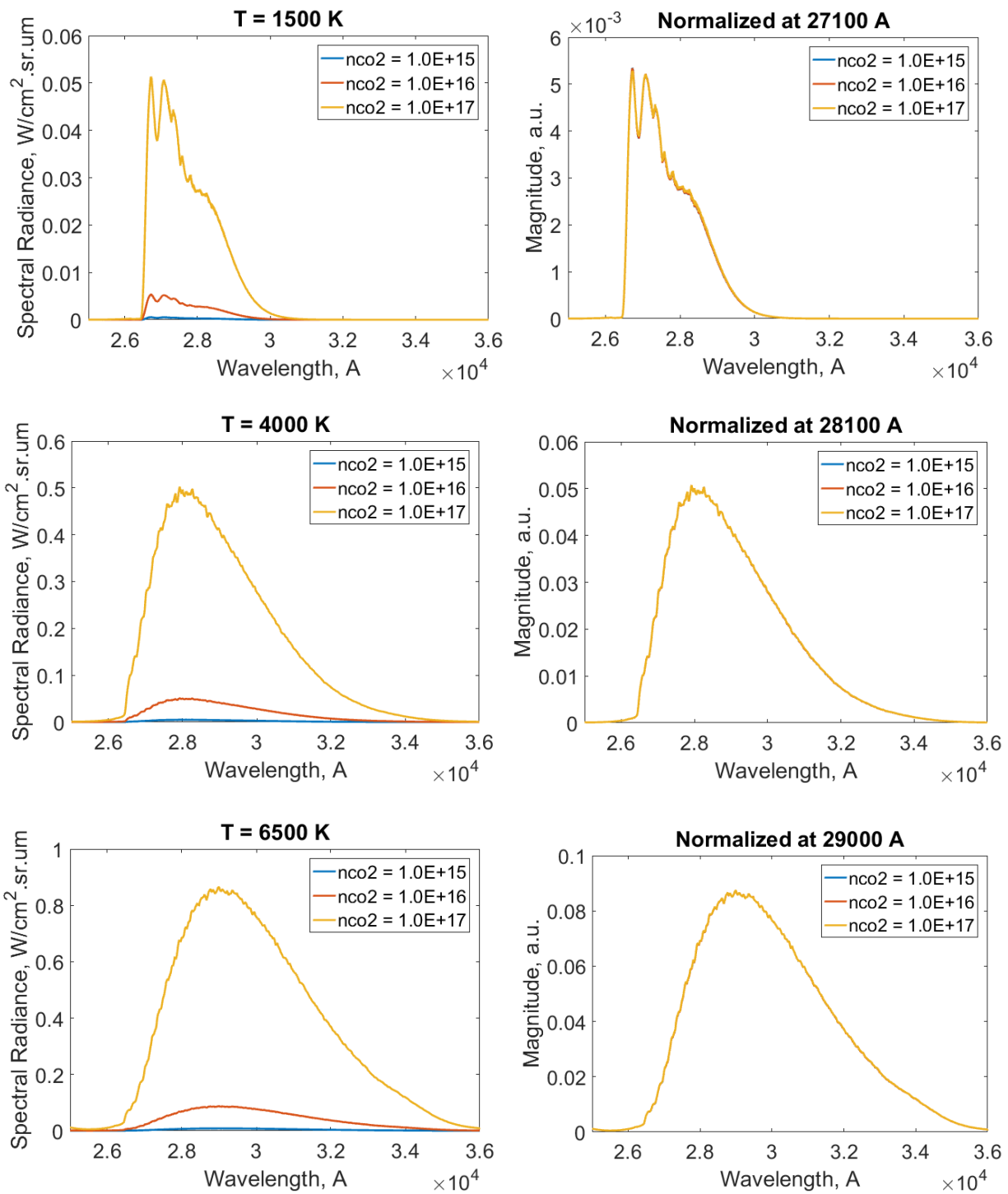


Figure 5.8. The effect of changing the carbon dioxide number density (cm^{-3}) on the $2.7 \mu\text{m}$ spectral radiance curve. Absolute spectral radiance curves are plotted on the graphs on the left column. Normalized spectral radiance curves are plotted on the graphs on the right column.

Figure 5.6 shows how the $2.7 \mu\text{m}$ band changes when the vibrational temperature is changed while the rotational temperature is kept constant. From the figure, the influence of the vibrational temperature on the $2.7 \mu\text{m}$ band is seen to be more complex than that on the $4.3 \mu\text{m}$ band. The way the magnitude of the peak of the band varies depends on whether the vibrational temperature is greater than or less than the rotational temperature. In most cases, if the vibrational temperature is greater

than the rotational temperature, increasing the vibrational temperature increases the magnitude of the peak of the band. On the other hand, in most cases, if the vibrational temperature is less than the rotational temperature, the increasing vibrational temperature decreases the magnitude of the peak of the band. The exception to this is at high temperatures, round 6000 K, when increasing the vibrational temperature increases the magnitude of the peak of the spectrum even when the vibrational temperature is less than the rotational temperature. Nevertheless, in all the cases studied, increasing the vibrational temperature always increases the width of the band by increasing the radiation emitted in the tail and shifts the location of the peak towards the higher wavelength. Figure 5.7 shows how the 2.7 μm band changes when the rotational temperature is changed while the vibrational temperature is kept constant. From the figure, increasing the rotational temperature always increases the magnitude of the peak of the spectrum. In general, changing the rotational temperature does not shift the location of the peak of the spectrum on the wavelength axis. In addition, in most cases, increasing the rotational temperature does not change the band width of the spectrum. The exception to this occurs at low temperatures, around 2000 K. Compared to the 4.3 μm band, the normalized shape of the 2.7 μm band does not change as significantly when changing the rotational temperature. This is particularly the case at higher temperatures, such as temperatures greater than 4000 K.

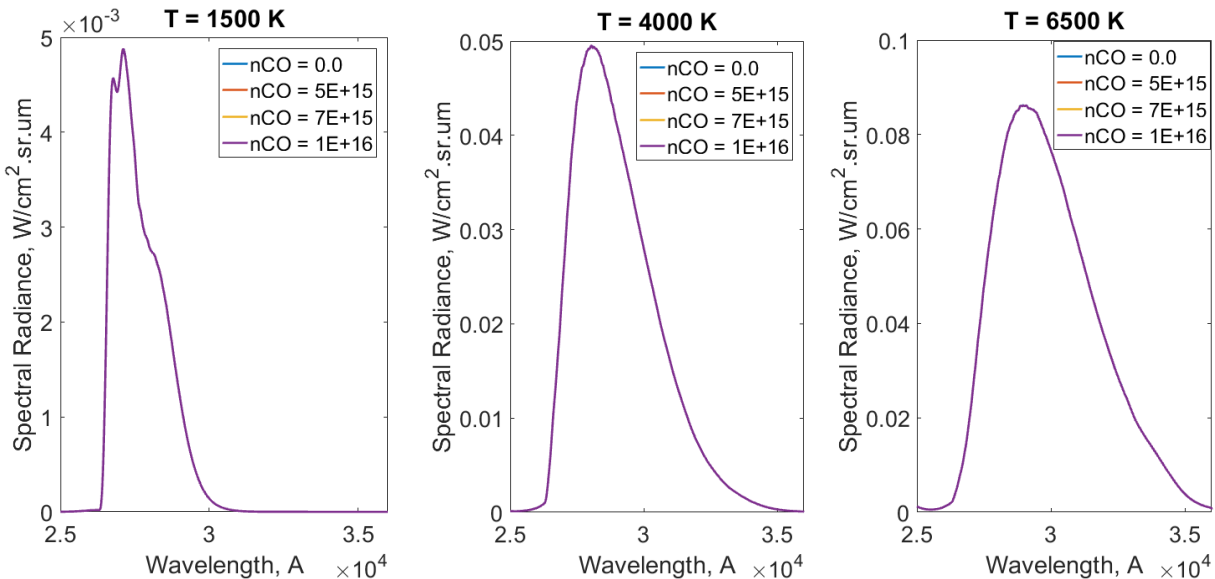


Figure 5.9. The effect of carbon monoxide number density (cm^{-3}) on the absolute 2.7 μm spectral radiance curve. Carbon dioxide number density is kept constant at $1 \times 10^{16} \text{ cm}^{-3}$.

Figure 5.8 shows how the 2.7 μm band changes when the CO₂ number density is changed while the temperatures remain constant. From the figure, like for the 4.3 μm band, the influence of the CO₂ number density is to scale the spectrum by a constant scaling factor. Thus, the temperatures can be determined independently of the CO₂ number density. In addition, from Figure 5.9 which shows how the 2.7 μm band changes when the CO number density is changed, the CO number density was found

to have no influence on both the shape and the absolute value of the 2.7 μm spectrum. Consequently, unlike for the 4.3 μm band, unique solutions can be determined for the CO₂ number density using the 2.7 μm band without needing to assume a ratio of CO₂ to CO. Furthermore, from Figure 5.10 which shows the linear scaling of the 2.7 μm band by the CO₂ number density, the spectral curve scales directly with the CO₂ number density. Hence, for the conditions in the current work, the 2.7 μm band is optically thin.

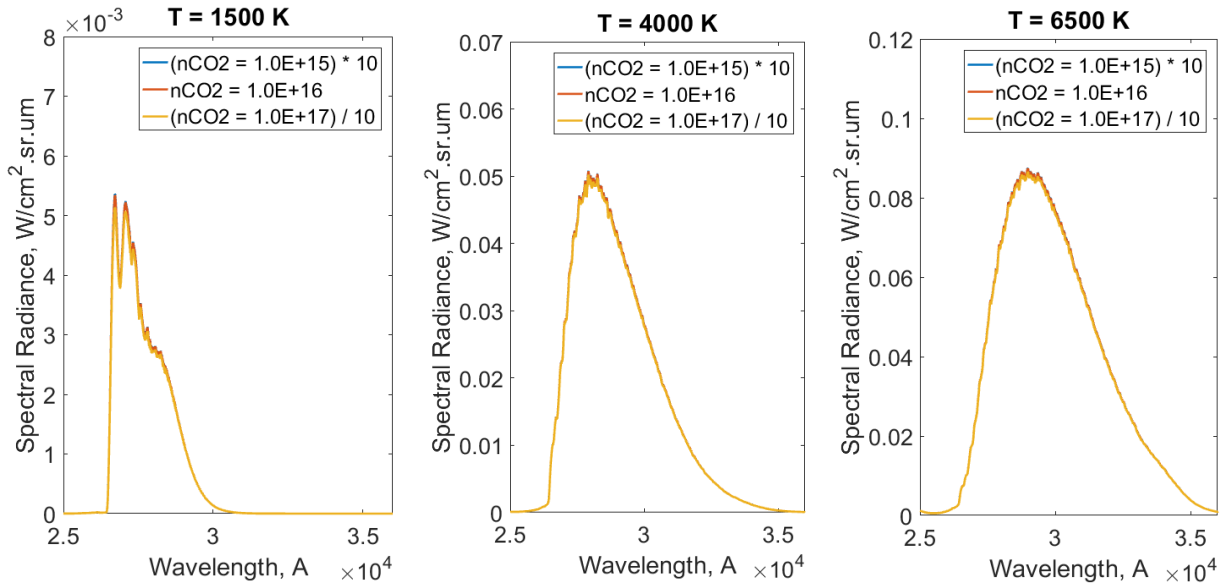


Figure 5.10. The significance of self-absorption at various temperatures and carbon dioxide number densities. The spectral radiance curves are scaled with the carbon dioxide number density of $1 \times 10^{16} \text{ cm}^{-3}$.

From the observations in Figure 5.6 to Figure 5.10, the methodology for performing the spectral fitting for the 2.7 μm band is to first estimate the rotational and vibration temperatures. The temperatures can be estimated independently of number density. The temperatures are estimated by finding the best fit spectrum by comparing normalized spectrums. Once the temperatures are estimated, the CO₂ number density is then determined directly from the scaling of the spectral radiance curves.

5.3 Nozzle Exit Freestream Results

For correct interpretation of the experimental results, it is important to accurately estimate the freestream flow properties for each condition. As presented in section 3.4, prior work has been done on this using the PITOT code. To support the work carried out in section 3.4, emission spectroscopy of the expansion tube freestream was carried out. The measurement is taken looking through the centre of the core flow. The spectroscopic measurements allow for an estimate of the rotational

temperature, vibrational temperature and carbon dioxide number density in the freestream. Measurements of the $4.3 \mu\text{m}$ band were taken and the spectral fitting method discussed in section 5.2 is used to estimate the temperature and carbon dioxide number density. The best fit curves were determined using the least squares technique. Carbon monoxide number density is assumed to be zero since there should be very little carbon monoxide in the freestream at these velocity conditions and any carbon monoxide will have minimal contribution to the radiation at temperatures around 1500 K, as shown on Figure 5.5. The core flow is assumed to have uniform properties with a diameter of 140 mm. The uncertainty for the rotational temperature, vibrational temperature and carbon dioxide number density is defined as fits with sum of squared residuals 5 % more than the sum of squared residuals of the best fit. The fitted spectra are presented in Figure 5.11 to Figure 5.13 and the deduced temperatures and number densities are presented in Table 5.2 to Table 5.4.

Firstly, the shot-to-shot variation of the estimated inflow properties from spectroscopic measurements are examined. Table 5.2 and Table 5.3 show the estimated freestream properties for the 2.8 and 3.4 km/s condition respectively. Noticeable variations are observed. The results show that the CO_2 number densities and vibrational temperature can vary by up to 30-40% (though the estimated vibrational temperature has large uncertainties). On the other hand, the variation of the rotational temperature is at most 15 %. Table 5.4 shows the estimated freestream properties from spectroscopic measurements for the 4.0 km/s condition. For the 4.0 km/s condition, the variation is less than 10 % for the freestream temperatures and number densities estimated from the spectroscopic measurements. Hence, the results show that the 4.0 km/s condition has noticeably smaller shot-to-shot variations compared to the 2.8 and 3.4 km/s conditions.

For the 2.8 and 3.4 km/s condition, the rather significant variation in the freestream CO_2 number density seen from the spectroscopic measurements is believed to be a main contributor to the shot-to-shot variation observed for the radiation of the flow around the wedge presented in section 4.2.6. This is because, although the freestream vibrational temperature has the larger shot-to-shot variation according to the spectroscopic measurements, the freestream CO_2 number density is a more sensitive variable to the flowfield radiation. Also, the PITOT code estimates support the belief that the CO_2 number density is responsible for a significant portion of the variation of the wedge flow as it shows that it is the inflow variable with the largest shot-to-shot variation. Nevertheless, the variation in the freestream CO_2 number density may not account for the entirety of the variation of the radiation around the wedge. Additional contribution to the variation of the radiation may be caused by possible variations in the freestream velocity because the radiation around the wedge is very sensitive to the freestream velocity.

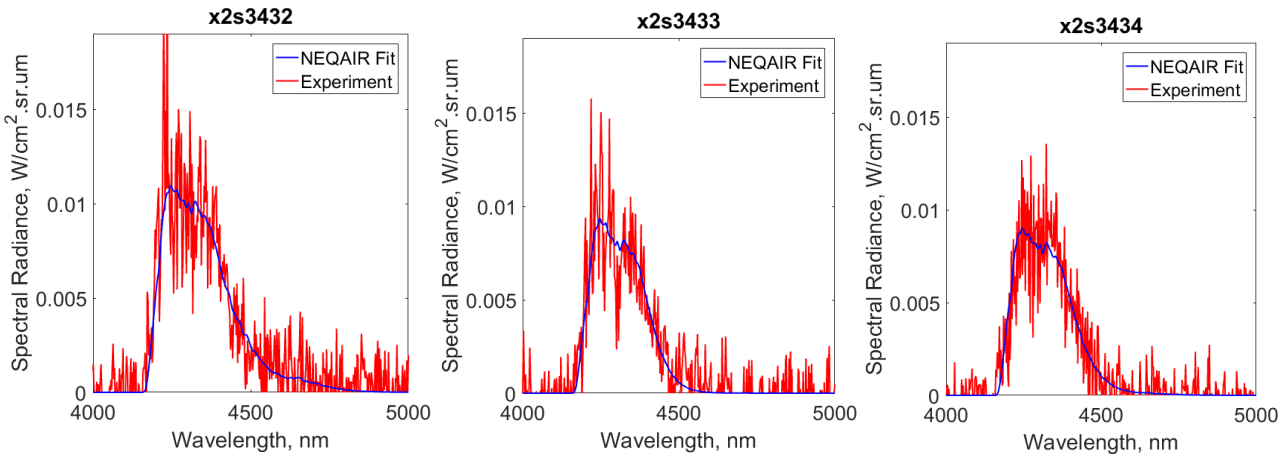


Figure 5.11. Spectral fitting showing the best least squares fit against the measured spectrum from the freestream (nozzle exit) of the 2.8 km/s condition.

Table 5.2. Comparison of the estimated temperatures and number densities from the spectroscopic measurement and the best estimate of the temperatures and number densities from the PITOT code for the 2.8 km/s condition at the nozzle exit.

Test	Tr (K)	Tv (K)	CO ₂ Number Density (cm ⁻³)	Freestream Pressure (Pa)
PITOT Code Estimates				
x2s2896	1170	2350	1.8×10^{16}	310
x2s2897	1264	2499	1.7×10^{16}	333
x2s2906	1191	2358	2.0×10^{16}	355
Spectroscopic Measurements				
x2s3432	1150 ± 100	1800 ± 250	$(4.7 \pm 0.5) \times 10^{15}$	81
x2s3433	1000 ± 100	1100 ± 250	$(3.9 \pm 0.5) \times 10^{15}$	58
x2s3434	1100 ± 100	1500 ± 250	$(3.4 \pm 0.5) \times 10^{15}$	56

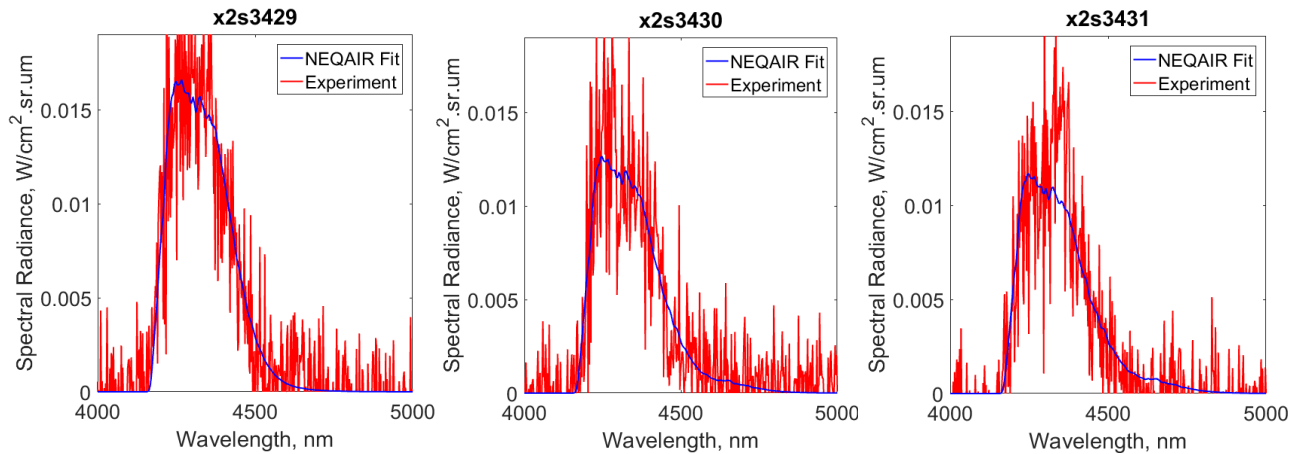


Figure 5.12. Spectral fitting showing the best least squares fit against the measured spectrum from the freestream (nozzle exit) of the 3.4 km/s condition.

Table 5.3. Comparison of the estimated temperatures and number densities from the spectroscopic measurement and the best estimate of the temperatures and number densities from the PITOT code for the 3.4 km/s condition at the nozzle exit.

Test	Tr (K)	Tv (K)	CO ₂ Number Density (cm ⁻³)	Freestream Pressure (Pa)
PITOT Code Estimates				
x2s2887	1370	2750	1.4 x 10 ¹⁶	347
x2s2890	1389	2757	1.5 x 10 ¹⁶	391
x2s2905	1378	2758	1.4 x 10 ¹⁶	360
Spectroscopic Measurements				
x2s3429	1250 ± 100	1400 ± 250	(3.8 ± 0.5) x 10 ¹⁵	86
x2s3430	1200 ± 100	1750 ± 250	(4.5 ± 0.5) x 10 ¹⁵	98
x2s3431	1200 ± 100	1800 ± 250	(4.3 ± 0.5) x 10 ¹⁵	93

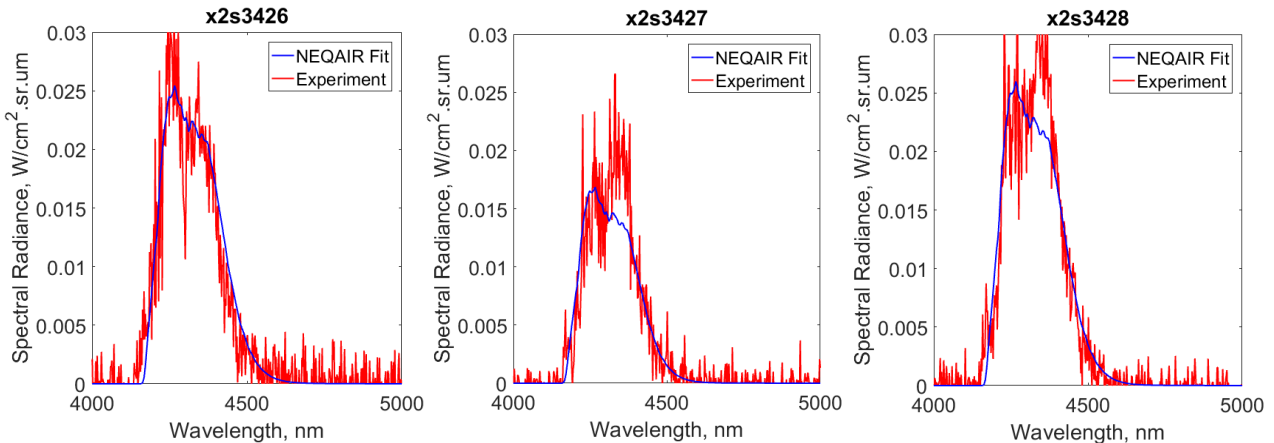


Figure 5.13. Spectral fitting showing the best least squares fit against the measured spectrum from the freestream (nozzle exit) of the 4.0 km/s condition.

Table 5.4. Comparison of the estimated temperatures and number densities from the spectroscopic measurement and the best estimate of the temperatures and number densities from the PITOT code for the 4.0 km/s condition at the nozzle exit.

Test	Tr (K)	Tv (K)	CO ₂ Number Density (cm ⁻³)	Freestream Pressure (Pa)
PITOT Code Estimates				
x2s2886	1289	2816	6.6 x 10 ¹⁵	161
x2s2892	1321	2818	8.3 x 10 ¹⁵	207
x2s2904	1281	2815	6.2 x 10 ¹⁵	150
Spectroscopic Measurements				
x2s3426	1150 ± 100	1200 ± 250	(7.4 ± 0.5) x 10 ¹⁵	161
x2s3427	1050 ± 100	1150 ± 250	(6.7 ± 0.5) x 10 ¹⁵	133
x2s3428	1150 ± 100	1150 ± 250	(7.3 ± 0.5) x 10 ¹⁵	159

Now, to assess the accuracy of the estimated freestream flow properties, the properties estimated using the PITOT code are compared to the properties estimated from the spectroscopic measurements. The estimated properties are all presented in Table 5.2, Table 5.3 and Table 5.4. The PITOT code estimates presented are taken from Table 3.12 and are determined from the average pitot pressures measured along the diameter of the core flow in the pitot survey experiments described in section 3.6. The freestream pressure for the estimates from the spectroscopic measurements is calculated using the average freestream CO₂ mole fraction from the PITOT code estimates. The average freestream CO₂ mole fraction is 0.90, 0.76 and 0.73 for the 2.8, 3.4 and 4.0 km/s condition respectively. The PITOT code estimates are produced using data from the pitot survey experiments previously presented in section 3.6.2 in Table 3.12. The PITOT code estimates are calculated assuming perfect gas for the unsteady expansion into the acceleration tube and the steady expansion through the nozzle, as discussed in section 3.4.4. In the PITOT code estimates, the vibrational temperature is assumed to be the equilibrium test gas temperature after being processed by the reflected shock at the secondary diaphragm; this corresponds to the upper bound of the vibrational energy in the test flow. The rotational temperature is assumed equal to the translational temperature at the nozzle exit.

Assuming that the rotational temperature and the translational temperature are equal, the estimated rotational temperature from the spectroscopic measurements match reasonably well with the PITOT code predictions for all three conditions; the estimated rotational temperatures from spectroscopy is slightly, but consistently, lower (100 – 200 K) than that predicted by the PITOT code. Furthermore, from the estimates made using the spectroscopic measurements, the rotational temperature is highest for the 3.4 km/s condition, followed by the 4.0 km/s condition. This is also consistent with the PITOT code predictions. The fact that the rotational temperature of the 3.4 km/s condition is higher than that of the 4.0 km/s is physically correct. This is because the process in generating the 3.4 km/s and 4.0 km/s conditions in the facility is identical prior to the unsteady expansion. The 4.0 km/s condition is expanded to a lower pressure therefore it must have a lower rotational temperature than the 3.4 km/s condition.

Examining the inflow thermal non-equilibrium, the estimated vibrational temperatures from spectroscopic measurements shows that the vibrational mode is generally at a higher energy state than the rotational mode. This result is consistent with the result in section 3.4.4 which showed that there is likely some excess thermochemical energy stored in the expansion tube freestream. However, the amount of frozen vibrational energy estimated from spectroscopy is significantly lower than that predicted in section 3.4.4. Using the PITOT code, the work in section 3.4.4 showed that assuming complete freezing of the thermochemical modes for the test gas during the expansions in generating the test conditions results in an inflow which better predicts the shock wave location

compared to assuming thermochemical equilibrium. However, the estimates from the spectroscopic measurements do not indicate this much frozen energy in the vibrational modes. The agreement between the computed shock wave location using the inflow estimated from the spectroscopic measurements and the measured shock wave location is assessed in section 6.5.1. Furthermore, from the spectroscopic measurements, the 4.0 km/s condition is shown to have the least non-equilibrium between the rotational and vibrational modes compared to the 2.8 and 3.4 km/s conditions. This is unexpected because, from section 3.4.4, the 4.0 km/s condition should have the most non-equilibrium since it is expanded to the lowest pressure and has the highest velocity. The reason for this observation is unknown. Nevertheless, it is important to mention that two of the measured 4.0 km/s condition spectra (x2s3427 and x2s3428) and one of the measured 3.4 km/s condition spectra (x2s3431) contain a spike feature at around 4.4 μm which cannot be replicated by NEQAIR simulations. It is a possibility that this feature is a consequence of complex thermal non-equilibrium effects. However, it is unclear why this feature is not always repeatable.

Examining the estimates of the CO₂ number density, the estimated CO₂ number density from spectroscopy compare well with the PITOT code predictions for the 4.0 km/s condition. However, the PITOT code predicted CO₂ number density for the 2.8 km/s and 3.4 km/s condition is significantly higher than the estimated value from the spectroscopic measurements. In fact, the estimated CO₂ number density from the spectroscopic measurement for the 2.8 km/s and 3.4 km/s condition is even lower than that for the 4.0 km/s condition. This result is supported by measurements of the inflow 4.3 μm band radiance (presented previously in Table 4.12 - Table 4.14) as well as measurements of the inflow using the mid-infrared sensor. These measurements showed that the freestream of the 4.0 km/s condition radiates the strongest, while the 2.8 km/s condition radiates the weakest. The temperature of the 2.8 km/s and 3.4 km/s condition is approximately equal to or greater than the temperature of the 4.0 km/s condition. Therefore, the fact that the 4.0 km/s condition has the strongest CO₂ emission indicates that the 4.0 km/s condition has the greatest CO₂ number density, as the conditions have similar core flow sizes (section 3.6.3).

The result from spectroscopy indicating that the 2.8 and 3.4 km/s inflows have lower CO₂ number densities than the 4.0 km/s inflow is unexpected. Using the inflow CO₂ mole fraction from the PITOT code, the inflow pressures corresponding to the inflow CO₂ number densities estimated from spectroscopy are calculated and shown in Table 5.2 to Table 5.4. From the spectroscopic measurements, as the estimated CO₂ number densities of the 2.8 and 3.4 km/s inflows are less than that of the 4.0 km/s inflow, the 2.8 and 3.4 km/s conditions duly have lower inflow pressures than that of the 4.0 km/s condition. However, from reasoning of the physical processes, the freestream pressure of the 2.8 km/s and 3.4 km/s condition should both be higher than the freestream pressure

of the 4.0 km/s condition. This is because the 4.0 km/s condition gets expanded to the lowest pressure during the unsteady expansion in the expansion tube. This reasoning is particularly valid when comparing the number density between the 3.4 km/s condition and the 4.0 km/s condition because the process involved in generating these two conditions are identical prior to the unsteady expansion.

Furthermore, the estimated number densities from the spectroscopic measurements do not allow for reconciliation with the measured pitot pressure for the 2.8 km/s and 3.4 km/s condition. The number densities estimated from the spectroscopic measurements is about a factor of 3 – 4 lower than that predicted by the PITOT code which is tuned based on the measured pitot pressure. The pressure measured by the flathead pitot probes is approximately equal to the product of freestream density and the square of the freestream velocity (impact pressure $\approx \rho U^2$) [125]. So, unless the actual freestream velocity is significantly higher, by a factor of approximately 1.5 – 2, than that predicted by the PITOT code, the CO₂ number density estimated from the spectroscopic measurements will not allow for consistency with the measured pitot pressure. However, the freestream velocity predicted by the PITOT code is unlikely to be incorrect by such a large degree as the predictions are made using the measured shock speeds. Since spectroscopic measurements concern the CO₂ density and pitot pressures concern the total density, the discrepancy between the CO₂ number densities estimated from the two different measurements indicate that there is a large difference between the CO₂ density and total density for the 2.8 and 3.4 km/s conditions.

The large difference between the CO₂ density and total density for the 2.8 and 3.4 km/s conditions is not believed to be caused by excessive CO₂ dissociation. The inflow CO₂ mole fractions used in this work already corresponds to the maximum possible CO₂ dissociation and assumes no recombination in the expansion tube. This upper limit of the amount of CO₂ dissociation is calculated based on using the measured primary shock speed and assuming the occurrence of a fully reflected shock at the secondary diaphragm and thermochemical equilibrium. Therefore, assuming even more CO₂ dissociation would not be physically consistent with the process of generating the test conditions.

Theoretically, the large difference between the deduced CO₂ density and total density for the 2.8 and 3.4 km/s conditions may be explained by complex non-Boltzmann distributions of the CO₂ vibrational modes. As the emission spectroscopy measurements are mainly influenced by vibrational states above ground state, having ground state populations not in thermal equilibrium with the other states may reconcile the deduced CO₂ density and total density. Furthermore, as the deduced CO₂ densities are obtained from measurements of the 4.3 μm band, which are caused by transitions in the v₃ asymmetric stretching mode, nonequilibrium between the different vibrational modes of CO₂ may also explain the density discrepancy.

Also, it is possible to reconcile the large difference between the CO₂ density and total density for the 2.8 and 3.4 km/s conditions if large amounts of contamination is assumed. Having small amounts of air contamination is common, but having large amounts of air contamination is unlikely. On the other hand, large amounts of helium contamination may be possible. Nevertheless, this still does not explain why the 2.8 km/s and 3.4 km/s inflows have lower CO₂ number densities than the 4.0 km/s inflow. In particular, the 3.4 km/s inflow should have a higher CO₂ number density than the 4.0 km/s inflow regardless of contamination. The only way to explain this is if the helium driver gas travelled downstream and displaced some of the CO₂ test gas, instead of just adding to the test gas. This would allow the 2.8 km/s and 3.4 km/s inflows to have lower CO₂ number densities but, at the same time, higher total densities compared to the 4.0 km/s inflow. Whether or not such a helium contamination process is physically possible in an expansion tube is unclear. Nevertheless, this idea is investigated further in section 5.5.

5.4 Wedge Flowfield Results

To investigate the radiative CO₂ expanding flow in detail, spectral fitting is performed for the emission spectroscopy measurements above the test model. This allows for an estimate of the rotational temperature, vibrational temperature and CO₂ number density at the measured locations in the wedge flowfield. Spectroscopic measurements of both the 4.3 μm band and 2.7 μm band were taken and the spectral fitting method discussed in section 5.2 is used to estimate the temperatures and CO₂ number densities from measurements of both the CO₂ bands.

It is noted that, due to significant edge effects, the length of the radiating lines of sight (width of the flowfield) measured in the spectroscopic measurements would vary in the downstream direction. This is discussed in detail in section 6.4. From spectral fitting, the temperatures can be estimated independently of the length of the radiating lines of sight. However, the estimate of the CO₂ number densities are dependent on the length of the radiating lines of sight and, therefore, estimates of this length were made using three-dimensional CFD simulations, discussed in detail in section 6.3. The CO₂ number densities were then deduced from spectral fitting using these estimated radiating path length values. A further consequence of significant edge effects is that the temperatures and number densities can vary along the measured lines of sight and, hence, values found here are likely a representative of the average along the lines of sight.

The best fit curves to the spectrum were determined using the least squares technique. Examples of fitted spectrums are presented in Figure 5.14. The experimental spectra are seen to be well fit by the numerical spectrums produced by the NEQAIR code. The 4.3 μm band measurements have minimal

noise and the mean absolute deviation of the data points from the best fit curve is typically only around $0.003 - 0.01 \text{ W/cm}^2 \cdot \text{sr} \cdot \mu\text{m}$ for this band.

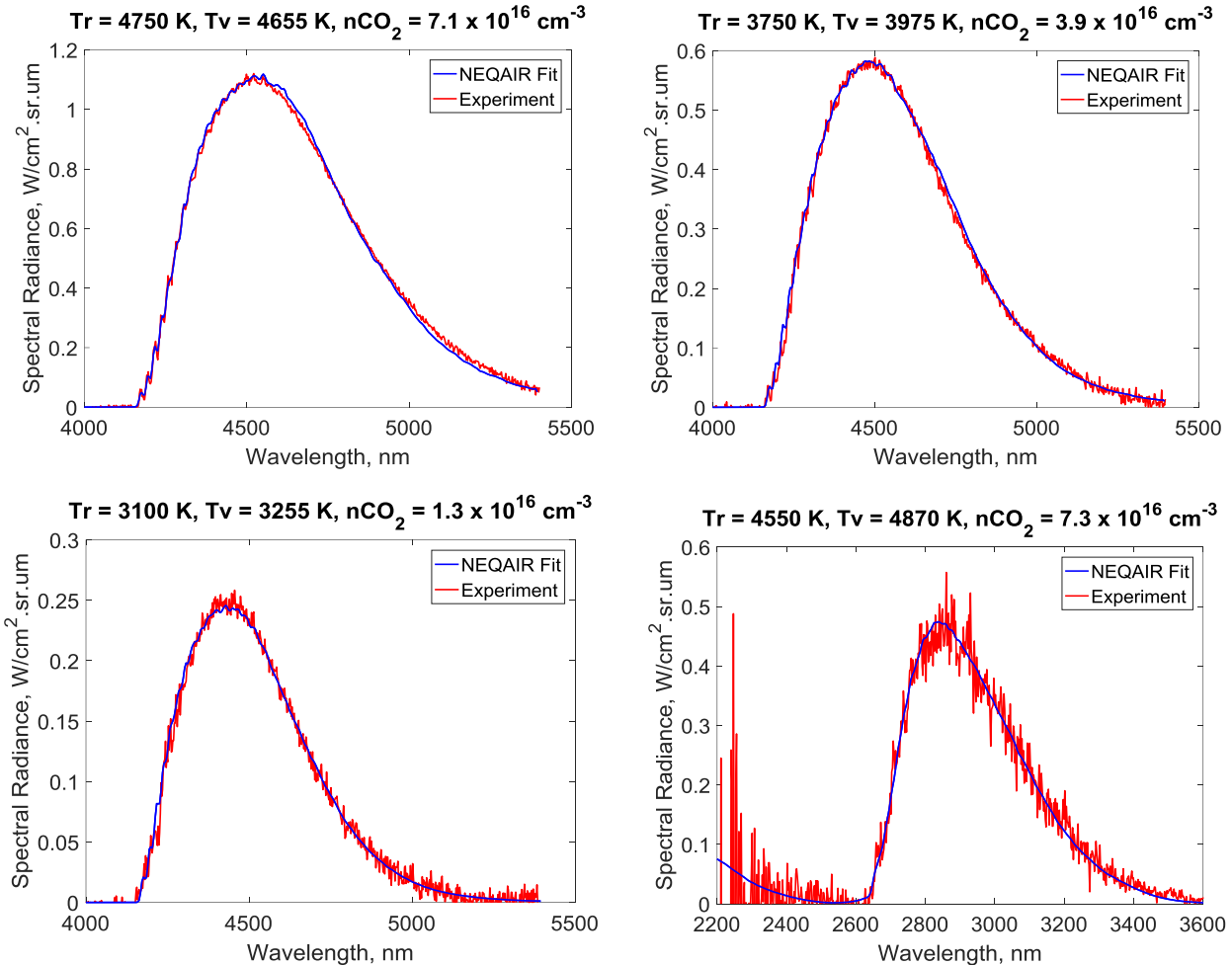


Figure 5.14. Examples of fitted spectrums. The bottom right graph shows an example of a fitted $2.7 \mu\text{m}$ band, while the others show fitted $4.3 \mu\text{m}$ bands.

The uncertainties for the rotational temperature, vibrational temperature and CO_2 number density are all defined as fits with sum of squared residuals 5 % more than the sum of squared residuals of the best fit. The exception is the CO_2 number density values deduced from the $4.3 \mu\text{m}$ band measurements. As discussed in section 5.2, the presence of CO can noticeably influence the absolute spectral radiance of the $4.3 \mu\text{m}$ band at higher temperatures. Hence, it is necessary to assume a relative mole fraction of CO_2 to CO in order to estimate the CO_2 number density. From CFD simulations, the bounds of the relative mole fraction in the flowfields are approximately $\text{CO}_2:\text{CO} = 1.0:0.0$ and $\text{CO}_2:\text{CO} = 0.4:0.6$. Therefore, the uncertainty for the CO_2 number density estimated from the $4.3 \mu\text{m}$ band is determined from fits with sum of squared residuals 5 % greater than the sum of squared residuals of the best fit using the bounds of the relative mole fraction.

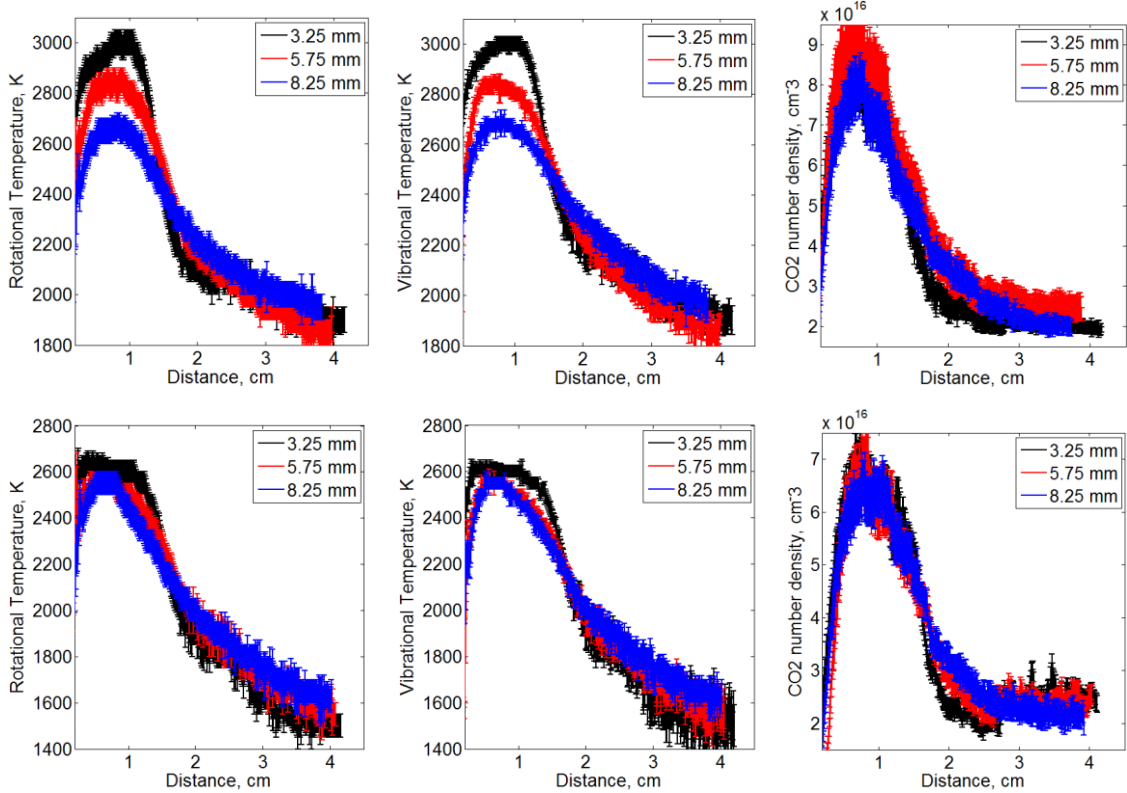


Figure 5.15. The estimated temperatures and carbon dioxide number densities for the 2.8 km/s condition. The top row corresponds to the upper bound measurements and the bottom row corresponds to the lower bound measurements.

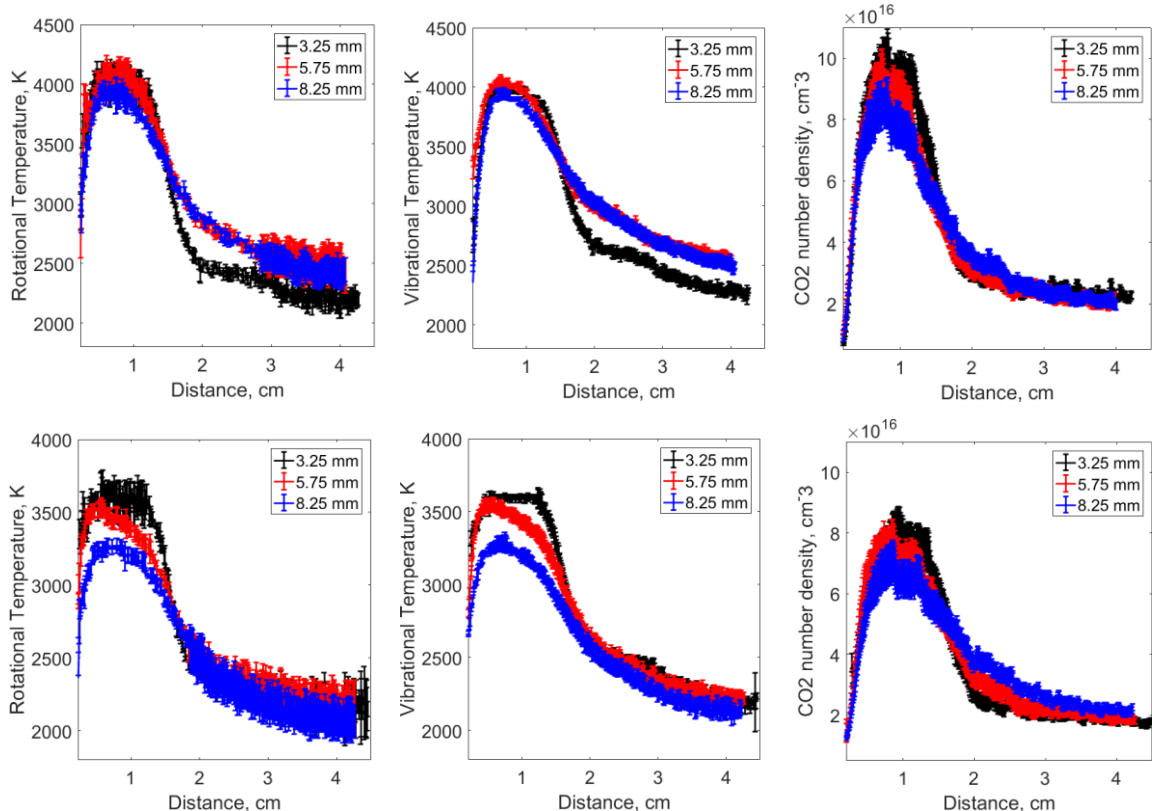


Figure 5.16. The estimated temperatures and carbon dioxide number densities for the 3.4 km/s condition. The top row corresponds to the upper bound measurements and the bottom row corresponds to the lower bound measurements.

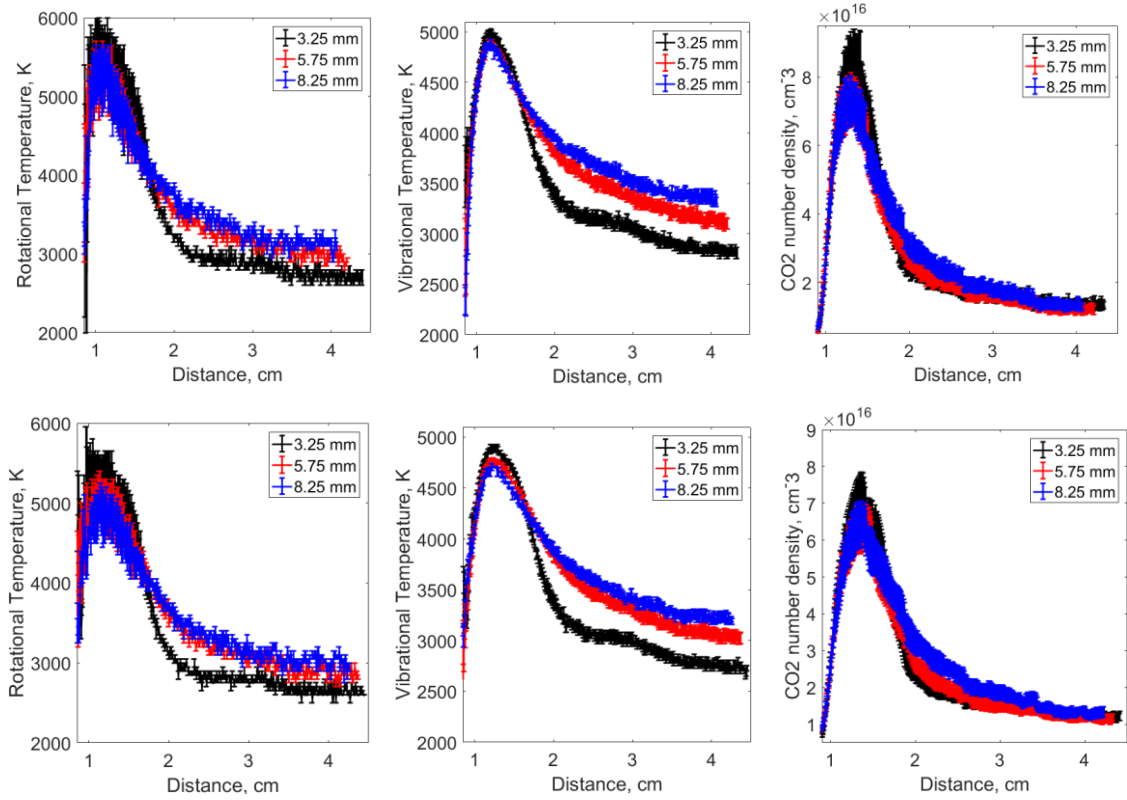


Figure 5.17. The estimated temperatures and carbon dioxide number densities for the 4.0 km/s condition. The top row corresponds to the upper bound measurements and the bottom row corresponds to the lower bound measurements.

Figure 5.15 to Figure 5.17 shows the measurements at different heights above the test model for each freestream condition. Each curve in the figures maintains the same shape as the band radiance curves, shown in Figure 4.27, and contains measurements in the shock layer and the expansion fan, through to the expanded flow region. The shot-to-shot variation for the 2.8 km/s and 3.4 km/s condition is large and can overshadow the changes due to the change in measurement height above the test model. Hence, the best way to conduct the comparison is to compare lower bound data with lower bound data and upper bound data with upper bound data, as mentioned in section 4.2.6.

In Figure 5.15 to Figure 5.17, the rate of expansion can be examined by looking at how rapidly the curve decreases from the peak towards the expanded region. For both the temperatures and the CO₂ number density, the largest rate of expansion is observed from the measurement at 3.25 mm above the test model in all conditions. On the other hand, the smallest rate of expansion is observed from the measurement at 8.25 mm above the test model in all conditions. This is an expected result as the rate of expansion decreases with increase in distance away from the convex corner. Also, the peak of the temperatures and the CO₂ number density profiles gets broader with decrease in height above the test model in all conditions. This is most noticeable in the temperature curves of the 2.8 km/s condition shown in Figure 5.15. This trend is due to the fact that the shock wave is closer to the expansion fan as the measurement is taken at higher locations above the test model. Consequently,

the measured post-shock region gets smaller at higher locations above the test model. Furthermore, for both the temperatures and the CO₂ number densities curves, the peak is seen to decrease with increase in measurement height above the test model for all conditions.

It is also interesting to compare how the temperatures and number densities vary, at constant heights above the test model, between different freestream conditions. This is presented in Figure 5.18 using the upper and lower bounds of each measurement. From the temperature curves, each test condition is seen to have its own distinct temperature profile, for all heights above the wedge; the bounds of each measurement do not overshadow the influence of the change in inflow condition. The region of the flow around the peak of the temperature profile is a representative of post-shock condition. The flow in this region corresponds to unexpanded flow or flow that is only beginning to expand, near the head of the expansion fan. This post-shock temperature seems to be particularly sensitive to the test condition. The most significant difference between the test conditions is the freestream velocity. Therefore, the freestream velocity is likely the main cause of the difference in flowfield temperature between the conditions. In the post-shock region from the 3.25 mm measurement, the temperature increased by about 1000 K from the 2.8 km/s condition to the 3.4 km/s condition and the temperature increased by about 1500 K from the 3.4 km/s condition to the 4.0 km/s condition. The trend of increasing post-shock temperature with increasing inflow velocity is physically valid. However, it is unclear if the magnitude of the changes to the flowfield temperatures are caused entirely by the changes to the inflow velocity; this is investigated further in section 5.5. The temperature profiles in Figure 5.18 also show that the temperature in the expanded flow region increase with increase in freestream velocity as well. This is because the temperature of the flow in the expanded region is dependent on the temperature of the flow entering the expansion fan. Since the temperature of the flow entering the expansion fan increases with increase in freestream velocity, the same trend is seen for the temperature in the expanded flow region.

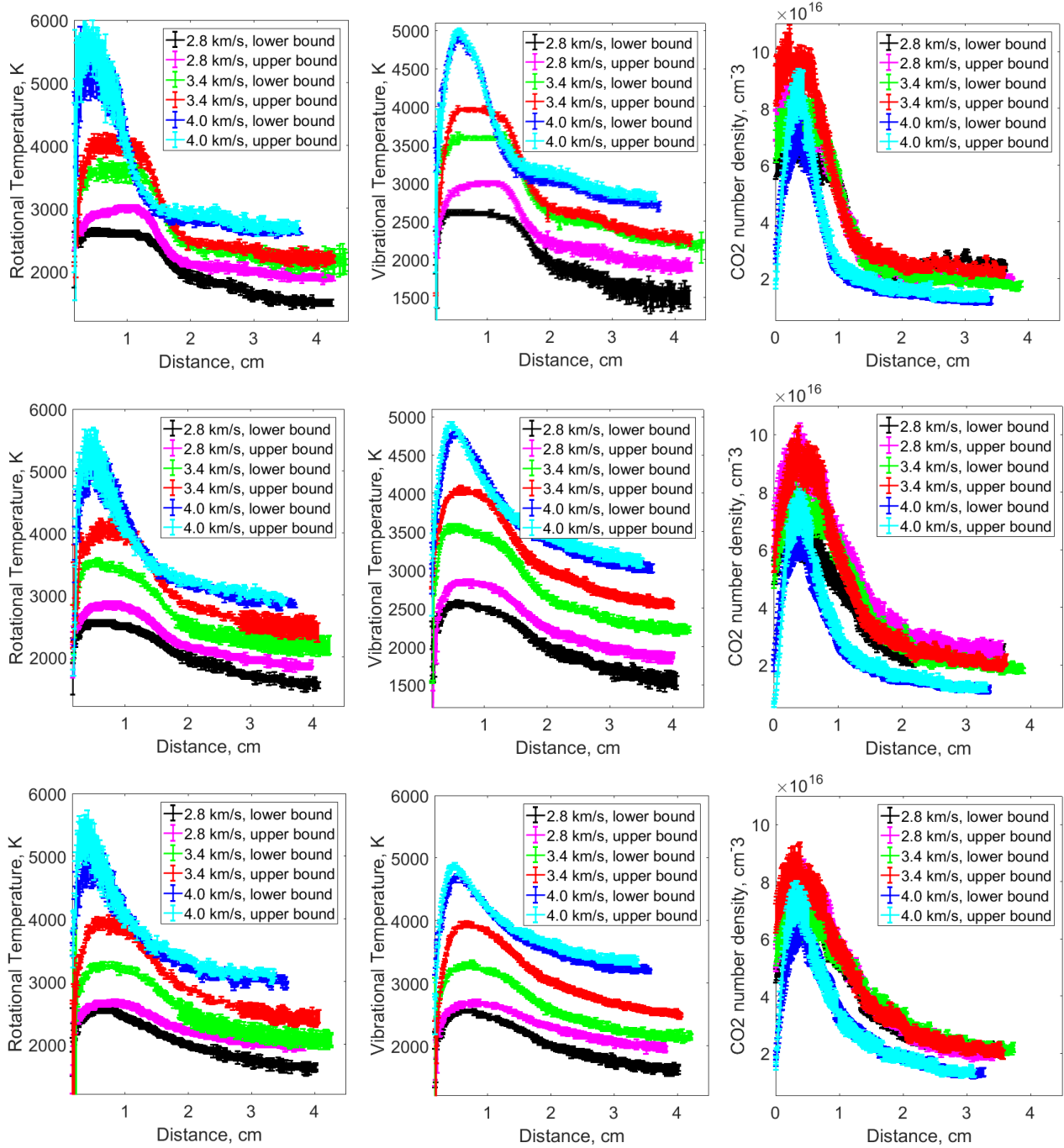


Figure 5.18. The measurements at 3.25 mm, 5.75 mm and 8.25 mm above the test model correspond to the top, middle and bottom row of plots respectively.

Table 5.5. Measured ratio of upstream to downstream temperature and CO₂ number density for the expansion fan, at 3.25 mm above the model.

Condition	CO ₂ Number Density Ratio (upstream/downstream)	Temperature Ratio (upstream/downstream)
2.8 km/s	3.5 ± 0.6	1.6 ± 0.1
3.4 km/s	4.4 ± 0.5	1.7 ± 0.1
4.0 km/s	6.2 ± 0.2	1.8 ± 0.1

When examining the CO₂ number density plots in Figure 5.18 for all heights above the test model, no obvious pattern can be observed when comparing between the different freestream conditions. This is because, in addition to the freestream velocity, the post-shock CO₂ number density is also highly dependent on the freestream CO₂ number density. It is also difficult to infer anything about the CO₂ recombination from the data in Figure 5.18. Nevertheless, a pattern which can be observed from Figure 5.18 is that the ratio of CO₂ number density upstream to downstream is largest for the 4.0 km/s condition and smallest for the 2.8 km/s condition, for all measurement heights. To check for consistency, the ratio of temperatures upstream to downstream of the expansion fan is also derived from the measurements for all three conditions. The results derived from the 3.25 mm above the model are summarized in Table 5.5. The trend seen from the temperature ratio of the different conditions is consistent with that of the CO₂ number density, although the trend observed from the temperature ratio is less distinct.

The trend seen in Table 5.5 is compared to calorically perfect gas calculations of a Prandtl-Meyer expansion fan. Assuming isentropic flow, the ratio of the temperature upstream to downstream, T_{ratio}, is given by

$$T_{ratio} = \frac{T_1}{T_2} = \left(\frac{1 + \frac{\gamma - 1}{2} M_1^2}{1 + \frac{\gamma - 1}{2} M_2^2} \right)^{-1} \quad 5.1$$

where T₁ is the temperature upstream, T₂ is the temperature downstream, M₁ is the Mach number upstream, M₂ is the Mach number downstream and γ is the specific heat capacity ratio. From the ideal gas equation of state (which is valid for high temperature and low density conditions concerned in this work), the ratio of the CO₂ number density, N_{ratio}, is equal to the ratio of the upstream P/T to downstream P/T. Thus, assuming isentropic flow, N_{ratio} is given by

$$N_{ratio} = \frac{\frac{P_1}{T_1}}{\frac{P_2}{T_2}} = \left(\frac{1 + \frac{\gamma - 1}{2} M_1^2}{1 + \frac{\gamma - 1}{2} M_2^2} \right)^{\frac{-1}{\gamma - 1}} \quad 5.2$$

The relationship between the Mach number upstream and Mach number downstream is given by

$$\theta = v(M_2) - v(M_1) \quad 5.3$$

where θ is the turn angle, which is 54 degrees for the current work and v(M) is the Prandtl-Meyer function. Equation 5.1 and 5.2 are plotted in Figure 5.19 for a range of upstream Mach numbers and specific heat capacity ratios. The result shows that the ratio of CO₂ number density upstream of the expansion fan to that downstream of the expansion fan generally increases with increase in upstream

Mach number. The ratio also increases with increase in specific heat capacity ratio, γ . From the perfect gas analysis, the ratio is more sensitive to γ than to the upstream Mach number. These same trends are also seen for the temperature ratio. Additionally, the calculations show that, for a given expansion, the temperature ratio is always smaller than the number density ratio and this is reflected in the measured results in Table 5.5.

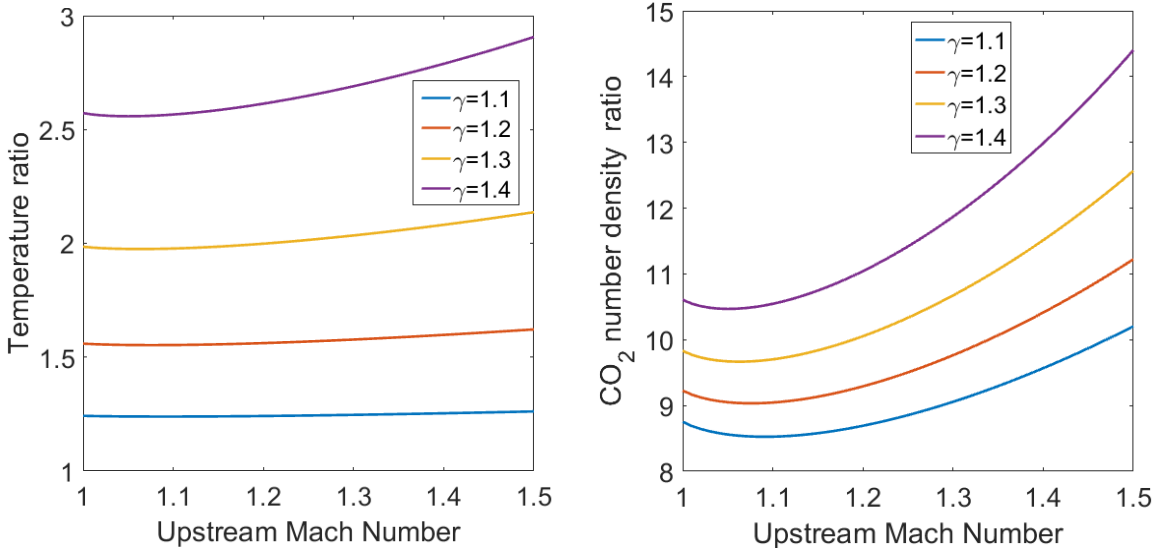


Figure 5.19. Calculated ratio of upstream to downstream temperature, left, and CO₂ number density, right, for the Prandtl-Meyer expansion fan assuming calorically perfect gas.

From the perfect gas Prandtl-Meyer expansion calculations, the reason the 4.0 km/s experiment was found to have the greatest temperature and number density ratio between upstream and downstream, shown in Table 5.5, could be because it has the highest post-shock Mach number and/or the highest post-shock specific heat capacity ratio, γ , compared to the other test conditions. However, it is more likely that the 4.0 km/s experiment has the highest post-shock Mach number rather than the highest post-shock γ . It seems unlikely that the 4.0 km/s condition could have the highest post-shock γ because it has the highest post-shock temperature which decreases γ . So unless the 4.0 km/s condition has significantly more dissociation, which increases γ , the post-shock γ should not be highest in the 4.0 km/s condition compared to the other test conditions. On the other hand, because the 4.0 km/s experiment has the highest freestream Mach number and the smallest shock angle, it should have the highest post-shock Mach number compared to the other test conditions.

Using the estimated rotational and vibrational temperatures, it is important to assess the thermal non-equilibrium in the flow around the wedge model. To study the non-equilibrium between the rotational and vibrational modes of the CO₂ molecule, it is useful to plot the ratio Tr/Tv along the measured spatial dimension. The plots of the ratio Tr/Tv are compared at different heights above the test model, as shown on Figure 5.20 - Figure 5.22. The results show that no clear differences can be seen when

comparing the thermal non-equilibrium at different heights above the test model. The noise and uncertainty masks the small differences between the thermal non-equilibrium at different heights above the test model.

When comparing the thermal non-equilibrium between different conditions, the results show that the 4.0 km/s condition has the most thermal non-equilibrium, while the 2.8 km/s condition has the least thermal non-equilibrium. This is an expected result since the non-equilibrium effects are expected to increase with increase in freestream velocity. For the 2.8 km/s condition, in Figure 5.20, an equilibrium region is seen prior to expansion. The largest non-equilibrium is seen in the expansion fan where the vibrational temperature reaches about 3% more than the rotational temperature. The vibrational mode then relaxes towards thermal equilibrium and equilibrium is reached within the spatial range of the measurement. For the 3.4 km/s condition, like the 2.8 km/s condition, an equilibrium region is seen near the shock wave as shown in Figure 5.21. In the expansion fan, the vibrational temperature is seen to be as much as 5 % greater than the rotational temperature. The vibrational mode slowly relaxes towards equilibrium as the flow travels downstream of the convex corner but it never reaches thermal equilibrium within the spatial range of the measurement. In the 4.0 km/s condition, a significant non-equilibrium region, in which the rotational temperature is greater than the vibrational temperature, is observed prior to expansion. Non-equilibrium as much as approximately 20 % is observed in this post shock region. The non-equilibrium then becomes reversed, where rotational temperature is lower than the vibrational temperature, as the flow travels through the expansion fan. The vibrational temperature becomes as much as approximately 7% more than the rotational temperature in the expansion fan. Afterwards, further downstream of the convex corner, the flow relaxes gradually towards thermal equilibrium. However, the flow never reaches equilibrium within the spatial range of the measurement.

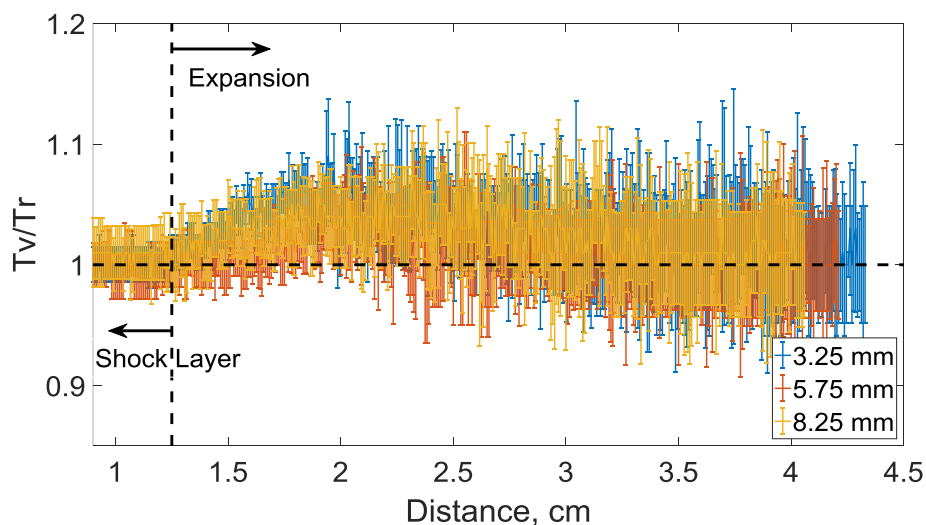


Figure 5.20. The ratio of the vibrational temperature to the rotational temperature for the 2.8 km/s condition.

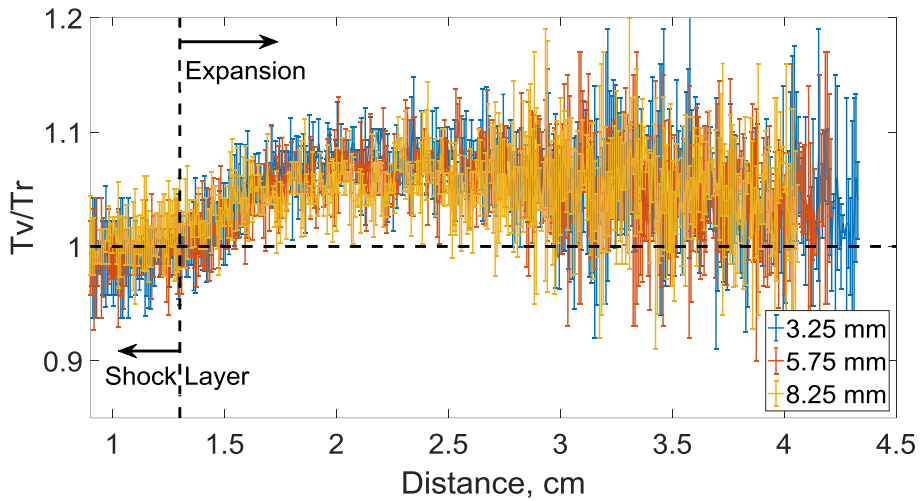


Figure 5.21. The ratio of the vibrational temperature to the rotational temperature for the 3.4 km/s condition.

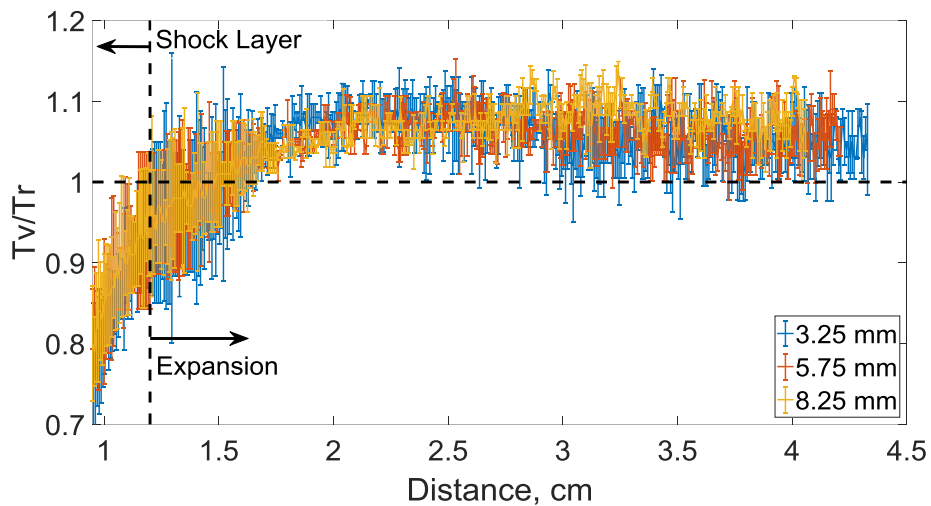


Figure 5.22. The ratio of the vibrational temperature to the rotational temperature for the 4.0 km/s condition.

In general, the results show that the thermal non-equilibrium induced by the expansion fan in the experiments is not significant – T_v/Tr is less than 1.1. The thermal non-equilibrium is particularly small for the 2.8 km/s and 3.4 km/s conditions. In the 4.0 km/s condition, since the flow initially has some thermal non-equilibrium ($Tr > T_v$) when entering the expansion fan, the non-equilibrium caused by the expansion fan ($T_v > Tr$) may have been reduced. Therefore, if the flow entering the expansion fan is in thermal equilibrium, then a slightly greater non-equilibrium will possibly be observed in the expansion fan for the 4.0 km/s condition. Furthermore, because the energy exchange between the translational-rotational mode and the vibrational mode is generally considered the slowest thermal non-equilibrium process [126], a consequence of not having significant non-equilibrium between T_v and Tr is that the vibrational energy levels are likely populated with a Boltzmann distribution during

the expansion. With the same argument, the different vibrational modes of CO₂ should also be in equilibrium with each other.

Another useful analysis is to compare the temperatures and CO₂ number densities derived from the 4.3 μm band to that derived from the 2.7 μm band for the same condition and measurement location. The results are shown in Figure 5.23 to Figure 5.25. As discussed in section 2.2, the 4.3 μm band corresponds to the fundamental transitions of the v_3 asymmetric stretching vibrational mode, while the 2.7 μm band corresponds to the combined transitions of two different vibrational modes. Hence, in addition to aiding the assessment of the accuracy of the temperatures and CO₂ number densities derived from the 4.3 μm band, comparison with the results derived from the 2.7 μm band also allows for the assessment of complex non-equilibrium influences. These influences may include the non-Boltzmann distribution of the internal energy levels as well as the non-equilibrium between the different vibrational modes of CO₂. Furthermore, the comparison may also provide an assessment of the accuracy of the NEQAIR code for simulating CO₂ radiation. This is because the spectral fitting done to estimate the temperatures and number densities was carried out using CO₂ spectra computed by NEQAIR.

For all the results in Figure 5.23 to Figure 5.25, the temperature and CO₂ number density derived from the 4.3 μm band measurement match with those derived from the 2.7 μm band measurement, within the uncertainties. However, the properties derived from the 2.7 μm band have large uncertainties/noise, particularly in the 2.8 km/s and 3.4 km/s conditions and, thus, it is hard to conclude whether or not there is an exact match between the properties derived from the two emission bands for these two conditions. Nevertheless, it can still be concluded that there is no significant disagreement between the properties derived from the two emission bands for these two conditions. On the other hand, for the 4.0 km/s condition, the uncertainties/noise in the properties derived from the 2.7 μm band is smaller (compared to those for the 2.8 and 3.4 km/s conditions) and, thus, a clearer match can be observed with the properties derived from the 4.3 μm band.

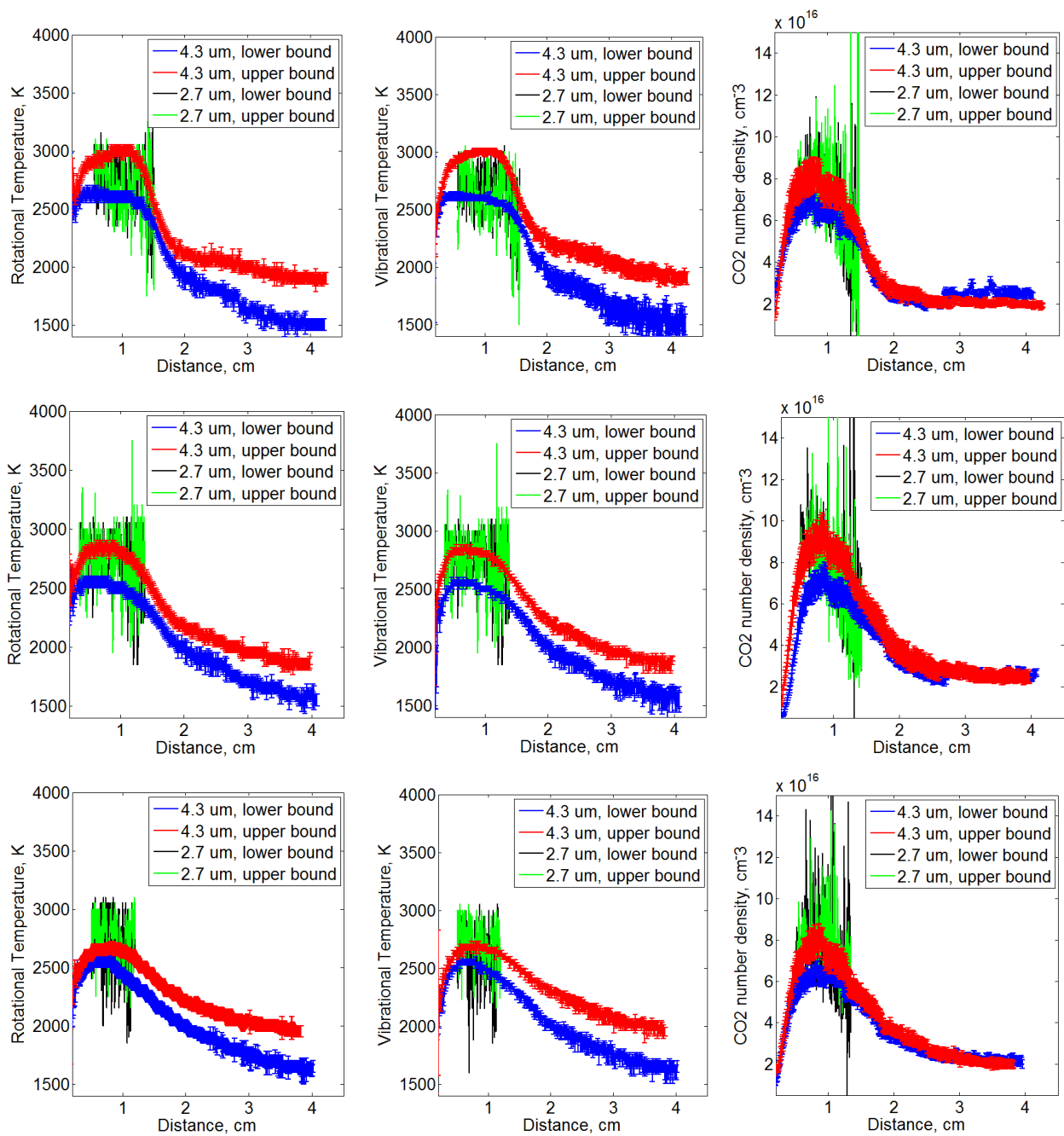


Figure 5.23. Comparison of the rotational temperature, vibrational temperature and carbon dioxide number density derived from the 4.3 μm and 2.7 μm band for the 2.8 km/s condition. Plots on the top, middle and bottom rows correspond to measurements made at 3.25 mm, 5.75 mm and 8.25 mm above the test model respectively.

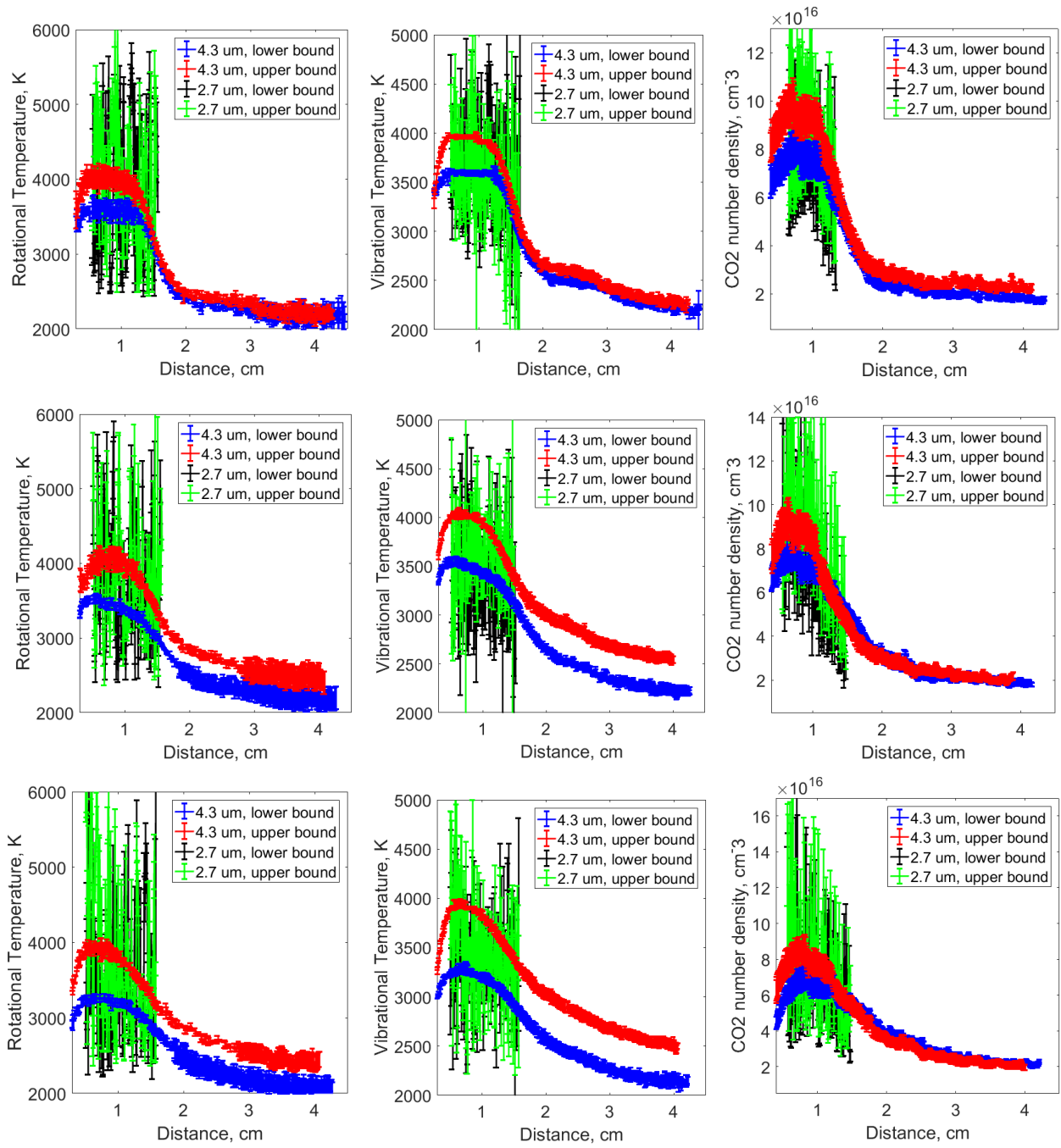


Figure 5.24. Comparison of the rotational temperature, vibrational temperature and carbon dioxide number density derived from the 4.3 μm and 2.7 μm band for the 3.4 km/s condition. Plots on the top, middle and bottom rows correspond to measurements made at 3.25 mm, 5.75 mm and 8.25 mm above the test model respectively.

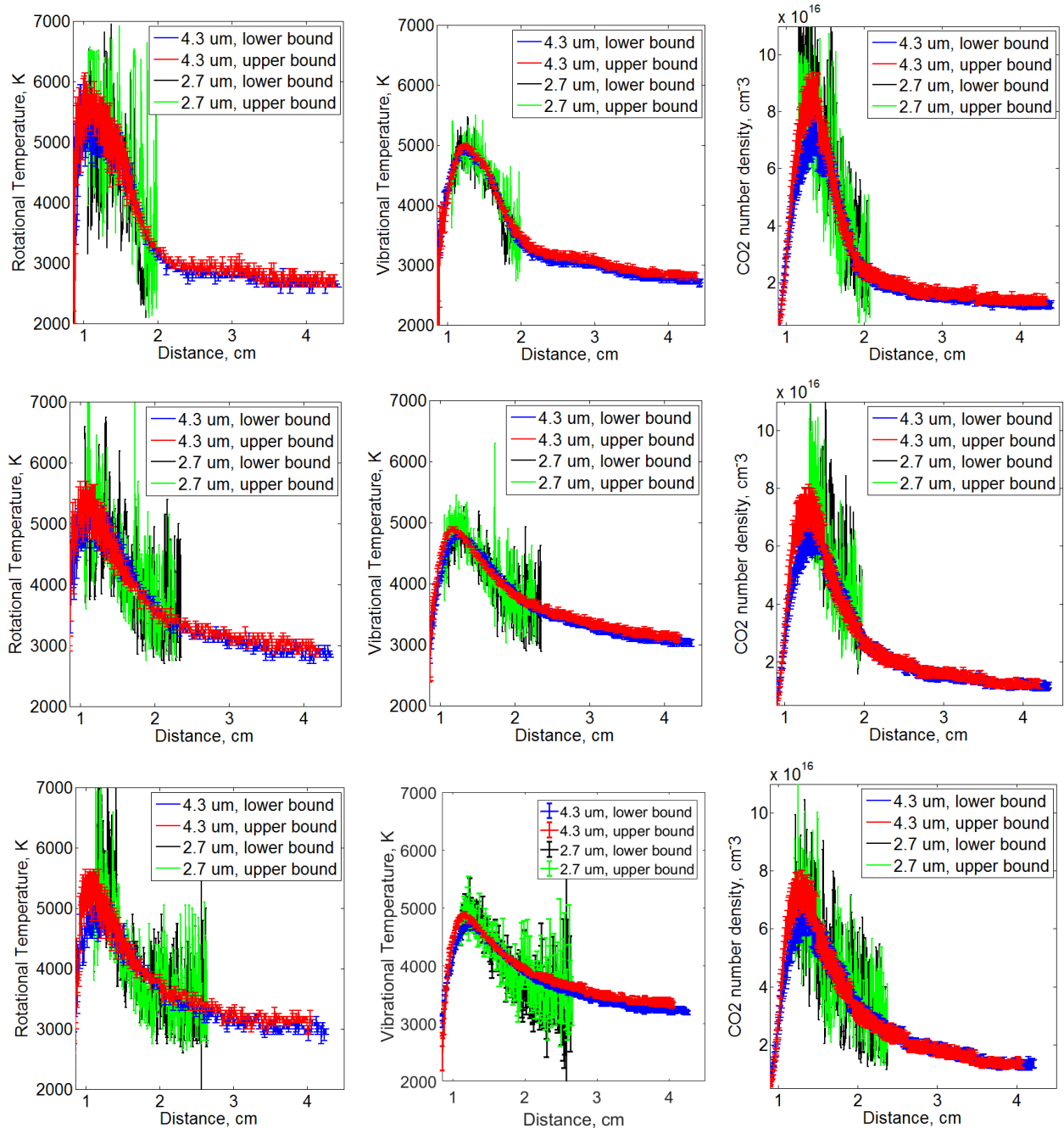


Figure 5.25. Comparison of the rotational temperature, vibrational temperature and carbon dioxide number density derived from the 4.3 μm and 2.7 μm band for the 4.0 km/s condition. Plots on the top, middle and bottom rows correspond to measurements made at 3.25 mm, 5.75 mm and 8.25 mm above the test model respectively.

Since no significant difference in the properties derived from the 4.3 μm and 2.7 μm measurement can be observed in Figure 5.23 to Figure 5.25, this may indicate equilibrium between the different vibrational modes of the CO₂. It may also indicate that the internal energy levels are in Boltzmann distribution. This argument is made stronger given the fact that a good agreement between the properties derived from the two emission bands is most obvious for the 4.0 km/s. The 4.0 km/s condition is expected to be the most likely condition to have complex thermal non-equilibrium effects. Therefore, as no complex thermal non-equilibrium effects are evident in the results of the 4.0

km/s condition, these effects, consequently, should probably not be present in the 2.8 km/s and 3.4 km/s condition.

Furthermore, in Figure 5.23 to Figure 5.25, the result that the properties derived from the two emission bands match within the uncertainties provides more confidence to the validity of the NEQAIR code using the CDSD-4000 database at predicting the 4.3 μm and 2.7 μm radiation. Although numerous work has already been done on validating the CDSD-4000 database for simulating CO₂ radiation [45] [48] [47], the experimental data used for the validation were mainly from plasma torch facilities (or other similar facilities) creating subsonic flows in thermochemical equilibrium. The characteristics of the flow around the wedge in the current work is supersonic with mild non-equilibrium between the rotational and vibrational modes and, mainly, frozen chemistry (this is shown in section 6.6). Additionally, part of the flow is under gas-dynamic expansion. Therefore, the results in this work provide some confidence to the validity of NEQAIR using the CDSD-4000 database at predicting CO₂ radiation under different gas-dynamic conditions – conditions which are more relevant to Mars entry.

The results shown in Figure 5.23 to Figure 5.25 can be compared to a similar study by Cruden et al. [44] for experiments performed in a non-reflected shock tube (an overview of non-reflected shock tubes is presented in appendix A.4) for post-shock conditions at velocities of 3.1 km/s and 3.75 km/s. For their 3.75 km/s condition, the temperature estimated from the 2.7 μm band agrees with the temperature estimated from the 4.3 μm band, within the uncertainties of the estimated temperatures. As the temperatures agree within the uncertainties, this result of Cruden et al. is consistent with the results seen in the current work. On the other hand, for the 3.1 km/s condition by Cruden et al., the temperature estimated from the 2.7 μm band is significantly greater than the temperature estimated from the 4.3 μm band. The 3.1 km/s normal shock condition of Cruden et al. is analogous to the 3.4 km/s oblique shock condition in this work when comparing the normal velocity component relative to the shock wave. The discrepancy of the estimated temperatures in their 3.1 km/s condition is not observed in the 3.4 km/s condition of the current work, or any other condition in the current work. The reason for this discrepancy in results is unclear.

5.5 Post Oblique Shock Results

In the previous section, the temperatures and number densities deduced from the horizontal measurements above the test model contain data across the flow including the post oblique shock region. In particular, the peak value of the temperatures and number density curves from the measurements at 3.25 mm above the test model are good representative values for the post oblique

shock properties. The approximate spatial location in the flowfields corresponding to the peak of the deduced curves from the 3.25 mm measurements are shown in Figure 5.26 labelled as the “Post-Shock Point”. The flow at these locations correspond to unexpanded flow, near the head of the expansion fan. Thus, the conditions at these points are good representatives of the oblique shock layer conditions. The temperatures and number densities at these points, extracted from the peak of the 3.25 mm temperature and number density curves in the previous section, are used for the shock layer study in the current section.

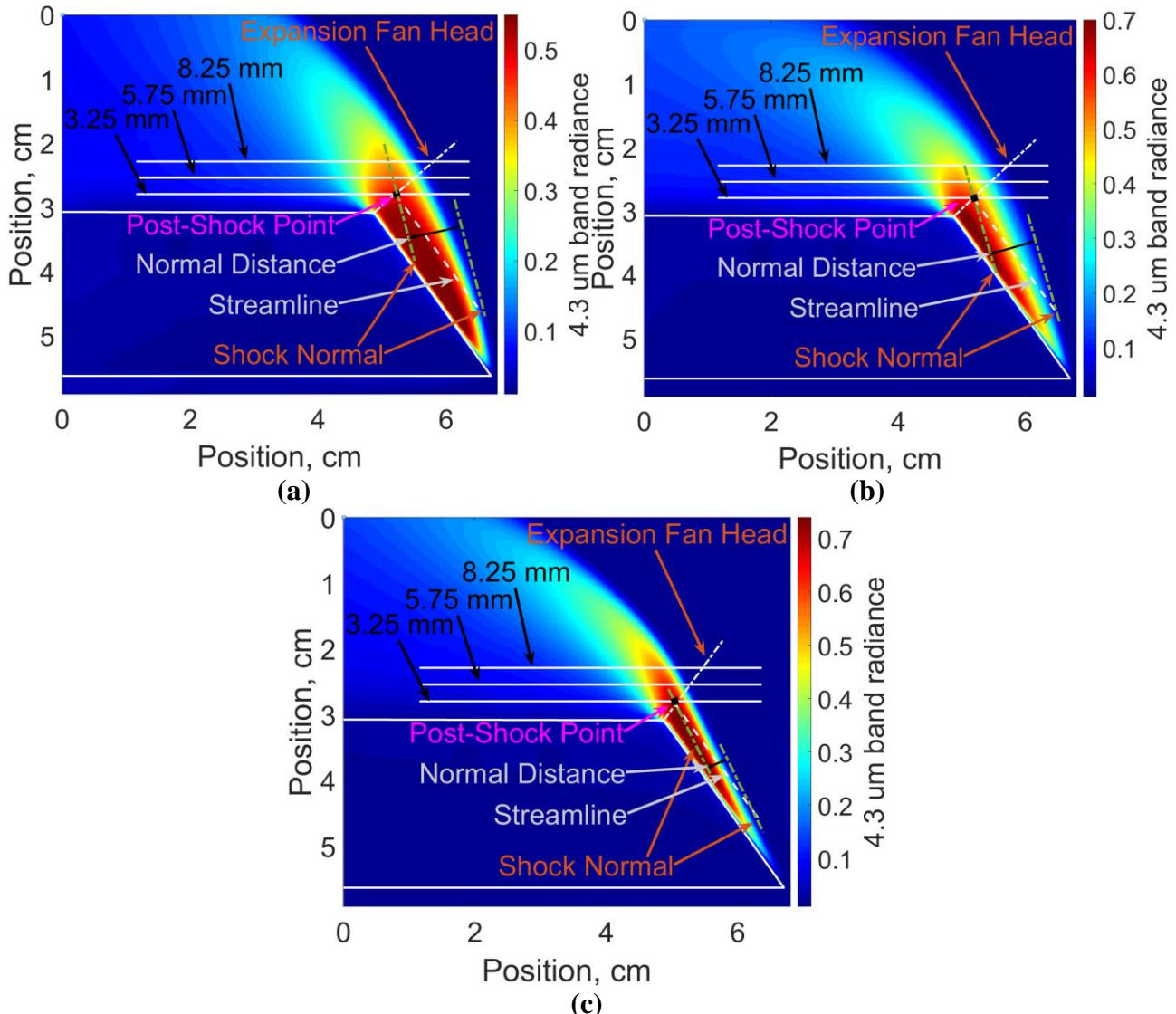


Figure 5.26. Flow around the wedge for the 2.8 km/s (a), 3.4 km/s (b) and 4.0 km/s (c) condition.

The estimated temperatures and CO₂ number densities at these post oblique shock locations would be useful for studying the post-shock chemical kinetics by comparing to the calculated frozen and equilibrium chemistry limits. However, the results of the comparison can only be interpreted correctly if the freestream condition is accurately defined. In the current work, the 2.8 and 3.4 km/s conditions in particular are not well defined, as discussed in section 5.3. So, instead of studying the post-shock

chemical kinetics, the measured post-shock temperatures and number densities in this work are used to further characterize the freestream conditions.

Table 5.6. Estimated freestream properties from both the PITOT code and spectroscopic measurements.

Condition	Source	P (Pa)	T (K)	Velocity (m/s)	Mole Fractions CO ₂ /CO/O ₂ /O	Shock Angle	Normal Velocity (m/s)
2.8 km/s	PITOT Code	332	1208	2935	0.90/0.064/0.031/0.001	72	2791
	Spectroscopic Measurement	65	1083	2935	0.90/0.064/0.031/0.001	72	2791
3.4 km/s	PITOT Code	366	1379	3471	0.76/0.158/0.076/0.006	70	3261
	Spectroscopic Measurement	92	1216	3471	0.76/0.158/0.076/0.006	70	3261
4.0 km/s	PITOT Code	172	1297	4006	0.73/0.18/0.083/0.007	62	3537
	Spectroscopic Measurement	151	1116	4006	0.73/0.18/0.083/0.007	62	3537

To assess the accuracy of the estimated freestream conditions, the experimental results of the post-shock temperature is compared to the calculated frozen and equilibrium limits. The frozen limit represents frozen chemistry but thermal equilibrium. The frozen and equilibrium limits are calculated from the CEA code [127] using the freestream estimates made from both the PITOT code and the spectroscopic measurements, shown on Table 5.6. These freestream estimates are the average from the values presented in Table 5.2, Table 5.3 and Table 5.4. In Table 5.6, both sources of freestream estimates use the same mole fractions - the average of the mole fractions estimated from the PITOT code. Thermal equilibrium in the freestream is assumed for the work in this section and the estimated translational-rotational temperature is used as the equilibrium temperature. The shock angle in Table 5.6 is measured at the point on the shock wave where the streamline of the selected representative post-shock point originates, as illustrated in Figure 5.26. The shock angle is measured from the filtered images which were discussed in section 4.3.

Using the freestreams in Table 5.6, the calculated frozen and equilibrium post-shock temperatures are presented in Table 5.7 along with the measured post-shock temperature. These results show that the 2.8 km/s condition is close to the equilibrium post-shock solution. The 3.4 km/s condition is approximately in the middle of the frozen and equilibrium post-shock solution. The 4.0 km/s condition is close to the frozen post-shock solution. However, these results for the 2.8 km/s and 3.4 km/s conditions are not consistent with other results. The CFD computations, presented in detail in chapter 6, as well as past experimental results by Cruden et al. [44] indicate that the measured

temperatures at the extracted post-shock locations shown in Figure 5.26 should be near the frozen limit for both the 2.8 and 3.4 km/s condition.

Table 5.7. The measured post-shock temperature compared with the calculated frozen and equilibrium limits from two different freestream estimates.

Condition	PITOT Code		Spectroscopic Measurement		Measured (K)	Normal distance behind shock (cm)
	Frozen (K)	EQ (K)	Frozen (K)	EQ (K)		
2.8 km/s	3871	2584	3792	2429	2800 ± 250	0.8
3.4 km/s	5181	2892	5025	2745	3750 ± 300	0.7
4.0 km/s	5887	2928	5771	2934	5400 ± 500	0.3

Cruden et al. [44] experimentally deduced the temperature profiles behind propagating normal shock fronts. They studied velocities of 3.1, 3.75 and 4.9 km/s and the results for the 3.1 and 3.75 km/s conditions are shown on Figure 5.27. The figure shows the relaxation of the post-shock temperature from the frozen temperature at the shock front to the equilibrium temperature more than 7 cm behind the shock front. The temperatures are deduced from emission spectroscopy measurements from both the 2.7 and 4.3 μm bands. The uncertainties of the estimated temperatures from the 4.3 μm band are 50 K and 200 K for conditions 3.1 and 3.75 km/s respectively. The freestream pressure Cruden et al. used in their study is 133 Pa, which is similar to the freestream pressure used in the current experiments. Furthermore, in both the experiment by Cruden et al. and the experiments in the present study, there is no stagnation point behind the shock wave. Thus, the post-shock characteristics from Cruden et al. can be compared with the current work [128]. The 3.4 km/s condition in the present work has a normal velocity of 3.3 km/s, while the 4.0 km/s condition in the present work has a normal velocity of 3.6 km/s. Therefore, in particular, the 3.4 km/s and 4.0 km/s condition in the present work can be compared to the Cruden et al. 3.1 km/s and 3.75 km/s conditions respectively. Interpretation of the results of Cruden et al. with the results in the current work is made by considering the normal distance behind the oblique shock wave shown in Table 5.7.

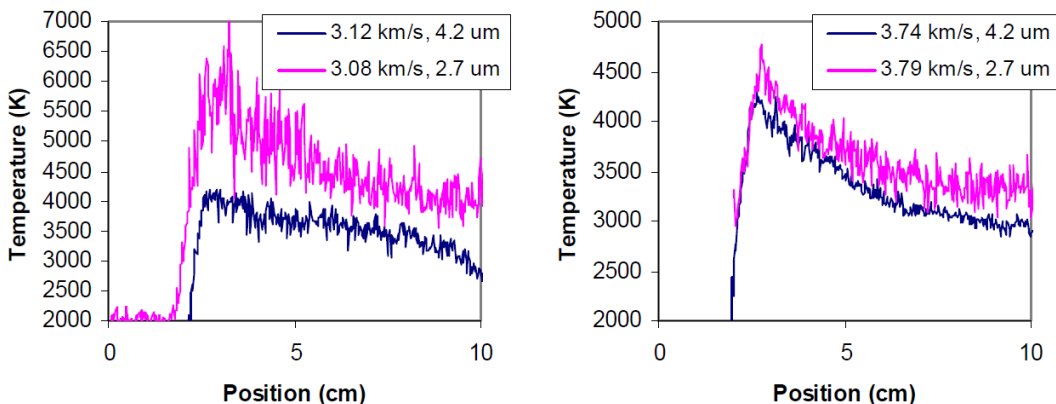


Figure 5.27. Estimated post-shock temperatures for nominal shock velocities of 3.1 and 3.75 km/s [44].

Because the temperatures and number densities estimated from the spectroscopic measurements for the 4.0 km/s inflow matched well with that predicted by the PITOT code, the 4.0 km/s condition is believed to be the most accurately characterized test condition in the current work. The result in Table 5.7 shows that, at 0.3 cm behind the shock, the chemistry is near frozen for the 4.0 km/s condition. This result is consistent with finite rate chemistry CFD predictions, discussed further in chapter 6. This result is also consistent with the temperature profile of the 3.75 km/s condition by Cruden et al. in Figure 5.27 where the temperature at 0.3 cm behind the shock front is around the frozen temperature. Thus, this provides further confidence that the freestream estimates for the 4.0 km/s condition is accurate.

The result in Table 5.7 indicates that, for the 3.4 km/s condition at 0.7 cm behind the shock, the chemistry is approximately in the middle of the frozen and equilibrium post-shock solution. This is not consistent with the result by Cruden et al. shown on Figure 5.27. The 3.1 km/s result of Cruden et al. shows that at about 0.7 cm behind the shock front, the temperature should be very close to the frozen chemistry limit. Likewise, for the 2.8 km/s condition in the current work, the result in Table 5.7, showing that the chemistry at 0.8 cm behind the shock is close to chemical equilibrium, is believed to be misleading. This is because, even though Cruden et al. do not have suitable experimental results for comparison with this condition, they showed that the length of the post-shock chemical relaxation increases with decrease in velocity. Therefore, given that their result in Figure 5.27 for the 3.1 km/s shows it takes more than 7 cm behind the shock to reach chemical equilibrium, the chemistry at 0.8 cm behind the shock for the 2.8 km/s condition in this work should be close to the frozen limit rather than close to the equilibrium limit. Additionally, finite rate chemistry CFD simulations, discussed in detail in section 6.5.3 and 6.6, indicate that the post-shock temperatures at the measured locations in Figure 5.26 should be near the frozen chemistry limit for both the 2.8 and 3.4 km/s condition. Therefore, there is significant evidence, experimental and numerical, suggesting that the post-shock properties at the measured locations for the 2.8 and 3.4 km/s condition should be near the frozen limit.

The reason for the disagreement between the calculated frozen temperature and the measured temperature for the 2.8 and 3.4 km/s condition is not believed to be due to incorrect estimates of the freestream temperature. The freestream temperature would have to be over-estimated by around 1000 K to explain the disagreement in the post-shock temperature and this is extremely unlikely. Also, the reason for the discrepancy between the calculated frozen temperature and the measured temperature is probably not due to incorrect estimates of the freestream velocity. If the freestream velocities were over-estimated, it would have to be over-estimated by about 600 m/s to cause the over-estimation in frozen post-shock temperature seen in the 2.8 and 3.4 km/s condition. This would correspond to a

freestream velocity that is about 20% slower than the measured secondary shock velocity; having such a large difference is not impossible but is believed to be unlikely, particularly because the nozzle accelerates the test gas. On the other hand, the reason for the discrepancy in temperature may be due to helium contamination of the freestream in the experiments. The fact that the measured temperature is not near the frozen temperature indirectly supports the belief that there is helium in the 2.8 and 3.4 km/s freestream conditions, discussed in section 5.3, because having helium in the freestream decreases the post-shock frozen temperature.

Table 5.8. Mole fraction of helium required to match the frozen post-shock temperature to the measured post-shock temperature for the 2.8 and 3.4 km/s conditions.

Condition	Source of Freestream Temperature, T	T (K)	Normal Velocity (m/s)	Mole Fraction He/CO ₂	Frozen Temperature (K)	Measured Temperature (K)
2.8 km/s	PITOT Code	1208	2791	0.77/0.23	2802	2800 ± 250
	Spectroscopic Measurement	1083	2791	0.74/0.26	2801	
3.4 km/s	PITOT Code	1379	3261	0.72/0.28	3763	3750 ± 300
	Spectroscopic Measurement	1216	3261	0.68/0.32	3745	

The post-shock frozen chemistry temperature is independent of the freestream pressure. Therefore, assuming helium contamination, it is possible to determine the mole fraction of helium in the inflow required to match the computed frozen temperature to the measured temperature for the 2.8 and 3.4 km/s condition. In Table 5.8, assuming the same inflow temperature and normal velocity as presented in Table 5.6 and assuming a mixture of just CO₂ and helium, the inflow helium mole fraction required for the match in temperature is about 0.68 – 0.77. This is a large amount of helium but it is consistent with the result in section 5.3 where the inflow total density, from pitot pressure, was shown to be significantly greater than the inflow CO₂ density, from spectroscopic measurements, for the 2.8 and 3.4 km/s condition. Given significant dissociation of CO₂ should not occur, it was postulated that the discrepancy could, instead, be explained by large amounts of contamination in the inflow.

In addition to analysing the post-shock temperatures, studying the post-shock CO₂ number densities provides further information to help characterize the freestream condition. Using the estimated properties in Table 5.6, the frozen and equilibrium chemistry limits for the post-shock CO₂ number densities are calculated and compared to the experimental measurements. This is shown in Table 5.9. The results show that the measured post-shock CO₂ number density matches well with the frozen solution for the 4.0 km/s condition. This is consistent with the temperature analysis where the

measured post-shock temperature for the 4.0 km/s condition is found to be near the frozen temperature. This provides further confidence that the 4.0 km/s freestream condition is well characterized. On the other hand, the measured post-shock CO₂ number density for the 2.8 and 3.4 km/s condition lies outside the frozen and equilibrium limits calculated from both sources of freestream estimates; the PITOT code inflow over-predicts the number density while the spectroscopic measurement inflow under-predicts the number density. This further suggests that the 2.8 and 3.4 km/s inflows are not well characterized.

Table 5.9. The measured post-shock carbon dioxide number density compared with the calculated frozen and equilibrium limits from two different freestream estimates.

Condition	PITOT Code		Spectroscopic Measurement		Post-shock	
	Frozen (cm ⁻³)	EQ (cm ⁻³)	Frozen (cm ⁻³)	EQ (cm ⁻³)	Measured (cm ⁻³)	Normal distance (cm)
2.8 km/s	1.8 x 10 ¹⁷	1.7 x 10 ¹⁷	3.1 x 10 ¹⁶	3.1 x 10 ¹⁶	(7.6 ± 1.1) x 10 ¹⁶	0.8
3.4 km/s	1.3 x 10 ¹⁷	9.7 x 10 ¹⁶	4.2 x 10 ¹⁶	3.2 x 10 ¹⁶	(8.7 ± 1.3) x 10 ¹⁶	0.7
4.0 km/s	6.8 x 10 ¹⁶	4.0 x 10 ¹⁶	7.3 x 10 ¹⁶	4.5 x 10 ¹⁶	(7.8 ± 1.4) x 10 ¹⁶	0.3

Using the helium/CO₂ mole fractions shown in Table 5.8, it is possible to calculate the freestream pressure such that there is a simultaneous match with both the post-shock temperature and post-shock CO₂ number density between the measurements and frozen calculations for the 2.8 and 3.4 km/s conditions. As shown in Table 5.10, assuming the same freestream temperatures and normal velocities presented in Table 5.6, the freestream pressure required for the match in post-shock CO₂ number density is about 900 – 1500 Pa for the 2.8 and 3.4 km/s conditions. To check if these tuned freestream conditions are consistent with the available freestream measurements, the corresponding freestream CO₂ number densities, pitot pressures and conehead pressures were calculated. The results are presented in Table 5.10. The CO₂ number density of the tuned freestream conditions were found to be significantly greater than the measured freestream CO₂ number density from the spectroscopic measurements. On the other hand, the pitot pressure of the tuned freestream conditions compared well with the measured freestream pitot pressures. However, the conehead pressure of the tuned freestream conditions were found to be significantly greater than the measured freestream conehead pressure. Therefore it can be concluded that, even assuming helium contamination, it is not possible to find a freestream condition which is simultaneously consistent with the measured freestream CO₂ number density, pitot pressure and conehead pressure and post-shock CO₂ number density and temperature.

Table 5.10. Freestream condition tuned to match the post-shock frozen CO₂ number density to the measured CO₂ number density for the 2.8 and 3.4 km/s conditions.

Condition	2.8 km/s		3.4 km/s	
Tuned freestream condition				
Source of Freestream Temperature, T	PITOT Code	Spectroscopic Measurement	PITOT Code	Spectroscopic Measurement
T (K)	1208	1083	1379	1216
Normal Velocity (m/s)	2791		3261	
Mole Fraction He / CO₂	0.77 / 0.23	0.74 / 0.26	0.72 / 0.28	0.68 / 0.32
Freestream Pressure (Pa)	1520	1084	1367	932
Comparison to measured freestream properties				
Tuned Freestream CO₂ Number Density (cm⁻³)	2.09 x 10 ¹⁶	1.89 x 10 ¹⁶	2.01 x 10 ¹⁶	1.78 x 10 ¹⁶
Measured Freestream CO₂ Number Density (cm⁻³)	$(4.0 \pm 0.5) \times 10^{15}$		$(4.2 \pm 0.5) \times 10^{15}$	
Tuned Freestream Pitot Pressure (kPa)	11.9	12.9	18.4	15.7
Measured Freestream Pitot Pressure (kPa)	13.2 ± 2.85		14.5 ± 1.42	
Tuned Freestream Conehead Pressure (kPa)	2.92	2.25	3.00	2.28
Measured Freestream Conehead Pressure (kPa)	1.35 ± 0.25		1.51 ± 0.19	
Comparison to measured post-shock properties				
Frozen Post-shock CO₂ Number Density (cm⁻³)	7.59 x 10 ¹⁶	7.59 x 10 ¹⁶	8.73 x 10 ¹⁶	8.64 x 10 ¹⁶
Measured Post-shock CO₂ Number (cm⁻³)	$(7.6 \pm 1.1) \times 10^{16}$		$(8.7 \pm 1.3) \times 10^{16}$	
Frozen Post-shock Temperature (K)	2802	2801	3763	3745
Measured Post-shock Temperature (K)	2800 ± 250		3750 ± 300	

Another influence of having helium in the freestream is to increase the shock standoff distance. Therefore, to further investigate the possibility of helium contamination, the location of the shock wave generated by the made-up inflow conditions are computed and compared to the experimentally measured shock wave locations. The made-up helium-contaminated inflows are summarized in Table 5.11. The temperature and velocities are taken from the estimates made using the PITOT code. The simulation methodology is identical to that used in section 3.4.4 to study the shock wave location, with the addition of helium. In the current simulations, helium is assumed to takes part in the chemical

reactions equally as much as the other species (the Arrhenius rates remain independent of the collision partner). Additionally, helium takes part in the V-T thermal energy exchange with the vibrational relaxation time calculated according to the Millikan and White theory [129].

Table 5.11. Freestream conditions used to study the influence of having helium in the freestream.

Condition	P (Pa)	T (K)	Velocity (m/s)	Mole Fraction He/CO ₂
2.8 km/s	1520	1208	2877	0.77 /0.23
3.4 km/s	1367	1379	3484	0.72 /0.28

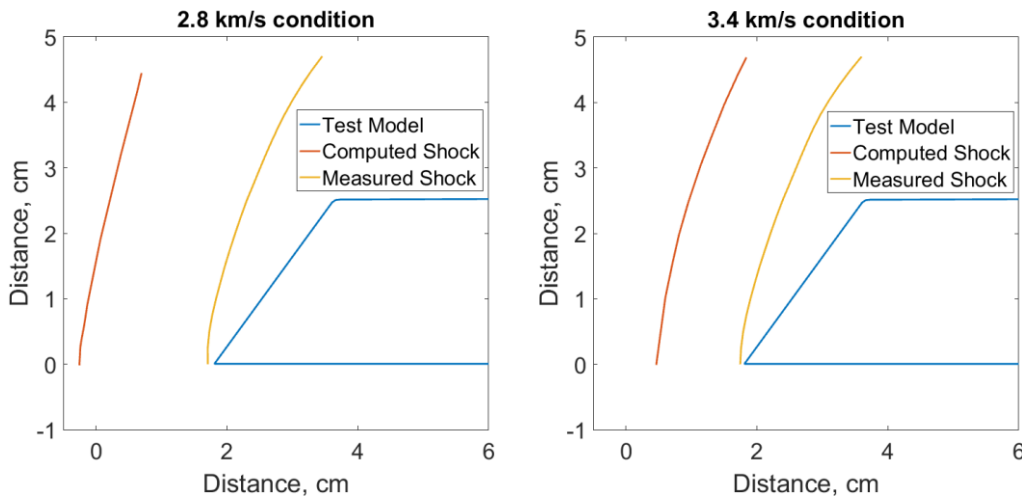


Figure 5.28. Comparison of the computed shock wave location to the measured shock wave location.

As the inflow conditions in Table 5.11 were tuned to match the measured post-shock temperatures and CO₂ number densities, the simulations duly computed post-shock temperatures and CO₂ number densities which matched with the experimentally measured values. Interestingly, these simulations also computed temperatures and CO₂ number densities in the expanded flow region which matched well (within 10%) with the experimental measurements. However, the shock wave locations presented in Figure 5.28 shows vast discrepancies between the computed shock location from the helium contaminated inflow and the measured shock location. The 0.7 mole fraction of helium shown in Table 5.11 was required in the inflow to obtain a match in post-shock temperature. However, such a large amount of helium would increase the shock standoff distance significantly. The experimentally measured shock wave location shows that there could not be such a large amount of helium in the freestream. Therefore, it can be concluded that helium contamination, even though it allows for reconciliation between CFD predictions and experimental measurements, cannot be responsible for the large discrepancies seen in the post-shock temperature. Analogously, helium contamination would also not be able to explain the inconsistency seen between the estimated inflow CO₂ density from spectroscopic measurements and the estimated inflow total density from pitot

pressure measurements, discussed in section 5.3, as it would also require a helium mole fraction of around 0.7-0.8 to reconcile.

5.6 Conclusion

The spectroscopic measurements at the nozzle exit were used to deduce the rotational temperature, vibrational temperature and carbon dioxide number density of the freestream for each condition. The subsequent results were compared to the estimate made using the PITOT code. For all three conditions, the estimated translational-rotational temperatures agree within 200 K between the estimates made using the PITOT code and spectroscopic measurements. Examining the thermal non-equilibrium of the freestreams, the spectroscopic measurements showed that the vibrational temperature is generally higher than the rotational temperature. However, the degree of thermal non-equilibrium estimated from the spectroscopic measurements is significantly less than that estimated by the PITOT code based on matching the shock wave location in CFD simulations to experimental measurements. The CO₂ number densities matched well, within 10%, for the 4.0 km/s condition between the two sources of the freestream estimates. However, for the 2.8 and 3.4 km/s inflows, the CO₂ number densities deduced from the spectroscopic measurements were significantly lower, by factors of 4 – 5, compared to the PITOT code estimates. The PITOT code estimates are derived from the measured pitot pressure, which is indicative of the total density. On the other hand, the estimates from the spectroscopic measurement are derived from the CO₂ 4.3 μm band emission which is indicative of the CO₂ density. Hence, the significant discrepancy might be due to significant amounts of contaminant species in the freestream making up for the large difference between the total density and CO₂ density.

To study the radiative heating during Mars entry, spectroscopic measurements were taken at three different heights above the wedge test model for three different freestream conditions. The measurement captures the shock wave, post-shock region, Prandtl-Meyer expansion fan and the expanded flow region. Similar to the spectroscopic measurement of the freestream, the spectroscopic measurement of the flow around the wedge was used to deduce the temperatures and number densities. To study the thermal non-equilibrium in the flowfield, the ratio of vibrational temperature to rotational temperature was determined from the estimated temperatures. The result showed that the thermal non-equilibrium in the expansion fan was generally not significant. The 4.0 km/s condition contains the most thermal non-equilibrium with a non-equilibrium of up to 7% in the expansion region. The 2.8 km/s condition contains the least thermal non-equilibrium with a non-equilibrium of up to 3% in the expansion region. The lack of non-equilibrium between the rotational

mode and vibrational mode may indicate that there are no complex thermal non-equilibrium effects in the flow. Furthermore, the temperatures and CO₂ number densities deduced from spectroscopic measurements of the 4.3 μm band and the 2.7 μm band are compared. Good agreements were observed. This provides confidence that the estimated temperatures and number densities are accurate within the given uncertainties. This may also indicate that there are no complex thermal non-equilibrium effects in the flowfield. In addition, the good agreement provides some confidence to the validity of NEQAIR at predicting CO₂ radiation under gas-dynamic conditions which are more relevant to Mars entry.

To further characterize the experimental freestream conditions, the temperatures and carbon dioxide number densities at representative post-shock locations were compared to frozen and equilibrium chemistry limits using the estimated freestream conditions. Experimental results from past literature, as well as finite rate chemistry CFD simulations conducted in the current study, indicate that, at the investigated post-shock location, the condition should be close to the frozen chemistry condition. Therefore, for all three freestream conditions, the measured temperature and CO₂ number density should be close to that calculated assuming frozen chemistry. However, only the measured properties of the 4.0 km/s condition matched with frozen chemistry calculations. For the 2.8 and 3.4 km/s condition, the measured temperature was significantly lower than the frozen temperature. In addition, for these two conditions, the measured CO₂ number densities were found to be outside the calculated frozen and equilibrium bounds. The frozen post-shock temperature being significantly greater than the measured post-shock temperature could be explained by helium contamination of the 2.8 and 3.4 km/s inflows, which may also explain the large difference between the inflow total density and inflow CO₂ density mentioned previously. Subsequently, inflow conditions were created for the 2.8 and 3.4 km/s condition by tuning the freestream helium mole fraction and freestream pressure such that the post-shock frozen temperature and CO₂ number density match with the measured values. The properties - pitot pressure, conehead pressure and CO₂ number density - of this made-up freestream were compared to the corresponding measured values. The result showed that, although the pitot pressure agreed well, the conehead pressure and CO₂ number density differed significantly. Therefore, it was concluded that helium contamination could not simultaneously reconcile the measured freestream CO₂ number density, pitot pressure and conehead pressure, and the measured post-shock CO₂ number density and temperature. In addition, the shock location study presented in this chapter showed that having 0.7 mole fraction of helium in the inflow would produce a shock wave at a location nowhere near the measured shock wave location. Consequently, it is concluded that helium contamination of the freestream is unlikely the cause of the discrepancy in post-shock temperatures.

6 Numerical Study and Comparison to Experimental Results

6.1 Introduction

A parametric study was carried out to investigate the importance of various gas properties on the 2.7 μm and 4.3 μm band radiance. Numerical reconstructions of the experiments were then performed. Three-dimensional simulations were done using the Eilmer3 [97] code for the flowfield and the NEQAIR v14.0 [49] code for the radiation. The two-temperature model was used to describe the non-equilibrium thermochemical kinetics. The numerically computed radiation as well as the temperatures and carbon dioxide number densities are compared to the values derived from experiments, presented in the previous chapters. The comparison allows for the examination of the accuracy of the current numerical models at simulating high-temperature CO₂ flows. Possible reasons causing discrepancies between the measured and the computed results are investigated. Furthermore, to examine the characteristics of high temperature CO₂ flows, the influence of the carbon dioxide dissociation rate used in the CFD is studied.

6.2 Band Radiance Parametric Study

In the framework of the NEQAIR radiation code [49], carbon dioxide radiation is defined by the rotational temperature, vibrational temperature and carbon dioxide number density. In addition, the carbon monoxide radiation can also contribute to the emission of the 4.3 μm and 2.7 μm bands due to overlap. To investigate these emission bands from carbon dioxide mixtures, it is necessary to study the influence of these temperatures and number densities on the band radiance. Hence, a parametric study is carried out using the NEQAIR code. This allows the importance of each variable, in the context of accurately calculating the intensity of the band radiances, to be determined. The study is conducted using a line of sight length of 130 mm which is representative of the radiating length of the lines of sight measured in the emission spectroscopy above the wedge model.

The normalized plots on Figure 6.1 show the variation of the band radiance when the CO₂ number density is varied at different temperatures. The radiance of the 2.7 μm band increases linear with CO₂ number density indicating that it is optically thin. However, the 4.3 μm band radiance does not

increase linearly which means it has self-absorption. The amount of self-absorption decreases at higher temperatures. Consequently, for the 4.3 μm band, the band radiance is more affected by CO₂ number density at higher temperatures. Furthermore, at higher temperatures, the 4.3 μm band radiance is almost directly proportional to the CO₂ number density. For the 2.7 μm band, at all the studied temperatures, the band radiance is directly proportional to the CO₂ number density.

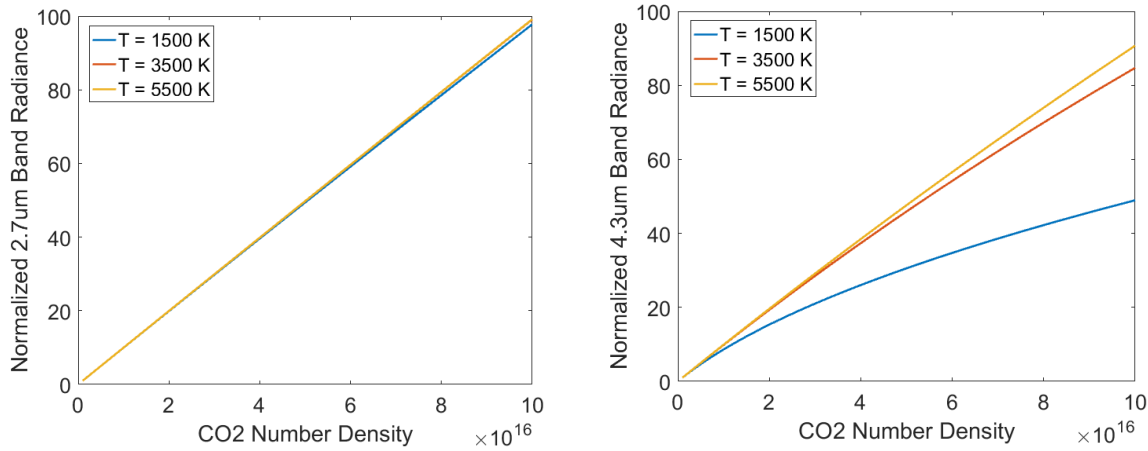


Figure 6.1. Influence of the carbon dioxide number density (cm^{-3}) to the band radiance with no carbon monoxide. Each curve is normalized to the band radiance value at a carbon dioxide number density of $1.0 \times 10^{15} \text{ cm}^{-3}$.

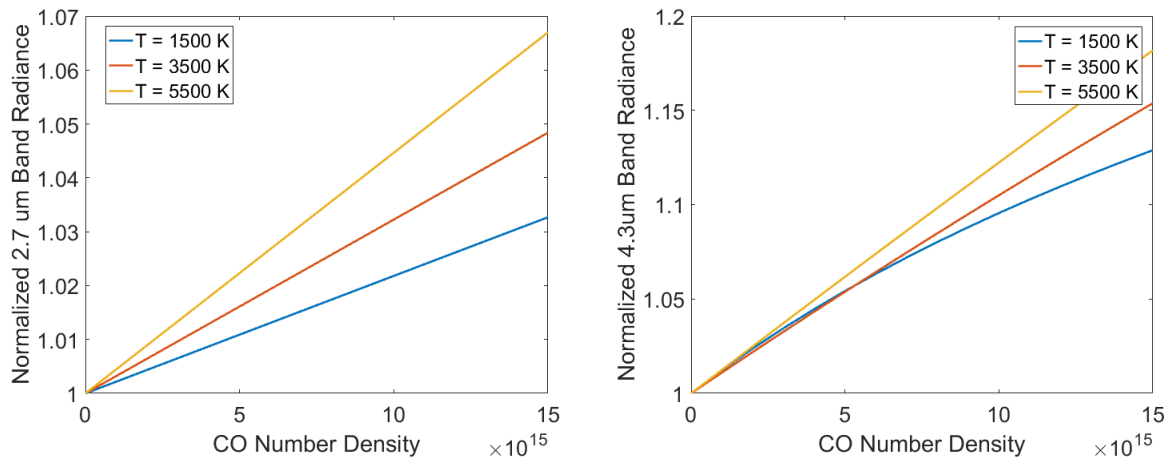


Figure 6.2. Influence of carbon monoxide number density (cm^{-3}) to the band radiance with carbon dioxide number density constant at $1.0 \times 10^{16} \text{ cm}^{-3}$. Each curve is normalized to the band radiance with zero carbon monoxide.

The plots in Figure 6.2 show the variation of the band radiance when the CO number density is varied at different temperatures while the CO₂ number density is kept constant at $1.0 \times 10^{16} \text{ cm}^{-3}$. For both the 2.7 and 4.3 μm band, the sensitivity of the CO number density increases with increase in temperature. The CO radiation is optically thin in the 2.7 μm band at all temperatures studied. The CO radiation is optically thin for the 4.3 μm band at temperatures greater than 3500 K, while some self-absorption occurs at lower temperatures such as at 1500 K. Furthermore, since the upper bound

of the CO number density to CO₂ number density in the flowfield is roughly 1:1, CO can contribute up to around 10 % of the 4.3 μm band radiance at some locations in the flowfield, according to the result on Figure 6.2. For the 2.7 μm band, CO radiation can contribute up to 5 % of the total band radiance at some locations in the flowfield. The results show that CO radiation is not completely negligible and, thus, it is included when numerically reconstructing the experiments presented later in this chapter.

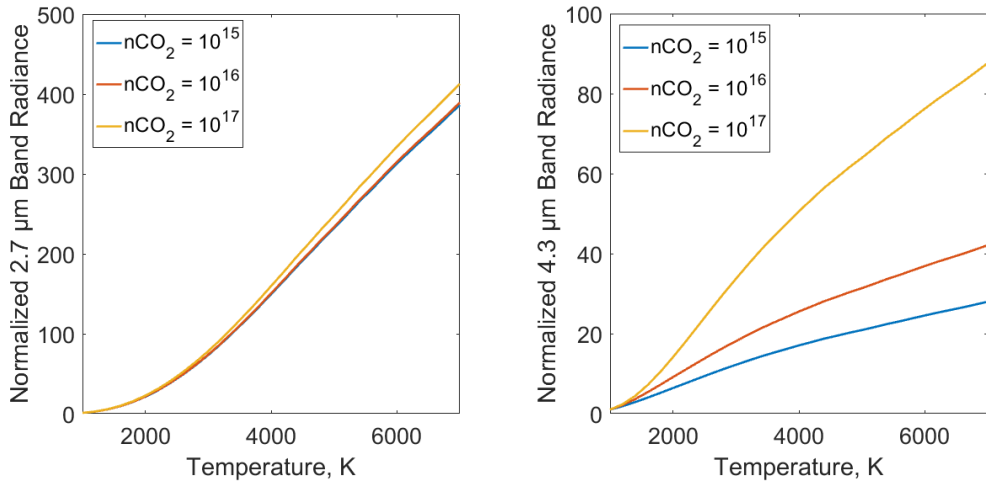


Figure 6.3. Influence of thermal equilibrium temperature on band radiance at different CO₂ number densities (cm⁻³). Each curve is normalized to the band radiance value at 1000 K.

The plots on Figure 6.3 show the variation of the band radiance at thermal equilibrium when the temperature is varied between 1000 – 7000 K at different CO₂ number densities (cm⁻³). For both the 2.7 μm and 4.3 μm band, temperature influences the band radiance more at higher CO₂ number densities. This is due to the fact that the band emission moves towards the blackbody limit, where the total energy emitted is proportional to the 4th power of the temperature, as the CO₂ number density increases. Furthermore, Figure 6.3 shows that the 2.7 μm band increases more rapidly with increase in temperature compared to the 4.3 μm band.

Figure 6.4 shows the change in band radiances when either the rotational temperature or vibrational temperature is varied while the other temperature is kept constant, and it shows how the non-equilibrium between the rotational and vibrational temperature influences the 2.7 μm and 4.3 μm band radiance. In general, thermal non-equilibrium has the potential to influence the band radiance intensities significantly. For both emission bands, the influence of the non-equilibrium between the rotational and vibrational temperature on the band radiance is greater at lower temperatures. Comparing the influence of changing the rotational temperature and vibrational temperature on the 4.3 μm band radiance, the rotational temperature has marginally greater influence than the vibrational temperature at higher temperatures such as 5500 K. However, the rotational temperature is distinctly more influential than the vibrational temperature at lower temperatures such as 1500 K. For the 2.7

μm band, at higher temperatures such as 5500 K, the vibrational temperature has marginally more influence than the rotational temperature on the band radiance. On the other hand, at lower temperatures such as 1500 K, the rotational temperature is distinctly more influential than the vibrational temperature, as with the 4.3 μm band. In addition, for both emission bands, increasing the rotational temperature increases the band radiance while the vibrational temperature is constant. However, for both emission bands, increasing the vibrational temperature decreases the band radiance when the rotational temperature is constant at lower temperatures such as 1500 K. On the other hand, increasing the vibrational temperature increases the band radiance when the rotational temperature is constant at higher temperatures such as 5500 K.

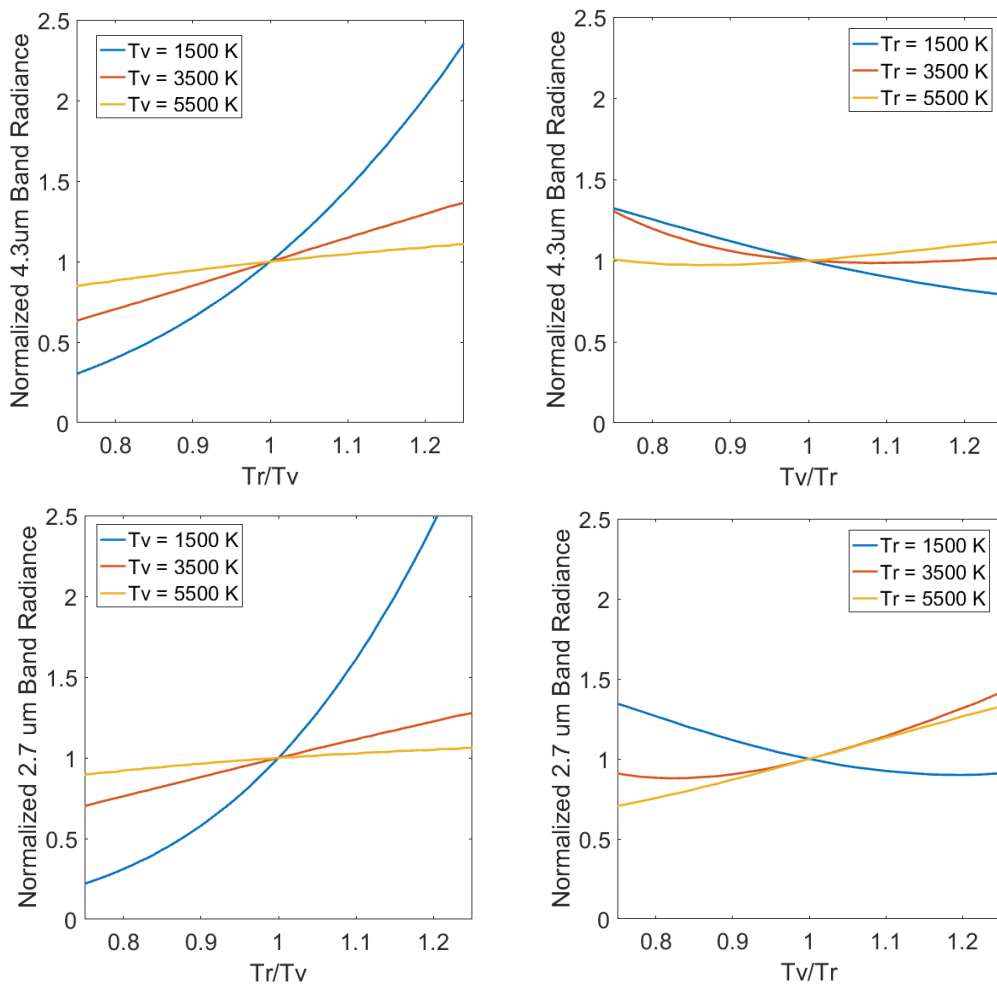


Figure 6.4. Influence of Tr - Tv non-equilibrium on band radiance at a constant CO₂ number density of $1.0 \times 10^{16} \text{ cm}^{-3}$. The left column shows the influence of changing the Tr while Tv is constant. The right column shows the influence of changing the Tv while Tr is constant.

In summary, the results show that the temperature is the most influential variable towards the band radiance of the 4.3 μm band. The CO₂ number density, although not as influential towards the band radiance as the temperature, is believed to be just as important as the temperature because the number density has a greater variation in the flowfield than the temperature. The thermal non-equilibrium is

the third most influential variable towards the band radiance. Lastly, the CO number density is seen to be the least influential variable to the band radiance, though it is still accounted for in the numerical reconstruction of the experiments presented later in this chapter.

6.3 Numerical Simulation Methodology

Full numerical reproductions of the experiments are carried out using the Eilmer3 flowfield code [97] along with the NEQAIR v14.0 radiation code [49]. The simulation of the wedge in Eilmer3 was carried out using the two-temperature thermochemical model. For the current test conditions, the high temperature gas mixture consists of CO₂, CO, O₂ and O. The chemical reactions occurring in the flow are shown in Table 6.1 along with the corresponding rate coefficients for the modified Arrhenius equation according to

$$k = AT^n \exp\left(-\frac{T}{T_a}\right) \quad 6.1$$

Here k is the reaction rate coefficient, T is the rate controlling temperature, T_a is the activation temperature, A is called the pre-exponential factor (also called the temperature-independent constant) and n is a constant. The reverse reactions are calculated from the corresponding equilibrium constants. For both the carbon dioxide dissociation reaction and the oxygen dissociation reaction, the reaction rates are independent of the collision partner. This assumption of the dissociation reactions being roughly independent of the collision partner is supported by Saxena et al. [28]. The geometrically averaged temperature, $\sqrt{TT_v}$, is used as the controlling temperature for the two dissociation reactions reaction rates as proposed by Park [107]. The neutral exchange reaction is controlled by the translational temperature. The Eilmer3 configuration file which specifies the chemical kinetics model is shown in appendix D.1.

Table 6.1. The kinetics model proposed by Cruden et al [44] for use with the modified Arrhenius equation.

Equation	A (cm ³ mol ⁻¹ s ⁻¹)	n	T _a (K)
CO ₂ + M → CO + O + M	7.47 x 10 ¹²	0.50	52321
O ₂ + M → O + O + M	1.20 x 10 ¹⁴	0.0	54246
CO ₂ + O → CO + O ₂	1.69 x 10 ¹³	0.0	26461

The thermochemical model used in the current work is a two-temperature model without ionization (the free electron is not included as a chemical species). In the two-temperature model, the thermal

exchange model contains only the vibrational relaxation, V-T, mechanism. This is due to the fact that the two-temperature model differentiates only two thermal modes, thus, resulting in only one possible thermal exchange mode. The vibrational relaxation rates depend on the colliding species. For the conditions in the current work, the overall V-T mechanism consists of CO₂ and CO colliding with CO₂, CO and O [107]. The V-T mechanism is modelled using the Landau-Teller equation

$$\frac{d\varepsilon_v(T_v)}{dt} = \frac{\varepsilon_{v,eq}(T) - \varepsilon_v(T_v)}{\tau_v} \quad 6.2$$

where ε_v is the vibrational energy per unit mass (function of the vibrational temperature, T_v), $\varepsilon_{v,eq}$ is the equilibrium vibrational energy per unit mass at the translational temperature, T , and τ_v is called the vibrational relaxation time. The value of τ_v is dependent on the colliding particles, pressure and the translational temperature only, and it is calculated from the Millikan-White equation without Park's high temperature correction [107]. Park's high temperature correction is not believed to be necessary for the conditions concerned in this work because the velocities involved are relatively low. The Millikan-White equation [129] is given by

$$p\tau_v = \exp \left[a \left(T^{-\frac{1}{3}} - b \right) - 18.42 \right] \quad 6.3$$

where p is the pressure, a and b are constants and T is the translational temperature. The values of the two vibrational constants, a and b, used in the equation depend on the colliding species. These values are determined theoretically for all the encounters concerned except the CO₂ - CO₂ encounter, using [129]

$$a = 0.00116\mu^{0.5}\Theta_{vib}^{1.333}, \quad b = 0.015\mu^{0.25} \quad 6.4$$

where μ is the reduced molecular mass in g/mol and Θ is the characteristic temperature of the vibrational mode under consideration in K. For the CO₂ - CO₂ encounter, experimentally determined values by Camac [37] were used where a=36.5 and b=-0.0193. The Eilmer3 configuration file which specifies this thermal kinetics model is shown in appendix D.2.

Table 6.2. Estimated freestream properties from both the PITOT code and radiation measurements used for the CFD simulation of the experiments.

Condition	Source (Experiment number)	P (Pa)	T (K)	T _v (K)	Velocity (m/s)	Mole Fraction CO ₂ /CO/O ₂ /O
2.8 km/s	PITOT Code (x2s2906)	355	1191	2358	2877	0.92/0.054/0.0267/0.0
	Spectroscopic Measurement (x2s3433)	58	1000	1100	2877	0.92/0.054/0.0267/0.0
3.4 km/s	PITOT Code (x2s2905)	360	1378	2758	3484	0.76/0.158/0.076/0.006
	Spectroscopic Measurement (x2s3430)	98	1200	1750	3484	0.76/0.158/0.076/0.006
4.0 km/s	PITOT Code (x2s2904)	150	1281	2815	4077	0.73/0.18/0.083/0.007
	Spectroscopic Measurement (x2s3426)	161	1150	1200	4077	0.73/0.18/0.083/0.007

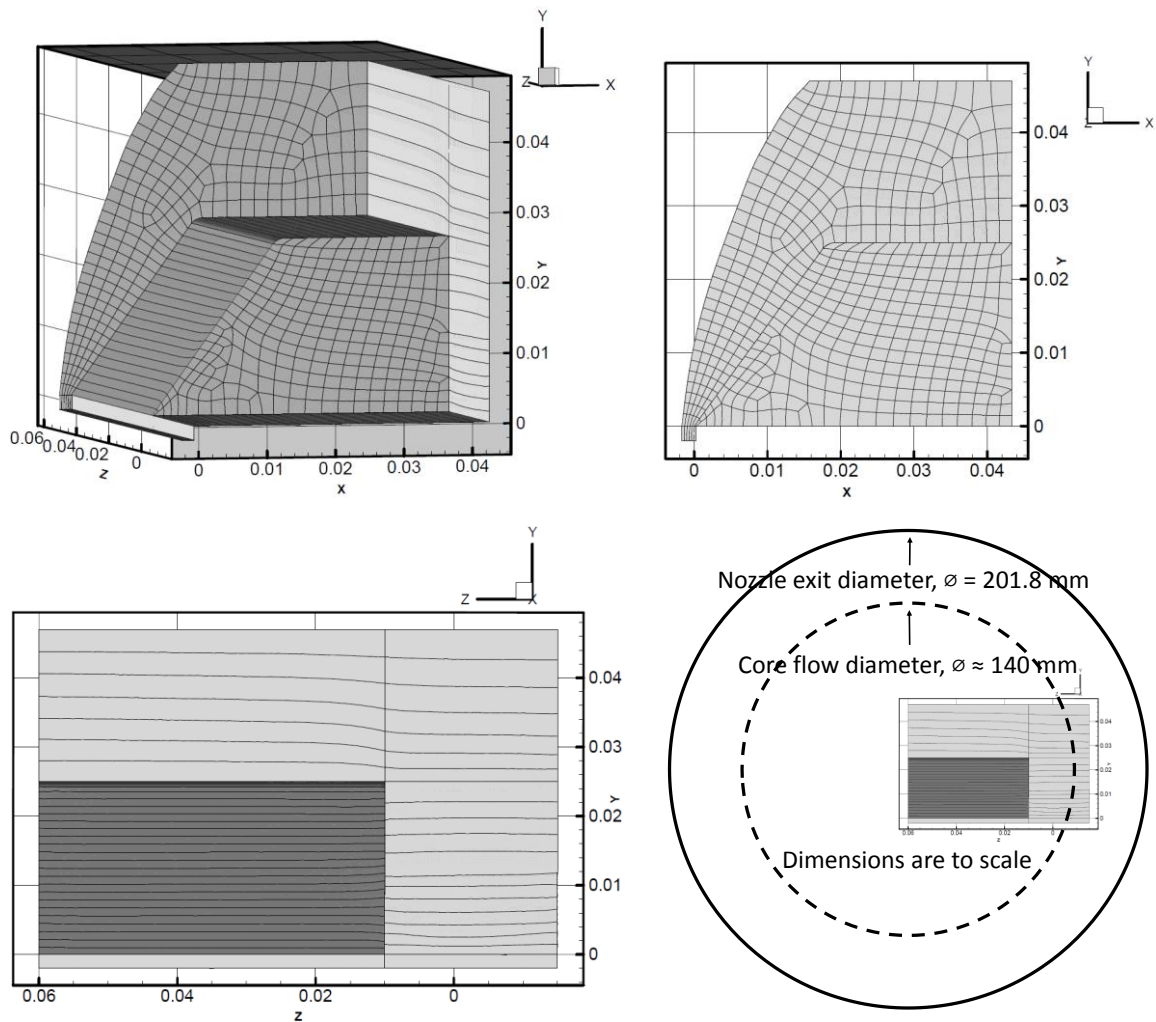


Figure 6.5. Dimensions of the three-dimensional simulation domain for simulating the flowfield around the wedge model. Also shown is the block topology.

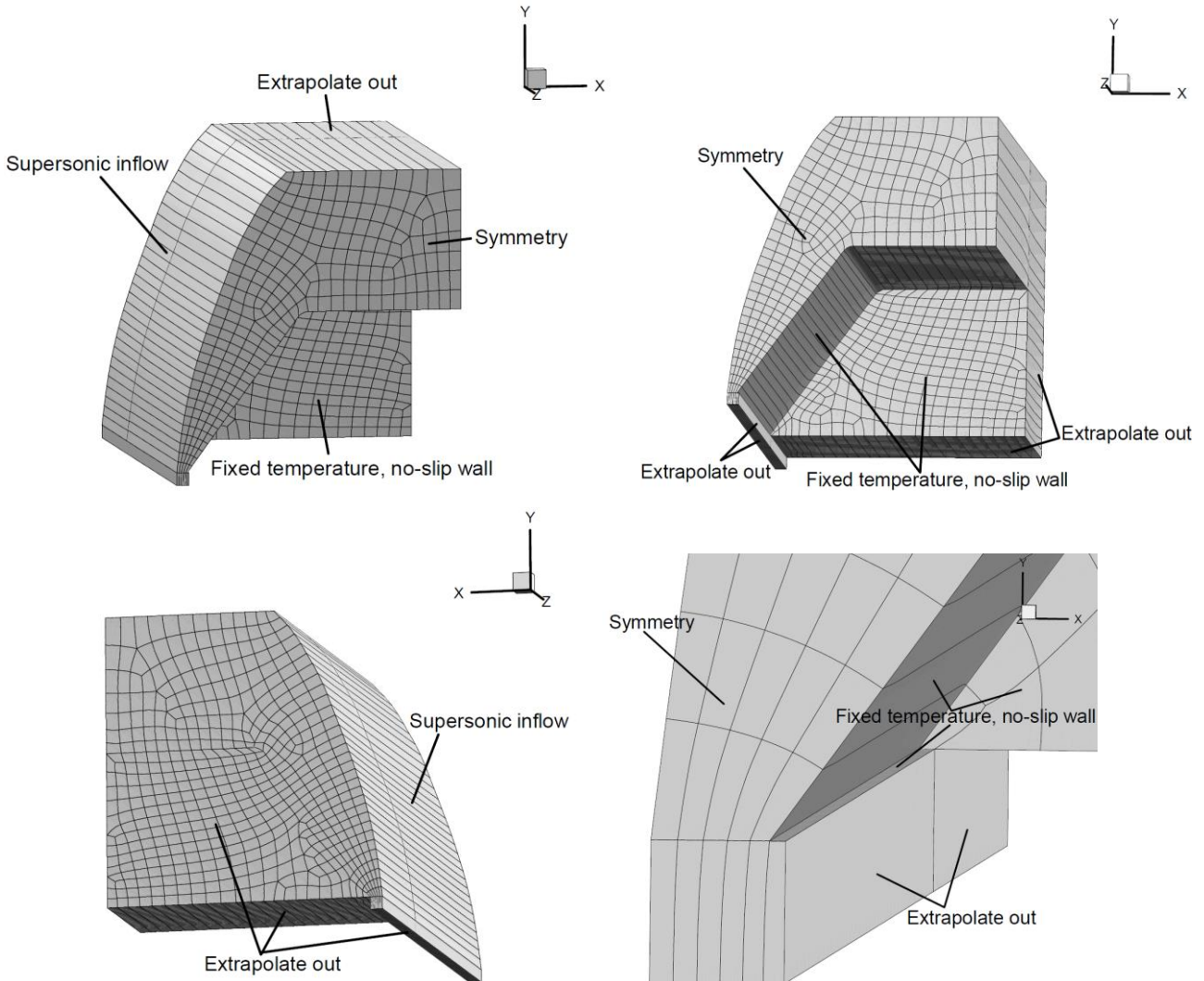


Figure 6.6. Boundary conditions used for the simulation of the flowfield around the wedge. Also shown is the block topology.

Although the test model is a quasi-2d model, three-dimensional numerical simulations of the test model are required due to significant edge effects on the test model. This is discussed in detail in section 6.4. The dimensions of the simulation domain are shown in Figure 6.5. The simulation domain contains approximately 3.1 million cells in total and 773 blocks in total. The mesh is structured and it is created using the Gridpro software [130]. Clustering is done around the model edge and boundary layer. The block topology is shown in Figure 6.5 and Figure 6.6. The boundary conditions are shown in Figure 6.6. The simulation is viscous; fixed temperature (fixed at 300 K), no slip walls are used as the boundary condition for the model surfaces. Supersonic outflow is used as the outflow boundary condition. A supersonic inflow, with the estimated inflow properties in Table 6.2, is used to simulate the freestream. Inflow conditions estimated using both the PITOT code and the spectroscopic measurements are used in the CFD simulation. The comparison with corresponding experimental measurements, in section 6.5, is subsequently done with simulation solutions from both sources of the inflow estimates.

6.4 Three-Dimensional Effects of the Test Model

A perfectly two-dimensional flowfield can only exist if an infinite width model is used. For all finite length two-dimensional test models, there will exist three-dimensional effects. Therefore, in reality, due to edge effects, the width of the flowfield generated around the test model is generally not equal to the width of the test model. The width of the flow significantly affects the line of sight emission spectroscopy measurements as radiation is integrated across the measured lines of sight. Hence, for correct interpretation of the spectroscopic measurements, it is important to characterize the flow around the test model correctly. The particular three-dimensional effects that need to be characterized for interpreting the spectroscopic measurements are the path length of the lines of sight parallel to the width of the model, and the variation of the flow properties across each line of sight.

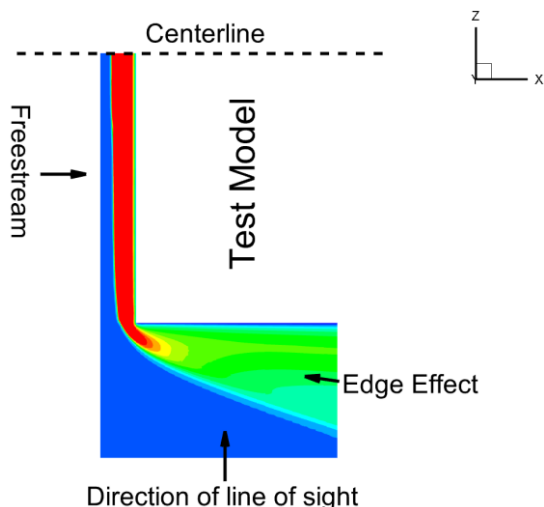


Figure 6.7. Edge effects of the two-dimensional wedge model.

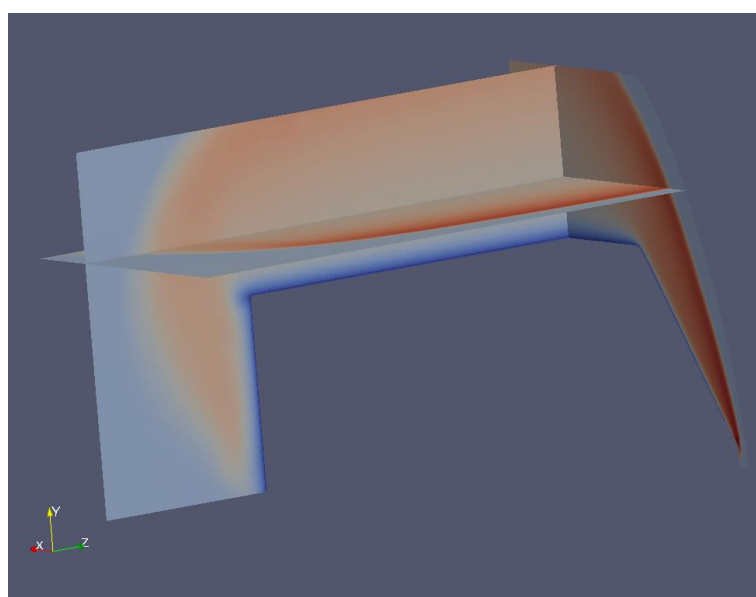


Figure 6.8. A slice in each of the X-Z, X-Y and Y-Z plane showing the temperature contour.

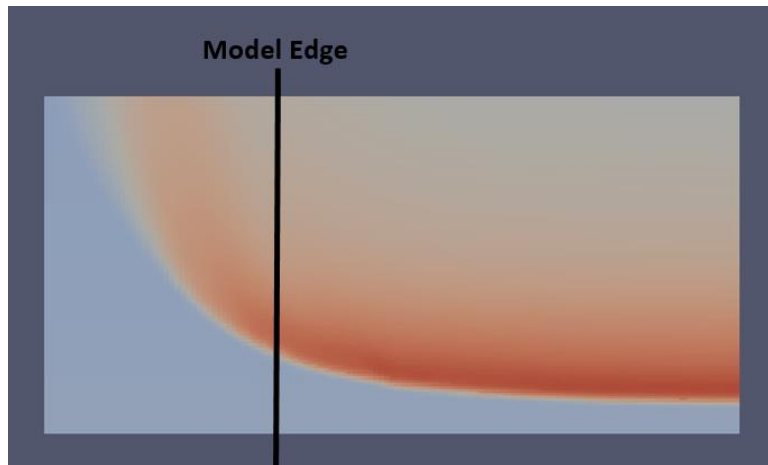


Figure 6.9. A slice in the X-Z plane at 5.75 mm above the top surface of the wedge model showing the temperature contour. Flow direction is from bottom to top.

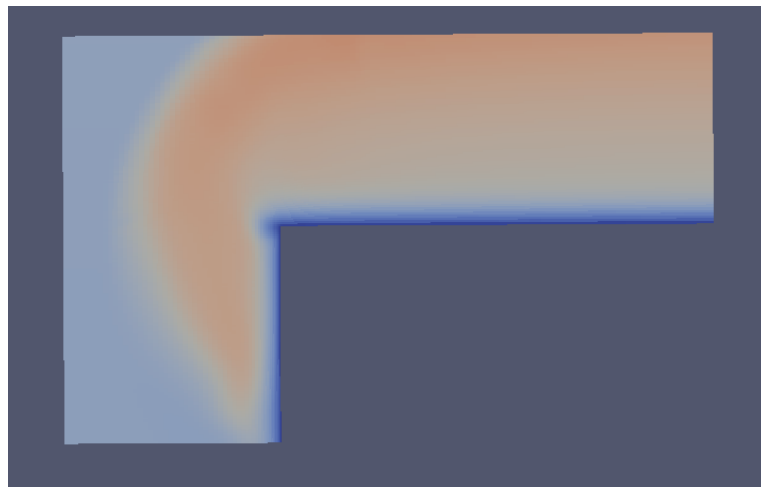


Figure 6.10. A slice in the Y-Z plane at 10 mm behind the convex corner showing the temperature contour.

The three-dimensional, laminar, viscous CFD simulations of the test model, discussed in section 6.3, are used to investigate the edge effects. A slice in each of the three planes in the simulation domain is shown in Figure 6.8 for the 3.4 km/s condition. An X-Z plane slice at 6 mm above the top surface of the test model for the 3.4 km/s condition is shown in Figure 6.9. The results show that near the shock wave, the width of the flow is less than the width of the test model. This is due to the curvature of the shock wave. However, the flow near the back of the test model has a width much greater than the width of the model. This is due to the expansion of the flow beyond the edge of the model.

The flow in the region beyond the edge of the model can produce significant radiation. Line of sight emission spectroscopy measurements along the width of the test model looks through this region of flow beyond the edge of the model, hence the radiation from this region will be captured in the spectroscopic measurements. This is why three-dimensional modelling of the flow around the wedge is critical for comparison with experimental data. Additionally, a Y-Z slice at 10mm behind the

convex corner of the model reveals that the amount of flow beyond the model edge changes only mildly with height above the test model as shown in Figure 6.10. Since the emission spectroscopy measurements differ by only 5 mm in height, the amount of flow beyond the edge of the model is approximately the same for the measurements at different heights above the model, for a given test condition.

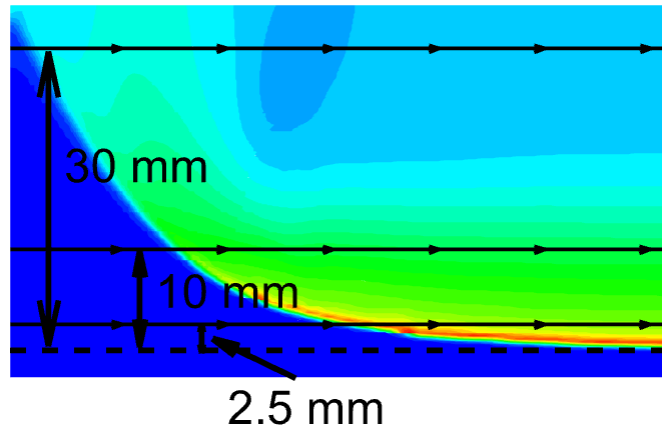


Figure 6.11. Locations of the lines of sight across the test model extracted to study the variation of the flow properties along the width of the test model. Flow direction is from bottom to top.

Using the three-dimensional CFD computations to investigate the variation of the flow properties across each line of sight, the CO₂ number density, rotational temperature and vibrational temperature across three lines of sight are extracted in the X-Y plane at 5.75 mm above the test model for each test condition. The three lines of sight are located at 2.5, 10 and 30 mm behind the shock front at 5.75 mm above the test model in the X-Y plane slice, as illustrated in Figure 6.11. The results for each line of sight are normalized with the corresponding CO₂ number density/temperature value at the centreline. The results are shown in Figure 6.12. This study uses results computed from the PITOT code estimated inflows shown in Table 6.2

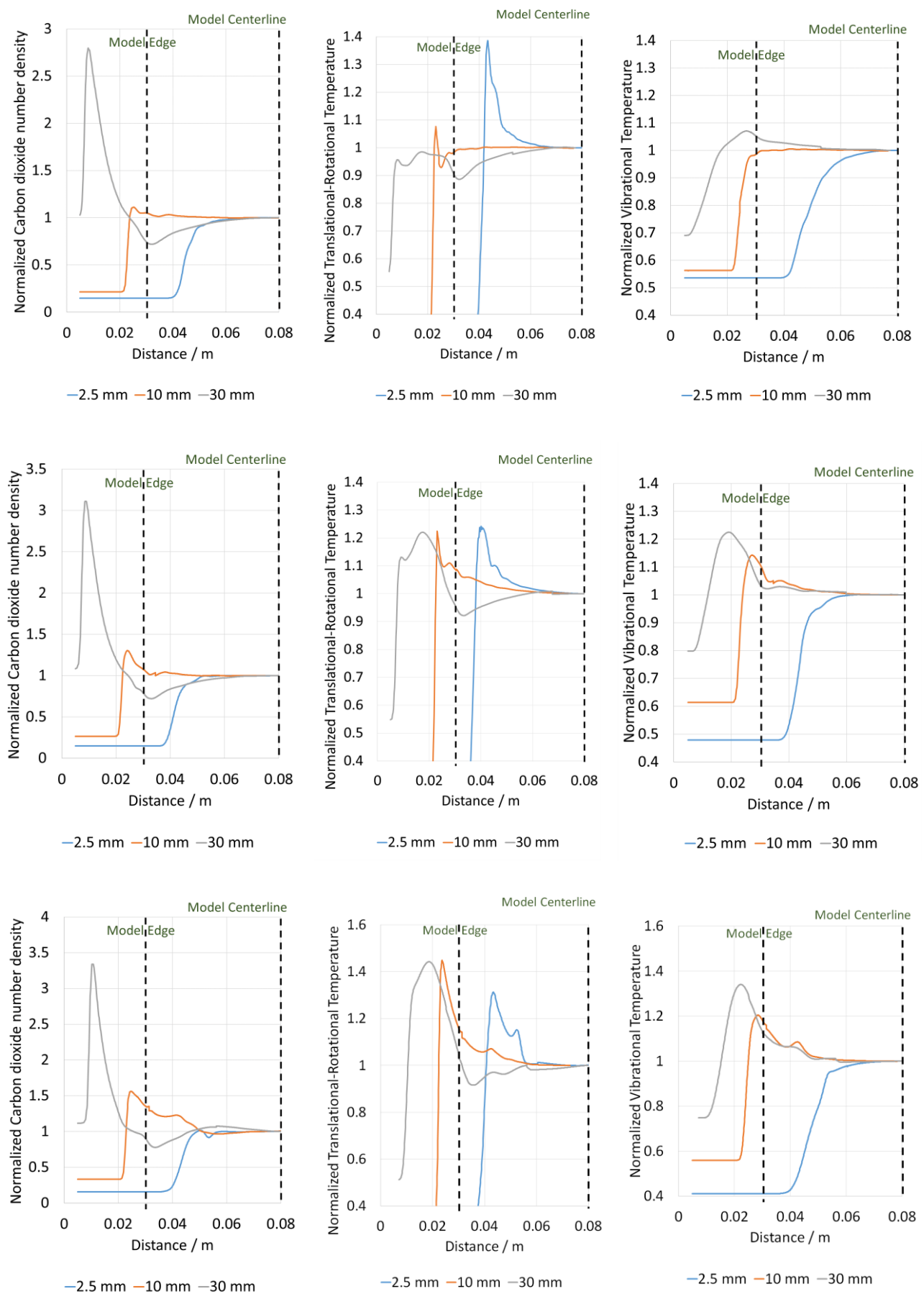


Figure 6.12. Normalized carbon dioxide number density and temperature across lines of sight. Top, middle and bottom rows correspond to the 2.8, 3.4 and 4.0 km/s conditions.

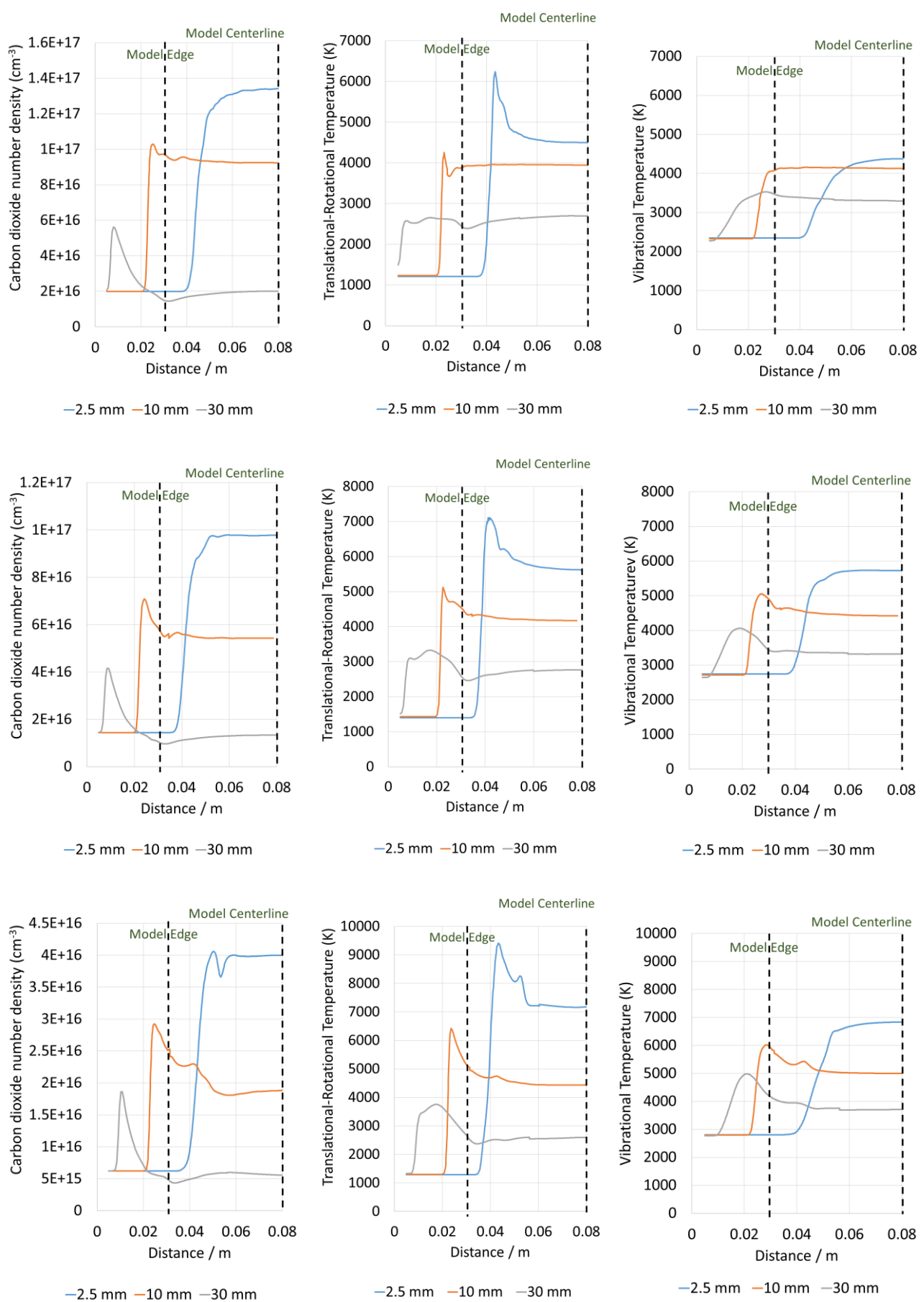


Figure 6.13. Carbon dioxide number density and temperature across lines of sight. Top, middle and bottom rows correspond to the 2.8, 3.4 and 4.0 km/s conditions.

The normalized and absolute results in Figure 6.12 and Figure 6.13 respectively show how the temperatures and CO₂ number density vary across the width of the test model. In particular, it is interesting to look at how the properties vary in the region within the edge of the test model as well as how properties in the flow beyond the edge differ with the properties in the flow within the model edge. For the 2.8 km/s condition, the properties within the edge of the test model are generally uniform across the lines of sight with variations of less than 10 %. The exception is the translational-rotational temperature of the 2.5 mm line of sight in which the line of sight sees through the curved shock wave. This results in the sharp peak in translational-rotational temperature near the end of the line of sight. Another exception is the CO₂ number density of the 30 mm line of sight in which the number density differs markedly within the edge of the test model. In all cases, except the CO₂ number density of the 30 mm line of sight, the properties beyond the edge of the model do not vary more than 10 % from that at the centreline. The CO₂ number density of the 30 mm line of sight is the exception. For the 3.4 km/s condition, as with the 2.8 km/s condition, the properties within the edge of the test model are generally uniform across the lines of sight with variations of less than 10 %. Similar to the 2.8 km/s condition, the exception is also the translational-rotational temperature of the 2.5 mm line of sight and the CO₂ number density of the 30 mm line of sight. For the flow beyond the edge of the model, the variation is less than 20 % with the properties at the centreline. The exception is the CO₂ number density of the 30 mm line of sight. For the 4.0 km/s condition, the properties within the edge of the test model vary by less than 10 % of the properties at the centreline, except the translational-rotational temperature across the 2.5 mm line of sight and the CO₂ number density across the 10 and 30 mm lines of sight. For the flow beyond the edge of the model, the variation is less than 50 % with the properties at the centreline. Like with the 3.4 km/s condition, the expectation is the CO₂ number density of the 30 mm line of sight.

The results in Figure 6.12 and Figure 6.13 show that, in general, the vibrational temperature remains the most constant across each line of sight. In general, the translational-rotational temperature remains the least constant across each line of sight. The CO₂ number density remains rather constant across lines of sights near the shock wave. However, when flow starts to exist beyond the edge of the model, the CO₂ number density varies significantly across lines of sight near the back of the test model. In general, the results show that the non-uniformity in flow properties across lines of sight generally increase in the downstream direction. Overall, the 2.8 km/s condition has the most uniform properties across the lines of sight, while the 4.0 km/s condition has the least uniform properties across the lines of sight.

Three-dimensional effects, in addition to influencing CFD computations, might also influence the experimental temperature and number density estimates, from spectra fitting, presented in chapter 5.

To examine the extent of the influence of the three-dimensional effects on the temperature and number density estimates, flow data along the lines of sight of Figure 6.11 - Figure 6.13 were used to compute a numerical spectra integrated along each line of sight. These numerical spectra were then treated as experimental spectra and the spectra fitting technique used in chapter 5 were used to estimate a rotational temperature, vibrational temperature and CO₂ number density for each line of sight. Visual inspection of these spectra fits showed that the fits are good, like the ones shown in Figure 5.14, and the uncertainties of the spectra fitting estimated values were defined in the same way as described earlier in section 5.4. The estimated temperatures and number densities were compared to the CFD centreline and averaged temperature (averaged along the distance with radiation on the line of sight) for each line of sight. The results are presented in Table 6.3.

Table 6.3. Comparison of the spectra fitting estimated temperatures and number densities, to the CFD centreline and average temperatures and number densities, for each line of sight.

Condition	Line of sight	Tr, K	Tv, K	Tv/Tr	nCO ₂ , 10 ¹⁶ cm ⁻³
		(centreline /average /estimated)	(centreline /average /estimated)	(centreline /average /estimated)	(centreline /average /estimated)
2.8 km/s	2.5 mm	4505 / 4675 / 5000 ± 100	4374 / 3876 / 4050 ± 100	0.97 / 0.83 / 0.81 ± 0.04	13.4 / 11.7 / 11.8 ± 0.5
		3944 / 3923 / 4100 ± 100	4127 / 4044 / 4120 ± 100	1.05 / 1.03 / 1.00 ± 0.05	9.3 / 9.3 / 9.5 ± 0.4
	10 mm	2694 / 2596 / 2700 ± 100	3295 / 3264 / 3213 ± 100	1.22 / 1.26 / 1.19 ± 0.06	2.0 / 2.2 / 2.2 ± 0.1
		5613 / 5659 / 6450 ± 100	5720 / 5040 / 5420 ± 100	1.02 / 0.89 / 0.84 ± 0.04	9.8 / 8.5 / 9.0 ± 0.4
	30 mm	4168 / 4281 / 4450 ± 100	4418 / 4487 / 4519 ± 100	1.06 / 1.05 / 1.02 ± 0.05	5.4 / 5.5 / 5.6 ± 0.3
		2762 / 2804 / 2900 ± 100	3316 / 3431 / 3451 ± 100	1.20 / 1.22 / 1.19 ± 0.06	1.3 / 1.5 / 1.5 ± 0.1
3.4 km/s	2.5 mm	7121 / 7344 / 8000 ± 100	6850 / 5831 / 6180 ± 100	0.96 / 0.79 / 0.77 ± 0.04	4.0 / 3.5 / 3.6 ± 0.2
		4449 / 4719 / 5050 ± 100	5006 / 5144 / 5151 ± 100	1.13 / 1.09 / 1.02 ± 0.05	1.9 / 2.1 / 2.1 ± 0.1
	10 mm	2598 / 2780 / 3050 ± 100	3708 / 3915 / 3935 ± 100	1.43 / 1.41 / 1.29 ± 0.06	0.56 / 0.66 / 0.63 ± 0.03
	30 mm				

The results in Table 6.3 show that, for all three conditions, the influence of three-dimensional effects on spectra fitting estimates increase when moving closer towards the shock front as the 2.5 mm line of sight is the most affected by the three-dimensional effects. This is because the lines of sight closer

to the shock front sees through the shock front due to the shock curvature. The estimated property most affected by three-dimensional effects is the rotational temperature. In all cases, the edge effects cause an over-estimate of rotational temperature from spectra fitting; the over-estimate is most severe for the 2.5 mm line of sight with the estimated rotational temperature being about 10 – 15 % greater than the centreline and averaged rotational temperatures. On the other hand, the edge effects have a lesser influence on the vibrational temperature estimates, with the estimates generally matching within 100 K of the centreline and averaged temperatures. Due to the estimated rotational temperatures being consistently greater than the centreline and averaged rotational temperatures, the estimated T_v/Tr ratios are consistently lower than the centreline and averaged values, though the under-estimates are not large – less than 10 % compared to the averaged values in all cases. Furthermore, as is with the vibrational temperature estimates, the CO₂ number densities estimates are hardly influenced by the edge effects, with the estimated values generally matching the centreline and averaged values within the uncertainties. Finally, overall, the spectra fitting estimated values better represent the averaged values, compared to the centreline values. While the current results are obtained from the CO₂ 4.3 μm band spectra, the same results are obtained from the CO₂ 2.7 μm band spectra because the fitted temperatures match to within 100 K. Thus, the 2.7 μm band results are not presented here.

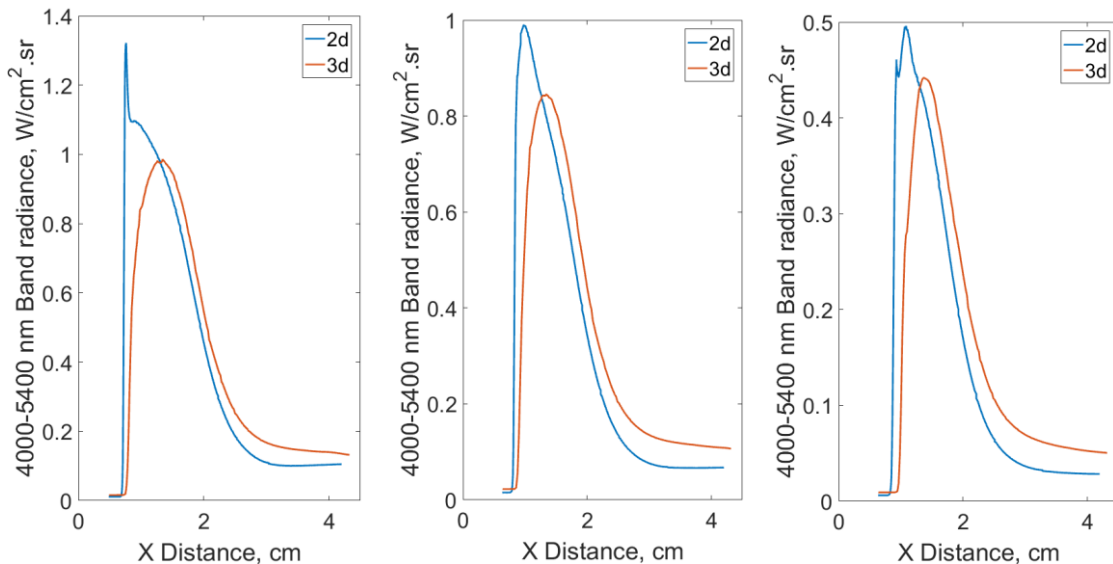


Figure 6.14. Comparison of the band radiance calculated from two-dimensional and three-dimensional simulations. The left, middle and right figures correspond to the 2.8, 3.4 and 4.0 km/s conditions respectively. The two-dimensional radiation calculation assumes a path length of 100 mm.

To investigate the three-dimensional effects on the absolute radiation measurements, NEQAIR calculations using both a two-dimensional and a three-dimensional flowfield are conducted to simulate the emission spectroscopy measurements. For the comparison, the two-dimensional case assumes a width of 100 mm for the lines of sight, which is equal to the width of the wedge model.

The two-dimensional and three-dimensional flowfields are both generated using the Eilmer3 code with the same two-temperature thermochemical model discussed in section 6.3. Line of sight properties at the measurement location of 5.75 mm above the test model in Figure 4.5 are extracted and imported into NEQAIR for radiation calculations. The results are shown on Figure 6.14. The results show that, in general, the radiation is 20 % higher in the two-dimensional case for lines of sight near the shock wave. This is due to the curvature of the shock wave in three-dimensions resulting in fewer radiating particles in these lines of sight. On the other hand, in general, radiation is 30 % higher in the three-dimensional case for lines of sight around the rear of the test model. This is due to the expanded width of the flow beyond the edge of the model resulting in more radiating particles in the lines of sight. Also, in Figure 6.14, the shock standoff is slightly smaller for the three-dimensional case, which is consistent with the investigation by Eichmann [131] who showed that three-dimensional effects decrease the shock standoff.

To support the numerical results, radiation measurements of the flow beyond the edge of the wedge model are taken. The radiation measurement is conducted using the filtered imaging system described in section 4.3. The filtered images are taken by imaging the test model from the top. The results are shown in Figure 6.15. They show significant amounts of radiating flow beyond the edge of the test model downstream of the convex corner. Looking from the top, the radiation beyond the edge is of a comparable value to the radiation inside the edge above the model. The amount of radiating flow beyond the edge increases downstream. Comparing between the three different conditions, the 4.0 km/s condition is observed to have the least flow beyond the edge, while the 2.8 km/s condition is observed to have the most flow beyond the edge. Thus, the amount of flow beyond the edge of the model is seen to decrease with increase in freestream velocity.

From the top views, the measured radiation is strongest at the centreline of the test model and it is estimated that there is a roughly uniform region of about ± 35 mm either side of the centreline before the radiation decreases rapidly. Nevertheless, the size of the region of uniformity seen in Figure 6.15 is believed to be significantly less than that in slices at around 3.25 – 8.25 mm above the test model, which corresponds to the location of the spectroscopic measurements. It is believed that the amount of uniformity in the width direction decreases with increase in height above the test model. This is because the curvature of the shock wave increases with height and the freestream core flow in the width direction decreases with height. Looking from the top, the measurement integrates the radiation through the entire height of the flowfield, thus, observing more three-dimensional effects. Therefore, for the emission spectroscopy measurements in the current work, the flow properties across the measured lines of sight should be more uniform than what it may seem from Figure 6.15.

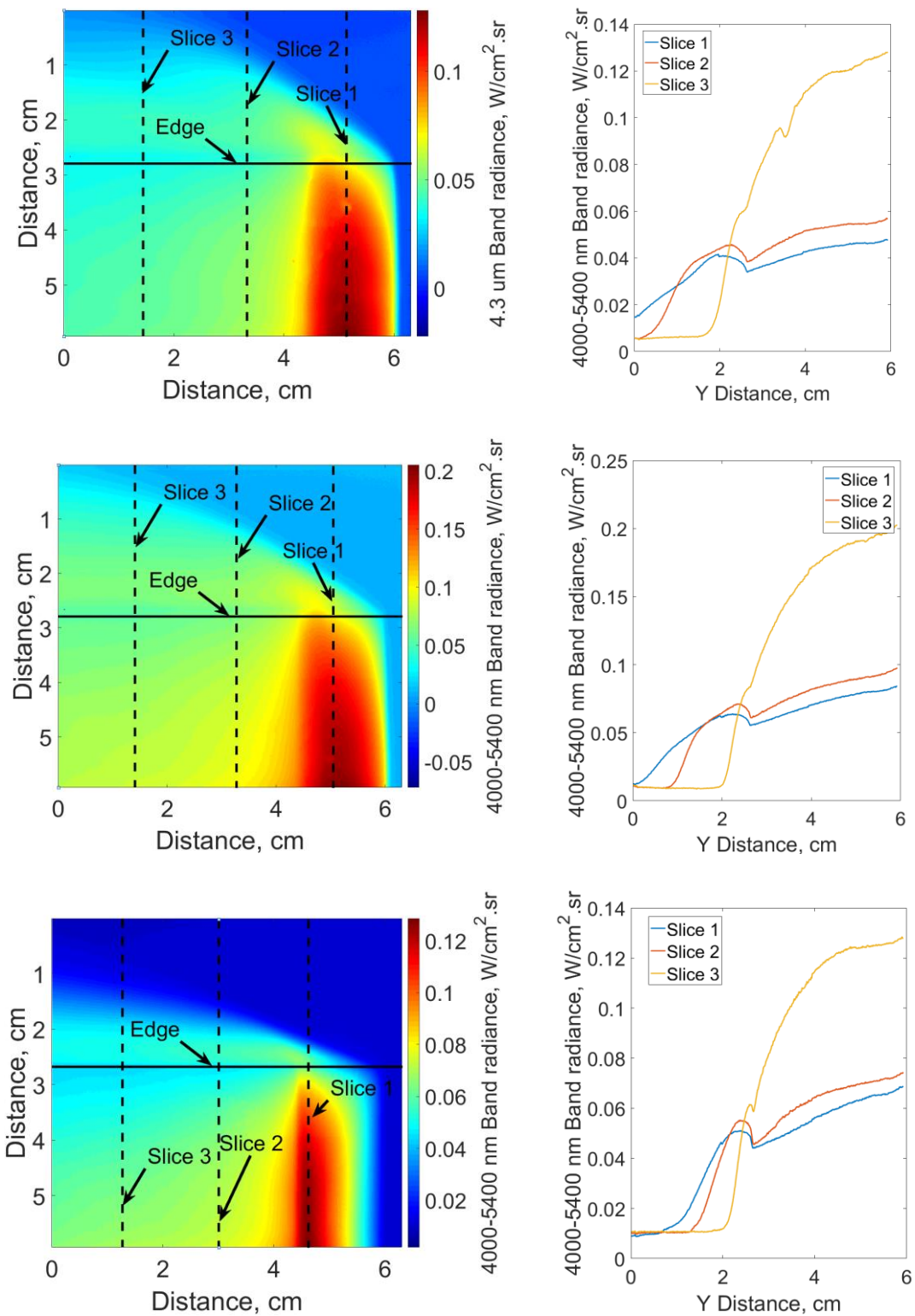


Figure 6.15. Filtered images of the radiating flow beyond the edge of the wedge model; flow direction is from right to left. Vertical slices are extracted at various locations in the images and plotted in the graphs in the right column. The top, middle and bottom rows correspond to the 2.8, 3.4 and 4.0 km/s conditions respectively.

In conclusion, the results presented in this section show that the flowfield cannot be well approximated as two-dimensional. Three-dimensional analysis is required for correct interpretation of the experimental measurements.

6.5 Comparison between CFD and experiment

In this section, the available experimental measurements of the flow around the wedge model are compared to that calculated from numerical simulations using the computational methodology described in section 6.3. In particular, the comparison between experimental measurements and numerical predictions is done for the shock wave location, band radiance, temperatures, CO₂ number density and the degree of thermal non-equilibrium.

6.5.1 Shock Wave Location

Given the correct inflow, the two-temperature model has been shown to be capable of predicting the shock wave location well at similar conditions [52] [89] [105]. Therefore, comparing the computed shock wave location to the measured shock wave location can help assess the validity of the estimated inflow conditions. Significant discrepancy between the measured shock wave location and the computed shock wave location would most likely indicate the inflow is inaccurate [90]. However, a good match in the location of the shock wave would not necessarily indicate the inflow is accurate because there may exist a large range of inflow conditions that give a good match in the shock wave location. In section 3.4.4, the measured shock wave locations from the high-speed videos were compared to the computed shock wave location in two-dimensional simulations using the inflows estimated from the PITOT code. Further work is presented in the current section by comparing multiple measurements of the shock wave location from the filtered images, discussed in section 4.3, with the computed shock wave location in three-dimensional simulations (Eilmer3) using the inflows estimated from the PITOT code and from the spectroscopic measurements in Table 6.2.

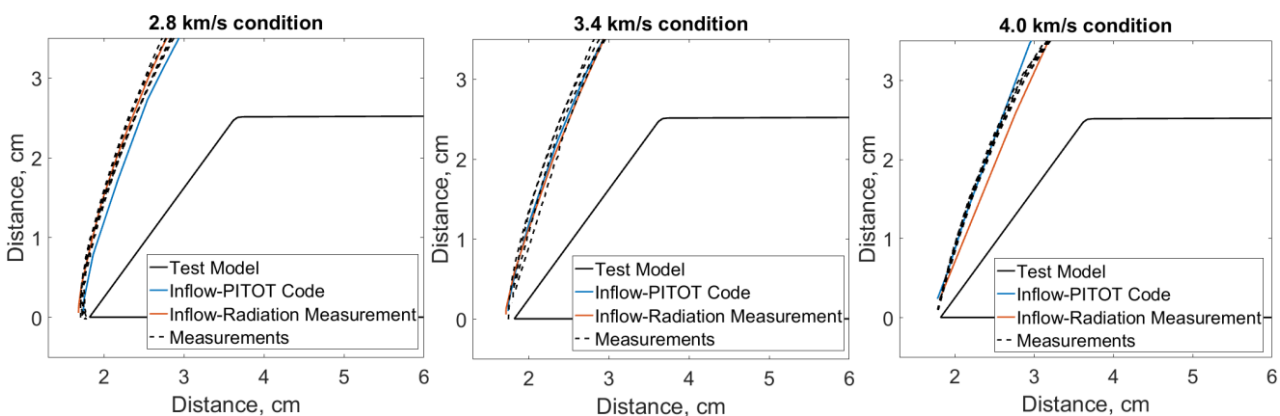


Figure 6.16. Comparison of the measured shock wave locations to the simulated shock wave locations.

The results of the comparison of the shock wave locations, presented in Figure 6.16, show that the inflow from the PITOT code compute shock wave locations that agree well with the measured

locations for all three test conditions. This is consistent with the result in section 3.4.4 where the same comparison is made with shock wave locations computed from two-dimensional simulations. In addition, for the 2.8 and 3.4 km/s conditions in particular, the shock locations computed from the spectroscopic measurement inflows also matched well with measurements. For the 2.8 and 3.4 km/s condition, although the spectroscopic measurement inflow has distinctly less thermochemical excitation than the PITOT code inflow, the shock location computed using the spectroscopic measurement inflow still matched well with the measured shock location. This is because the shock location also depends on the inflow density [132] [133]. For the 2.8 and 3.4 km/s condition, the spectroscopic measurement estimated inflow has a significantly lower density than the PITOT code estimated inflow. Hence, the effect of the difference in the inflow density cancelled out the effect of the difference in the inflow thermochemical excitation on the shock location. For the 4.0 km/s condition, the shock location computed using the inflow estimated from the spectroscopic measurements is slightly different to that computed from the PITOT code inflow. This difference in shock location is due to the two inflows having significantly different degrees of thermochemical excitation but similar inflow densities. Nevertheless, this difference in shock location, although observable, is also small. Such a small discrepancy may be attributed to the limitations of the numerical model at predicting the shock location [105].

As there are no significant discrepancies between the measured shock wave location and the computed shock wave location, the results in Figure 6.16 do not show any of the inflow estimates as being certainly incorrect. Nevertheless, the results also do not provide any information as to which inflow estimates are more accurate.

6.5.2 Band Radiance

To compare the numerically predicted band radiance with the measured band radiance, scaling factors are determined. The scaling factor is defined as the measured band radiance divided by the corresponding numerically predicted band radiance. A scaling factor of one indicates a perfect match between experiment and numerical prediction. A scaling factor of more than one indicates that the numerical predictions underestimate the radiation, while a scaling factor of less than one indicates that the numerical predictions over-estimate the radiation. In the current work, for each measurement, scaling factors are obtained at two locations in the band radiance profile, as shown in Figure 6.17; one at the peak of the band radiance profile, referred to as ‘point 1’, and one in the expanded flow region, referred to as ‘point 2’. The scaling factors are obtained from simulations using the freestream estimate from both the PITOT code and from the spectroscopic measurements. The inflow conditions used in the simulations are shown in Table 6.2. The calculated scaling factors for both the $2.7 \mu\text{m}$ and

$4.3 \mu\text{m}$ band at all the measured locations and for all the conditions are shown in Figure 6.18. The plots in Figure 6.18 shows the scaling factors at various locations against the freestream velocity of the test conditions. The error bars shown correspond to the bounds of the band radiance measured due to the shot-to-shot variation discussed in section 4.2.6.

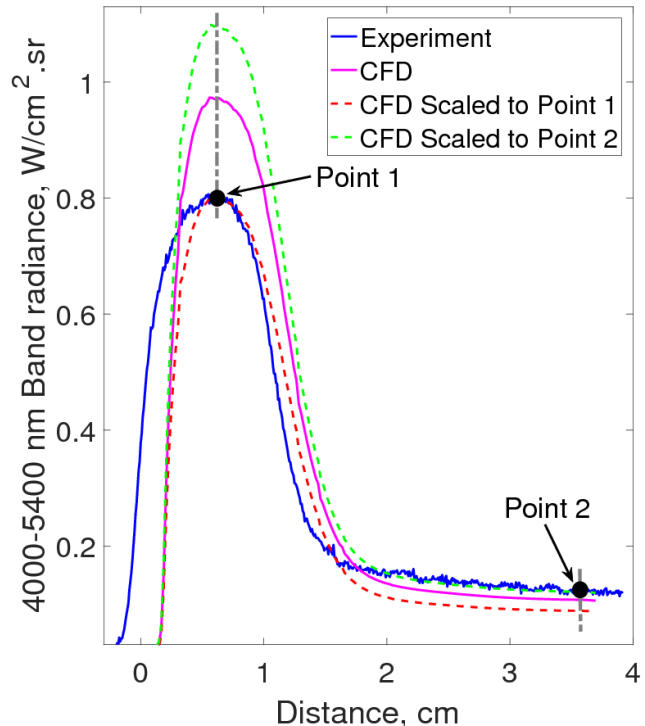


Figure 6.17. Scaling the CFD curve to match the experimentally measured curve at ‘point 1’ and ‘point 2’.

First, it is necessary to examine how the scaling factors differ between simulations done using the freestream condition estimated from the spectroscopic measurements and the freestream condition estimated from the PITOT code. From Figure 6.18, the freestream estimates from the two different sources produce significantly different results, particularly for the case of the 2.8 km/s and 3.4 km/s condition. For the 2.8 and 3.4 km/s condition, the freestream derived from the spectroscopic measurements has a significantly lower pressure, about 300 Pa lower, and a slightly lower temperature, about 200 K lower, compared to that derived from the PITOT code, while the velocity and mole fractions are identical. For the 2.8 km/s condition, the $4.3 \mu\text{m}$ band radiance at point 1 is slightly (less than 30 %) under-predicted by Eilmer3/NEQAIR when using the freestream condition estimated from the spectroscopic measurements. On the other hand, the $4.3 \mu\text{m}$ band radiance at point 1 is significantly, almost 200 %, over-predicted by Eilmer3/NEQAIR when using the freestream condition estimated from the PITOT code. An even larger variation is seen for the $2.7 \mu\text{m}$ band radiance at point 1 where the emission is almost 200 % over-predicted when using the freestream condition estimated from the PITOT code but under-predicted by a factor of around 2 when using the freestream condition estimated from the spectroscopic measurements. For both the 2.7 and $4.3 \mu\text{m}$

band, the errors of under-estimation and over-estimation at point 1 are carried on to the respective point 2. Therefore, similarly large variations in emission are seen at point 2 between the two different freestream estimates. Additionally, similarly large variations are seen for the 3.4 km/s condition where the emission is over-estimated by the freestream estimated from the PITOT code and under-estimated by the freestream estimated from the spectroscopic measurements.

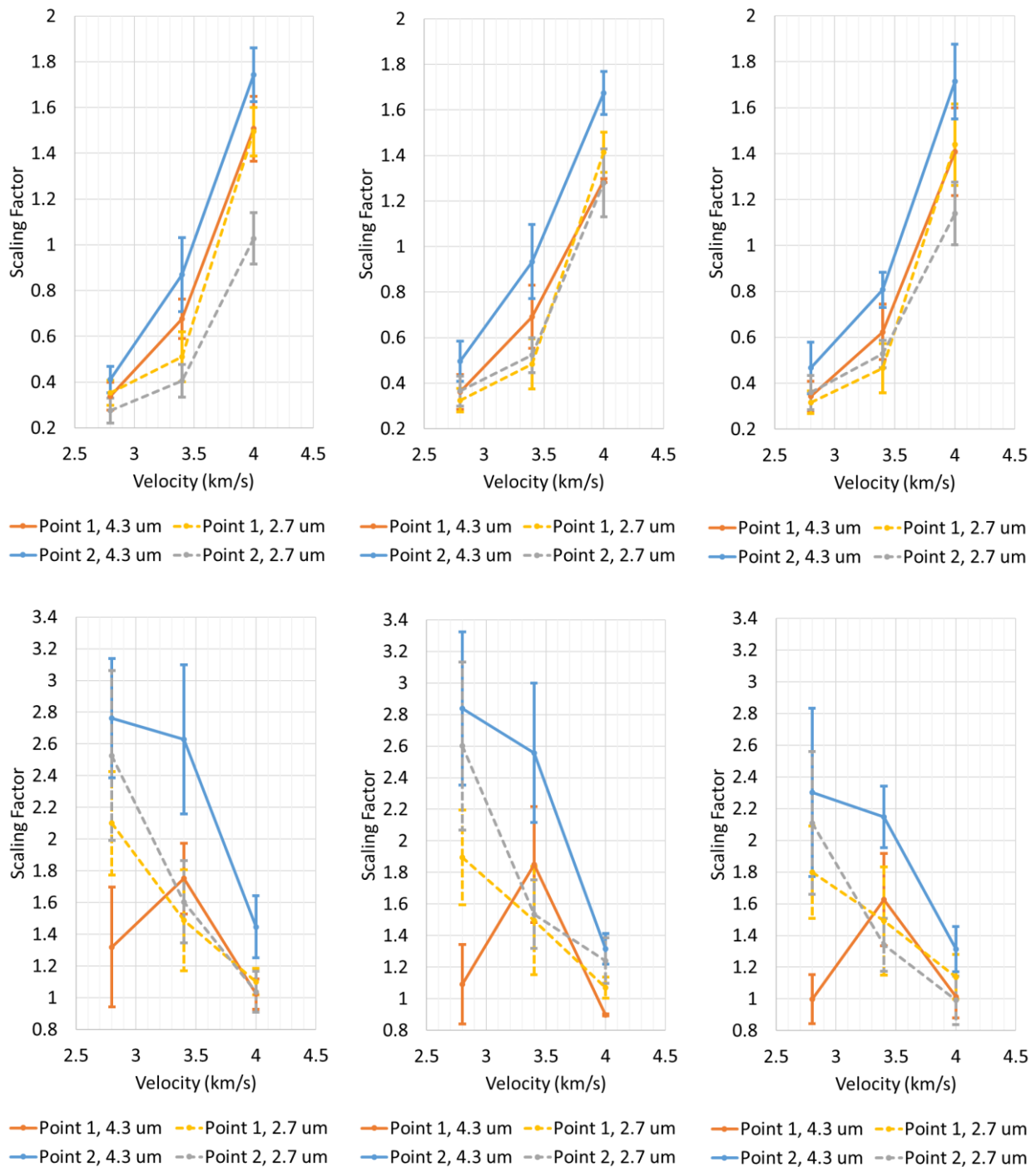


Figure 6.18. Scaling factors for point 1 and 2 and for the 2.7 and 4.3 μm band. The top and bottom rows correspond to comparisons made with the PITOT code and spectroscopic measurement estimated inflow conditions respectively. The left, middle and right columns correspond to the measurements at 3.25, 5.75 and 8.25 mm above the test model.

Substantial sensitivity of the wedge flow radiation emission on the freestream condition is demonstrated by the 4.0 km/s condition. For the 4.0 km/s condition, the freestream estimate derived from the radiation measurements has a slightly higher pressure, about 10 Pa higher, and a slightly lower temperature, about 100 K, compared to that derived from the PITOT code. The velocity and mole fractions are identical. The only significant difference is that the vibrational temperature estimated from the spectroscopic measurement is more than 1000 K lower than that from the PITOT code. The results show that the radiation calculated from the inflow estimated from the PITOT code is up to 40 % lower than that calculated with the freestream estimated from the spectroscopic measurement even though the freestream estimated with the PITOT code has a significantly higher vibrational temperature. Thus, it seems that the inflow estimated from the radiation measurements computes more radiation because the 10 Pa greater in freestream pressure outweighs the 1000 K lower in freestream vibrational temperature. Subsequently, this result indicates that the freestream CO₂ number density has significantly more influence on the flowfield emission than the freestream vibrational temperature.

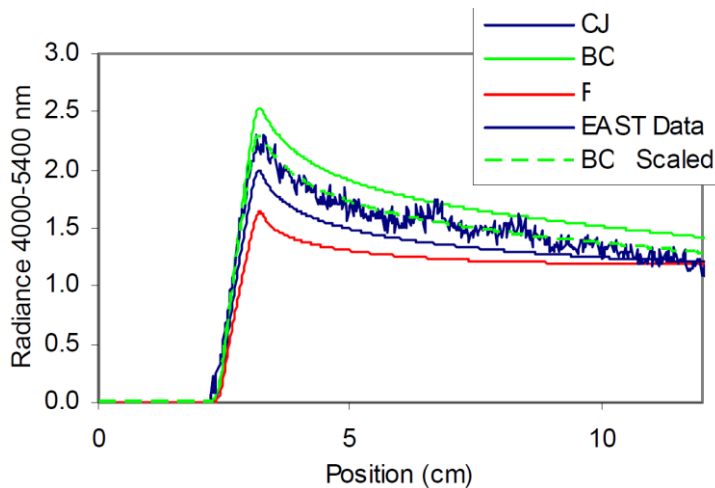


Figure 6.19. Comparison of post-shock band radiance between experiment and CFD using various chemical kinetics model [44]. The model ‘BC’ is the same model used in the current work.

The comparison of the measured radiation with the computed radiation is supposed to provide an assessment of how well the current numerical models predict the CO₂ radiating flow. However, due to the uncertainty in the freestream conditions generated in the expansion tube, it is difficult to provide any conclusions in regards to how well the current numerical models can predict the CO₂ radiation. This is particularly the case for the 2.8 and 3.4 km/s condition where significant uncertainties exist in the freestream condition, as discussed in chapter 5. To further assess the accuracy of the estimated inflow conditions, the scaling factors derived in the current work are compared to the scaling factors derived by Cruden et al. [44], shown in Figure 6.20, which are considered accurate benchmark data. Cruden et al. [44] showed that, using the same chemical kinetics model described in section 6.3, the

entire non-equilibrium relaxation profile of the radiance behind shock waves travelling in pure CO₂ can be reconciled between numerical predictions and experimental measurements by applying a constant scaling factor. This is illustrated in Figure 6.19 where the chemical kinetics model ‘BC’ is the same model used in the CFD simulations in the current work. Hence, their scaling factor is independent of the location behind the shock wave. In the current work, as mentioned in section 5.5, the point 1 on Figure 6.18 for measurements at 3.25 mm above the test model corresponds to a post-shock measurement in the flowfield around the wedge model. Thus, the scaling factors at point 1 for measurements at 3.25 mm above the wedge model can be compared to the scaling factors from Cruden et al. for similar conditions.

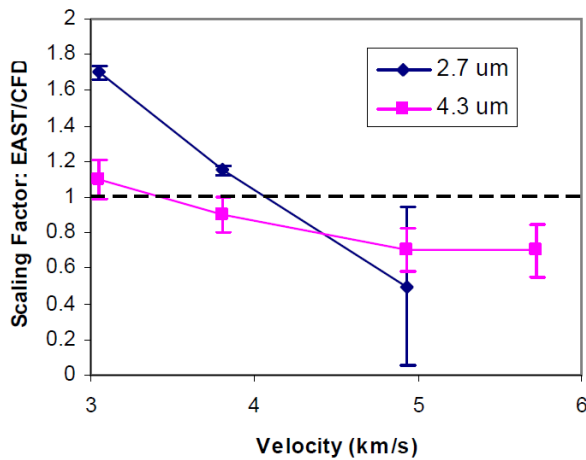


Figure 6.20. The scaling factors behind normal shock waves derived by Cruden et al. [44].

For the 2.8 and 3.4 km/s condition, neither the freestream estimated from the PITOT code nor the freestream estimated from the spectroscopic measurements are believed to be good representations of the actual freestream conditions. This has already been discussed in detail in section 5.3 and 5.5. The results in Figure 6.18 further support this belief. As discussed in section 5.5, the 3.4 km/s condition in the current work is comparable to the 3.1 km/s of Cruden et al. [44]. The scaling factors obtained for the 3.4 km/s condition at point 1 at 3.25 mm above the test model is inconsistent with the scaling factors derived by Cruden et al. [44] for their 3.1 km/s condition. The scaling factor for the 3.1 km/s condition for the 4.3 μm band is 1.1, as shown on Figure 6.20. This is significantly different to the scaling factor of 0.7 and 1.7, from the PITOT code and spectroscopic measurement estimated inflow conditions respectively, for the 3.4 km/s condition at point 1 at 3.25 mm above the test model. The discrepancy seen between the scaling factor from Cruden et al. and the scaling factor from the current work is believed to be due to incorrect freestream estimates of the 3.4 km/s condition in this work. For the 2.8 km/s condition, Cruden et al. do not have data for a similar condition. However, from the trend in Figure 6.20, the fact that the inflow estimate from the PITOT code for the 2.8 km/s condition significantly over-predicts the measured radiation at point 1 at 3.25 mm above

the test model, shown in Figure 6.18, indicates that this inflow estimate is likely incorrect. This is because the trend in Figure 6.20 shows that the numerical calculations should under-predict the measured radiation for this condition. On the other hand, the scaling factor of 1.3 for the 2.8 km/s condition at point 1 at 3.25 mm above the test model, derived from using the inflow estimated from the spectroscopic measurements, is possible given the trend in Figure 6.20. Nevertheless, this still does not confirm whether or not this inflow estimate is correct.

Compared to the 2.8 and 3.4 km/s condition, the 4.0 km/s condition is believed to be characterized well, as discussed in detail in section 5.3 and 5.5. For the 4.0 km/s condition, the scaling factors presented in the current section, when compared to that from the work of Cruden et al. [44], show that the inflow estimated using the spectroscopic measurements is likely a more accurate representation compared to that estimated from the PITOT code. The scaling factor at point 1 at 3.25 mm above the test model for the 4.0 km/s condition is comparable to the scaling factor of the 3.75 km/s experiment by Cruden et al. [44]. The scaling factors in this work is approximately 1.0 and 1.1 for the 4.3 and 2.7 μm band radiance respectively using the inflow estimated from the spectroscopic measurements. This result compares well with scaling factors of 0.9 and 1.1 for the 4.3 and 2.7 μm band radiance respectively obtained by Cruden et al. for their 3.75 km/s condition. Thus, the freestream estimated from the spectroscopic measurements is believed to be the most accurate representation of the actual freestream for the 4.0 km/s test condition.

Given the inflow condition is accurately defined, obtaining the scaling factors is useful for examining how well the current numerical models predict the 2.7 and 4.3 μm band radiance. As only the inflow of the 4.0 km/s condition estimated by the spectroscopic measurements is believed to be accurate, the following discussion is limited to this case. Comparing scaling factors at different heights above the test model, variations of less than 0.2 are observed and no distinct patterns can be observed in the variations to correlate to the change in height. In general, the computations and measurements match within 20 % and 40 % for the radiation at point 1 and point 2 respectively. Examining how the scaling factors vary between that of the 2.7 μm and 4.3 μm band at the same location, a pattern observed is that, at point 1, the scaling factors for the 2.7 μm band is consistently about 0.1 – 0.2 greater than that of the 4.3 μm band. Conversely, at point 2, the scaling factors for the 4.3 μm band is consistently about 0.1 – 0.4 greater than that of the 2.7 μm band. Examining how the scaling factors vary between point 1 and point 2, a pattern observed is that the scaling factor for the 4.3 μm band at point 2 is consistently larger than that at point 1. The scaling factor for the 4.3 μm band changes from a value of approximately 1 at point 1 to a value of approximately 1.3 – 1.4 at point 2. This result may indicate that the expansion fan causes an under-estimate of the 4.3 μm band radiance in the Eilmer3/NEQAIR simulation when compared to experiments. On the other hand, the change in scaling factor for the 2.7

μm band between point 1 and point 2 is seen to have no consistent pattern and it changes by less than 0.2.

6.5.3 Temperatures and carbon dioxide number density

As the previous section showed that there is significant discrepancy between the radiation measured and the radiation calculated, it is now necessary to investigate the cause of this discrepancy. Same band radiance values can be obtained from different combinations of rotational temperature, vibrational temperature and CO₂ number density. Therefore, it is necessary to compare the rotational temperature, vibrational temperature and CO₂ number density deduced from experiments to those calculated in CFD in order to examine the cause of the discrepancy in band radiance. The results are shown in Figure 6.21 to Figure 6.23 where the lower and upper bounds of the properties deduced from experiments are compared to the properties calculated from CFD using the two different freestream estimates for each test condition. Since it was shown in section 6.4 that the flow properties change noticeably along the width of the flowfield, the CFD results presented in Figure 6.21 to Figure 6.23 are the average values along the width of the flowfield. The inflow conditions used in the numerical simulations are presented in Table 6.2.

Firstly, from the results shown in Figure 6.21 to Figure 6.23, the spike in rotational temperature at the shock front seen in the numerical results are not observed in the experimental results. This is caused by a combination of shock wave oscillation due to noise, spatial resolution limitations of the spectroscopy system, three-dimensional effects (in particular, shock wave curvature) and the lack of emission at the shock front. A general observation is that the temperatures are consistently over-estimated in the CFD in the regions near the beginning of the expansion fan (post-shock region). The results show that the simulations compute temperatures at the measured post-shock location that are close to the post-shock chemically frozen temperatures calculated in section 5.5 in Table 5.7. The over-estimation of the temperature by CFD is particularly severe for the 2.8 and 3.4 km/s condition. Examining the translational-rotational temperature, the over-estimate is almost 1500 K for the 2.8 km/s condition and about 1000 K for the 3.4 km/s condition. This large discrepancy seen in the flowfield temperature is believed to be caused by poorly characterized inflow conditions instead of any issues relating to the thermochemical kinetics model used to simulate the flowfield, as discussed earlier in section 5.5. In particular, presented in detail in section 6.6, the CO₂ dissociation rate would have to be more than an order of magnitude greater than that used in the current CFD simulations in order to compute post-shock temperatures close to the experimental values and this is very unlikely.

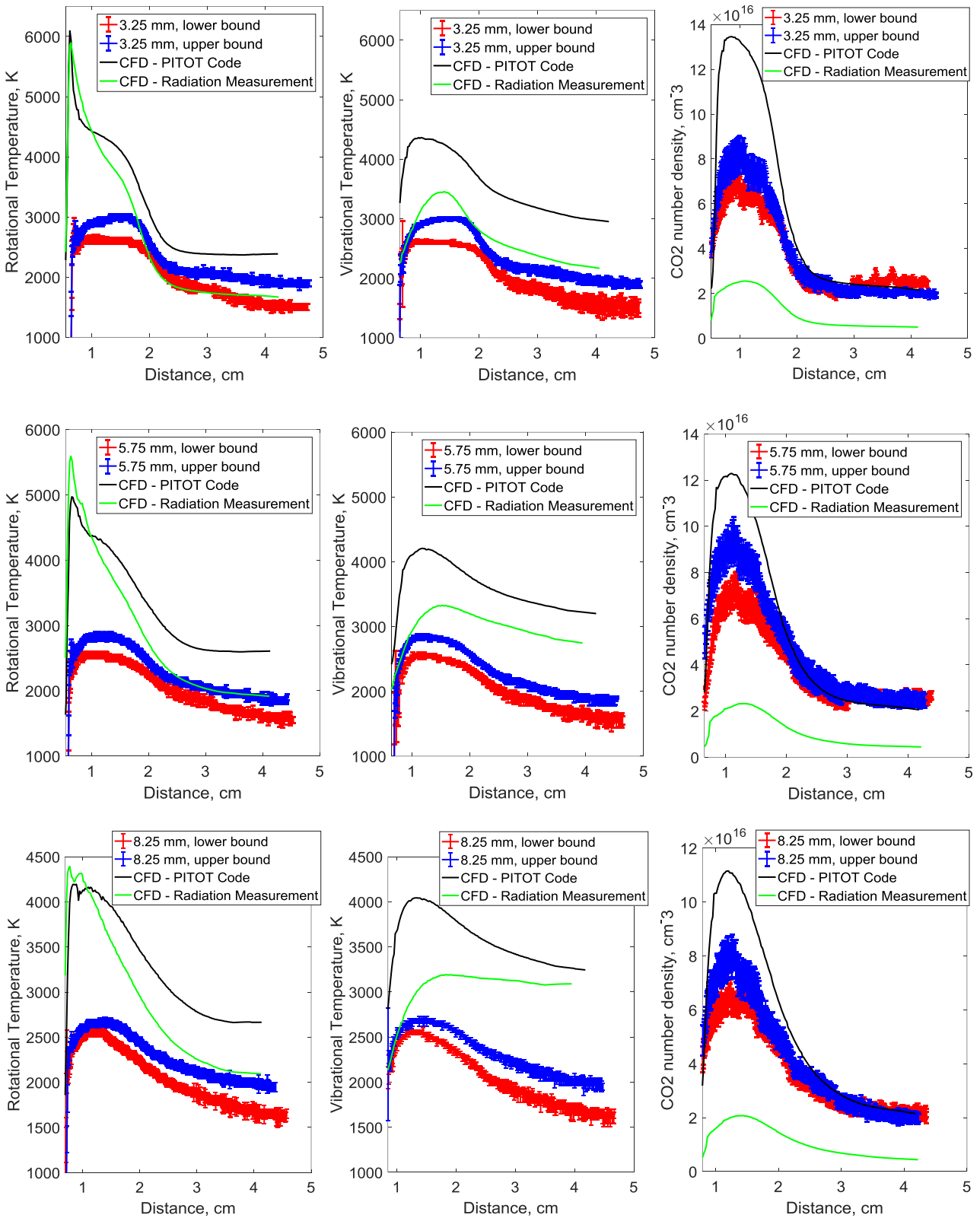


Figure 6.21. Comparison of the rotational temperature, vibrational temperature and CO₂ number density between experiment and CFD for the 2.8 km/s condition. The top, middle and bottom row correspond to the 3.25, 5.75 and 8.25 mm measurement above the test model.

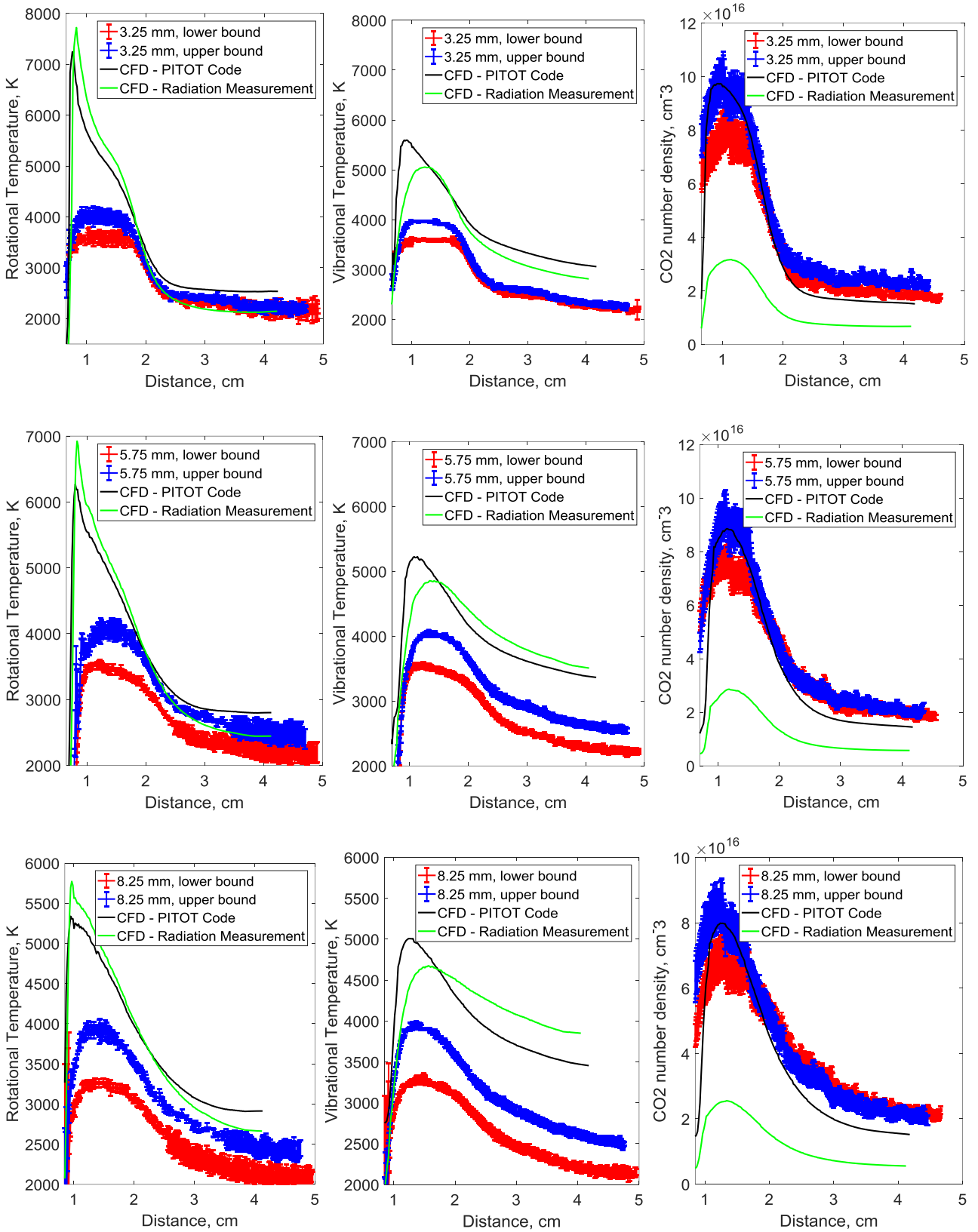


Figure 6.22. Comparison of the rotational temperature, vibrational temperature and CO₂ number density between experiment and CFD for the 3.4 km/s condition. The top, middle and bottom row correspond to the 3.25, 5.75 and 8.25 mm measurement above the test model.

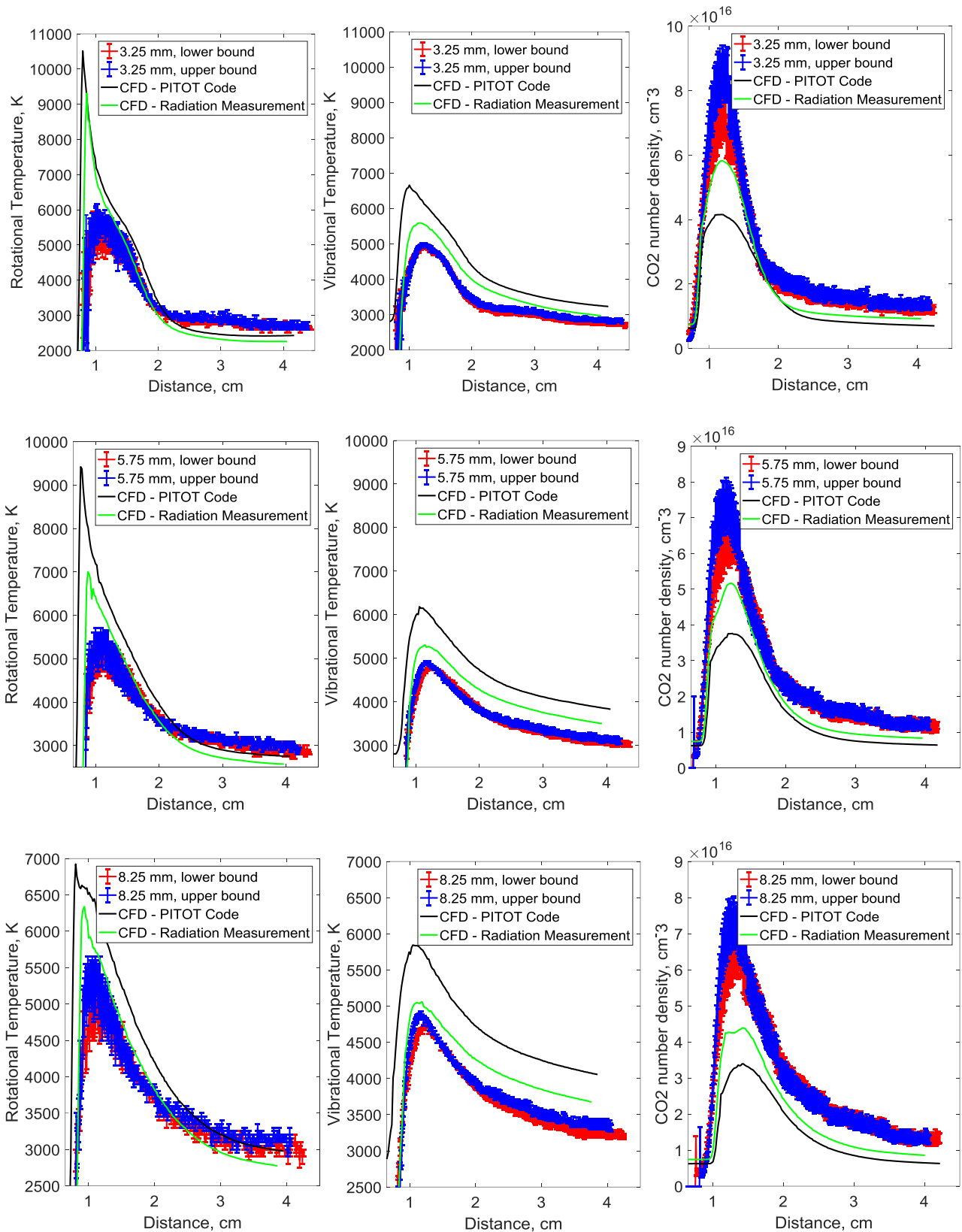


Figure 6.23. Comparison of the rotational temperature, vibrational temperature and CO_2 number density between experiment and CFD for the 4.0 km/s condition. The top, middle and bottom row correspond to the 3.25, 5.75 and 8.25 mm measurement above the test model.

Only slight over-estimations in temperature of about 500 K (approximately 10 %) at the measured post-shock location are seen in the 4.0 km/s condition when using the freestream estimated from the spectroscopic measurements. For the 4.0 km/s condition, it is possible that the moderate discrepancy seen in flowfield temperature is caused by a combination of small inaccuracies in the estimated inflow velocity and in the CO₂ dissociation rate. As discussed in section 6.5.2, the 4.0 km/s condition inflow estimated from the radiation measurements is believed to be an accurate representation of the actual freestream. However, it is still possible for small inaccuracies to exist in the estimated inflow velocity to contribute to the 500 K temperature discrepancy in the flowfield. A decrease in inflow velocity by only 100 m/s would decrease the post-shock frozen temperature by 200 K. At the same time, errors in the CO₂ dissociation rate can also contribute to the observed temperature discrepancy, shown later in section 6.6. Hence, the discrepancy in flowfield temperature in the post-shock region may be caused by a combination of small inaccuracies in the estimated inflow velocity and in the CO₂ dissociation rate.

In general, comparing between the three test conditions, the best match in temperature in the expanded flow region between CFD and experiment is seen for the 4.0 km/s condition because it has the best agreement in post-shock temperature. In addition, due to the significant amount of thermal non-equilibrium predicted by the CFD, discussed in further detail in section 6.5.4, the rotational temperature is much lower than the vibrational temperature in the expanded flow region for all three conditions. Consequently, in the case of the 3.4 km/s condition, the rotational temperature calculated by CFD matches well with the measured temperature in the expanded flow region even though the post-shock temperature is over-predicted by CFD. In the case of the 4.0 km/s condition, the freestream estimated from the radiation measurement even slightly under-predicts the rotational temperature in the expanded flow region. On the other hand, the vibrational temperature is significantly over-predicted by the CFD for the 2.8 and 3.4 km/s condition where over-predictions of 1000 - 2000 K are seen in the expanded flow region. For the 4.0 km/s condition, the vibrational temperature is only slightly over-predicted by about 400 K. The consistent over-prediction of the vibrational temperature in the expanded flow region is due to the inability of the simulation to capture the correct degree of thermal non-equilibrium; the thermal non-equilibrium is over-predicted in the simulation. This is discussed in detail in section 6.5.4.

From Figure 6.21 to Figure 6.23, in general, the different inflow estimates of the same condition produce large differences in flowfield CO₂ number density. The possible inflow variables which can influence the flowfield CO₂ number density include the inflow CO₂ number density (pressure), the inflow temperatures and the inflow velocity. For the 2.8 and 3.4 km/s condition, the very large difference in computed flowfield CO₂ number density between the inflow estimated from the PITOT

code and from the spectroscopic measurements is mainly due to the large difference in freestream CO₂ number density between the two inflow estimates. Even the two estimates of the inflow for the 4.0 km/s condition produce a significantly large difference in flowfield CO₂ number density despite the fact the two inflow estimates are fairly similar. This shows that the flowfield CO₂ number density is very sensitive to the inflow condition.

Interpreting the results of the CO₂ number density is more complex because it is also directly related to the flowfield temperature. The species number density decreases with increase in temperature. Consequently, the good agreement seen in the 3.4 km/s condition between the calculated, using the PITOT code estimated freestream, and measured CO₂ number density is believed to be a coincidence caused by cancelation of errors in the CFD simulation. This is because the computed flowfield temperature for the 3.4 km/s condition, shown in Figure 6.22, does not match with the experimental measurements. For the 4.0 km/s condition, the CO₂ number densities compare with moderate discrepancy between experiment and CFD using the inflow estimated from the radiation measurements, in both the post-shock region and the expanded flow region. In both the post-shock region and the expanded flow region, the computed CO₂ number density using the spectroscopic measurement inflow under-predicts the measurement by around 20-30%. This discrepancy would be related to the slight over-prediction in temperature by CFD, but it may also indicate that the inflow CO₂ number density (and/or pressure) used in the simulation is slightly underestimated because the flowfield CO₂ number density was shown to be quite sensitive to the inflow CO₂ number density. Nevertheless, as both the temperatures and CO₂ number densities compare without significant discrepancies between experiment and CFD, this inflow estimated from the spectroscopic measurements is believed to be a reasonably good representation of the actual inflow for the 4.0 km/s condition.

6.5.4 Thermal non-equilibrium

To assess the accuracy of the thermal kinetics model used in the CFD, it is necessary to compare the degree of thermal non-equilibrium deduced from the experimental measurements with that calculated from CFD. This can be assessed by comparing the ratio between the vibrational temperature and rotational temperature between experiment and CFD. The results are shown on Figure 6.24. The results show that degree of thermal non-equilibrium is predicted well in the region prior to expansion by CFD. But, the results show that the thermal non-equilibrium during, and after, the expansion is significantly over-estimated in the CFD results for all cases.

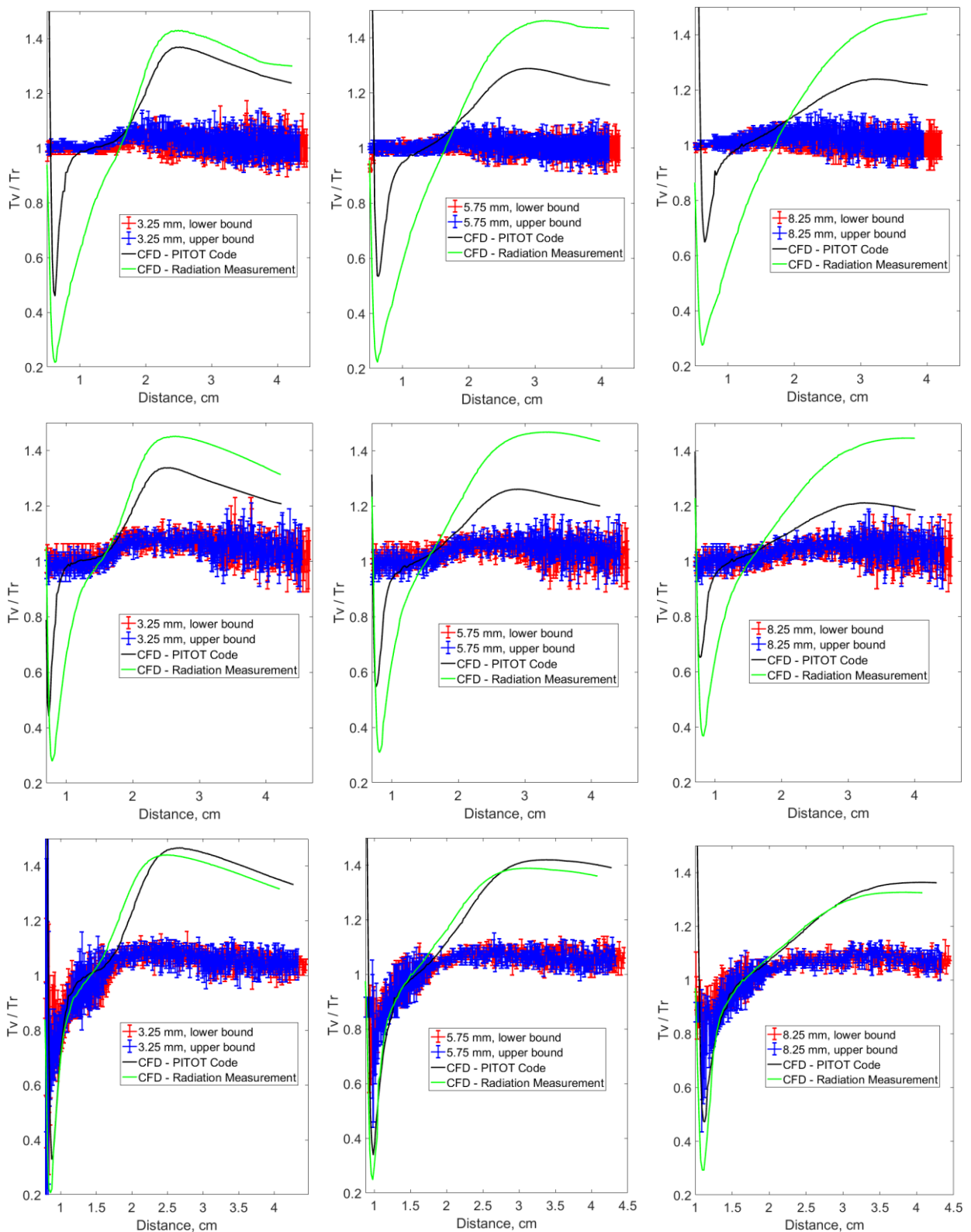


Figure 6.24. Comparison of the ratio between the vibrational temperature and rotational temperature from experiment and CFD. The top, middle and bottom row correspond to the 2.8, 3.4 and 4.0 km/s condition respectively. The left, middle and right column correspond to the 3.25, 5.75 and 8.25 mm measurement above the test model respectively.

Examining the region before the expansion fan, the spike which drops below the value of one in the computed T_v/Tr curves near the immediate vicinity of the shock front is not seen in the experimental

data. This is likely because the radiation at the vicinity of the shock front is weak, the shock wave in the experiment is constantly moving, the shock wave is curved and the spatial resolution of the optical system is limited, as mentioned earlier in section 6.5.3. Therefore, the vicinity of the shock front is not resolved in the radiation measurements. Examining the region near the beginning of the expansion fan behind the vicinity of the shock front, the thermal non-equilibrium is generally predicted well by CFD in this region. For the 4.0 km/s condition, the T_v/Tr curve has a region near the beginning of the expansion fan with a value which increases from approximately 0.8 to 1. This is seen in both the experimental curve and the computed curves. For the 2.8 and 3.4 km/s condition, the T_v/Tr curve has a flat region near the beginning of the expansion fan with a value of about 1. This is seen in both the experimental curve and the computed curve using the inflow estimated from the PITOT code. On the other hand, for the 2.8 and 3.4 km/s condition, using the inflow estimated from the radiation measurements significantly over-predicts the degree of thermal non-equilibrium in this region. This is because the degree of thermal non-equilibrium increases with decrease in total density. For the 2.8 and 3.4 km/s condition, the freestream condition estimated from the radiation measurements has a significantly lower total density compared to that estimated from the PITOT code. Thus, CFD predicts the correct thermal non-equilibrium when using the inflow estimated from the PITOT code. This consequently means that the inflow total density estimated from the PITOT code is a more accurate representative of that in the actual inflow. This makes sense as the PITOT code estimate is produced based on the measured pitot pressure which is a measure of the inflow total density, whereas the inflow estimated from the radiation measurements is based on the measure of the inflow CO₂ density and assuming a CO₂ mole fraction. This result would support the theory of contamination proposed in chapter 5, however, this theory is disproved in the same chapter.

Although CFD can predict the degree of thermal non-equilibrium well in the region prior to expansion, deeper into the expansion fan, the thermal non-equilibrium becomes significantly over-predicted by CFD for all cases. For all three conditions, the CFD can over-predict the non-equilibrium by as much as 40-45% in the expansion fan. For the 2.8 km/s and 3.4 km/s condition, the over-estimate of the thermal non-equilibrium in the CFD is most severe when using the inflow estimated from the spectroscopic measurements due to the lower densities. Nevertheless, for the 2.8 and 3.4 km/s condition, even the computations produced using the inflow estimated from the PITOT code over-predicts the thermal non-equilibrium by as much as 30-35%. For the 4.0 km/s condition, the inflow estimated from the PITOT code and from the radiation measurements are very similar. Thus, this produced a very similar T_v/Tr curve between the two inflow estimates and both inflow estimates over-predicted the thermal non-equilibrium by as much as 40%.

The cause of the significant over-prediction of thermal non-equilibrium in the expansion by the two-temperature model for all the conditions is believed to be due to incorrect thermal kinetic rates. The vibrational relaxation rates used in the simulations, discussed in section 6.3, are derived from post-shock conditions. The CO₂ vibrational relaxation rate behind shock waves have been studied extensively in the past [36] [37] [28]. The results of these previous studies were all consistent. Hence, the current vibrational relaxation model should accurately describe the thermal non-equilibrium under post-shock conditions. However, it is widely believed that the relaxation rates for post-shock conditions are not applicable for expanding flow conditions. Despite various experimental results showing complex thermal non-equilibrium effects in high temperature CO₂ expanding flows [51] [54] [53] [90], numerous expanding flow experiments done using N₂ and CO [66] [75], as well as CO₂ at lower temperatures of 600 – 1400 K [50], provide evidence that vibrational relaxation is faster under expanding flow conditions. The experiments showed that the vibration relaxation times under expanding flow conditions for N₂, CO and CO₂ were around 5 – 70, 1 – 1000 and 1.06 – 1.14 times shorter respectively than the corresponding vibrational relaxation times under post-shock conditions. The result in the current work for high temperature CO₂ is consistent with the trend of these previous experimental results and also provides stronger evidence for this behavior because the measurements in this work simultaneously capture both the shock layer and the expanding flow; the past experiments measured just the expanding flow. The physical mechanisms causing the accelerated vibrational relaxation in expanding flows are still unconfirmed [134] [135] and, thus, this behavior could not be successfully recreated through computations for realistic gas-dynamic environments [136] [137].

6.6 Influence of the Carbon Dioxide Dissociation Rate

A possible source of discrepancy between CFD calculations and experimental measurements may be caused by the CO₂ dissociation rate. Numerous experimental measurements of the CO₂ dissociation rate has been made and noticeable variations were observed between the different studies as discussed in section 2.2. The Arrhenius CO₂ dissociation rate constant relationship measured by different authors can vary by up to approximately an order of magnitude for relevant post-shock conditions [26] [27] [28]. A possible source of this error is believed to be caused by the CO₂ dissociation rate constant displaying dependences to the pressure [28]. The popular two-temperature thermochemical model used in the current work, described in section 6.3, assumes that the dissociation rate constant depends on only temperature ($\sqrt{TT_v}$), according to the Arrhenius relationship. Hence, to investigate how the uncertainty in the CO₂ dissociation rate can influence the numerical calculations presented

in section 6.5, a study is conducted to look at how the band radiance and flowfield properties change when the CO₂ dissociation rate, controlled by $\sqrt{TT_v}$, is changed.

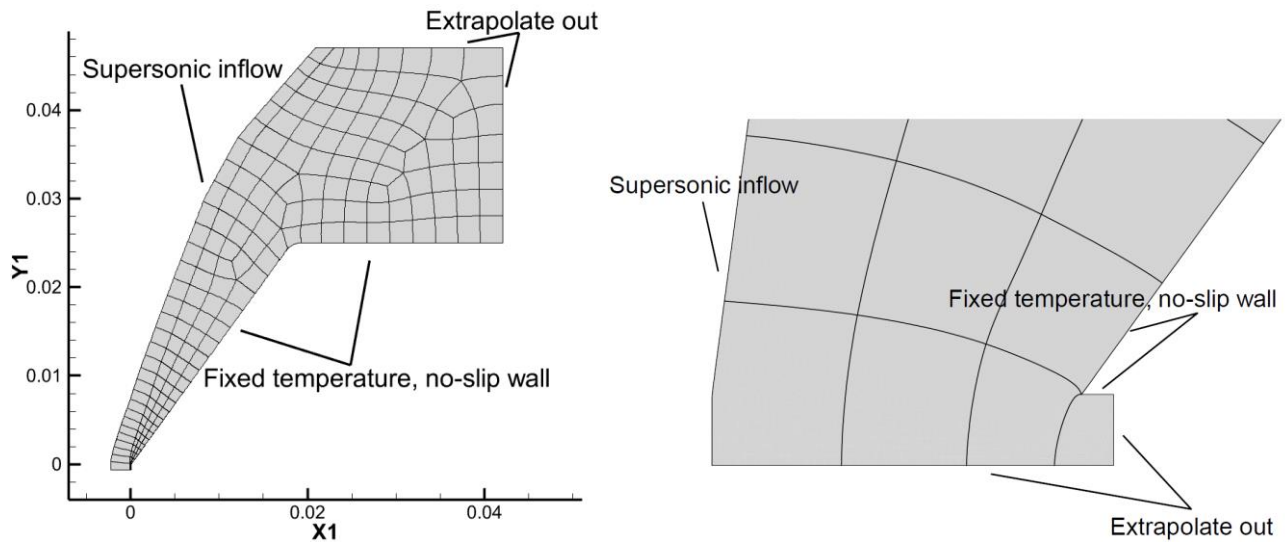


Figure 6.25. The two-dimensional simulation domain of the wedge model along with the boundary conditions and the block topology. The figure on the right shows the zoomed in view of the simulation domain around the leading edge.

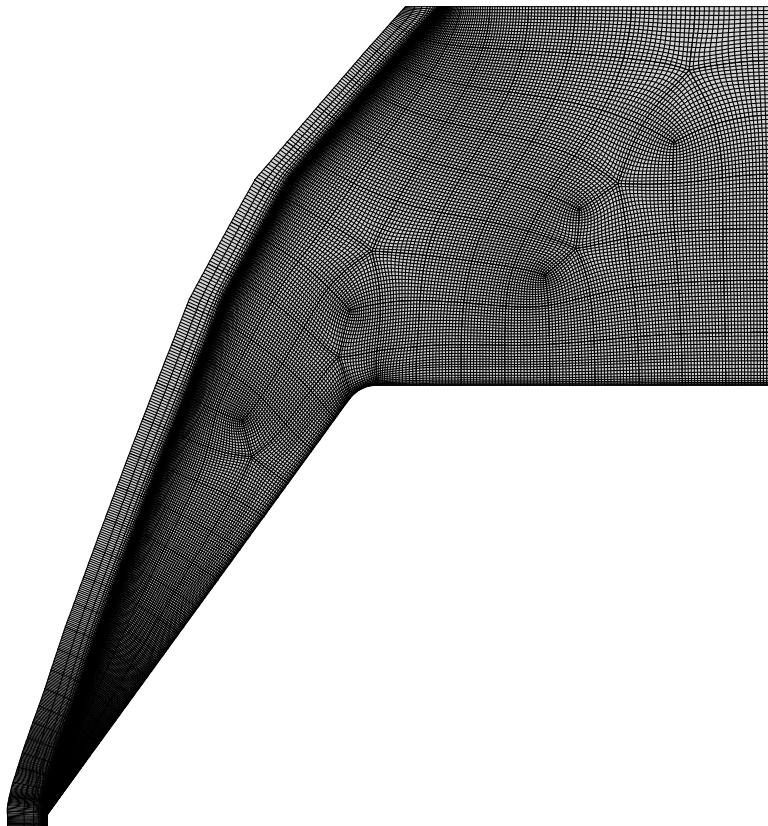


Figure 6.26. The two-dimensional simulation mesh.

The study in this section is conducted by increasing and decreasing the value of the constant 'A' in Arrhenius equation, often called the pre-exponential factor or the temperature-independent constant,

from the original value of 7.47×10^{12} shown in Table 6.1, by an order of magnitude larger and smaller. In the CFD calculations in the current work, the recombination rate constant is calculated from the dissociation rate constant using the equilibrium constant. Consequently, increasing and decreasing the CO₂ dissociation rate also increases and decreases the CO₂ recombination rate respectively. The numerical models used in this study are the same as that described in section 6.3 except the CFD simulation domain is two-dimensional. The two-dimensional simulation domain and the boundary conditions are shown in Figure 6.25. The inlet boundary is fitted closely to the shock wave. To capture the slightly detached shock wave, a small region surrounding the leading edge is simulated. The simulation domain contains approximately 40,000 cells in total and 144 blocks in total. The block topology is shown in Figure 6.25. The mesh is structured and it is created using the Gridpro software. As shown in Figure 6.26, strong clustering is done around the shock wave and mild clustering is done around the wall. For this study, the inflow conditions used are shown on Table 6.4. The conditions were estimated from the PITOT code and were presented previously in Table 6.2.

Table 6.4. Freestream properties used for the CFD simulation for the carbon dioxide dissociation rate study in this section.

Condition	P (Pa)	T (K)	T _v (K)	Velocity (m/s)	Mole Fraction CO ₂ /CO/O ₂ /O
2.8 km/s	355	1191	2358	2877	0.92/0.054/0.0267/0.0
3.4 km/s	360	1378	2758	3484	0.76/0.158/0.076/0.006
4.0 km/s	150	1281	2815	4077	0.73/0.18/0.083/0.007

It is first necessary to assess the influence of the CO₂ dissociation rate on the 2.7 and 4.3 μm band radiance. For this study, the band radiance is calculated at the location of the 5.75 mm measurement above the test model and compared between the different reaction rates. The result of this study is shown in Figure 6.27 and how the dissociation rate influences the radiation prior to expansion and after expansion are examined. For the 2.8 km/s condition, the CO₂ dissociation rate has very little influence on the band radiance around the peak of the radiance profile for both the 2.7 and 4.3 μm band. A change in an order of magnitude in the reaction rate results in less than 10 % change in the 2.7 μm band radiance around the peak, while the 4.3 μm band radiance is almost unaffected by the change in dissociation rate. For the 2.8 km/s condition, a larger influence by the reaction rate on the radiation is seen in the expanded flow region. A change in an order of magnitude in the reaction rate can result in up to 50 % and 30 % change in the 2.7 μm and 4.3 μm band radiance respectively. For the 3.4 km/s condition, a change in an order of magnitude in the reaction rate can result in up to around 20 % and 10 % change in 2.7 μm and 4.3 μm band radiance respectively, around the peak of the band radiance curve. Like with the 2.8 km/s condition, a larger influence of the reaction rate is seen in the expanded flow region; a change in an order of magnitude can result in up to around 70 %

and 50 % change in 2.7 and 4.3 μm band radiance respectively. For the 4.0 km/s condition, a change in an order of magnitude in the reaction rate can result in up to around 30 % and 10 % change in the 2.7 and 4.3 μm band radiance respectively around the peak. Like with the other test conditions, a larger influence of the reaction rate is seen in the expanded flow region, where a change in an order of magnitude can result in around 50 % and 30 % change in the 2.7 and 4.3 μm band radiance respectively.

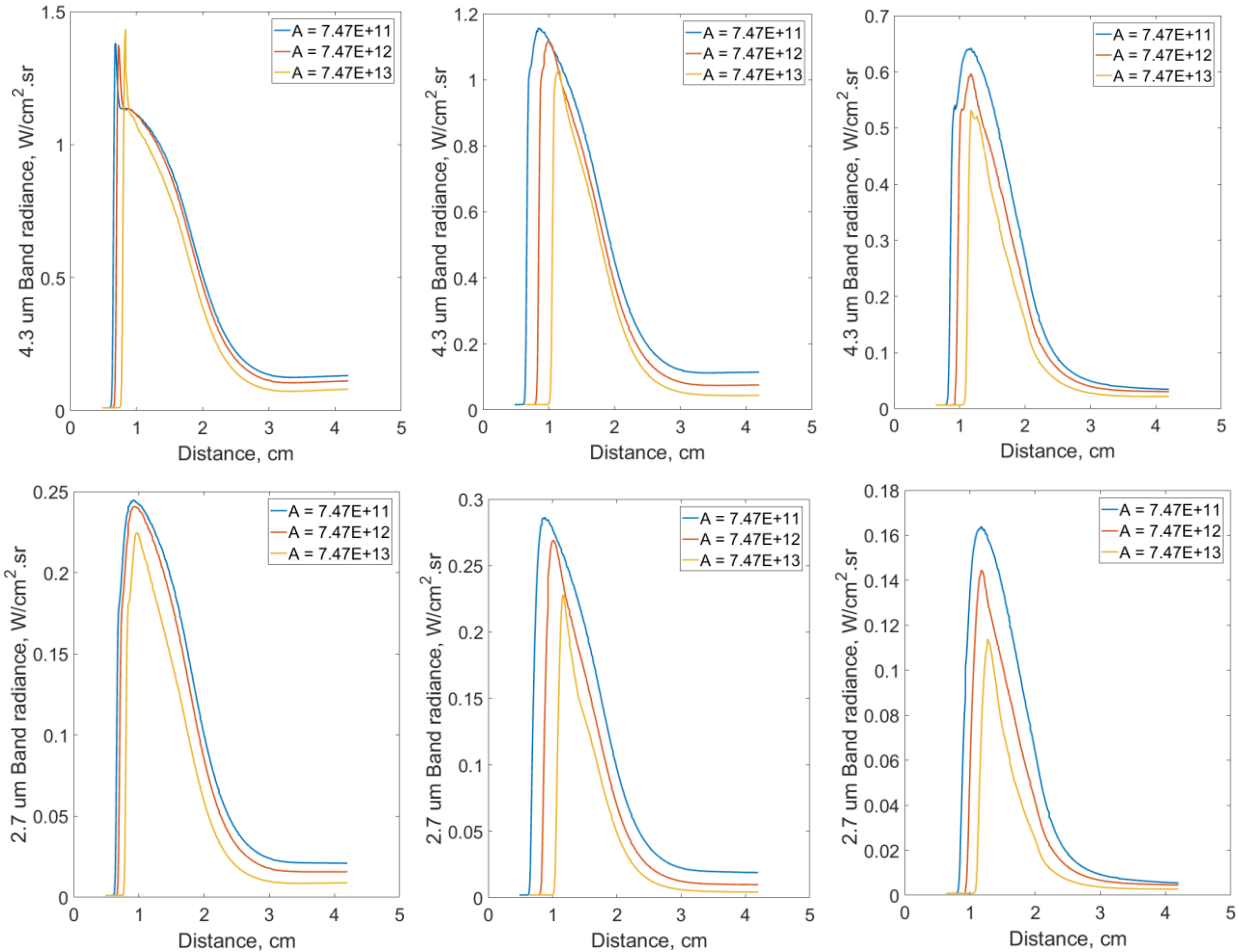


Figure 6.27. Comparison of the 2.7 and 4.3 μm band radiance from simulations using different CO_2 dissociation rates. The left, middle and right columns correspond to the 2.8, 3.4 and 4.0 km/s conditions respectively.

The general pattern seen on Figure 6.27 is that the 2.7 μm band is more sensitive to the CO_2 dissociation rate compared to the 4.3 μm band. Also, the emission in the expanded flow region is more sensitive to the reaction rate compared to the emission near the beginning of the expansion. Furthermore, an increase in an order of magnitude from the nominal reaction rate has a larger influence on both the 2.7 and 4.3 μm band radiance compared to a decrease in an order of magnitude from the nominal reaction rate. Also, in all cases, increasing the CO_2 dissociation rate decreases the band radiance at all locations in the flowfield.

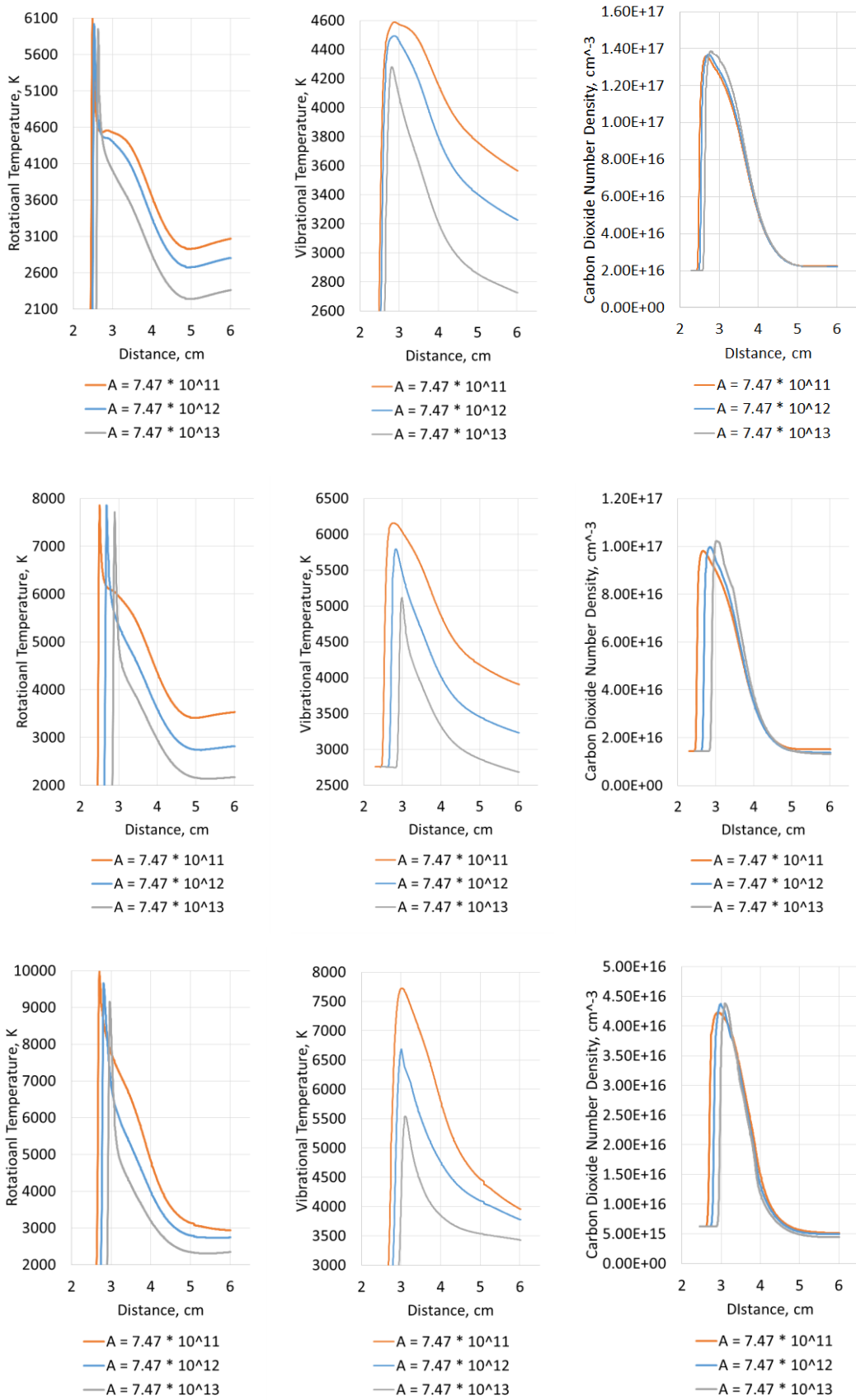


Figure 6.28. Comparison of the temperatures and CO₂ number density from simulations using different CO₂ dissociation rates. The top, middle and bottom rows correspond to the 2.8, 3.4 and 4.0 km/s conditions respectively.

It is now necessary to study how the CO₂ dissociation rate influence the flowfield temperatures and CO₂ number density. Data is extracted from the simulations at a horizontal slice 5.75 mm above the test model and compared between the different reaction rates. This result is shown in Figure 6.28. An interesting result is that the flowfield CO₂ number density hardly changes when changing the CO₂ dissociation rate by an order of magnitude. However, the temperatures do change noticeably. Both the vibrational and rotational temperature decrease with increase in the CO₂ dissociation rate. This is expected as the temperature behind the shock is at maximum when the chemistry is frozen and at minimum when the reaction rate is infinitely fast.

Table 6.5. The CO₂ mole fraction at the peak of the temperature curves in Figure 6.28. Also presented is the inflow and equilibrium post-shock CO₂ mole fractions.

Condition	Inflow CO ₂ Mole Fraction	Post-Shock CO ₂ Mole Fraction			Equilibrium CO ₂ Mole Fraction
		A=7.47 x 10 ¹¹	A=7.47 x 10 ¹²	A=7.47 x 10 ¹³	
2.8 km/s	0.92	0.91	0.89	0.84	0.55
3.4 km/s	0.76	0.74	0.69	0.60	0.30
4.0 km/s	0.73	0.68	0.62	0.5	0.22

For the 2.8 km/s condition, increasing the CO₂ dissociation rate by an order of magnitude from the nominal decreases the peak temperature in the extracted profile by about 300 K, which corresponds to a decrease in CO₂ mole fraction of 0.05. This is shown in Table 6.5, which presents the CO₂ mole fractions at the peak of the curves in Figure 6.28 for the different CO₂ dissociation rates. Also presented in Table 6.5 is the inflow CO₂ mole fractions and post-shock equilibrium CO₂ mole fractions calculated from CEA [127]. In section 5.5, it was discussed that there should be only small amounts of dissociation should have occurred at the post-shock location corresponding to the peak of the temperature profiles. The results in Table 6.5 supports this statement. It shows that, for the 2.8 km/s condition, the peak of the profile should be close to the frozen condition even when the dissociation rate is increased by an order of magnitude. Therefore, an incorrect CO₂ dissociation rate cannot explain the approximate 1500 K discrepancy in temperature in the post-shock region between experiment and simulation shown in Figure 6.21. Furthermore, from Figure 6.28, changes to the temperature in the post-shock region due to changes in the dissociation rate is carried over to the temperature in the expanded flow region. Hence, increasing the dissociation rate decreases the temperature in both the post-shock region and the expanded flow region, while decreasing the dissociation rate increases the temperature in both the post-shock region and the expanded flow region.

For the 3.4 km/s condition, increasing the CO₂ dissociation rate decreases the temperature by about 700 K in the region near the beginning of the expansion fan and, as shown in Table 6.5, this

corresponds to a decrease in CO₂ mole fraction from 0.69 to 0.60. As the frozen and equilibrium CO₂ mole fraction is 0.76 and 0.30 respectively, the peak of the profile is close to the frozen condition even when the dissociation rate is increased by an order of magnitude. Like with the 2.8 km/s condition, an incorrect CO₂ dissociation rate alone cannot explain the approximate 1000 K discrepancy in temperature in the post-shock region between experiment and simulation shown in Figure 6.22. Also, like with the 2.8 km/s condition, changes to the temperature in the post-shock region due to changes in the dissociation rate is carried over to the temperature in the expanded flow region.

For the 4.0 km/s condition, increasing the CO₂ dissociation rate decreases the temperature by about 1000 K in the region near the beginning of the expansion fan. As shown in Table 6.5, this corresponds to a decrease in CO₂ mole fraction from 0.62 to 0.50 at the peak of the temperature profile. In this case, an incorrect CO₂ dissociation rate can reconcile the approximate 500 K discrepancy in temperature in the post-shock region between experiment and simulation shown in Figure 6.23. Additionally, like with the 2.8 and 3.4 km/s conditions, changes to the temperature in the post-shock region due to changes in the dissociation rate is carried over to the temperature in the expanded flow region.

Overall, the result on Figure 6.28 shows that the CO₂ dissociation rate has the most influence on the post-shock flowfield temperature in the 4.0 km/s condition. On the other hand, the dissociation rate has the least influence on the post-shock flowfield temperature in the 2.8 km/s condition. Additionally, for all three conditions, changes to the temperature in the post-shock region due to changes in the dissociation rate is carried over to the temperature in the expanded flow region. These results are consistent with the results for the band radiance, shown on Figure 6.27, discussed previously. It should also be mentioned that the CO₂ dissociation rate causes only marginal changes to the ratio between upstream and downstream of the expansion fan in the temperature and number density profiles for all three conditions. The ratios of the flow properties between upstream and downstream do not differ by more than 10% between the three different CO₂ dissociation rates. Lastly, although these results from Figure 6.28 are from data extracted at 5.75 mm above the test model, very similar results are observed in the data extracted at 3.25 mm and 8.25 mm above the test model.

The two-dimensional simulations can also be used to study how the CO₂ mole fraction changes along different streamlines in the flowfield for different CO₂ dissociation rates. For this study, data along two different streamlines are extracted. Figure 6.29 shows the location of the two streamlines. The extracted data from the two streamlines are shown in Figure 6.30 and the vertical black lines on each curve represents the approximate location of the expansion fan head. The results show that, for all cases, the chemistry freezes from around the start of the expansion. In the top streamline, marginal

dissociation continues to occur after passing the expansion fan head prior to complete freezing. Consequently, unless the actual CO₂ recombination rate differs by more than an order of magnitude from the nominal rate, CO₂ recombination would not occur in the framework of the current experiments. The nominal recombination rate used in the simulations is calculated from the nominal dissociation rate using the equilibrium constant. The nominal dissociation rate is determined from experimental measurements made in post-shock conditions. It is unclear how the CO₂ dissociation/recombination rate differs under expanding flow conditions as no related research could be found in past literature. Another observation from Figure 6.30 is that the bottom streamline always freezes at a more dissociated state compared to the top streamline in a given flowfield. The CO₂ mole fraction after freezing could differ by as much as around 0.15 between the top and bottom streamline. This is due to a combination of three reasons. Firstly, in all cases, the flow enters the expansion fan prior to reaching chemical equilibrium. Secondly, in the shock layer, the bottom streamline has a higher rate of dissociation compared to that of the top streamline, due to the slight curvature of the shock wave. The curvature of the shock wave causes the bottom streamline to have a higher post-shock temperature than that of the top streamline and this results in a higher rate of dissociation. Lastly, the bottom streamline has a longer distance to travel prior to reaching the expansion fan head compared to the top streamline. The longer distance allows more dissociation to occur before the expansion. The combination of these reasons results in the observation that the bottom streamline always freezes with a lower mole fraction than the corresponding top streamline.

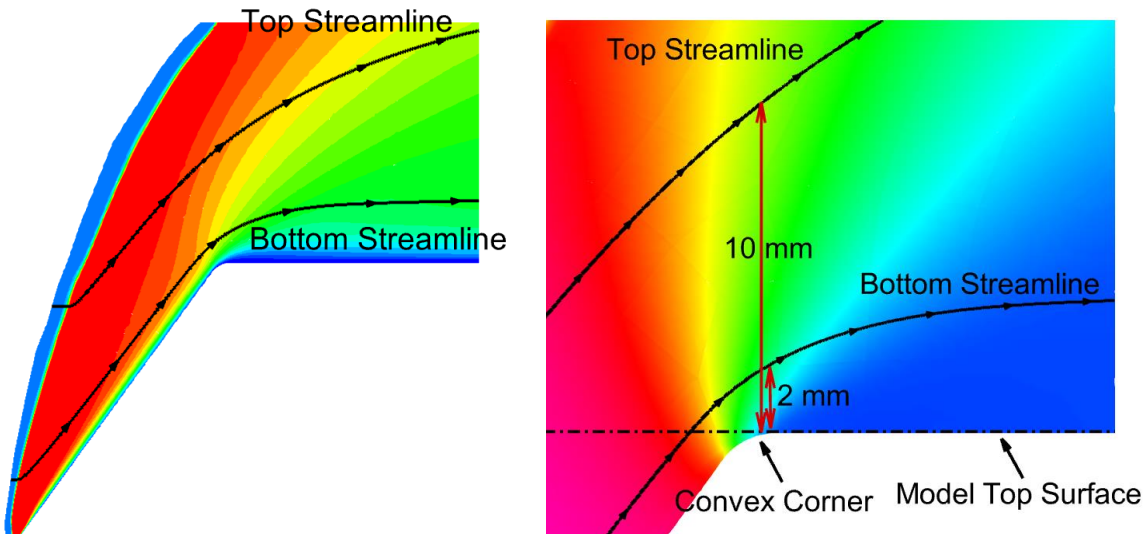


Figure 6.29. Locations of the extracted top and bottom streamlines data in Figure 6.30.

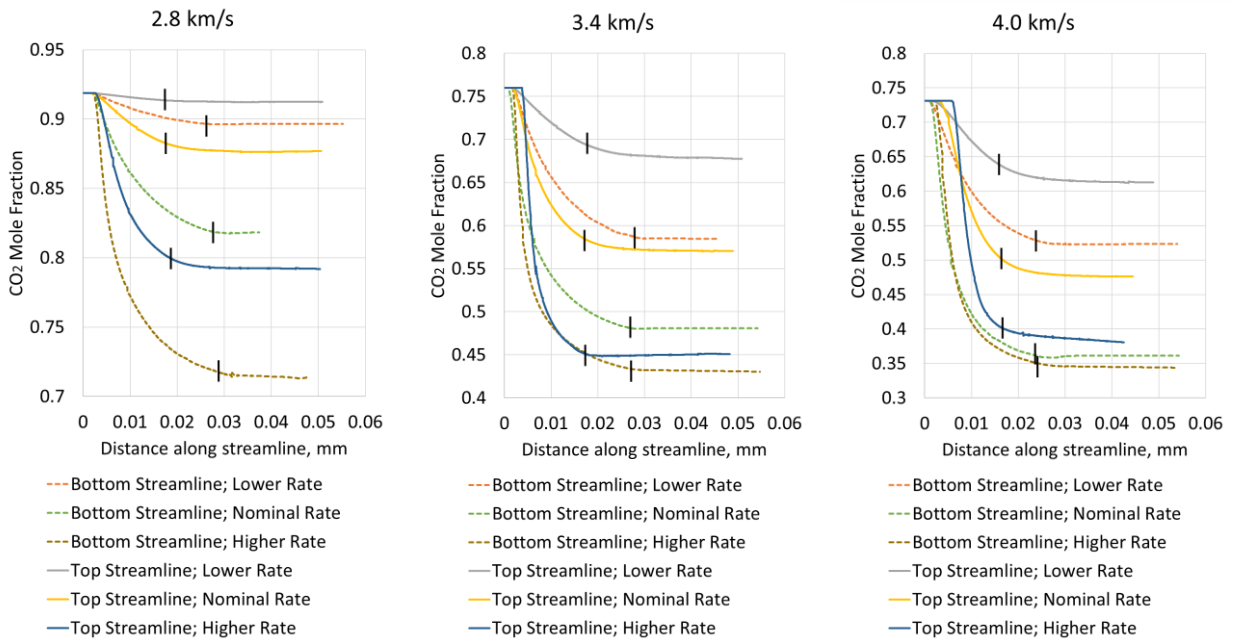


Figure 6.30. Simulated CO₂ mole fraction along the top and bottom streamline for different CO₂ dissociation rates. The vertical black lines on each curve represents the approximate location of the expansion fan head.

6.7 Conclusion

A parametric study of the CO₂ 2.7 μm and 4.3 μm band radiance showed that the temperature, CO₂ number density, CO number density and the degree of thermal non-equilibrium are all important parameters influencing the emission intensity. Consequently, accurate thermochemical kinetics modelling is required to reliably predict the CO₂ radiation. To simulate the wedge model experiments, a computation methodology was proposed. The methodology included using a two-temperature thermochemical model based on the thermal kinetics model by Park et al. [107] and the chemical kinetics model by Cruden et al. [44]. The methodology also required the use of three-dimensional CFD simulations as it was shown that three-dimensional effects were significant in the experiment. Using the proposed methodology, simulations were conducted to compute the flow around the wedge model during the experiment using the Eilmer3 code [97]. The simulations were done using inflows estimated from two different sources; for a given condition, the two inflow estimates produce significantly different flowfields, particularly for the 2.8 and 3.4 km/s conditions. Data from the computed three-dimensional flowfield were used to compare to the various available experimental measurements.

The computed flowfield data were used to calculate the CO₂ 2.7 μm and 4.3 μm band radiance using the NEQAIR code [49] and this was compared to the experimental measurements. The comparison revealed that, for the 2.8 and 3.4 km/s condition, the discrepancy in the post-shock region between

numerical predictions and experimental measurements is much larger than that seen by Cruden et al. [44] in their comparable benchmark experiments. This indicates that the inflows estimated for the 2.8 and 3.4 km/s condition could be inaccurate even though these inflows computed shock locations which matched well with the measured shock locations. Comparison of the post-shock temperature between CFD and experiment showed that the temperature was significantly over-predicted, by around 1000 K, in the CFD results for the 2.8 and 3.4 km/s condition. This discrepancy in post-shock temperature could, in theory, be attributed to the CO₂ dissociation rate. However, further investigation showed that the CO₂ dissociation rate could not explain the discrepancy in post-shock temperature seen in the 2.8 and 3.4 km/s conditions. A study of the influence of the CO₂ dissociation rate showed that the dissociation rate would need to be more than an order of magnitude faster than that used in the three-dimensional CFD simulations to match the measured temperature. This is highly unlikely as numerous experimental measurements of the post-shock CO₂ dissociation rate at similar conditions showed variations only within an order of magnitude. Hence, it is still unclear what is causing this discrepancy for the 2.8 and 3.4 km/s condition.

On the other hand, the 4.0 km/s condition is believed to be the best characterized condition of all three conditions. For this condition, the inflow estimated from the spectroscopic measurements is believed to be a good representation of the experimental inflow. Using this inflow, the calculated 2.7 μm and 4.3 μm band radiances in the post-shock region under-predicted the measured values by within approximately 20 % and 10 % respectively. This discrepancy between numerical prediction and experiment is consistent with comparable benchmark results by Cruden et al. [44]. For the 4.0 km/s condition, both the rotational and vibrational temperature in the post-shock region is over-predicted by about 10 % (500 K) by CFD using the radiation measurement inflow. This slight discrepancy could be caused by small inaccuracies in the CO₂ dissociation rate and/or estimated inflow velocity used in the simulation. In the expanded flow region of the 4.0 km/s experiment, the calculated band radiances using the spectroscopic measurement inflow under-predicts the measured band radiances by within approximately 20 % and 40 % for the 2.7 μm and 4.3 μm band respectively. In this region, the rotational temperature is under-predicted by CFD by about 10 – 20 % while the vibrational temperature is over-predicted by CFD by about 10 – 20 %. This is mainly because the thermal kinetics model used in the simulations could not describe the thermal non-equilibrium accurately in the expanding flow. Furthermore, using the inflow estimated from the spectroscopic measurements, the CO₂ number density is under-predicted by CFD by about 20 – 30 % in both regions of the flowfield for the 4.0 km/s condition. This explains the under-prediction of band radiance by computations, in both regions of the flowfield. The flowfield CO₂ number density was shown to be quite sensitive to the inflow CO₂ number density. Consequently, the under-prediction of the CO₂ number density by CFD may indicate that the estimated inflow pressure is slightly underestimated.

The degree of thermal non-equilibrium predicted in CFD was compared to experimental measurements. The result showed that the degree of thermal non-equilibrium in the post-shock region is generally predicted well by CFD. However, for all cases, CFD significantly over-predicted the degree of thermal non-equilibrium in the expanding flow. The thermal kinetics model used in the CFD simulations is designed to model the thermal kinetics behind shock waves. Therefore, the result indicates that the vibrational relaxation in expanding flows is faster than the vibrational relaxation behind shock waves. This result for high temperature CO₂ is consistent with previous experimental results for N₂ and CO [66] [75], as well as CO₂ at lower temperatures [50].

Additionally, the possibility of whether CO₂ recombination could have occurred in the experiment was assessed. The study showed that the CO₂ recombination rate would need to be significantly more than an order of magnitude faster than that used in the three-dimensional CFD simulations in order for CO₂ recombination to occur in the experiment; the chemistry would otherwise freeze in the expansion fan. The recombination rate used in the three-dimensional simulations was calculated from the specified dissociation rate in Table 6.1 using the equilibrium constant. This dissociation rate was determined from experimental measurements made in post-shock conditions. It is unclear how likely it is for the CO₂ dissociation/recombination rate to be more than an order of magnitude faster under expanding flow conditions because no study of this could be found in literature. Consequently, it is still uncertain whether any CO₂ recombination occurred during the experiment.

7 Conclusions and Future Work

7.1 Summary of Work Done

Mid-infrared radiative heating from CO₂ molecules is considered important for the sizing of the TPS on Mars entry vehicles. CO₂ radiative heating is most important on the afterbody of the entry vehicle. The afterbody radiative heating originates from CO₂ molecules under expanding flow conditions. Literature review revealed a lack of experimental research on high temperature CO₂ flows under rapidly expanding conditions. Therefore, the objective of this thesis was to study the thermochemical nonequilibrium and radiation of CO₂ flows in the laboratory and examine the appropriateness of the current thermochemical and radiation models in describing the flows; the focus of the research was on the CO₂ flow under expanding conditions relevant to Mars entry in particular.

To address this objective, three new low enthalpy conditions were developed in the X2 expansion tube which involved designing a new driver. The expansion tube conditions were designed based on flight conditions where CO₂ radiation is most important according to data from the literature review. Throughout the thesis, numerous analyses were done to help characterize these new test conditions. In addition, a new mid-infrared spectroscopy system suitable for use with expansion tube experiments was assembled. A corresponding methodology for absolute radiance calibration of the mid-infrared spectroscopy measurements was developed. Using a wedge model with a convex corner, the new expansion tube conditions were used to generate an expanding flow around the corner of the test model. The mid-infrared spectroscopy system was used to take horizontal one-dimensional measurements of both the 2.7 μm and 4.3 μm CO₂ bands at three different heights above the convex corner. The measurements not only covered the expansion region but also covered the shock front and the post-shock region too. Using the spectroscopy measurements, spectral fitting was done to deduce the rotational temperature, vibrational temperature and CO₂ number density. Filtered images of the 2.7 μm and 4.3 μm CO₂ bands were also taken to provide a spatially resolved (in two-dimension) view of the experimental flowfield. Lastly, three-dimensional numerical simulations of the experiments were done and the computed results were compared to the available experimental measurements.

7.2 Outcomes

Characterizing the low velocity and low pressure CO₂ test conditions was found to be difficult, particularly for the 2.8 and 3.4 km/s conditions, with the discovery of some interesting anomalies. CFD modeling of the flow in the expansion tube did not accurately predict the test conditions, because the simulated secondary shock speeds were significantly slower than those measured. So, instead, numerous experimental measurements were taken to help characterize the experimental test conditions. These measurements include:

- shock speeds, acceleration tube wall pressure and nozzle exit pitot pressure which were used with the PITOT code to produce tuned estimates of the test conditions;
- mid-infrared emission spectroscopy of the nozzle exit flow which was used to estimate the rotational and vibrational temperatures and CO₂ number densities of the test conditions;
- post-shock temperatures which were used to gauge the accuracy of the estimated test conditions; and
- test model shock wave locations which were also used to gauge the accuracy of the estimated test conditions.

Some major inconsistencies were discovered from these measurements. For the 4.0 km/s condition, the estimated freestream CO₂ number density from the PITOT code matched well, within around 10%, with that determined from the spectroscopic measurements. However, for the 2.8 and 3.4 km/s condition, the estimated freestream CO₂ number density from the spectroscopic measurements was significantly lower, by a factor of 4-5, than the estimated CO₂ number density from the PITOT code. The freestream pitot pressure measurements, which the PITOT code uses to produce the freestream estimates, are a measure of the total density. On the other hand, the spectroscopic measurements are a measure of the CO₂ density. Therefore, the significant over-prediction of the CO₂ number density by the PITOT code indicates significant discrepancy between CO₂ density and total density in the freestream of the 2.8 and 3.4 km/s condition. Examination of the post-shock thermal non-equilibrium also supports this result. This discrepancy cannot be explained by an amount of CO₂ dissociation that is physically possible based on the measured primary shock speed. Helium contamination cannot explain the discrepancy as well because the measured shock wave location indicates that there could not be significant amounts of helium in the freestream. Therefore, it is currently unclear what is causing the discrepancy between the freestream total density and freestream CO₂ density for the 2.8 and 3.4 km/s conditions.

Another major inconsistency found is between the measured and calculated post-shock temperatures. Post-shock temperatures were calculated using the estimated test conditions and then compared to

the experimental measurements. A good match, within 10 %, was seen for the 4.0 km/s condition. However, the calculated post-shock temperatures significantly over-predicted the measured post-shock temperatures, by more than 30%, for the 2.8 and 3.4 km/s conditions. This discrepancy in temperature cannot be explained by varying the CO₂ dissociation rate within a reasonable range in CFD. Furthermore, the discrepancy is not believed to be due to an incorrect freestream velocity because the velocity would have to be about 20% slower than the measured secondary shock velocity to reconcile the post-shock temperatures which is unlikely. Helium contamination cannot explain the discrepancy as well because the amount of helium required would result in a computed shock location nowhere near the measured shock location. Therefore, it is currently unclear what is causing the discrepancy between the computed post-shock temperature and the measured post-shock temperature for the 2.8 and 3.4 km/s conditions. However, it is believed to be due to something about the experimental condition rather than the numerical model used in computing the post-shock temperature. This belief is supported by the results of Cruden et al. [44] who showed that CFD is capable of predicting similar post-shock condition without much discrepancy.

A more minor discrepancy is seen for the degree of thermal excitation of the test conditions. The spectroscopic measurements of the expansion tube freestreams indicated that the flow generally does have some excess energy in the vibrational modes. However, the degree of thermal non-equilibrium predicted from the spectroscopic measurements is noticeably less than that of the frozen PITOT code freestream - which produced a better match with the measured shock location than the equilibrium PITOT code freestream. Nevertheless, the use of the spectroscopic measurement estimated freestream still resulted in a good match in the shock location due to the low freestream static pressure. Therefore, for the current work, the inability of the equilibrium freestream to predict the correct shock location may not necessarily indicate severe thermochemical non-equilibrium in the experimental freestream as first proposed by Maclean and Holden [51]. This is because the shock location mismatch from the equilibrium freestream in the current work is not as large as that seen by Maclean and Holden. Thus, the mismatch seen in the current work may be explained by freestream thermochemical excitation and/or incorrect estimates of other freestream parameters.

Using other impulse facilities, numerous researchers have already discovered the difficulty in characterizing similar CO₂ test conditions [51] [54] [53] [90]. The difficulty in characterizing these conditions is believed to come from the fact that generating these conditions in impulse facilities involves expanding the CO₂ test gas. This means that accurately characterizing the conditions requires a good understanding of CO₂ expanding flows. However, a good understanding of CO₂ expanding flows is currently absent because this is what is being studied in the first place. Furthermore, CFD simulations carried out using both the PITOT code estimated freestream and the spectroscopic

measurement estimated freestream for each test condition produced significantly different flowfield properties and radiation intensities, particularly for the 2.8 and 3.4 km/s condition, showing that the flowfield is considerably sensitive to the freestream condition. Therefore, the consequence of the inability to accurately characterize the test conditions is that it is not possible to quantify the exact error of numerical codes at predicting CO₂ radiation using the experimental data from the current work. Even the scaling factors for 4.0 km/s condition, believed to be the most accurately characterized condition, may not necessarily be interpreted as an exact measure of the error from the computations. Nevertheless, important qualitative findings were obtained from the expansion tube experiments.

The temperatures estimated in the wedge flow using both the 2.7 and 4.3 μm spectroscopic measurements matched with no obvious discrepancies. The 4.3 μm band and the 2.7 μm band originates from different ro-vibrational transitions. Therefore, any complex thermal non-equilibrium effects may show up as a mismatch between the temperatures deduced from the two different radiation bands. However, as the comparison did not reveal any obvious mismatch between the temperatures derived from the different emission bands, this may indicate no complex thermal non-equilibrium effects in the flow around the wedge. This match in temperature also provides some confidence to the validity of NEQAIR, using CDSD-4000, at predicting CO₂ radiation under gas-dynamic conditions which it has not been validated for – expanding flow, supersonic, mild thermal non-equilibrium and, mainly, frozen chemistry – and which are more relevant to Mars entry.

Furthermore, the thermal non-equilibrium between the rotational mode and vibrational mode was measured to be small, less than 10 %, in the expansion region. Using vibrational relaxation rates derived from post-shock conditions, CFD significantly over-predicts the degree of thermal non-equilibrium between the rotational mode and vibrational mode in the expansion region. This showed that the CO₂ vibrational relaxation is significantly faster in expanding flow conditions than in post-shock conditions. This result is consistent with results from numerous expanding flow experiments which were done for N₂ and CO [66] [75], as well as CO₂ at lower temperatures [50]. A possible consequence of having small non-equilibrium between the rotational mode and the vibrational mode of CO₂ is that complex non-equilibrium effects, such as non-equilibrium between the different vibrational modes of CO₂ and non-Boltzmann distribution within vibrational energy levels, are likely negligibly small in the expanding flow. This is because the energy exchange between the translational-rotational mode and the vibrational mode is generally considered the slowest thermal non-equilibrium process [126].

The qualitative results in general seem to indicate a lack of significant thermal non-equilibrium effects in the expanding flow in the experiment. As the experiments simulate the expanding flow around the shoulder of an entry vehicle, the result of the current work seems to be consistent with the result of

Sahai et al [13] who showed that the flow around the shoulder of the Mars entry vehicle is Boltzmann distributed. An important consequence of the lack of severe thermal non-equilibrium effects is that state specific numerical models may not be necessary to describe the CO₂ expanding flow in the framework of the current experiments. Knowing the correct test conditions, multi-temperature models with appropriate thermochemical kinetic rates are believed to be enough to describe the CO₂ expanding flow in the current experiments; even a one-temperature finite rate chemistry model may provide a good approximation of the expanding flows as the non-equilibrium between the rotational mode and vibrational mode is seen to be small. In fact, Sahai et al [13] did show that the expanding flow near the shoulder of an entry vehicle is modelled well by a one-temperature model when compared to their state-specific model. In addition, as the expanding flow is close to thermal equilibrium, the NEQAIR code is expected to predict the CO₂ radiation from the expanding flow accurately because NEQAIR simulations of CO₂ radiation has been validated under equilibrium conditions [48].

Nevertheless, the expanding flow simulated in the current experiments around the wedge corresponds to the expanding flow around the shoulder of an entry vehicle which is only a small region of the entire afterbody flowfield around an entry vehicle. Also, the expanding flow around the wedge should be different to expanding flows involved in impulse facilities. Therefore, the qualitative results discovered in the current study would not extend to CO₂ expanding flows in general. In fact, Sahai et al. [13] did show that the vibrational energy levels are populated with a non-Boltzmann distribution in the wake region of the afterbody flowfield around a Mars entry vehicle, while Maclean et al. [53] provide strong arguments for the existence of severe thermal non-equilibrium at the exit of reflected shock tube nozzles in CO₂ conditions. Therefore, it is speculated that thermal non-equilibrium forms far downstream of the start of the expansion rather than near the start of the expansion for CO₂ expanding flows; the cause of this might be related to the CO₂ recombination process.

7.3 Future Work

The current work is one of the first investigations of high-temperature CO₂ expanding flows. Therefore, further work in regards to studying these flows, specifically through experiments, is recommended. The future works should aim to provide quantitative results for a wide range of different expanding flow conditions.

Continuation of the current study of CO₂ expanding flow using the X2 expansion tube would involve developing new and improved test conditions - better characterized test conditions with improved core flow uniformity. However, it is recommended that future ground testing is conducted in large

expansion tubes, such as the X3 expansion tube at The University of Queensland. The main benefit is that, as discussed by Maclean et al. [53], the use of large expansion tube allows for more accurate characterization of these low velocity CO₂ test conditions. This may consequently allow for the production of quantitative data. The test model used should not be limited to the current wedge model; a variety of different test models should be used, such as axisymmetric aeroshell models, two-dimensional shock-less convex corners and nozzles (internal flows). This allows for the study of a variety of CO₂ expanding flows and would help to confirm, as well as extend, the qualitative results of the current work.

Future ground testing should also include the investigation of CO₂ in the unsteady expansion along a tube. The large time scales necessary for the study of CO₂ recombination can be created if the unsteady longitudinal expansion inherent in the expansion tube facility operation is used. Therefore, not only would this be investigating a different expanding flow environment but it would also allow for the study of CO₂ recombination under expanding conditions. CO₂ recombination during expansion is an important process in both the expanding flow during Mars entry and the expanding flow involved in impulse facilities. Thus, the CO₂ unsteady expansion along a tube is an important experiment for the future.

In addition to emission spectroscopy, more advanced optical diagnostic methods should be used to investigate the CO₂ expanding flows in future ground based experiments. Mach-Zehnder interferometry, previously used by Ebrahim and Sandeman to study CO₂ post-shock conditions [27], should be done in future expansion tube experiments. The laser-schlieren technique used by Saxena et al. to study CO₂ post-shock conditions [28] could be particularly useful in the CO₂ unsteady expansion experiments to investigate the thermochemical non-equilibrium processes. The diode laser absorption spectroscopy technique for CO₂ developed by Meyers et al. [91] could also be particularly useful in the CO₂ unsteady expansion experiments.

The better understanding of high temperature CO₂ expanding flows obtained from future research would be applied to produce more accurate predictions of the aeroheating encountered during Mars entry. This could help in the design of improved Mars entry vehicles which would allow for higher mission success rate. The final result would be the improvement in capability for Mars exploration.

References

- [1] Potter, D., Karl, S., Lambert, M., & Hannemann, K., "Computation of radiative and convective contributions to Viking afterbody heating," in *44th AIAA Thermophysics Conference*, AIAA paper 2013-2895, San Diego, 2013.
- [2] Edquist, K. T., Dyakonov, A. A., Wright, M. J., and Tang, C. Y., "Aerothermodynamic environments definition for the Mars Science Laboratory entry capsule," in *45th AIAA Aerospace Sciences Meeting and Exhibit*, AIAA paper 2007-1206, Reno, 2007.
- [3] Surzhikov, S., & Gromov, V., "Convective and radiative heating of a Martian space vehicle base surface," in *Fourth Symposium on Aero thermodynamics for Space Vehicles*, Capua, Italy, 2001.
- [4] Rouzaud, O., Tesse, L., Soubrie, T., Soufiani, A., Rivière, P., & Zeitoun, D. , "Influence of radiative heating on a martian orbiter," *Journal of Thermophysics and Heat Transfer*, vol. 22, no. 1, pp. 10-19, 2008.
- [5] Lino Da Silva, M., & Beck, J., "Contribution of CO₂ IR Radiation to Martian Entries Radiative Wall Fluxes," in *49th AIAA Aerospace Sciences Meeting including the New Horizons Forum and Aerospace Exposition*, AIAA paper 2011-135, Orlando, 2011.
- [6] Fujita, K., Matsuyama, S., & Suzuki, T., "Prediction of Forebody and Aftbody Heat Transfer Rate for Mars Aerocapture Demonstrator," in *43rd AIAA Thermophysics Conference*, AIAA paper 2012-3001, New Orleans, 2012.
- [7] Surzhikov, S., "Radiative Gas Dynamics of MSL at Angle of Attack," in *46th AIAA Thermophysics Conference*, AIAA paper 2016-0742, Washington, D.C., 2016.
- [8] Brandis, A. M., Saunders, D., Johnston, C., Cruden, B., and White, T., "Radiative Heating on the After-Body of Martian Entry Vehicles," in *45th AIAA Thermophysics Conference*, AIAA paper 2015-3111, Dallas, 2015.

- [9] Jaffe, R., "Vibrational and Rotational Excitation and Dissociation of CO₂ Reexamined," in *49th AIAA Aerospace Sciences Meeting including the New Horizons Forum and Aerospace Exposition*, AIAA paper 2011-447, Orlando, 2011.
- [10] West IV, T. K., Theisinger, J. E., Brune, A. J., & Johnston, C. O., "Backshell Radiative Heating on Human-Scale Mars Entry Vehicles," in *47th AIAA Thermophysics Conference*, AIAA paper 2017-4532, Denver, Colorado, 2017.
- [11] Cruden, Brett A., "Absolute Radiation Measurements in Earth and Mars Entry Conditions," in *Radiation and Gas-surface Interaction Phenomena in High-speed Reentry Lecture Series*, STO AVT-218, Urbana-Champaign, 2014.
- [12] Edquist, K. T., Hollis, B. R., Johnston, C. O., Bose, D., White, T. R., & Mahzari, M., "Mars science laboratory heat shield aerothermodynamics: Design and reconstruction," *Journal of Spacecraft and Rockets*, vol. 51, no. 4, pp. 1106-1124, 2014.
- [13] Sahai, A., Lopez, B. E., Johnston, C. O., & Panesi, M., "Novel Approach for CO₂ State-To-State Modeling and Application to Multidimensional Entry Flows," in *55th AIAA Aerospace Sciences Meeting*, AIAA paper 2017-0213, Grapevine, Texas, 2017.
- [14] Sahai, A., Lopez, B. E., Johnston, C. O., & Panesi, M., "A Reduced Order Maximum Entropy Model for Chemical and Thermal Non-equilibrium in High Temperature CO₂ Gas," in *46th AIAA Thermophysics Conference*, AIAA paper 2016-3695, Washington, D.C., 2016.
- [15] Colonna, G., and M. Capitelli, "The influence of atomic and molecular metastable states in high-enthalpy nozzle expansion nitrogen flows," *Journal of Physics D: Applied Physics*, vol. 34, no. 12, pp. 1812-1818, 2001.
- [16] Colonna, G., Armenise, I., Bruno, D., & Capitelli, M., "Reduction of state-to-state kinetics to macroscopic models in hypersonic flows," *Journal of thermophysics and heat transfer*, vol. 20, no. 3, pp. 477-486, 2006.
- [17] Xu, L. T., Jaffe, R. L., Schwenke, D. W., & Panesi, M., "The Effect of the Spin-forbidden CO ($1\Sigma^+$) + O ($3P$) → CO₂ ($1\Sigma^g$) Recombination Reaction on Afterbody Heating of Mars Entry Vehicles," in *47th AIAA Thermophysics Conference*, AIAA paper 2017-3486, Denver, Colorado, 2017.
- [18] Hollas, J. M., Basic atomic and molecular spectroscopy, Chichester: Wiley, 2002.

- [19] Kudriavtsev, N. N., Novikov, S. S., & Svetlichnyi, I. B., "CO₂ vibrational temperature measurements in CO + N₂O gasdynamic laser," *Acta Astronautica*, vol. 6, no. 3, pp. 391-399, 1979.
- [20] Park, C., Nonequilibrium hypersonic aerothermodynamics, New York: Wiley, 1989.
- [21] Fridman, A., & Kennedy, L. A., Plasma physics and engineering, New York: CRC press, 2004.
- [22] Sharma, R. D., "Infrared airglow," in *Progress in Atmospheric Physics*, Netherlands, Springer, 1988, pp. 177-186.
- [23] Williams, A. P., "Relaxation of the 2.7 μ and 4.3 μ Bands of Carbon Dioxide," in *Mesospheric Models and Related Experiments*, Netherlands, Springer, 1971, pp. 177-187.
- [24] Ferriso, C. C., & Ludwig, C. B., "Spectral Emissivities and Integrated Intensities of the 2.7- μ CO₂ Band between 1200° and 1800° K," *Journal of the Optical Society of America*, vol. 54, no. 5, pp. 657-662, 1964.
- [25] ron, "Is carbon dioxide IR inactive?", Chemistry Stack Exchange, 14 November 2014. [Online]. Available: <http://chemistry.stackexchange.com/questions/19119/is-carbon-dioxide-ir-inactive>. [Accessed 4 April 2015].
- [26] Burmeister, M., & Roth, P., "ARAS measurements on the thermal decomposition of CO₂ behind shock waves," *AIAA Journal*, vol. 28, no. 3, pp. 402-405, 1990.
- [27] Ebrahim, N. A., & Sandeman, R. J., "Interferometric studies of carbon dioxide dissociation in a free-piston shock tube," *The Journal of Chemical Physics*, vol. 65, no. 9, pp. 3446-3453, 1976.
- [28] Saxena, S., Kiefer, J. H., & Tranter, R. S., "Relaxation, incubation, and dissociation in CO₂," *The Journal of Physical Chemistry A*, vol. 111, no. 19, pp. 3884-3890, 2007.
- [29] Fujii, N., Kakuda, T., Takeishi, N., & Miyama, H., "Kinetics of the high temperature reaction of carbon monoxide with nitrous oxide," *Journal of Physical Chemistry*, vol. 91, no. 8, pp. 2144-2148, 1987.
- [30] Lin, M. C., & Bauer, S. H., "Bimolecular Reaction of N₂O with CO and the Recombination of O and CO as Studied in a Single-Pulse Shock Tube," *The Journal of Chemical Physics*, vol. 50, no. 8, pp. 3377-3391, 1969.

- [31] Fujii, N., Sagawai, S., Sato, T., Nosaka, Y., & Miyama, H., "Study of the thermal dissociation of nitrous oxide and carbon dioxide using oxygen (3P) atomic resonance absorption spectroscopy," *The Journal of Physical Chemistry*, vol. 93, no. 14, pp. 5474-5478, 1989.
- [32] Griffith, W., Brickl, D., & Blackman, V., "Structure of shock waves in polyatomic gases," *Physical Review*, vol. 102, no. 5, p. 1209, 1956.
- [33] Greenspan, W. D. & Blackman, V. H., "Approach to thermal equilibrium behind strong shock waves in carbon dioxide and carbon monoxide," *Bulletin of the American Physical Society*, vol. 217, no. 2, 1957.
- [34] Johannesen, N. H., Zienkiewicz, H. K., Blythe, P. A., & Gerrard, J. H., "Experimental and theoretical analysis of vibrational relaxation regions in carbon dioxide," *Journal of Fluid Mechanics*, vol. 13, no. 02, pp. 213-224, 1962.
- [35] Zienkiewicz, H. K., & Johannesen, N. H., "Departures from the linear equation for vibrational relaxation in shock waves in oxygen and carbon dioxide," *Journal of Fluid Mechanics*, vol. 17, no. 4, pp. 499-505, 1963.
- [36] Simpson, C. M., Bridgman, K. B., & Chandler, T. R., "Shock-Tube Study of Vibrational Relaxation in Carbon Dioxide," *The Journal of Chemical Physics*, vol. 49, no. 2, pp. 513-522, 1968.
- [37] Camac, M., "CO₂ Relaxation Processes in Shock Waves," in *Fundamental Phenomena in Hypersonic Flow*, New York, Cornell University Press, 1966, pp. 195-215.
- [38] Hindelang, F. J., "Coupled vibration and dissociation relaxation behind strong shock waves in carbon dioxide," NASA Technical Report R-253, Moffett Field, 1967.
- [39] Oehlschlaeger, M. A., Davidson, D. F., Jeffries, J. B., & Hanson, R. K., "Carbon dioxide thermal decomposition: Observation of incubation," *Zeitschrift für Physikalische Chemie*, vol. 219, no. 5, pp. 555-567, 2005.
- [40] Yatsiv, S., Greenfield, E., Dothan-Deutsch, F., Chuchem, D., & Bin-Nun, E., "Pulsed CO₂ Gas-Dynamic Laser," *Applied Physics Letters*, vol. 19, no. 3, pp. 65-68, 1971.
- [41] Lee, G., Gowen, F. E., & Hagen, J. R., "Gain and power of CO₂ gasdynamic lasers," *AIAA Journal*, vol. 10, no. 1, pp. 65-71, 1972.

- [42] Anderson Jr, J. D., Humphrey, R. L., Vamos, J. S., Plummer, M. J., & Jensen, R. E., "Population inversions in an expanding gas: theory and experiment," *The Physics of Fluids*, vol. 14, no. 12, pp. 2620-2624, 1971.
- [43] Sato, K., & Sekiguchi, T., "Experimental Studies of CO₂ Gas-Dynamic laser by Means of a Shock Tube," *Journal of the Physical Society of Japan*, vol. 36, no. 3, pp. 808-814, 1974.
- [44] Cruden, B. A., Prabhu, D. K., & Brandis, A. M., "Measurement and Characterization of Mid-wave Infrared Radiation in CO₂ Shocks," in *11th AIAA/ASME Joint Thermophysics and Heat Transfer Conference*, AIAA paper 2014-2962, Atlanta, 2014.
- [45] Depraz, S., Perrin, M. Y., Rivière, P., & Soufiani, A., "Infrared emission spectroscopy of CO₂ at high temperature. Part II: Experimental results and comparisons with spectroscopic databases.," *Journal of Quantitative Spectroscopy and Radiative Transfer*, vol. 113, no. 1, pp. 14-25, 2012.
- [46] Tashkun, S. A., & Perevalov, V. I., "High-resolution, high-temperature carbon dioxide spectroscopic databank," *Journal of Quantitative Spectroscopy and Radiative Transfer*, vol. 112, no. 9, pp. 1403-1410, 2011.
- [47] Lemal, A., Takayanagi, H., Nomura, S., & Fujita, K., "Simulations of Carbon-Dioxide Equilibrium Infrared Radiation Measurements," *Journal of Thermophysics and Heat Transfer*, vol. 0, no. 0, pp. 1-12, 2017.
- [48] Palmer, G., & Cruden, B., "Experimental Validation of CO₂ Radiation Simulations," in *43rd AIAA Thermophysics Conference*, AIAA paper 2012-3188, New Orleans, Louisiana, 2012.
- [49] Brandis, A., & Cruden, B., "NEQAIR v14. 0 User Tutorial," NASA, Moffet Field, 2016.
- [50] Ibraguimova, L., & Shatalov, O., "Non-equilibrium Kinetics behind Shock Waves Experimental Aspects," in *High Temperature Phenomena in Shock Waves*, Berlin, Springer Berlin Heidelberg, 2012, pp. 99-147.
- [51] MacLean, M., & Holden, M., "Numerical assessment of data in catalytic and transitional flows for Martian entry," in *9TH AIAA/ASME Joint Thermophysics and Heat Transfer Conference*, AIAA paper 2006-2946, San Francisco, 2006.

- [52] Holden, M. S., Wadhams, T. P., MacLean, M., Mundy, E., & Parker, R. A., "Experimental studies in LENS I and X to evaluate real gas effects on hypervelocity vehicle performance," in *45th AIAA Aerospace Sciences Meeting and Exhibit*, AIAA paper 2007-204, Reno, 2007.
- [53] MacLean, M., Dufrene, A., & Holden, M., "Spherical Capsule Heating in High Enthalpy Carbon Dioxide in LENS-XX Expansion Tunnel," in *51st AIAA Aerospace Sciences Meeting and Exhibit*, AIAA Paper 2013-906, Grapevine (Dallas/Ft. Worth Region), Texas, 2013.
- [54] Doraiswamy, S., Kelley, J. D., & Candler, G. V., "Vibrational modeling of co₂ in high-enthalpy nozzle flows," *Journal of Thermophysics and Heat Transfer*, vol. 24, no. 1, pp. 9-17, 2010.
- [55] Takayanagi, H., Lemal, A., Nomura, S., & Fujita, K., "Measurement of Carbon Dioxide Infrared Radiation in the Afterbody of a Mars entry Capsule," in *55th AIAA Aerospace Sciences Meeting*, AIAA paper 2017-1369, Grapevine, Texas, 2017.
- [56] Bender, D. J., Mitchner, M., & Kruger, C. H., "Measurement of vibrational population distributions in a supersonic expansion of carbon monoxide," *Physics of Fluids*, vol. 21, no. 7, pp. 1073-1085, 1978.
- [57] Park, C., "Measurement of Ionic Recombination Rate of Nitrogen," *AIAA Journal*, vol. 6, no. 11, pp. 2090-2094, 1968.
- [58] Park, C., "Comparison of electron and electronic temperatures in recombining nozzle flow of ionized nitrogen–hydrogen mixture. Part 2. Experiment," *Journal of Plasma Physics*, vol. 9, no. 02, pp. 217-234, 1973.
- [59] Igra, O., "An experimental investigation of a nonequilibrium corner-expansion flow of ionized argon," Technical report (No. UTIAS-161), Toronto University Institute for Aerospace Studies, Toronto, 1970.
- [60] Drewry, J. E., "An experimental investigation of nonequilibrium corner expansion flows of dissociated oxygen," Technical report (No. UTIAS-124), Toronto University Institute for Aerospace Studies, Toronto, 1967.
- [61] Wilson, J., "An experiment to measure the recombination," *Journal of Fluid Mechanics*, vol. 15, no. 04, pp. 497-512, 1962.

- [62] Blom, A. P., & Pratt, N. H., "Vibrational energy excitation and de-excitation of CO," *Nature*, vol. 223, pp. 1052-1053, 1969.
- [63] Nagamatsu, H. T., "Hypersonic nozzle expansion of air with atom recombination present," *Journal of the Aerospace Sciences*, vol. 28, no. 11, pp. 833-837, 1961.
- [64] Just, T., & Roth, P., "Measurements of CO Relaxation in an Unsteady Expansion Wave," *The Journal of Chemical Physics*, vol. 55, no. 5, pp. 2395-2399, 1971.
- [65] Sharma, S. P., Ruffin, S. M., Gillespie, W. D., & Meyer, S. A., "Vibrational relaxation measurements in an expanding flow using spontaneous Raman scattering," *Journal of thermophysics and heat transfer*, vol. 7, no. 4, pp. 697-703, 1993.
- [66] Sharma, S. P., Ruffin, S. M., Meyer, S. A., Gillespie, W. D., & Yates, L. A. , "Density measurements in an expanding flow using holographic interferometry," *Journal of thermophysics and heat transfer*, vol. 7, no. 2, pp. 261-268, 1993.
- [67] Nagamatsu, H. T., & Sheer, Jr, R. E., "Vibrational relaxation and recombination of nitrogen and air in hypersonic nozzle flows," *AIAA Journal*, vol. 3, no. 8, pp. 1386-1391, 1965.
- [68] Hurle, I. R., Russo, A. L., & Hall, J. G., "Spectroscopic studies of vibrational nonequilibrium in supersonic nozzle flows," *The Journal of Chemical Physics*, vol. 40, no. 8, pp. 2076-2089, 1964.
- [69] Holbeche, T. A., "Spectrum-line-reversal temperature measurements through unsteady rarefaction waves in vibrationally-relaxing oxygen," Technical report, Royal Aircraft Establishment, Farnborough (UK), 1964.
- [70] Holbeche, T. A., "Spectrum-Line-Reversal temperature measurements through unsteady rarefaction waves in vibrationally relaxing gases," in *AGARD Conference Proceedings No. 12*, Oslo, 1966.
- [71] Hall, J. G., & Treanor, C. E., "Nonequilibrium effects in supersonic-nozzle flows," Technical report (No. AGARD-OGRAPH-124), Advisory Group for Aerospace Research and Development (AGARD), Neuilly-sur-Seine (France), 1967.
- [72] Russo, A. L., "Spectrophotometric Measurements of the Vibrational Relaxation of CO in Shock-Wave and Nozzle Expansion-Flow Environments," *The Journal of Chemical Physics*, vol. 47, no. 12, pp. 5201-5210, 1967.

- [73] Rich, J. W., "Study of Nonequilibrium Flows," Technical report, AFOSR 68-0240, Cornell Aeronautical Laboratory, Buffalo, New York, 1968.
- [74] Dunn, M. G., & Lordi, J. A., "Measurement of N₂/plus/plus e-/dissociative recombination in expanding nitrogen flows," *AIAA Journal*, vol. 8, no. 2, pp. 339-345, 1970.
- [75] McLaren, T. I., & Appleton, J. P., "Vibrational Relaxation Measurements of Carbon Monoxide in a Shock-Tube Expansion Wave," *The Journal of Chemical Physics*, vol. 53, no. 7, pp. 2850-2857, 1970.
- [76] von Rosenberg Jr, C. W., Taylor, R. L., & Teare, J. D., "Vibrational relaxation of CO in nonequilibrium nozzle flow, and the effect of hydrogen atoms on CO relaxation," *The Journal of Chemical Physics*, vol. 54, no. 5, pp. 1974-1987, 1971.
- [77] Cleaver, J. W., & Crow, I. G., "Vibrational relaxation of oxygen in an unsteady expansion wave," *The Journal of Chemical Physics*, vol. 59, no. 4, pp. 1592-1598, 1973.
- [78] Sebacher, D. I., & Guy, R. W., "Vibrational relaxation in expanding N₂ and air," NASA TM X- 71988, NASA Langley Research Center, Hampton, 1974.
- [79] Nasser, A. E., & Cleaver, J. W., "Vibrational relaxation of carbon monoxide in an unsteady expansion wave," *Acta Astronautica*, vol. 4, no. 3, pp. 357-373, 1977.
- [80] Beck, W. H., & Mackie, J. C., "Application of the shock tube unsteady expansion wave technique to the study of chemical reactions," *Journal of Physics D: Applied Physics*, vol. 11, no. 9, p. 1249, 1978.
- [81] Hollis, B. R., Prabhu, D. K., Maclean, M., & Dufrene, A., "Blunt-Body Aerothermodynamic Database from High-Enthalpy Carbon-Dioxide Testing in an Expansion Tunnel," *Journal of Thermophysics and Heat Transfer*, vol. 31, no. 3, pp. 712-731, 2017.
- [82] Bray, K. N. C., "Atomic recombination in a hypersonic wind-tunnel nozzle," *Journal of Fluid Mechanics*, vol. 6, no. 1, pp. 1-32, 1959.
- [83] James, C. M., Gildfind, D. E., Lewis, S. W., Morgan, R. G., & Zander, F., "Implementation of a state-to-state analytical framework for the calculation of expansion tube flow properties," *Shock Waves*, pp. 1-29, 2017.

- [84] Johnston, C. O., & Brandis, A. M., "Features of Afterbody Radiative Heating for Earth Entry," *Journal of Spacecraft and Rockets*, vol. 52, no. 1, pp. 105-119, 2015.
- [85] James, C., Gildfind, D. E., Morgan, R. G., Jacobs, P. A., & Zander, F., "Designing and simulating high enthalpy expansion tube conditions," in *Proceedings of the 2013 Asia-Pacific International Symposium on Aerospace Technology*, Japan Soc. for Aeronautical and Space Sciences, 2013.
- [86] Paull, A., & Stalker, R. J., "Test flow disturbances in an expansion tube," *Journal of Fluid Mechanics*, vol. 245, pp. 493-521, 1992.
- [87] Morgan., R.G., "Chapter 4.3 Free-Piston Driven Expansion Tubes," in *Handbook of Shock Waves*, vol. 1, Academic Press, 2001, pp. 603-622.
- [88] Jacobs, P. A., "Shock Tube Modelling with L1d," University of Queensland, Brisbane, 1998.
- [89] Doraiswamy, S., "Computational Study of Nonequilibrium Chemistry in High Temperature Flows," The University of Minnesota, Minnesota, 2010.
- [90] Hollis, B. R., & Prabhu, D. K., "Assessment of laminar, convective aeroheating prediction uncertainties for Mars-entry vehicles," *Journal of Spacecraft and Rockets*, vol. 50, no. 1, pp. 56-68, 2013.
- [91] Meyers, J. M., Paris, S., & Fletcher, D. G., "Characterization of CO₂ flow in a hypersonic impulse facility using DLAS," *Experiments in Fluids*, vol. 57, no. 2, pp. 1-13, 2016.
- [92] MacLean, M., Dufrene, A., Wadhams, T., & Holden, M., "Numerical and Experimental Characterization of High Enthalpy Flow in an Expansion Tunnel Facility," in *48th AIAA Aerospace Sciences Meeting*, AIAA paper 2010-1562, Orlando, Florida, 2010.
- [93] Mirels, H., "Shock tube test time limitation due to turbulent-wall boundary layer," *AIAA Journal*, vol. 2, no. 1, pp. 84-93, 1964.
- [94] Bakos, R. J., & Morgan, R. G., "Chemical recombination in an expansion tube," *AIAA journal*, vol. 32, no. 6, pp. 1316-1319, 1994.
- [95] Nishida, M., & Lee, M. G., "Propagation Behaviour of Strong Shock Waves with Chemical Reactions in a Shock Tunnel Nozzle," in *Shock Waves@ Marseille II*, Berlin, Springer, Berlin, Heidelberg, 1995, pp. 301-306.

- [96] Park, C., "Thermochemical relaxation in shock tunnels," *Journal of thermophysics and heat transfer*, vol. 20, no. 4, pp. 689-698, 2006.
- [97] Jacobs, P., Gollan, R., Jahn, I., & Potter, D., "The eilmer3 code: user guide and example book 2015 edition," The University of Queensland, Brisbane, Australia, 2015.
- [98] Fahy, E. J., "Superorbital re-entry shock layers: flight and laboratory comparisons," Phd thesis, School of Mechanical and Mining Engineering, The University of Queensland, Brisbane, 2017.
- [99] Potter, Daniel F., "Modelling of Radiating Shock Layers for Atmospheric Entry at Earth and Mars," Phd thesis, University of Queensland, Brisbane, 2011.
- [100] Potter, D., Gollan, R., Eichmann, T., McIntyre, T., Morgan, R., & Jacobs, P., "Simulation of CO₂-N₂ expansion tunnel flows for the study of radiating shock layers," in *46th AIAA Aerospace Sciences Meeting and Exhibit*, AIAA paper 2008-1280, Reno, Nevada, 2008.
- [101] Jacobs, P., Silvester, T., Morgan, R., Scott, M., Gollan, R., & McIntyre, T., "Superorbital expansion tube operation: estimates of flow conditions via numerical simulation," in *43rd AIAA Aerospace Sciences Meeting and Exhibit*, AIAA paper 2005-694, Reno, Nevada, 2005.
- [102] Gildfind, David, "High Total Pressure Scramjet Flow Conditions using the X2 Expansion Tube," Phd thesis, Centre for Hypersonics, Department of Mechanical Engineering, University of Queensland, Brisbane, 2012.
- [103] McGilvray, M., Austin, J. M., Sharma, M., Jacobs, P. A., & Morgan, R. G., "Diagnostic modelling of an expansion tube operating condition," *Shock Waves*, vol. 19, no. 1, pp. 59-66, 2009.
- [104] Pakdaman, S. A., Garcia, M., Teh, E., Lincoln, D., Trivedi, M., Alves, M., & Johansen, C., "Diaphragm opening effects on shock wave formation and acceleration in a rectangular cross section channel," *Shock Waves*, vol. 26, no. 6, pp. 799-813, 2016.
- [105] Liao, D., Liu, S., Jian, H., Xie, A., Wang, Z., & Huang, J., "Measurement and Calculation of Shock Stand-off Distances over Hypersonic Spheres in CO₂," in *21st AIAA International Space Planes and Hypersonics Technologies Conference*, AIAA paper 2017-2124, Xiamen, 2017.

- [106] Nikitin, E. E., & Troe, J., "70 years of Landau–Teller theory for collisional energy transfer. Semiclassical three-dimensional generalizations of the classical collinear model.," *Physical Chemistry Chemical Physics*, vol. 10, no. 11, pp. 1483-1501, 2008.
- [107] Park, C., Howe, J. T., Jaffe, R. L., & Candler, G. V., "Review of chemical-kinetic problems of future NASA missions. II-Mars entries," *Journal of Thermophysics and Heat transfer*, vol. 8, no. 1, pp. 9-23, 1994.
- [108] Sharma, M., "Post-shock thermochemistry in hypervelocity CO₂ and air flow," Phd thesis, University of Illinois, Urbana-Champaign, 2010.
- [109] Hollis, B. R., & Perkins, J. N., "High-enthalpy aerothermodynamics of a Mars entry vehicle part 1: Experimental results," *Journal of Spacecraft and Rockets*, vol. 34, no. 4, pp. 449-456, 1997.
- [110] Hollis, B. R., "Experimental and computational aerothermodynamics of a Mars entry vehicle," Phd thesis, NASA Langley Research Center, Hampton, VA United States, 1996.
- [111] Sharma, M., Swantek, A. B., Flaherty, W., Austin, J. M., & Glumac, N. G., "Expansion tube investigation of shock stand-off distances in high-enthalpy CO₂ flow over blunt bodies," in *48th AIAA Aerospace Sciences Meeting and Exhibit*, AIAA paper 2010-1566, Orlando, 2010.
- [112] Scott, M. P., "Development and modelling of expansion tubes," Phd thesis, School of Engineering , University of Queensland, St Lucia, Brisbane, 2007.
- [113] Chue, R. S. M., Bakos, R. J., Tsai, C. Y., & Betti, A., "Design of a shock-free expansion tunnel nozzle in HYPULSE," *Shock Waves*, vol. 13, no. 4, pp. 261-270, 2003.
- [114] Jacobs, C. M., "Radiation in low density hypervelocity flows," Phd thesis, School of Mechanical and Mining Engineering, The University of Queensland, Brisbane, Australia, 2011.
- [115] "Spectrometer," K-MAC, [Online]. Available: <http://kmacever.en.ec21.com/Spectrometer--5585825.html>. [Accessed 5 february 2015].
- [116] Richardson, A, *Private Communication*, 2016.
- [117] Fischer, R. E., Tadic-Galeb, B., Yoder, P. R., & Galeb, R., Optical system design, New York: McGraw Hill, 2008.

- [118] "IRC800 User's Guide," IRCameras, Santa Barbara, 2014.
- [119] "Section 1: Diffraction Gratings Ruled & Holographic," HORIBA Scientific, [Online]. Available: <http://www.horiba.com/scientific/products/optics-tutorial/diffraction-gratings/>. [Accessed 22 December 2017].
- [120] Eichmann, T. N., "Radiation measurements in a simulated Mars atmosphere," Phd thesis, Centre for Hypersonics, Department of Mechanical Engineering, University of Queensland, Brisbane, 2012.
- [121] Cruden, B, *Private Communication*, 2015.
- [122] Sheikh, U., "Re-entry radiation aerothermodynamics in the vacuum ultraviolet," Phd thesis, School of Mechanical and Mining Engineering, The University of Queensland, St Lucia, 2014.
- [123] Griffiths, R. W., Sandeman, R. J., & Hornung, H. G., "The stability of shock waves in ionizing and dissociating gases," *Journal of Physics D: Applied Physics*, vol. 9, no. 12, pp. 1681-1691, 1976.
- [124] Pert, G. J., "Flow modes in shock tubes with electromagnetic driving sections," *Journal of Physics D: Applied Physics*, vol. 3, no. 2, pp. 203-209, 1970.
- [125] Payne, W. F., "Diagnostics of an Argon Free Jet Expanded from a High Pressure Inductive Arc Source," in *Astronautical Research 1971*, Springer Netherlands, 1973, pp. 557-576.
- [126] Kustova, E. V., Nagnibeda, E. A., Shevelev, Y. D., & Syzranova, N. G., "Non-Equilibrium Kinetics and Transport Processes in a Hypersonic Flow of CO 2/CO/O 2/C/O Mixture," in *AIP Conference Proceedings*, 2011.
- [127] Gordon, S., & McBride, B. J., "Computer program for calculation of complex chemical equilibrium compositions and applications. Part 1: Analysis," NASA reference publication 1311, NASA Lewis Research Center, Cleveland, OH, 1994.
- [128] Anderson, J. D., Hypersonic and high temperature gas dynamics., Reston, Virginia, USA: AIAA Education Series, 2006.
- [129] Millikan, R. C., & White, D. R., "Systematics of vibrational relaxation," *The Journal of chemical physics*, vol. 39, no. 12, pp. 3209-3213, 1963.

- [130] GridPro, "GridPro GUI Manual Version 2.2," 15 March 2017. [Online]. Available: http://sp.gridpro.com/docs/WS_GUI_Manual_v6.6.pdf. [Accessed 31 August 2017].
- [131] Eichmann, T. N., "An Experimental Investigation of Shock Shapes and Shock Stand-offs in a Super-orbital Facility," Master thesis, University of Queensland, St Lucia, 2004.
- [132] Hu, Y., Huang, H., & Zhang, Z., "New formulas for standoff distance in front of spacecraft in hypersonic flow," *Journal of Spacecraft and Rockets*, vol. 53, no. 5, pp. 993-997, 2016.
- [133] Furudate, M., Nonaka, S., & Sawada, K., "Behavior of two-temperature model in intermediate hypersonic regime," *Journal of thermophysics and heat transfer*, vol. 13, no. 4, pp. 424-430, 1999.
- [134] Ruffin, S. M., "Prediction of Vibrational Relaxation in Hypersonic Expanding Flows Part 1: Model Development," *Journal of thermophysics and heat transfer*, vol. 9, no. 3, pp. 432-437, 1995.
- [135] Hsu, C. T., & McMillen, L. D., "Time-Dependent Solutions for De-excitation Rates of Anharmonic Oscillators," *The Journal of Chemical Physics*, vol. 56, no. 11, pp. 5327-5334, 1972.
- [136] Kewley, D. J., "Numerical study of anharmonic diatomic relaxation rates in shock waves and nozzles," *Journal of Physics B: Atomic and Molecular Physics*, vol. 8, no. 15, pp. 2565-2579, 1975.
- [137] Ruffin, S. M., "Prediction of vibrational relaxation in hypersonic expanding flows part 2: Results," *Journal of thermophysics and heat transfer*, vol. 9, no. 3, pp. 438-445, 1995.
- [138] Allen, H. J., & Eggers Jr, A. J., "A study of the motion and aerodynamic heating of missiles entering the earth's atmosphere at high supersonic speeds," NACA-RM-A53D28, Moffett Field, 1953.
- [139] Martinez-Sanchez, Manuel, "Reacting Nozzle Flow - MIT OpenCourseWare," [Online]. Available: http://ocw.mit.edu/courses/aeronautics-and-astronautics/16-512-rocket-propulsion-fall-2005/lecture-notes/lecture_14.pdf. [Accessed 5 May 2016].
- [140] Benson, Tom, "Real Gas Effects," NASA, 12 June 2014. [Online]. Available: <https://www.grc.nasa.gov/www/BGH/realgas.html>. [Accessed 31 March 2017].

- [141] Rathakrishnan, E., *Theoretical Aerodynamics*, Singapore: John Wiley & Sons, 2013.
- [142] Dyakonov, A. A., Schoenenberger, M., & Van Norman, J. W., "Hypersonic and supersonic static aerodynamics of Mars science laboratory entry vehicle," in *43rd AIAA Thermophysics Conference*, AIAA paper 2012-2999, New Orleans, Louisiana, 2012.
- [143] "Prandtl-Meyer Expansion," The University of Sydney, 2015. [Online]. Available: http://aerodynamics.aeromech.usyd.edu.au/gasdynamics_w.php?page=6&. [Accessed 15 January 2015].
- [144] Capitelli, M., Colonna, G., & Esposito, F., "On the coupling of vibrational relaxation with the dissociation-recombination kinetics: From dynamics to aerospace applications," *The Journal of Physical Chemistry A*, vol. 108, no. 41, pp. 8930-8934, 2004.
- [145] Munafò, A., Panesi, M., & Magin, T. E., "Boltzmann rovibrational collisional coarse-grained model for internal energy excitation and dissociation in hypersonic flows," *Physical Review E*, vol. 89, no. 2, p. 023001, 2014.
- [146] Lin, S., *Radiationless transitions*, New York: Academic, 1980.
- [147] Ter Haar, D., & Ruark, A. E., "The old quantum theory," *American Journal of Physics*, vol. 35, no. 11, pp. 1098-1099, 1967.
- [148] "Spontaneous emission," Wikipedia, 17 May 2017. [Online]. Available: https://en.wikipedia.org/wiki/Spontaneous_emission#/media/File:Spontaneousemission.png. [Accessed 2 July 2017].
- [149] "Stimulated emission," Wikipedia, 1 July 2017. [Online]. Available: https://en.wikipedia.org/wiki/Stimulated_emission. [Accessed 2 July 2017].
- [150] Goody, R. M., & Yung, Y. L., *Atmospheric radiation: theoretical basis*, 2nd ed., New York: Oxford University Press, 1989.
- [151] Zel'dovich, I. B., Zel'dovich, Y. B., & Raizer, Y. P., *Physics of shock waves and high-temperature hydrodynamic phenomena*, vol. I, New York: Academic Press, 1968.
- [152] Wood, Kenneth, "Thermal Radiation," [Online]. Available: http://www-star.st-and.ac.uk/~kw25/teaching/nebulae/lecture04_blackbody.pdf. [Accessed 15 December 2014].
- [153] Davidson, Norman R., *Statistical Mechanics*, New York: McGraw-Hill, 1962.

- [154] Robitaille, P. M., "Kirchhoff's Law of Thermal Emission: 150 Years," *Progr. Phys.*, vol. 4, pp. 3-13, 2009.
- [155] Panesi, M., Munafò, A., Magin, T. E., & Jaffe, R. L., "Nonequilibrium shock-heated nitrogen flows using a rovibrational state-to-state method," *Physical Review E*, vol. 90, no. 1, pp. 1-16, 2014.
- [156] Brandis, A., "Experimental Study and Modelling of Non-Equilibrium Radiation during Titan and Martian Entry," Phd thesis, Centre for Hypersonics, Department of Mechanical Engineering, University of Queensland, Brisbane, 2009.
- [157] Aliat, A., Kustova, E. V., & Chikhaoui, A., "State-to-state reaction rates in gases with vibration-electronic-dissociation coupling: the influence on a radiative shock heated CO flow," *Chemical physics*, vol. 314, no. 1, pp. 37-47, 2005.
- [158] Johnston, C. O., Hollis, B. R., & Sutton, K., "Non-Boltzmann modeling for air shock-layer radiation at lunar-return conditions," *Journal of Spacecraft and Rockets*, vol. 45, no. 5, pp. 879-890, 2008.
- [159] Kunova, O. V., & Nagnibeda, E. A., "State-to-state description of reacting air flows behind shock waves," *Chemical Physics*, vol. 441, pp. 66-76, 2014.
- [160] Liu, Y., Panesi, M., Vinokur, M., & Sahai, A., "Generalized Multi-Group Macroscopic Modeling for Thermo-Chemical Non-Equilibrium Gas Mixtures," in *7th AIAA Theoretical Fluid Mechanics Conference*, Atlanta, 2014.
- [161] Doraiswamy, S., Kelley, J. D., & Candler, G. V., "Energy Bin Model for High-Enthalpy Flows Using Prior Recombination Distribution," *Journal of Thermophysics and Heat Transfer*, vol. 26, no. 4, pp. 545-558, 2012.
- [162] Kustova, E. V., & Nagnibeda, E. A., "On a correct description of a multi-temperature dissociating CO₂ flow," *Chemical physics*, vol. 321, no. 3, pp. 293-310, 2006.
- [163] Bourdon, A., Panesi, M., Brandis, A., Magin, T. E., Chaban, G., Huo, W., ... & Schwenke, D. W., "Simulation of flows in shock-tube facilities by means of a detailed chemical mechanism for nitrogen excitation and dissociation," in *Proceedings of the Summer Program*, Palo Alto, 2008.

- [164] Park, C, "The limits of two-temperature model," in *48th AIAA Aerospace Science Meeting Including the New Horizons Forum and Aerospace Exposition*, AIAA paper 2010-911, Orlando, 2010.
- [165] Neely, A. J., & Morgan, R. G., "The superorbital expansion tube concept, experiment and analysis," *The Aeronautical Journal*, vol. 98, no. 973, pp. 97-105, 1994.
- [166] Doherty, L. J., "An experimental investigation of an airframe integrated three-dimensional scramjet engine at a Mach 10 flight condition," Phd thesis, School of Mechanical and Mining Engineering, The University of Queensland, Brisbane, Australia, 2014.

A Hypersonic Flow Background

A.1 Characteristics of High Enthalpy Flows

The study of the radiative heat transfer encountered during atmospheric entry involves studying high enthalpy flows. High enthalpy flow causes strong shock waves which results in real gas effects such as vibrational excitation, dissociation and ionization. As illustrated on Figure A.1, the vibrational modes are the first to be excited. Further excitation of the vibrational mode causes dissociation. At even higher enthalpy conditions, ionization occurs. Not shown in the figure is electronic excitation which occurs after dissociation and before ionization. Vibrational excitation and dissociation are important in the current work, while ionization is irrelevant.

To minimize the heat load, atmospheric entry vehicles are generally blunt bodies [138], as shown on Figure A.2. The thermochemistry of a flow around an entry vehicle can be characterized as either frozen, equilibrium or non-equilibrium. A flow possessing thermochemical equilibrium implies that the chemical reactions and thermal energy exchanges occur at an infinite rate, thus, adjusting instantaneously to the changing translational temperature and pressure as a fluid element moves through the flow field. The opposite of an equilibrium flow is a frozen flow where the thermochemical rates are zero. The thermochemical state of a fluid element in a frozen flow will, consequently, remain the same as it travels through the flow field. In this thermochemically frozen flow, the specific heats of the flow does not change with temperature. This means that the specific heat capacity ratio remains constant. This consequently means that a flow which is thermochemically frozen is a calorically perfect gas. Furthermore, for a flow process that is adiabatic, inviscid and shock-free, the frozen and equilibrium thermochemical limits are both isentropic processes [139]. In reality, however, no flow can have a truly infinite or zero reaction rate. Nevertheless, a flow can be approximated as equilibrium if the thermochemical relaxation time is much shorter compared to the time for a fluid element to traverse the flow field of interest [128]. The inverse can be approximated as a frozen flow. All other situations are considered non-equilibrium flows. The strongest non-equilibrium conditions occur when the thermochemical relaxation times are comparable with the time for a fluid element to traverse the flow field. During non-equilibrium flow, the thermal excitation of the vibrational mode and the chemical reactions associated with dissociation and ionization occur at finite rates. In addition, under severe non-equilibrium conditions, the internal energy modes may even be distributed with a non-Boltzmann population distribution. The finite rate of the thermochemical processes occurring in non-

equilibrium flows causes an entropy increase in the flow. Therefore, non-equilibrium flow processes are irreversible and not isentropic [139].

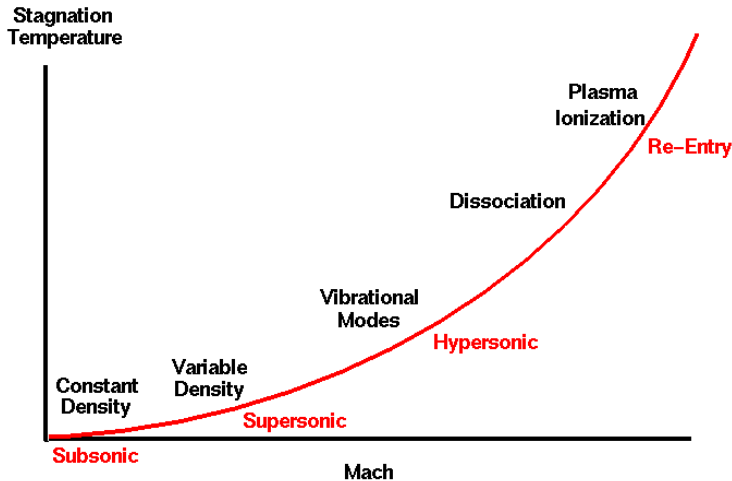


Figure A.1. Onset of real gas effects with increase in freestream Mach number. [140]

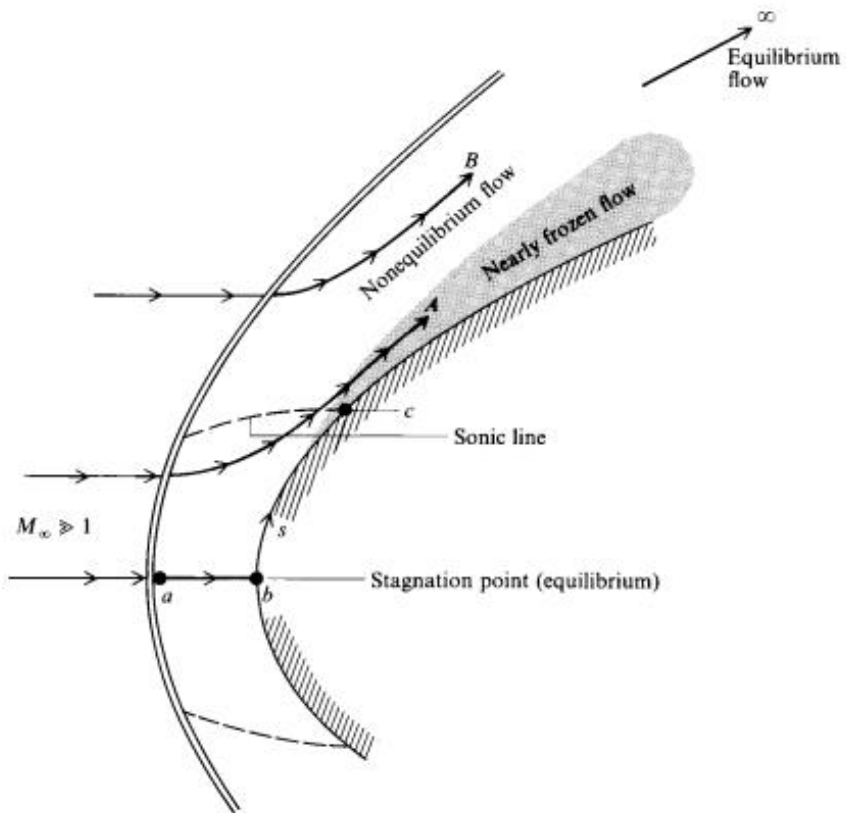


Figure A.2. Chemically reacting flow in the shock layer. [128]

Expanding flows are one of the less understood flow phenomena in hypersonics and has been of interest since the 1960s. As shown in Figure A.3, flow around an entry vehicle will travel through an expansion fan. It is the flow inside this expansion fan that is of interest in this project. Sudden expansion causes the translational energy of the gas particles to quickly decrease and a condition

where the translational energy is lower than the vibrational energy is created, which is the opposite of flow through a shock wave. Subsequently, thermochemical non-equilibrium is created. The vibrational relaxation rate and chemical reaction rate occurring in expanding flows may be different from that occurring behind shock waves.

A steady supersonic two-dimensional flow around a sharp convex corner, also known as Prandtl-Meyer flow, produces a centred expansion fan, as shown on Figure A.4. A centred expansion fan is described by Rathakrishnan [141] as being composed of an infinite number of Mach Waves and is, thus, a continuous region of expansion. However, unless the flow is nonreactive or reactive at infinite rates, the expanding flow is non-isentropic even if it is frictionless and adiabatic. The centred expansion fan is bounded upstream by the Mach wave from the freestream. The expansion fan is bounded downstream by the Mach wave from the expanded downstream condition. These Mach waves also coincide with the positive characteristic lines.

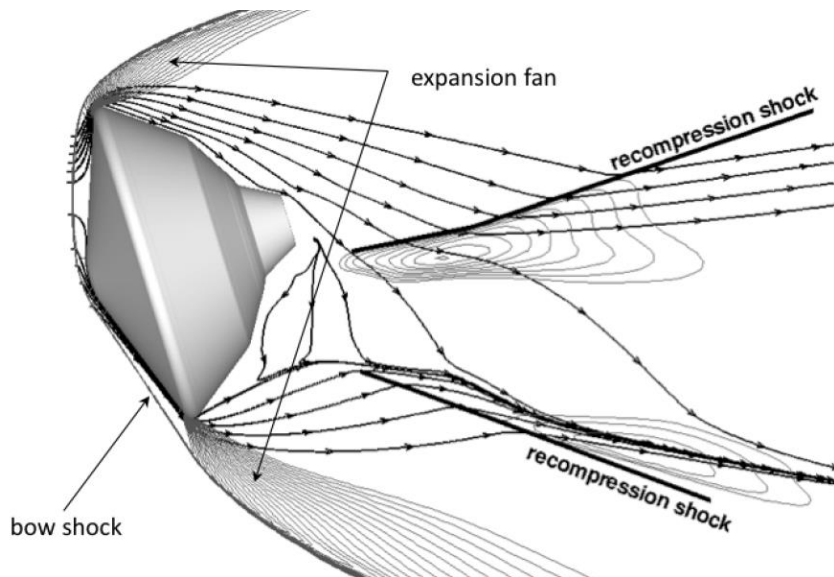


Figure A.3. Various flow phenomenon around the MSL entry vehicle. Adapted from. [142]

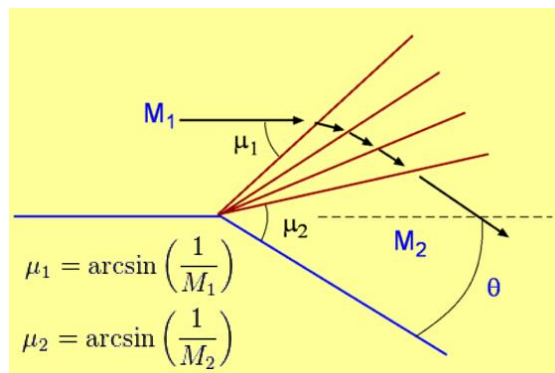


Figure A.4. A centred expansion fan where the fan region is determined by the two Mach angles. [143]

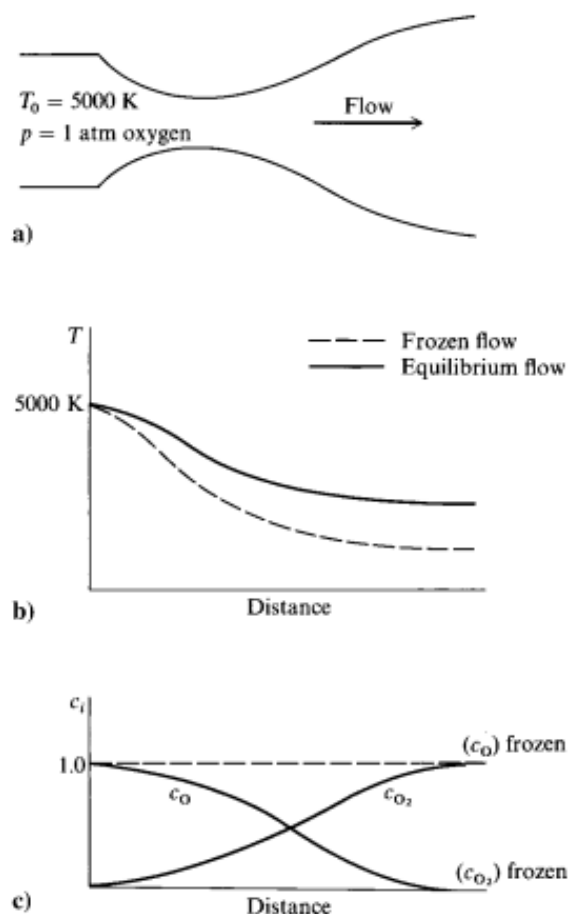


Figure A.5. Chemically reacting flow through a nozzle. [128]

Changes to the flow properties, such as density, pressure, temperature and velocity, occur uniformly inside the expansion fan. The rate of change of the flow properties will depend on the rate at which each streamline crosses the Mach waves. Thus, the rate of change will be greatest for streamlines near the convex corner while the rate will be lower for streamlines further away from the corner. Thus, a chemically reacting flow travelling through a centred expansion fan may experience both frozen flow and equilibrium flow. The streamlines near the corner will most likely be frozen while streamlines far away from the corner will be in equilibrium, while the streamlines in-between will experience non-equilibrium. The frozen and equilibrium chemical compositions represent the limits of the chemical composition in all reacting flows. Figure A.5 illustrates a chemically reacting flow through a nozzle. As shown in the figure, the frozen and equilibrium limiting flows also represent the temperature limits of the flow. For an expanding flow, as is the case illustrated in the figure, the frozen flow represents the lower bound of the temperature, while the equilibrium flow represents the upper bound. The opposite is true for the flow behind a shock. This is because the chemical reactions in the expanding flow are mostly exothermic, thus, transferring energy into the translational modes. On the other hand, for the flow behind a shock, the chemical reactions are mostly endothermic, thus, taking energy out of the translational modes. As for the transfer of energy between

the translational and vibrational modes, the thermal non-equilibrium in expanding flow conditions occur with the vibrational mode having more energy than the translational mode. The opposite is seen for thermal non-equilibrium behind a shock wave.

Flow separation will occur if the turn angle of the convex corner is too large, as shown on Figure A.6. In an inviscid flow, a slip line, the dashed line on Figure A.6, represents the boundary between the stationary fluid (vortices and eddies) and the separated flow. Additionally, across this slip line, there is a change in the fluid temperature and density. In a viscous flow, the slip line is replaced by a shear layer in order to satisfy the no-slip boundary condition.

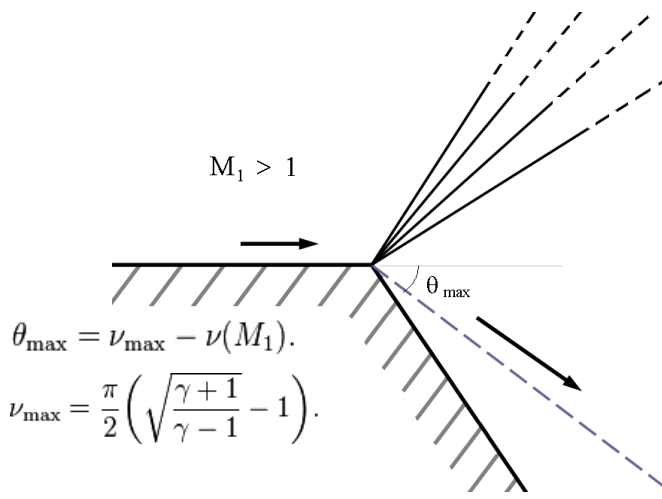


Figure A.6. A centred expansion fan where the maximum turn angle is determined by the two equations shown, where ν is the Prandtl-Meyer function and γ is the ratio of specific heat capacities.
Adapted from [141]

An important characteristic of expanding flows is that, due to the low densities involved during and after the expansion, the gas molecules may obtain a non-Boltzmann (non-equilibrium) population distribution in the internal energy modes. Various consequences result if the population is non-Boltzmann distributed. Firstly, the commonly used Landau-Teller vibrational relaxation model may not be able to describe the vibrational relaxation correctly if the vibrational energy population is non-Boltzmann distributed [134]. Secondly, the recombination and dissociation rates would be non-Arrhenius if the vibrational energy population is non-Boltzmann distributed [144]. Thirdly, the non-Boltzmann population formed during expanding flows is a distribution where there is an over population of high lying energy levels [144] [15] [145]. This over-population of high lying energy states has an important consequence on radiation emitted. The absorption and emission of spectral lines is proportional to the number density of the lower and upper energy levels, respectively. Thus, over population of the high lying energy levels will result in high radiation emission [84]. Furthermore, if the flow has a non-Boltzmann population distribution, complex numerical models

would need to be used in order to capture the non-Boltzmann effects and predict the radiative heating correctly.

A.2 Transitions between Energy Levels

In the context of describing high temperature radiating flows, understanding the mechanisms affecting the internal energy of the molecules is important. Both the collisional transitions and radiative transitions needs to be considered when describing high temperature radiative flows. The radiative transitions are important for determining the radiative emissions of the high temperature gas. The collisional transitions are important for describing the thermal non-equilibrium of the gas mixture.

A collision between two heavy particles (an atom or molecule) can cause changes in the electronic, vibrational and rotational energy modes of the particles in addition to the changes in translational energy [65]. Generally, collisional transitions during particle collisions do not involve absorption or emission of photons, and, thus, can be considered radiationless transitions (also known as non-radiative transitions) [146]. Due to the law of conservation of energy, rather than emitting or absorbing a photon, the transition energy of the particle is balanced out by an appropriate change in energy of the other particle. Collisions between atoms or molecules in an excited, high temperature, gas are rarely perfectly elastic as some of the kinetic energy is transferred to the molecules' internal energies. Consequently, the thermal properties of high temperature gas deviates from that of ideal gas and subsequent deviation are known as high temperature gas effects [128]. The rotational degree of freedom is the easiest to excite due to its small energy quanta. The vibrational degree of freedom is more difficult to excite than the rotational mode due to its larger quanta. The electronic state is the hardest to excite because it has largest quanta between the energy levels and, thus, requires higher temperature for excitation compared to the rotational and vibrational modes. For the atmospheric entry conditions concerned in this thesis, non-equilibrium of the vibrational mode is of interest. Relaxation of the vibrational mode is influenced by the vibrational – translational (V-T) exchange, which involves energy transfer between the translational energy of one particle and the vibrational energy of the other particle, and the vibrational – vibrational (V-V) exchange, which involves energy transfer between the vibrational energy of two molecules.

Radiative transitions involve absorption and emission of photons with energy equal to the energy difference between the initial and final energy level. There are three mechanisms occurring in the creation of spectral lines [147]. The three mechanisms are spontaneous emission, stimulated emission and absorption.

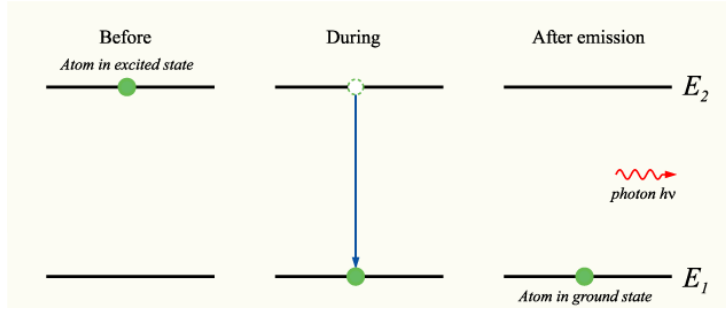


Figure A.7. The spontaneous emission process [148].

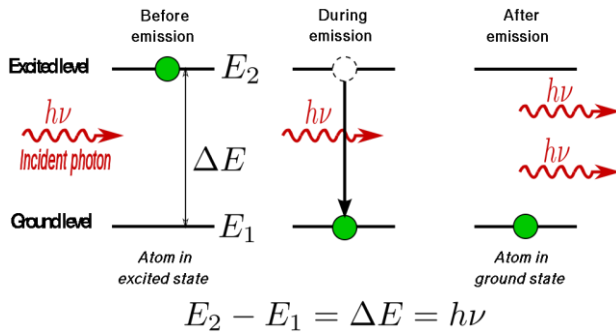


Figure A.8. The stimulated emission process [149].

Excited particles decay towards the ground state, thus, causing spontaneous emission as shown on Figure A.7. Such emissions occur more frequently when more gas particles get excited, as the emission rate is proportional to the number of excited particles present. The radiation caused by spontaneous emission increases with the number density of particles in the excited state of the relevant transition. The radiation also depends on the value of the Einstein coefficient for spontaneous emission. The Einstein coefficient for spontaneous emission is the probability per unit time that a particle in the excited state will spontaneously decay to the corresponding lower state, emitting a photon in the process. Stimulated emission, shown on Figure A.8, occurs when a photon of a particular wavelength interacts with a particle, causing it to emit a photon of the same wavelength and, subsequently, obtaining a new, lower, energy level. The opposite occurs in absorption as the particle absorbs the photon and obtains a new, higher, energy level. In order for stimulated emission or absorption to occur, the energy of the incident photon must be equal to the energy of the transition. The degree of excitation of the gas particles determines the likelihood of stimulated emission and absorption; highly excited gas will exhibit high stimulated emission and low absorption because there are more particles in the high energy state and less particles in the low energy state, thus, favouring emission [150]. The total stimulated emission or absorption depends on the path length, Einstein coefficient and the number density of particles in the lower and upper states of the relevant transition. The Einstein coefficient for stimulated emission and absorption is the probability per unit time per unit spectral energy density that a particle with the respective energy state will emit or absorb a photon

respectively. The spectral energy density refers to the respective photon energy per unit volume of the incident radiation field. The Einstein coefficients for spontaneous emission, stimulated emission and absorption are all universally constant probabilities associated with the particular particle. Thus, the coefficients do not depend on the state of the gas [151].

For a radiating gas with energy levels populated with a Boltzmann (equilibrium) distribution, the radiation emission will never exceed that given by Planck's law at the respective excitation temperature and frequency [152]. The emission nears the blackbody radiation limit when the particle number density and/or radiating path length increases. Subsequently, self-absorption is the mechanism which prevents the radiation from exceeding the blackbody limit [153]. For a Boltzmann population distribution, the number density in an upper energy state cannot exceed the number density in a lower energy state; at an infinite excitation temperature, the population of the upper and lower states becomes equal [154]. Nevertheless, conditions where an upper state is more populated than a lower state, called a 'population inversion', can be observed under some non-equilibrium processes, for example in lasers.

A.3 Numerical Modelling of Non-Equilibrium Flows

The current numerical models used to describe the thermochemical non-equilibrium in high enthalpy flows are discussed in this section. The models are briefly described and the advantages and disadvantages of each model are mentioned.

Also known as microscopic models and state specific models, the state-to-state approach is a non-Boltzmann model. It is based on modelling the individual internal energy levels of each gas particle and subsequent energy exchanges. Species that are chemically the same but have different internal energies (states) are modelled as, effectively, different species [155]. Thus, state-to-state modelling requires state specific thermochemical rate equations. Such state specific rates are determined theoretically through first principles. The full state-to-state model simulates the individual energy levels in all the internal energy modes and accounts for all the relevant radiative and collisional mechanism for transition within the internal energy modes. Thus, although accurate, the full state-to-state model is very computationally expensive. Currently, implementation of a full state-to-state model is non-existent in literature. This is due to its complexity and the large computational time required, as well as the absence of data for transitions between all states. However, implementation of reduced order state-to-state models has been described in recent literature [156] [157] [158] [159].

The current development on the reduced order state-to-state model is the multi-group model [145] [160] [161] [14]. The fundamental idea of the multi-group model involves lumping the internal states

into various grouped levels, or bins, thus reducing the amount of computations. This strategy is believed to be able to produce accurate simulations of strong non-equilibrium thermochemistry without compromising the computational time too much.

Also known as macroscopic models, the multi-temperature approach does not model individual internal energy levels of the gas particles. Instead, the internal energy level populations are assumed to be distributed through a Boltzmann distribution. The multi-temperature models describe thermal non-equilibrium by simulating different temperatures for different energy modes. The most commonly used multi-temperature model is the two-temperature model [107]. The conventional two-temperature model assumes the gas flow has two temperatures; a translational temperature and a vibrational temperature. The translational temperature is equal to the rotational temperature and the vibrational temperature is equal to both the electronic temperature and electron-translational temperature. The thermal non-equilibrium between the translational-rotational temperature and the vibrational-electron-electronic temperature is generally modelled using the Landau-Teller equation. The value of the vibrational relaxation time in the Landau-Teller equation is generally calculated from the Millikan and White equation [99] unless experimental data exists. The chemical non-equilibrium is modelled using the Arrhenius relationship with the chemical reaction rates generally deduced from experiments [20]. The controlling temperature of the chemical reactions is not always the translational temperature; the geometric average temperature, $T_{geo} = \sqrt{TT_v}$, is used for some reactions. Various other more complex forms of the multi-temperature model exist such as models with more than one vibrational temperature to account for the multiple vibrational modes of carbon dioxide molecules [7] [162].

The multi-temperature models are computationally quicker compared to the state-to-state approach. Due to the simplicity, the multi-temperature models are still the preferred method to use when describing non-equilibrium hypersonic flows [155]. However, the multi-temperature formulation is only valid if the internal energy modes have populations that can be approximated as Boltzmann distributions. Significant discrepancies are found when using the multi-temperature model if the distribution of the internal energy levels are highly non-Boltzmann [163]. In addition to the validity of the assumption of Boltzmann distributions, the accuracy of the multi-temperature model also depends on the validity of the thermochemical kinetics model and the assumption of various modes being in equilibrium (for example the rotational mode is in equilibrium with the translational mode) [164].

A.4 Impulse Facilities for Studying High Enthalpy Flows

The study of high enthalpy flows through experiments is critical for improving and validating the current numerical models. Studying high enthalpy flows through experiments require the use of impulse facilities. Impulse facilities produce hypervelocity flows for a very short duration of time. These facilities are required to study high enthalpy gas dynamics through experiments. Three commonly used impulse facilities are described below, along with the corresponding advantages and disadvantages of each facility.

Expansion Tube

The expansion tubes are commonly used to study very high enthalpy flows. The X2 expansion tube at the University of Queensland is shown on Figure A.9. To produce the test flow, the free piston compresses the driver gas which increases its temperature and pressure. Once the high pressure driver gas ruptures the primary diaphragm, a shock wave is created propagating down the shock tube. The shock tube is filled with the test gas. Once the shock wave reaches the secondary diaphragm, the diaphragm ruptures and an unsteady expansion is created. The test gas then expands through the acceleration tube where its velocity increases significantly. After that, the test gas expands through the nozzle where the core flow size and test time increases. The expansion tube experiments are always conducted with a test model.

The most well-known advantage of the expansion tube is its ability to generate high enthalpy flows. This is due to the fact that the unsteady expansion at the secondary diaphragm increases the total enthalpy of the test flow. Another advantage of the expansion tube is that, in most cases, the freestream condition generated is at thermochemical equilibrium [165]. The condition generated by the expansion tube is generally closer to equilibrium than that generated by the reflected shock tube. This is because the length of the acceleration tube assists the formation of equilibrium flow as it gives the flow more time to achieve equilibrium after the unsteady expansion. Hence, deviation from equilibrium will be smaller than that of the reflected shock tube. Additionally, the test gas is, in most cases, shocked only once so the pressures and temperature of the test gas never reaches the level of pressure reached in a reflected shock tube. Thus, even if the test flow fails to reach equilibrium by the time it arrives at the test section, it will be at a less excited state, compared to that of the reflected shock tube. The disadvantage of the expansion tube is the short test time (relative to the reflected shock tube), potentially large amounts of noise in the test flow and the difficulty in performing full facility simulations to predict freestream conditions.

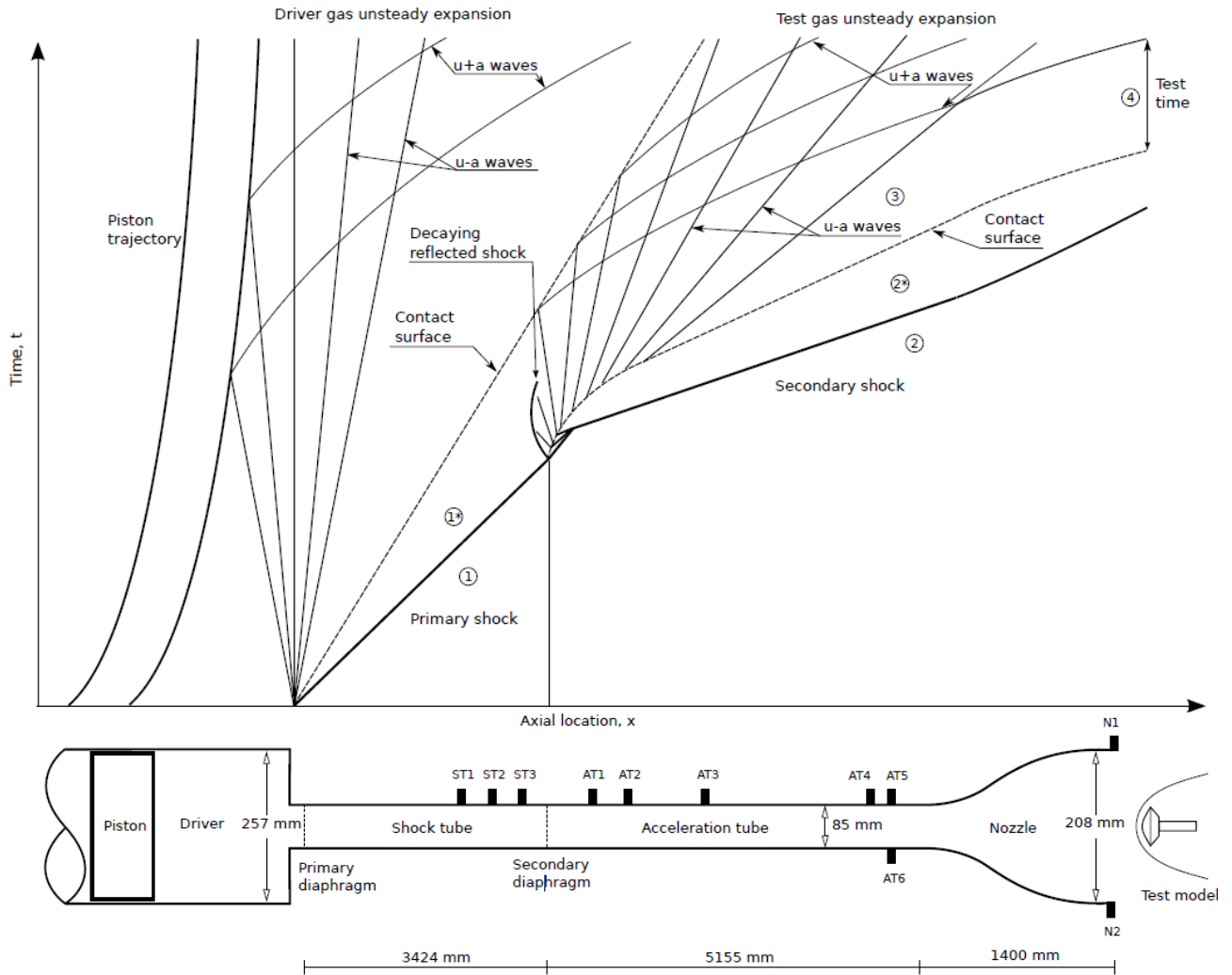


Figure A.9. X2 expansion tube. [99]

Non-reflected Shock Tube

Non-reflected shock tubes are commonly used to study moving normal shock waves. Generally, test models are not used in the non-reflected shock tube. X2 can be operated in non-reflected shock tube mode, as shown on Figure A.10. The non-reflected shock tube is used to generate a normal shock propagating down a tube. This is useful for studying the relaxation processes behind a normal shock in one-dimension. The benefit of the non-reflected shock tube experiment of studying the moving shock wave is that the freestream condition is accurately defined. The freestream condition is simply the fill condition in the shock tube. The disadvantage of this type of experiment is that radiation measurement of a moving shock can introduce blurring in the measurement. The blurring is reduced by using low exposure times. However, this decreases the signal to noise ratio in the image due to the lower intensities.

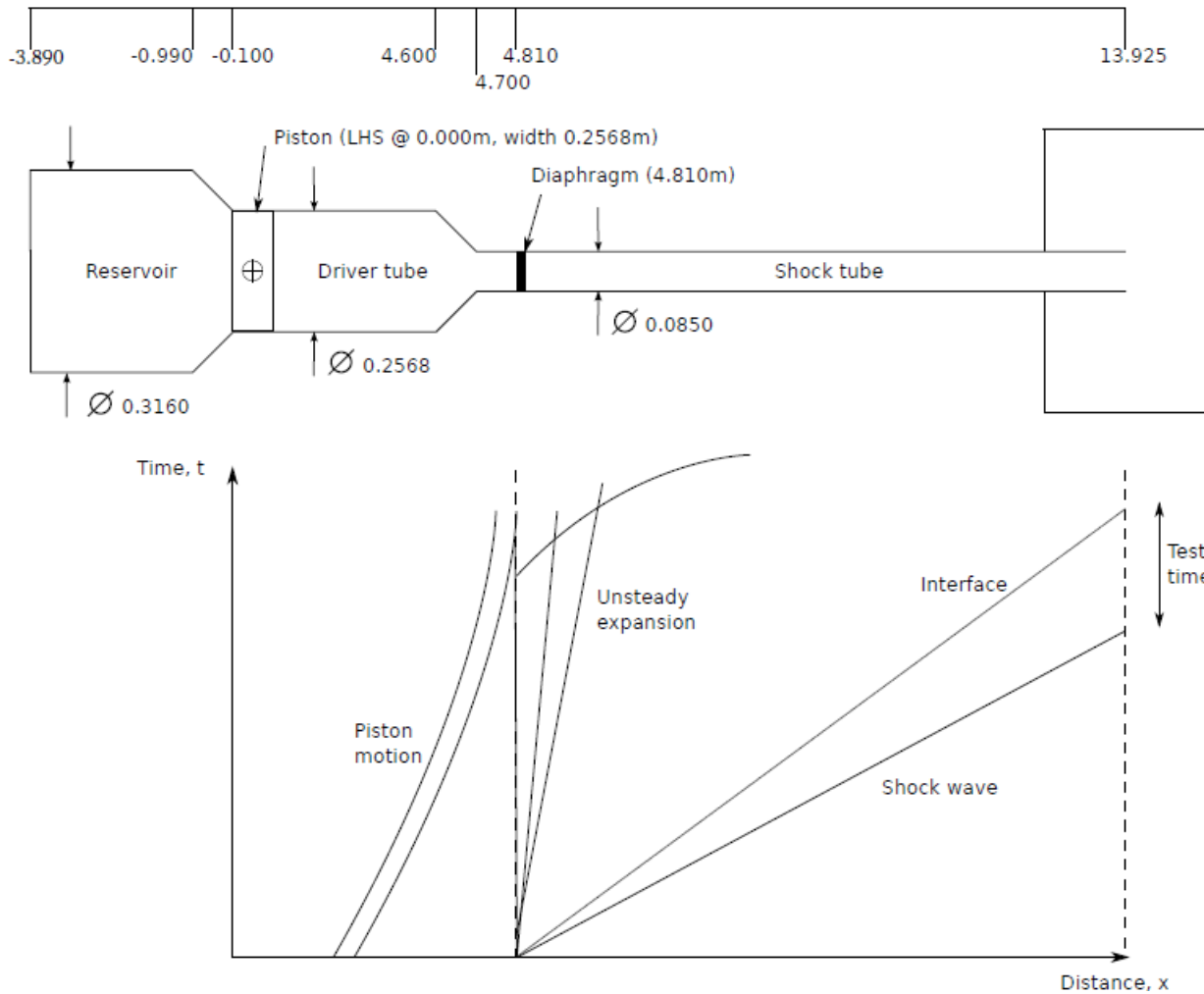


Figure A.10. X2 Non-Reflected Shock Tube [114].

Reflected Shock Tube

Like with the expansion tube, the reflected shock tube, Figure A.11, is used to study high enthalpy flows using test models. However, total enthalpy of the conditions generated in the reflected shock tube is generally significantly lower than that in the expansion tube. Like with the X2 expansion tube, the T4 reflected shock tube at the University of Queensland is driven with a free piston driver and there is a shock tube which is filled with the test gas. However, unlike the expansion tube, there is no acceleration tube. Instead, a reflected shock wave is formed at the secondary diaphragm creating a high temperature and high pressure reservoir of the test gas. The test gas in the reservoir then undergoes a steady expansion through the nozzle creating the freestream condition.

The biggest advantage of the reflected shock tube is that the condition produced have a very long test time compared to the expansion tube. One disadvantage of the reflected shock tube is that the freestream generated will have a higher degree of thermochemical excitation than that generated in

the expansion tube [51]. To generate the same freestream velocity condition, the reflected shock tube would need to shock process the test gas to higher temperatures as compared to the expansion tube. In the reflected shock tube, the test gas gets shock processed two times prior to being expanded through the nozzle. The stagnated test gas entering the nozzle may be dissociated as well as thermally excited. The flow through the nozzle might eventually freeze at some point inside the nozzle. As a result, the flow exiting the nozzle may have significant thermal excitation and a distorted chemical composition [82]. Thus, the chemical composition and degree of thermal excitation of the flow exiting the nozzle needs to be determined in order to correctly interpret the experimental results. Determining this is non-trivial. A major uncertainty associated with the generated conditions in the reflected shock tube is the chemical species in the flow and the degree of thermal excitation [54].

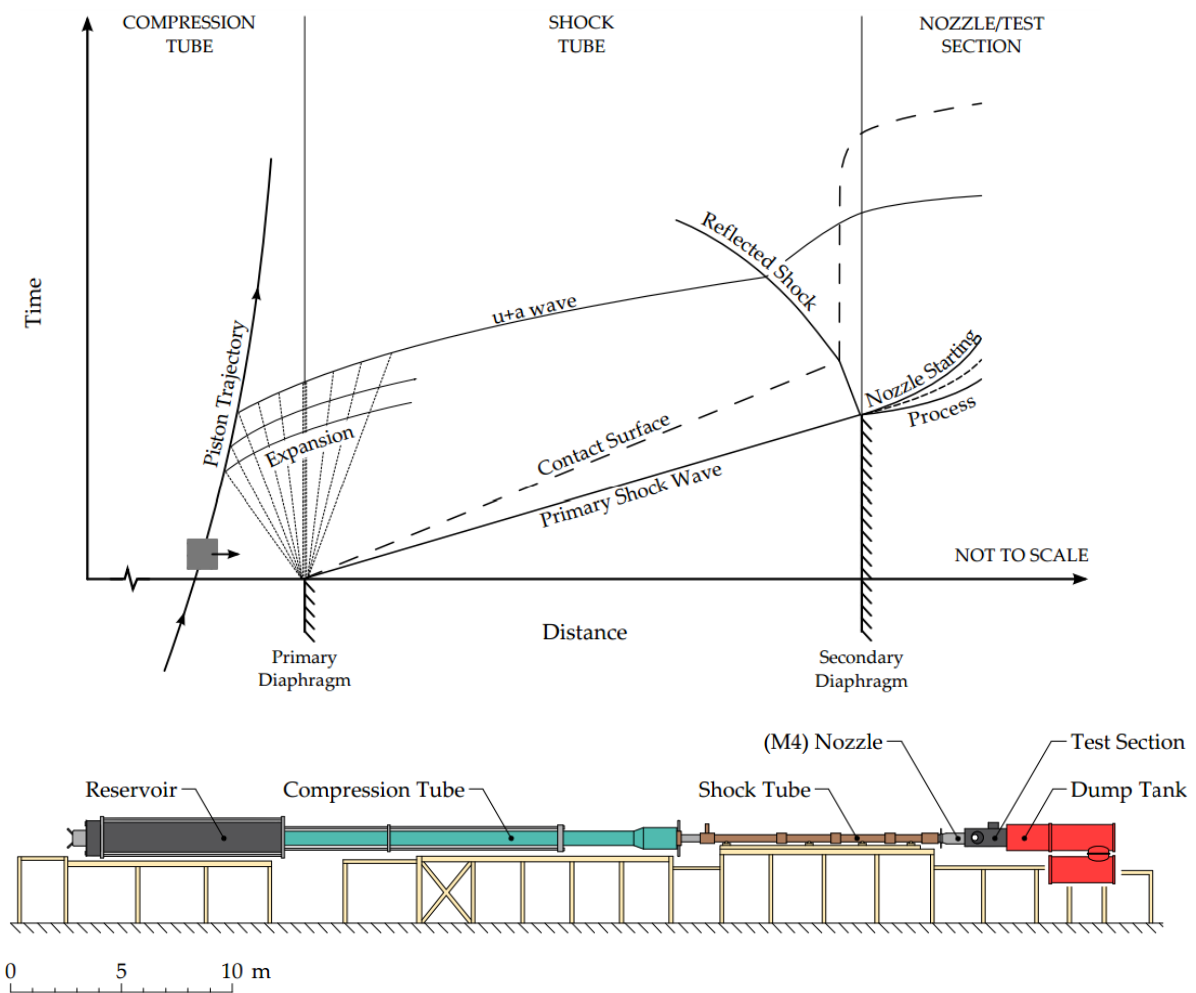


Figure A.11. T4 reflected shock tube [166].

B Engineering Drawings of Cold Driver

The cold driver configuration consists of the design of three parts; the buffer plate, the tension rods and the plug. The dimensions are sized with very large safety factors because the mass of the configuration is not important. All the tension carrying bolts are M16 bolts. Safety is the most important aspect, thus, a very conservative approach is applied. The system will consist of 7 O-rings to provide the necessary sealing for the high pressure helium involved. The seals include 1 face seal on each of the 6 rods, 1 face seal and 1 static piston seal on the buffer plate and 1 static piston seal on the plug. The assembly is inserted into the compression tube to create a fixed volume in the tube.

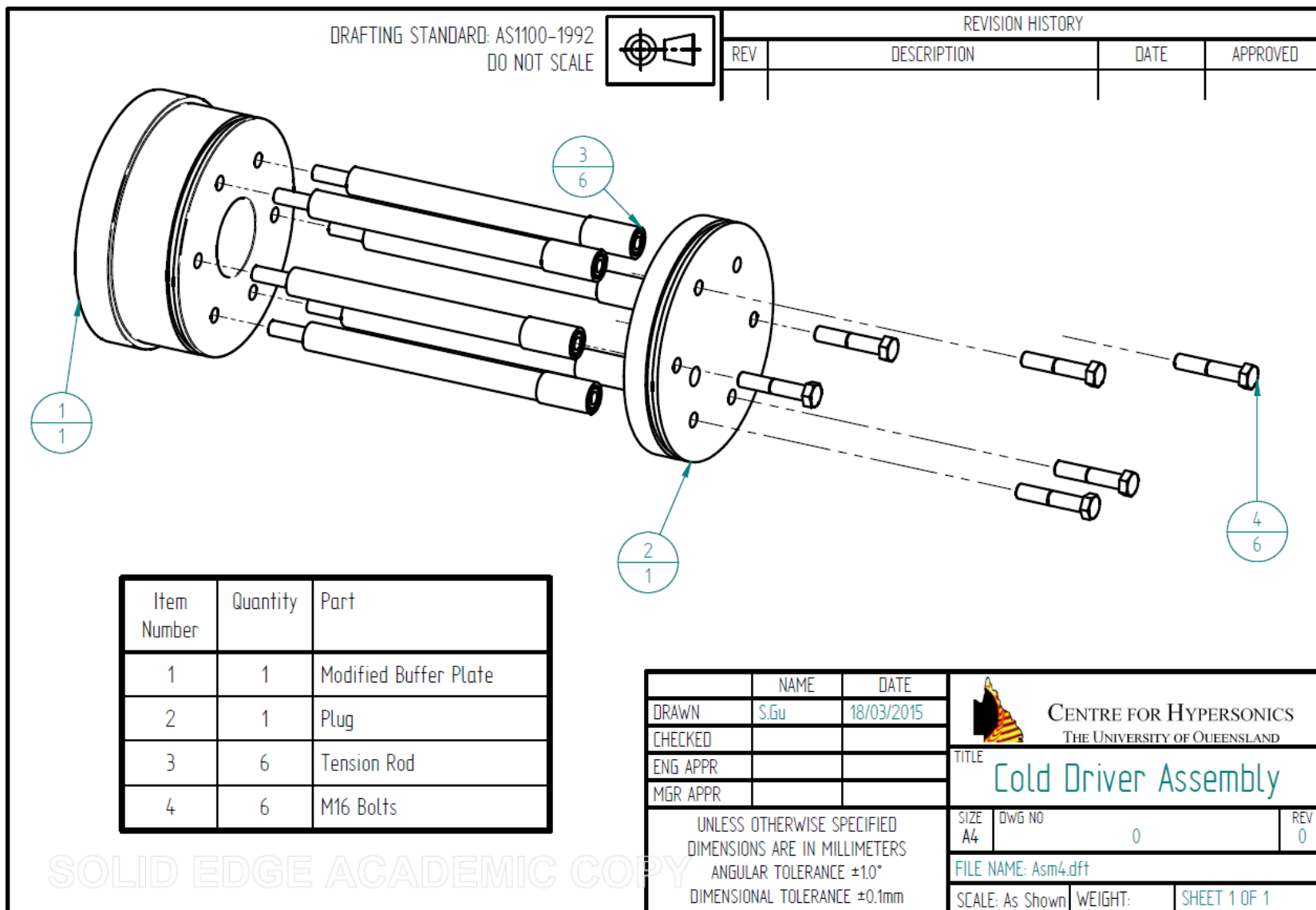


Figure B.1. Assembly drawing for the cold driver configuration.

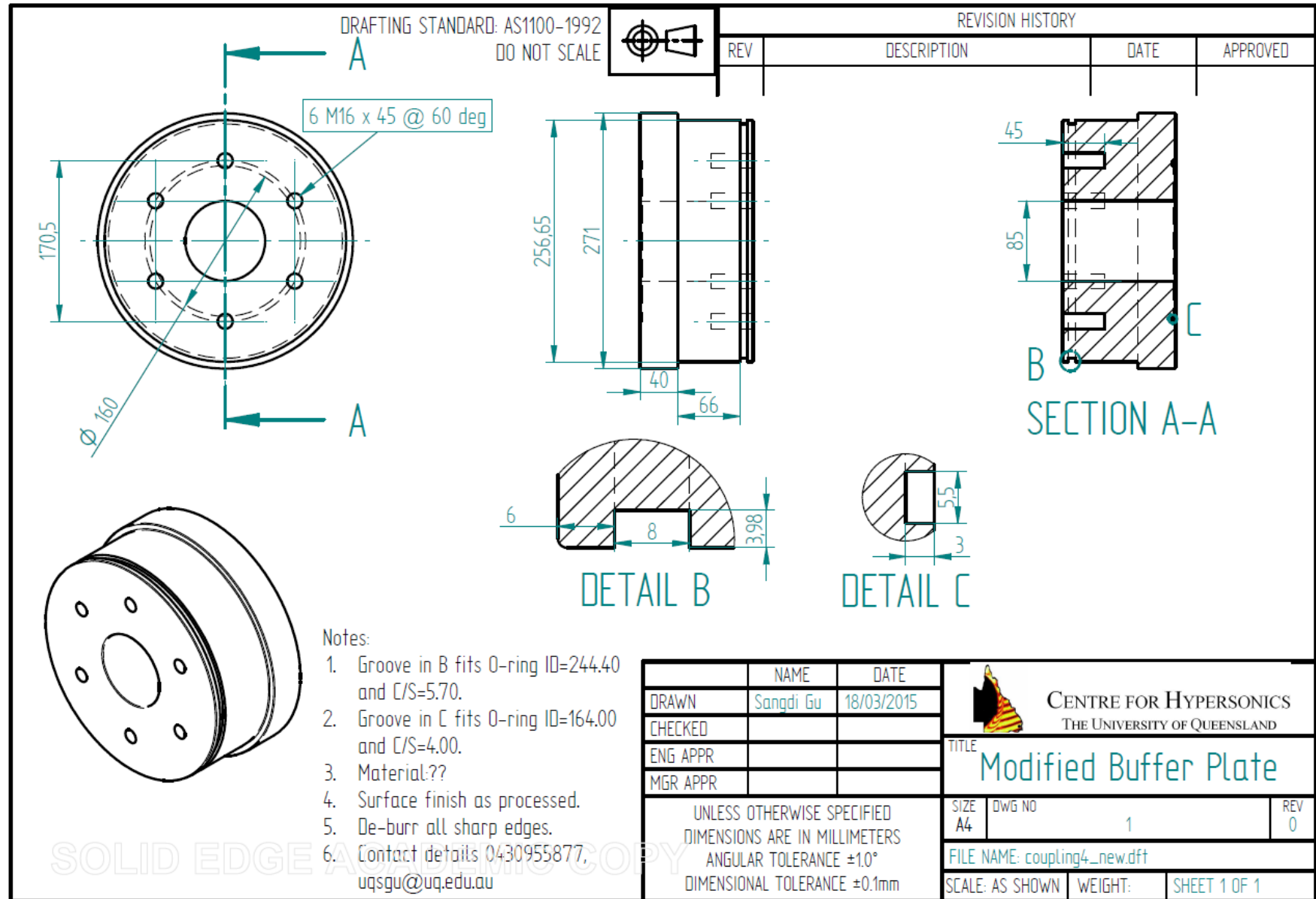


Figure B.2. Engineering drawing of the modified buffer plate.

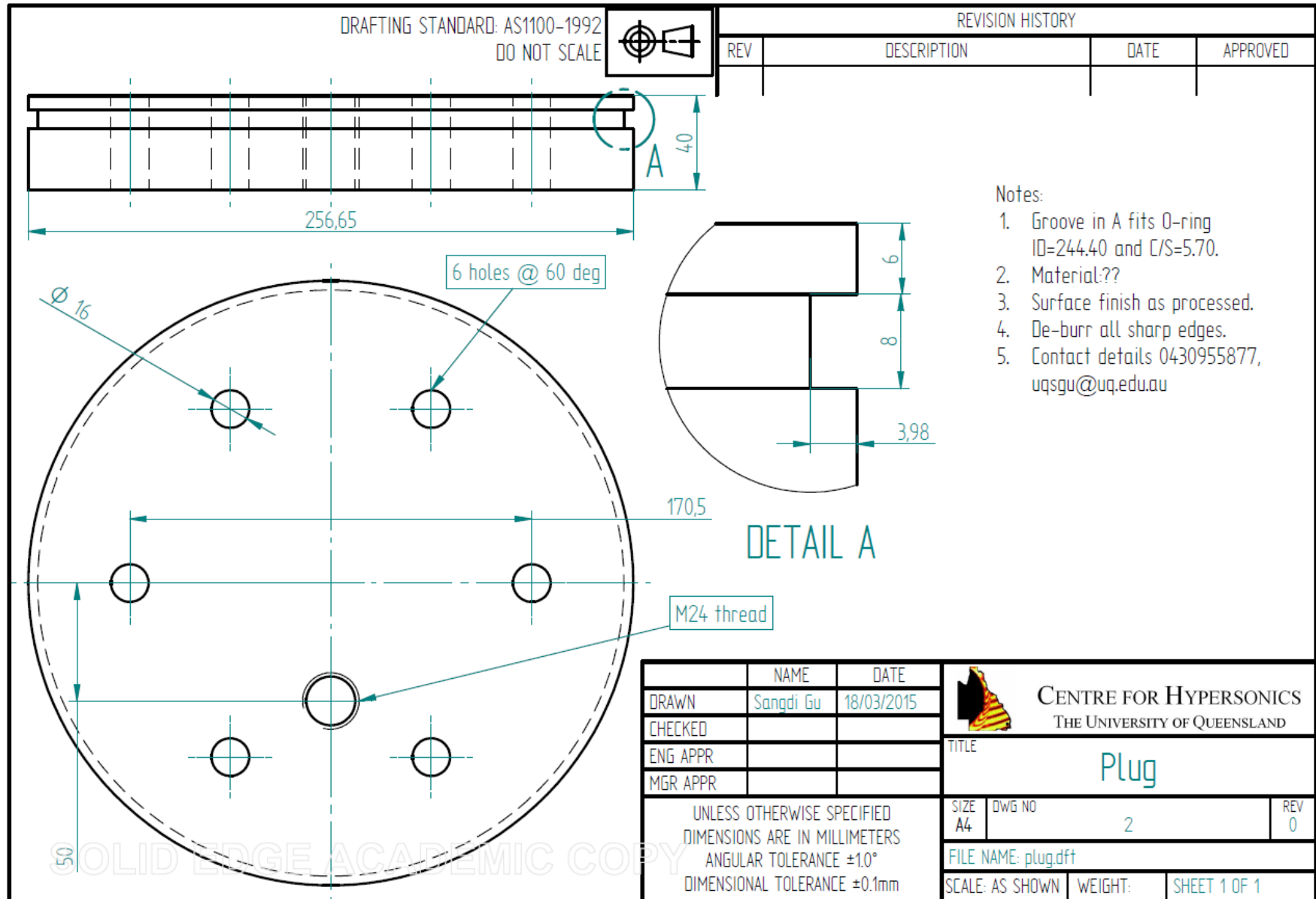


Figure B.3. Engineering drawing of the plug.

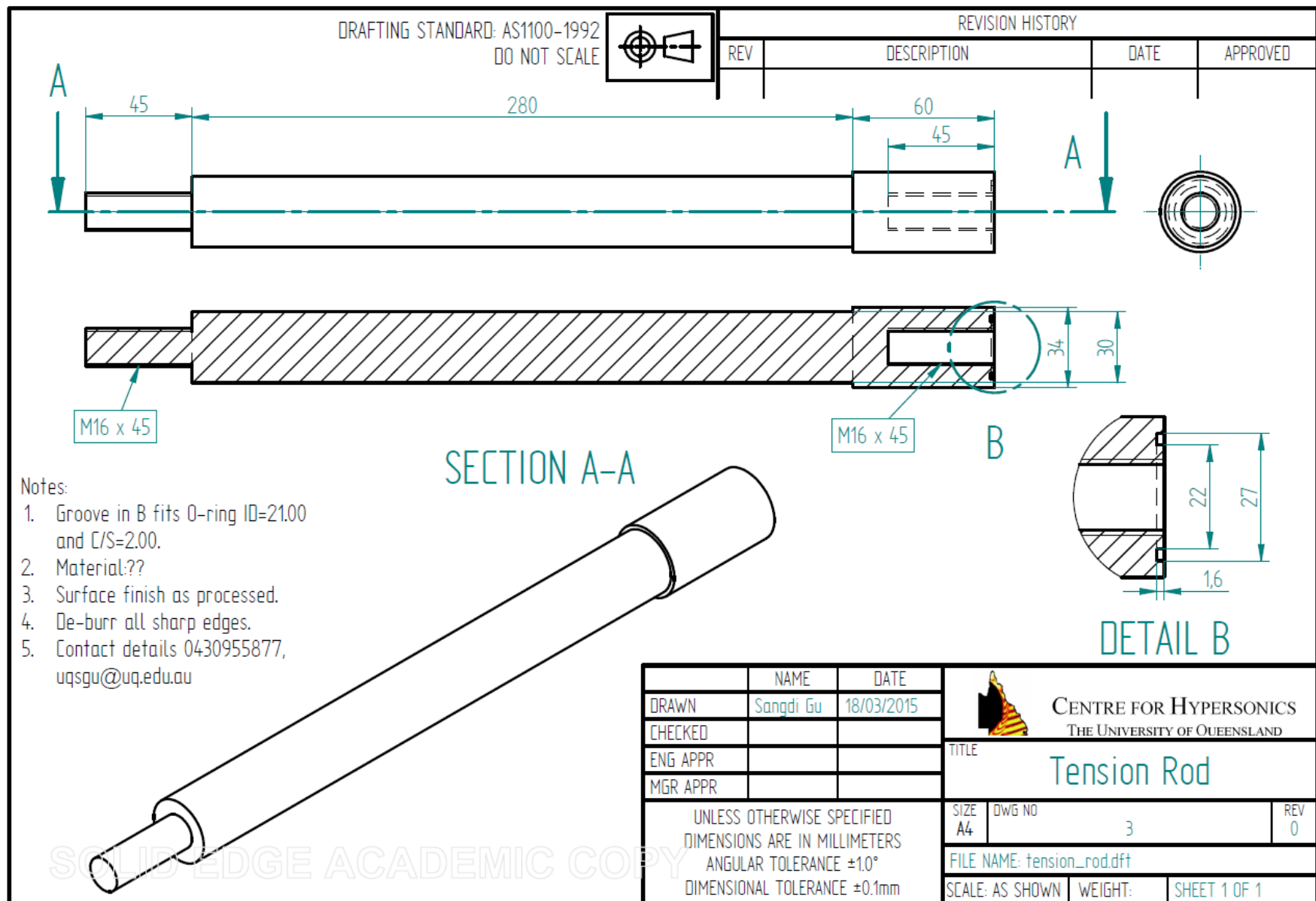


Figure B.4. Engineering drawing of the tension rod.

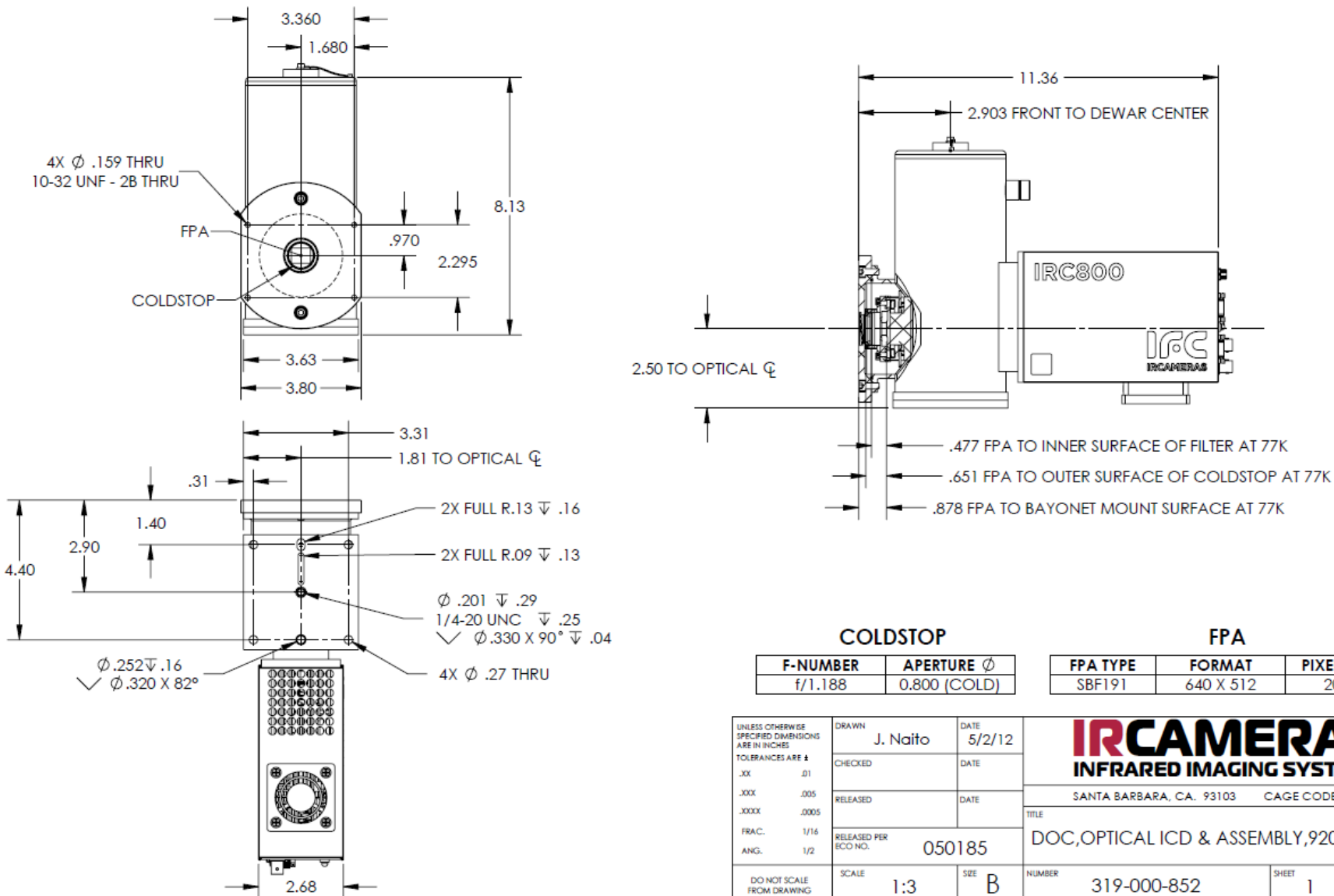
C IR Camera Dewar Modification Instructions

For the infrared to be compatible with the spectrometer, the spectrally resolved signal from the spectrometer needs to be incident on the FPA of the camera. Most spectrometers put the focal plane about 1" from the spectrometer exit, while the standard infrared camera design has the dewar window approximately 1.5" from the FPA. Consequently, the two components are generally incompatible. Thus, it was necessary to modify the camera such that the spectra is focused on the FPA once the camera is mounted on the spectrometer. To do this, the distance between the dewar window and the FPA needs to be shortened to help align the focal plane of the spectrometer with the FPA of the camera. IRCameras provided a dewar modifications kit which allows the dewar in the IRC806HS camera to be shortened. Additionally, the modification contains a custom vacuum cap front plate so that the camera with the shortened dewar can be mounted on the slide tube mount on the SP2556 spectrometer.

THIS DRAWING CONTAINS PROPRIETARY INFORMATION OF
IRCAMERAS INFRARED IMAGING SYSTEMS (IRCAMERAS), AND MAY
NOT BE USED FOR THE MANUFACTURE OF ANY PART DISCLOSED
HEREIN, NOR DUPLICATED, NOR DISCLOSED TO ANYONE,
WITHOUT THE PRIOR WRITTEN PERMISSION OF IRCAMERAS.

OPTICAL INTERFACE CONTROL DRAWING

DRAWN	CHECKED	RELEASED	DATE	REVISED PER ECO	REV.

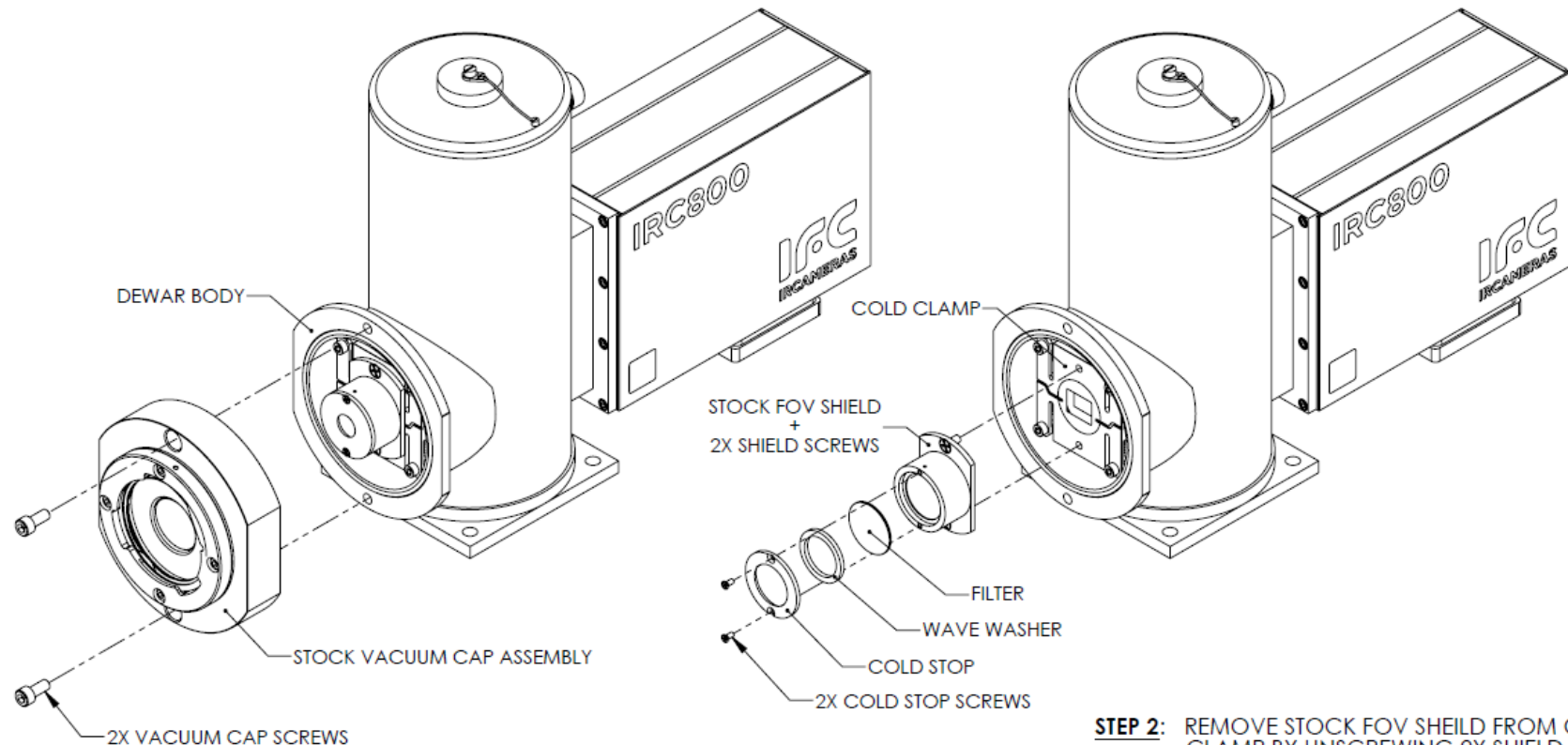


CAD GENERATED / SOLIDWORKS

UNLESS OTHERWISE SPECIFIED DIMENSIONS ARE IN INCHES TOLERANCES ARE ± .001 .005 .0005 1/16 1/2	DRAWN	J. Naito	DATE
	CHECKED		5/2/12
	RELEASED		
	RELEASED PER ECO NO.	050185	
	DO NOT SCALE FROM DRAWING	SCALE	1:3
		SIZE	B
		NUMBER	319-000-852
		SHEET	1 OF 4 NC

DEWAR MODIFICATION INSTRUCTIONS

SEE SHEET 1 FOR REVISIONS



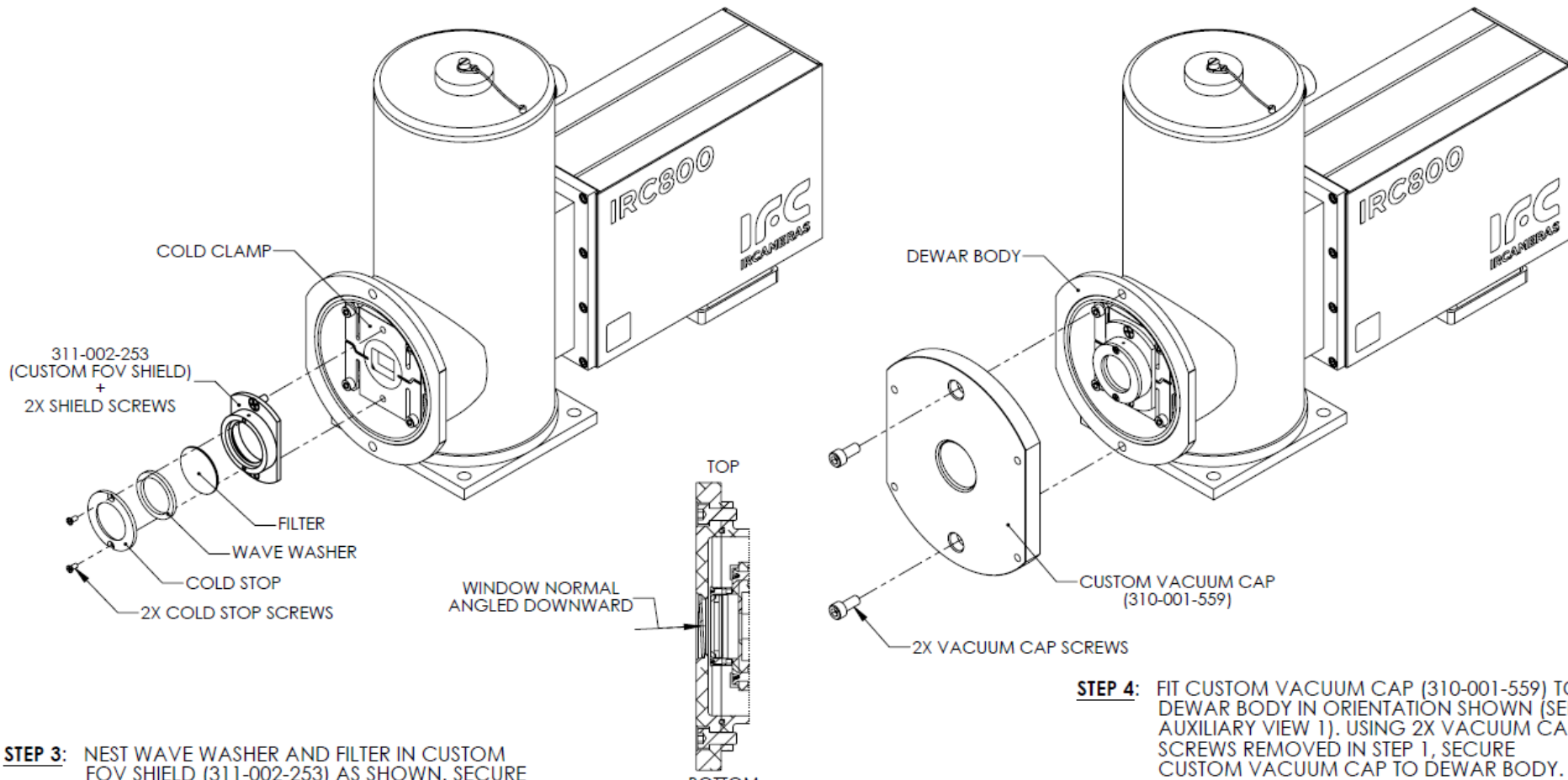
STEP 1: REMOVE 2X VACUUM CAP SCREWS FROM STOCK VACUUM CAP ASSEMBLY. RETAIN THESE SCREWS FOR STEP 4. DETACH STOCK VACUUM CAP ASSEMBLY FROM DEWAR BODY.

STEP 2: REMOVE STOCK FOV SHIELD FROM COLD CLAMP BY UNSCREWING 2X SHIELD SCREWS. BREAK DOWN FOV SHIELD SUB-ASSEMBLY AND RETAIN FILTER, WAVE WASHER, COLD STOP, 2X COLD STOP SCREWS, AND 2X SHIELD SCREWS FOR STEP 3.

TITLE			
SCALE	NUMBER	SHEET	REV
1:2	312-000-831	2	4

DEWAR MODIFICATION INSTRUCTIONS

SEE SHEET 1 FOR REVISIONS



AUXILIARY VIEW 1

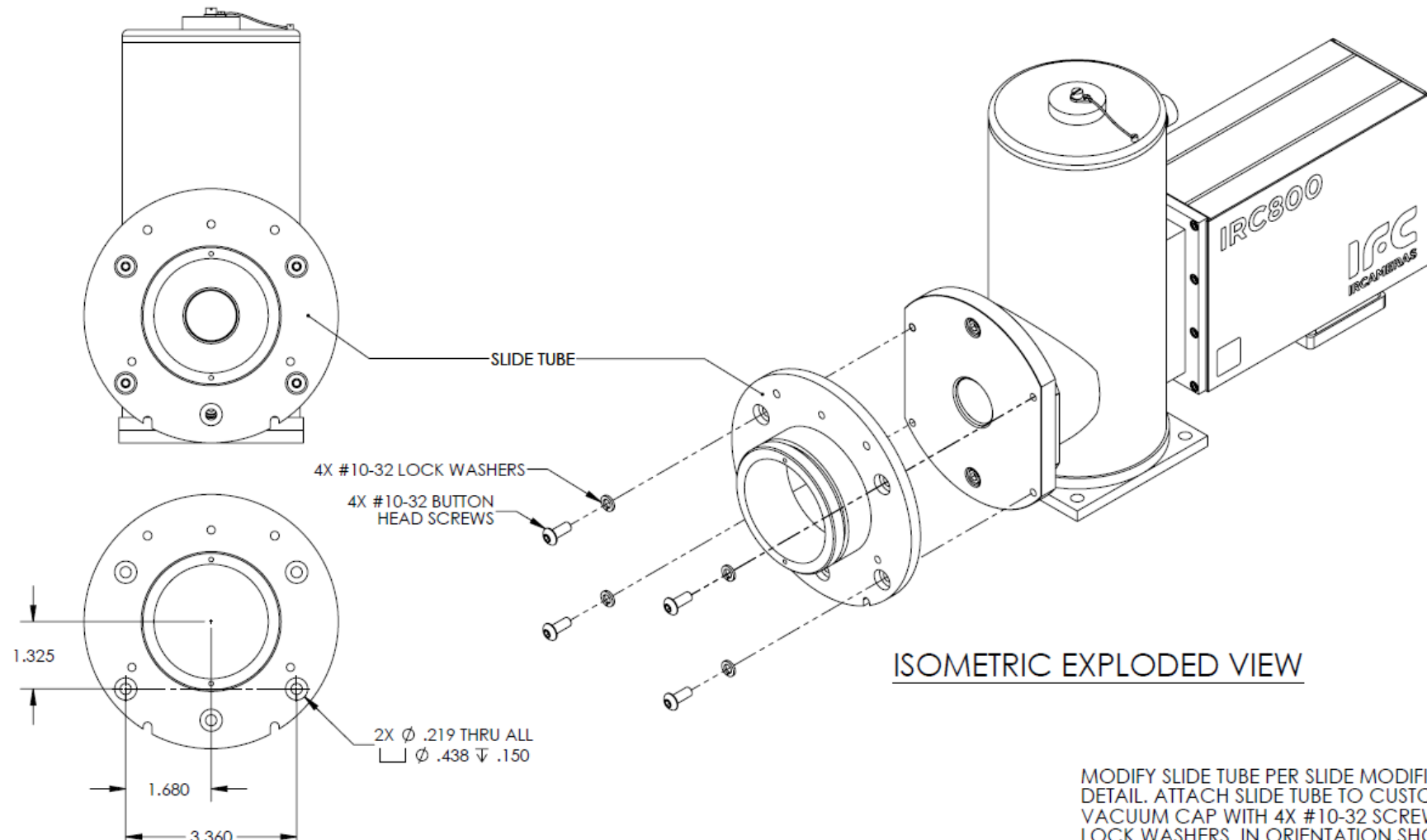
STEP 3: NEST WAVE WASHER AND FILTER IN CUSTOM FOV SHIELD (311-002-253) AS SHOWN. SECURE WAVE WASHER AND FILTER WITH COLD STOP AND 2X COLD STOP SCREWS. ATTACH THIS CUSTOM FOV SHIELD SUB-ASSEMBLY TO COLD CLAMP USING 2X SHIELD SCREWS.

STEP 4: FIT CUSTOM VACUUM CAP (310-001-559) TO DEWAR BODY IN ORIENTATION SHOWN (SEE AUXILIARY VIEW 1). USING 2X VACUUM CAP SCREWS REMOVED IN STEP 1, SECURE CUSTOM VACUUM CAP TO DEWAR BODY.

TITLE			
DOC,OPTICAL ICD & ASSEMBLY,92076 SYSTEM			
SCALE	NUMBER	SHEET	REV
1:2	319-000-852	3	4 NC

SLIDE TUBE INSTALLATION & MODIFICATION INSTRUCTIONS

SEE SHEET 1 FOR REVISIONS



TITLE			
DOC,OPTICAL ICD & ASSEMBLY,92076 SYSTEM			
SCALE	1:2	NUMBER	319-000-852
SHEET	4	OF	4
REV	NC		

D Eilmer3 Two-Temperature Model Configuration Script

D.1 Chemical Kinetics Model

```
-- chemical reaction script

-- From 2014 CO2 radiation paper by Cruden et al. [44]

scheme_t = {
    update = "chemical kinetic ODE MC",
    temperature_limits = {
        lower = 20.0,
        upper = 100000.0
    },
    error_tolerance = 0.000001
}

-- Dissociation reactions
-- forward reaction given, backward reaction calculated from equilibrium constant
reaction{
    'CO2 + M <=> CO + O + M',
    fr={'Park', A=7.47e12, n=0.5, T_a=52321.0, p_name='CO2', p_mode='vibration', s_p=0.5,
    q_name='CO2', q_mode='translation'},
    efficiencies={CO2=1.0, CO=1.0, O2=1.0, O=1.0},
    ec={model='from CEA curves',iT=0}
}

reaction{
```

```

'O2 + M <=> O + O + M',
fr={'Park', A=1.2e14, n=0.0, T_a=54246.0, p_name='O2', p_mode='vibration', s_p=0.5,
q_name='O2', q_mode='translation'},
efficiencies={CO2=1.0, CO=1.0, O2=1.0, O=1.0},
ec={model='from CEA curves',iT=0}
}

```

-- Neutral exchange reactions

```

reaction{
'CO2 + O <=> CO + O2',
fr={'Arrhenius', A=1.69e13, n=0.0, T_a=26461.0},
ec={model='from CEA curves',iT=0}
}

```

D.2 Thermal Kinetics Model

-- thermal energy exchange script

-- From Park et al. [107]

```

scheme_t = {
    update = "energy exchange ODE",
    temperature_limits = {
        lower = 20.0,
        upper = 100000.0
    },
    error_tolerance = 0.000001
}

```

}

-- the ode_t below is for the above scheme

ode_t = {

step_routine = 'rkf',

max_step_attempts = 4,

max_increase_factor = 1.15,

max_decrease_factor = 0.01,

decrease_factor = 0.333

}

mechanism{

'CO2 ~~ (CO, O) : V-T',

rt={'Millikan-White'}

}

mechanism{

'CO2 ~~ (CO2) : V-T',

rt={'Millikan-White', a=36.5, b=-0.0193}

}

mechanism{

'CO ~~ (CO2, CO, O) : V-T',

rt={'Millikan-White'}

}